



HAL
open science

Fractionnement élémentaire et isotopique des éléments sidérophiles : implications pour l'accrétion des éléments volatils sur Terre

Edith Kubik

► **To cite this version:**

Edith Kubik. Fractionnement élémentaire et isotopique des éléments sidérophiles : implications pour l'accrétion des éléments volatils sur Terre. Sciences de la Terre. Université Paris Cité, 2020. Français. NNT : 2020UNIP7097 . tel-03249578

HAL Id: tel-03249578

<https://theses.hal.science/tel-03249578>

Submitted on 4 Jun 2021

HAL is a multi-disciplinary open access archive for the deposit and dissemination of scientific research documents, whether they are published or not. The documents may come from teaching and research institutions in France or abroad, or from public or private research centers.

L'archive ouverte pluridisciplinaire **HAL**, est destinée au dépôt et à la diffusion de documents scientifiques de niveau recherche, publiés ou non, émanant des établissements d'enseignement et de recherche français ou étrangers, des laboratoires publics ou privés.



Université de Paris
Institut Physique du Globe de Paris

École doctorale Sciences de la Terre et de l'environnement et physique de l'Univers STEP'UP n°560

UMR 7154

**Elemental and stable isotopic fractionations of
siderophile elements—Implications for the delivery of
Earth's volatile elements**

Par Edith Kubik

Thèse de doctorat de Géochimie

Dirigée par Frédéric Moynier
Et par Julien Siebert

Soutenue publiquement le 10 décembre 2020 devant un jury composé de :

| | |
|--|-----------------------|
| Ali Bouhifd | Rapporteur |
| CNRS (Université de Clermont-Auvergne) | |
| Klaus Mezger | Rapporteur |
| Professeur (Université de Berne) | |
| Audrey Bouvier | Membre |
| Professeur (Université de Bayreuth) | |
| Catherine Chauvel | Membre |
| CNRS (Université de Paris) | |
| Caroline Fitoussi | Membre |
| CNRS (ENS Lyon) | |
| Wim van Westrenen | Membre |
| Professeur (Université d'Amsterdam) | |
| Frédéric Moynier | Directeur de thèse |
| Professeur (Université de Paris) | |
| Julien Siebert | Co-directeur de thèse |
| Maître de conférence (Université de Paris) | |

Elemental and stable isotopic fractionations of siderophile elements between metal and silicate—Implications for the delivery of Earth’s volatile elements

Abstract

The accretion of volatile elements on Earth continues to be debated despite intense research focusing on the topic. Geochemical and cosmochemical observables have been explained by a variety of scenarios ranging from (1) an accretion of the volatile elements during the main phases of Earth’s formation to (2) an accretion of volatile-poor material followed by a late accretion of volatile-rich material after core formation ceased, called the late veneer. The mantle signature of elements that are both volatile and siderophile record volatile-related processes as well as differentiation-related processes. Studying the behaviour of such elements at metal–silicate equilibrium at high pressure and high temperature allows to separate the effect of differentiation from volatile-related processes on their abundances, and hence to discriminate scenarios capable of explaining the observed abundances.

In this thesis work, the aim is to determine one or a variety of accretion scenarios of the Earth explaining the abundances of moderately volatile and siderophile elements in the mantle. Experiments were performed in piston cylinder and multi-anvil presses from 2 to 20 GPa and 1700 to 2600 K in order to measure the elemental and isotopic behaviour of a selection of moderately siderophile and volatile elements. Studying the partitioning of Sn, Cd, Bi, Sb and Tl allowed to determine the effect of temperature, pressure, fO_2 , and S content of the metal on the affinity of these elements for metal relative to silicate. The partitioning of these elements is reconstructed across Earth’s accretion, at appropriate pressure and temperature conditions. The studied elements present enhanced siderophilicity, preventing reconciliation of the experimental data with observed mantle abundances. A scenario involving partial equilibration of the mantle with the core, as well as a late delivery of volatile elements in the last 10 to 20 % of Earth’s accretion, as a large impactor, is able to explain the abundances of the studied elements, in agreement with other

studies based on distinct observables. Around 3 *wt.*% of S in the core is needed to explain the Sn abundance. A late veneer consisting of 0.5 % of Earth's mass is also required to explain the Bi abundance in the mantle. The study of Sn isotopic fractionation between metal and silicate yields a significant factor of ~ 0.3 ‰ at 2 GPa and 2000 K ($\Delta^{122/118}Sn_{metal-silicate}$), suggesting that Sn isotopes could be fractionated at core formation conditions, enriching the mantle in light isotopes. Carbonaceous chondrites present an identical Sn isotopic composition to the silicate Earth, making them the most likely contributors to the source of volatile elements on Earth, according to this study. These results are consistent with the favoured accretion scenario suggested by the elemental fractionation part of this study. As elemental and isotopic fractionations of siderophile elements between metal and silicate are strongly dependent on the metal composition, the effect of the Ni content of the metal on Fe isotopic fractionation was tested. The experiments performed in this study (22 experiments, from 0 to 70 % Ni in the metal) do not allow to detect any effect of Ni on the Fe fractionation factor. Therefore, this study brings new insight regarding the timing, process and origin of the volatile delivery on Earth, as well as information on the effect of core composition on the behaviour of siderophile elements during Earth's differentiation.

Key words: Metal–silicate partitioning, isotopic fractionation, volatile elements, planetary accretion, tin, core formation, high pressure.

Fractionnement élémentaire et isotopique des éléments sidérophiles entre métal et silicate – Implications pour l'accrétion des éléments volatils sur Terre

Résumé

L'accrétion des éléments volatils sur Terre continue d'être débattue malgré de nombreux travaux de recherche sur le sujet. Les observables géochimiques et cosmochimiques ont été expliquées par une large gamme de scénarios allant de (1) l'accrétion des éléments volatils durant les phases principales de l'accrétion terrestre, jusqu'à (2) l'accrétion de matériaux pauvres en volatils, avec une addition tardive de matériel riche en éléments volatils après la fin de la différenciation, aussi appelée vernis tardif. Les signatures mantelliques des éléments volatils et sidérophiles sont des enregistrements des processus liés à la volatilité et des processus de différenciation. L'étude du comportement de ces éléments dans un équilibre métal-silicate à haute pression et haute température permet de séparer l'effet de la différenciation de l'effet des processus volatils sur les abondances de ces éléments, et donc de discriminer les scénarios capables d'expliquer les abondances observées.

Dans ce travail de thèse, nous cherchons à déterminer le ou les scénarios d'accrétion de la Terre permettant d'expliquer les abondances en éléments volatils et sidérophiles observées dans le manteau. Des expériences menées dans des presses piston-cylindre et multi-enclume de 2 à 20 GPa et de 1700 à 2600 K ont permis d'observer les comportements élémentaires et isotopiques d'une sélection d'éléments volatils et sidérophiles. L'étude du coefficient de partage de Sn, Cd, Bi, Sb et Tl a permis de déterminer l'effet de la température, la pression, la fO_2 , et la concentration en S dans le métal sur l'affinité de ces éléments pour le métal relativement au silicate. Le coefficient de partage de ces éléments est reconstruit au cours de l'accrétion terrestre, aux conditions de pression et température appropriées. Différents scénarios d'accrétion sont testés dans le but de reproduire les mêmes abondances finales que celles observées dans le manteau. Les éléments étudiés présentent une sidérophilie élevée, qui ne permet pas d'expliquer les abondances élevées ob-

servées dans le manteau. Un scénario impliquant un équilibre partiel entre noyau et manteau ainsi qu'une arrivée des éléments volatils dans les 10-20 derniers pourcents des phases principales d'accrétion de la Terre, sous la forme d'un impacteur de grande taille, permettent d'expliquer les abondances de ces éléments, en accord avec d'autres études basées sur d'autres observables. Environ 3 *wt.%* de S dans le noyau sont également nécessaires afin d'expliquer l'abondance en Sn. Un vernis tardif représentant 0,5 % de la masse terrestre est également requis afin d'expliquer l'abondance en Bi dans le manteau. L'étude du fractionnement isotopique de l'Sn entre métal et silicate a permis de mesurer un facteur significatif de $\sim 0.3 \text{ ‰}$ à 2 GPa et 2000 K ($\Delta^{122/118}Sn_{metal-silicate}$), impliquant qu'un fractionnement isotopique de l'Sn pourrait avoir lieu aux conditions de la différenciation terrestre, ayant pour effet d'enrichir le manteau en isotopes légers. Les chondrites carbonées présentent une composition similaire à la Terre silicatée ce qui en fait les meilleures candidates comme source des volatils sur Terre, d'après les résultats de cette étude. Ces résultats sont compatibles avec le scénario d'accrétion favorisé au vu des données élémentaires. Les fractionnements élémentaires et isotopiques des éléments entre métal et silicate étant fortement dépendant de la composition du métal, l'effet de la teneur en Ni dans le métal sur le fractionnement isotopique du Fe est testé. Les expériences réalisées (22 expériences, de 0 à 70 % Ni) ne permettent pas de détecter un effet du Ni sur le fractionnement du Fe. Cette étude apporte donc de nouveaux éléments de réponse concernant le *timing* et le mécanisme d'accrétion, et l'origine des éléments volatils sur Terre, ainsi que des informations sur l'effet de la composition du noyau sur le comportement des éléments sidérophiles lors de la différenciation.

Mots clés : Partage métal-silicate, fractionnement isotopique, éléments volatils, accrétion terrestre, étain, différenciation terrestre, haute pression.

Contents

| | |
|--|-----------|
| Introduction générale | 1 |
| 0.1 Structure interne et composition de la Terre | 1 |
| 0.1.1 Historique | 1 |
| 0.1.2 La méthode géochimique | 2 |
| 0.2 L'accrétion terrestre | 5 |
| 0.2.1 Formation du système solaire et de la Terre | 5 |
| 0.2.2 Histoire thermique de la Terre | 9 |
| 0.2.3 Les météorites comme matériau de construction de la Terre | 11 |
| 0.2.4 Le vernis tardif | 13 |
| 0.3 La différenciation terrestre | 14 |
| 0.3.1 Principe, mécanismes et contraintes temporelles | 14 |
| 0.3.2 Efficacité de l'équilibration noyau-manteau | 16 |
| 0.3.3 Conditions physico-chimiques de la différenciation – Apports de la pétrologie expérimentale | 18 |
| 0.3.4 Le noyau terrestre | 19 |
| 0.4 Accrétion des éléments volatils | 22 |
| 0.4.1 Signature des éléments volatils dans la Terre silicatée | 22 |
| 0.4.2 Les scénarios d'accrétion | 23 |
| 0.4.3 Une méthode expérimentale | 28 |
| 0.5 Objectifs de la thèse | 29 |
| 1 Experimental and analytical methods | 31 |
| 1.1 Experimental methods | 32 |
| 1.1.1 Starting materials | 32 |
| 1.1.2 Piston cylinder experiments | 33 |

CONTENTS

| | | |
|----------|---|-----------|
| 1.1.3 | Multianvil experiments | 36 |
| 1.1.4 | Sample preparation | 38 |
| 1.2 | Analytical methods | 41 |
| 1.2.1 | Electron beam-based analytical methods | 41 |
| 1.2.2 | Laser-ablation inductively-coupled-plasma mass-spectrometry—LA-ICPMS | 46 |
| 1.2.3 | Multi-collector inductively-coupled-plasma mass-spectrometry—MC-ICPMS | 47 |
| 2 | Thermodynamics of metal–silicate equilibria | 53 |
| 2.1 | Achievement of elemental and isotopic equilibria | 53 |
| 2.1.1 | Elemental equilibrium | 54 |
| 2.1.2 | Isotopic equilibrium | 54 |
| 2.2 | Oxygen fugacity | 59 |
| 2.3 | Thermodynamic description of metal–silicate equilibria | 60 |
| 2.3.1 | Valence state determination | 65 |
| 2.3.2 | Activity coefficients | 67 |
| 2.4 | Isotopic equilibrium thermodynamics | 72 |
| 3 | Core formation modelling | 75 |
| 3.1 | Background principles and recent advances | 75 |
| 3.2 | Apparent core–mantle partitioning | 76 |
| 3.3 | Multi-stage continuous core formation models | 79 |
| 3.3.1 | Model parameters | 79 |
| 3.3.2 | Equilibration efficiency | 86 |
| 3.3.3 | Compositionally homogeneous versus heterogeneous accre- tion scenarios | 90 |
| 3.3.4 | Predicting isotopic fractionation factors | 91 |
| 3.4 | Model limitations and future improvements | 93 |
| 3.4.1 | Continuous core formation | 94 |
| 3.4.2 | Fully differentiated impactors | 94 |
| 3.4.3 | Mole fractions versus mass fractions | 95 |
| 4 | Tracing Earth’s volatile delivery with Sn | 97 |
| | Abstract | 98 |

| | |
|--|------------|
| Introduction | 99 |
| Experimental and analytical methods | 103 |
| Results | 107 |
| Discussion | 118 |
| Conclusions | 130 |
| Acknowledgements | 130 |
| Supplementary information | 131 |
| | |
| 5 Earth’s volatile accretion as told by Cd, Bi, Sb and Tl | |
| core–mantle distribution | 139 |
| Abstract | 140 |
| Introduction | 141 |
| Experimental and analytical methods | 144 |
| Results | 147 |
| Discussion | 152 |
| Conclusions | 166 |
| Acknowledgements | 167 |
| Supplementary information | 168 |
| | |
| 6 The effect of nickel on iron isotope fractionation during core for- | |
| mation | 171 |
| Abstract | 172 |
| Introduction | 173 |
| Method | 176 |
| Iron isotopic behavior in metal–silicate equilibrium experiments | 179 |
| Iron isotopic fractionation during core formation | 183 |
| Planetary iron isotopic variability | 184 |
| On ideality in Fe–Ni alloys | 186 |
| Conclusion | 187 |
| Supplementary materials | 188 |
| | |
| 7 Synthesis | 195 |
| 7.1 Conclusions | 195 |
| 7.2 Future work | 198 |
| 7.2.1 Further investigation of MSVE partitioning—Diamond anvil cell experiments | 198 |

CONTENTS

| | | |
|-------|---|-----|
| 7.2.2 | Further investigating the volatile delivery—Cadmium isotopic fractionation between core and mantle | 200 |
| 7.2.3 | Constraining the physical conditions of Earth’s differentiation—Molybdenum isotopic fractionation between core and mantle | 204 |

Introduction générale

0.1 Structure interne et composition de la Terre

0.1.1 Historique

Les premières preuves de la forme sphérique de la Terre sont apportées au IV^{ème} siècle avant J.C. par Aristote qui observa la forme arrondie de l'ombre de la Terre sur la Lune lors des éclipses. La nature et la structure interne de la Terre ont, quant à elles, été découvertes beaucoup plus tard dans l'Histoire. C'est avec l'invention de la sismologie moderne, au début du XX^{ème} siècle, que les différents réservoirs concentriques de la Terre sont distingués et identifiés. Les stations sismographiques permettent d'étudier le temps d'arrivée des ondes sismiques après leur passage dans la Terre profonde. Les ondes sont réfractées selon les propriétés de densité et d'élasticité des milieux traversés, et sont réfléchies sur les discontinuités qui marquent les limites de différents réservoirs. Ainsi, la croûte, les manteaux supérieur et inférieur, le noyau liquide et la graine sont définis spatialement. Le noyau interne, aussi appelé graine, constitue le réservoir le plus interne de la Terre et s'étend jusqu'à 5150 km de profondeur (figure 1). Il est formé par la cristallisation du noyau externe liquide qui l'entoure. À 2890 km, la limite noyau-manteau constitue une discontinuité majeure. Le manteau est divisé en deux réservoirs aux propriétés chimiques distinctes. Le manteau inférieur représente 56 % du volume de la Terre et s'étend de 2890 km à 660 km de profondeur (figure 1), où le manteau supérieur apparaît. Le manteau supérieur est surmonté par la croûte terrestre, tantôt continentale, tantôt océanique, ayant une épaisseur moyenne de 35 et 6 km respectivement. Les travaux de Francis Birch (1952), combinés avec l'étude de la

physique des minéraux à haute pression, dont les pionniers furent Percy Briggman, Alfred Ringwood et Syun-iti Akimoto, permettent d'explorer les propriétés physiques et chimiques de chaque réservoir.

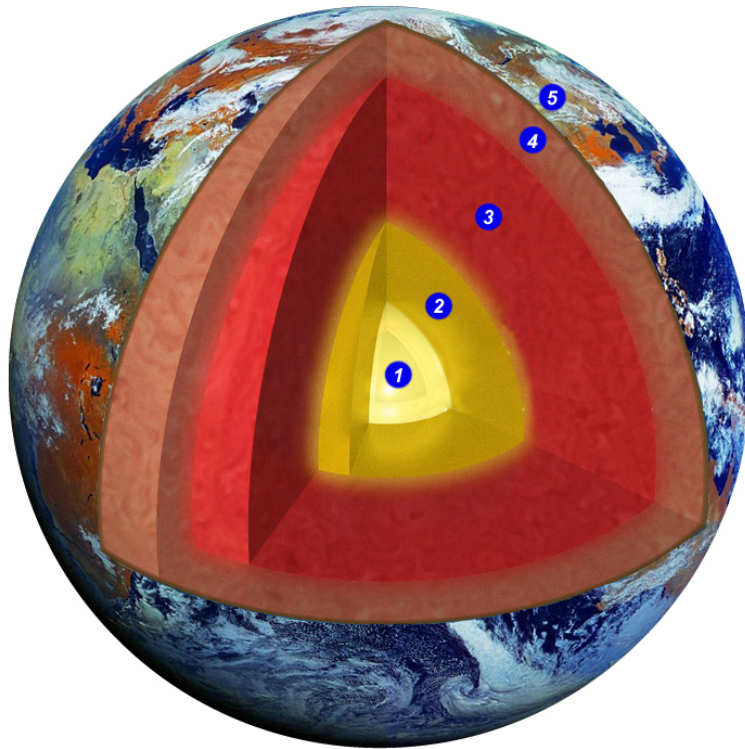


FIGURE 1 – Vue interne de la Terre avec ses principales enveloppes : (1) Noyau interne ou graine, (2) noyau externe, (3) manteau inférieur, (4) manteau supérieur, (5) croûte. Crédits : NASA.

0.1.2 La méthode géochimique

La structure stratifiée de la Terre, déterminée par des méthodes physiques, pose la question de la composition chimique des différentes enveloppes terrestres. C'est l'objet de la géochimie, née dans les années 1920 et fondée par Vladimir Vernadski et Victor Goldschmidt, qui a pour but de caractériser chimiquement les matériaux qui constituent la Terre, et ainsi utiliser ces informations pour déterminer les processus à l'origine des structures géologiques observables sur Terre. La

croûte, enveloppe solide la plus externe de la planète Terre, est aussi la mieux étudiée de par sa localisation favorisant les études géologiques. Le manteau terrestre, situé sous la croûte dont il est séparé par la discontinuité de Mohorovičić, peut être partiellement échantillonné et caractérisé géochimiquement, malgré sa profondeur. En effet, la remontée de fragments du manteau lors de processus volcaniques, appelés enclaves ou xénolithes, a permis de déterminer que le manteau lithosphérique est composé d'une roche appelée péridotite et constituée principalement de cristaux d'olivine et de pyroxène. Les conditions de pression, qui varient dans le manteau selon la profondeur, initient des transitions de phases qui provoquent des réarrangements cristallins. Cependant, la composition chimique du manteau est considérée comme relativement homogène. Cela est attribué à la convection mantellique, qui mélange continuellement le manteau et constitue le moteur de la tectonique des plaques, se manifestant à la surface de la Terre par la remontée de matériel mantellique au niveau des dorsales océaniques et son recyclage dans les zones de subduction. L'étude de reliquats de manteau apportés à la surface de la Terre par des processus magmatiques a permis d'établir une estimation de la composition chimique de la Terre silicatée, qui englobe le manteau et la croûte (McDonough 2003, McDonough and Sun 1995, Palme and O'Neill 2003). Les abondances relatives des éléments chimiques dans le manteau terrestre peuvent être comparées en normalisant les concentrations mesurées dans le manteau par la composition chimique estimée du Système Solaire, afin de faire apparaître les différences entre le manteau terrestre et les briques élémentaires qui ont formé la Terre (figure 2). Les éléments chimiques sont classifiés selon leur volatilité, c'est-à-dire leur capacité à passer d'un état gazeux à un état solide ou liquide, quantifiée par la température de demi-condensation (T_{C50}) qui indique la température à laquelle la moitié des éléments initialement sous forme de vapeur présente un état condensé, et qui correspond à l'échelle des abscisses sur la figure 2. Ces températures sont calculées à 10^{-4} bars, dans des conditions qui sont considérées être celles de la nébuleuse solaire à une distance du proto-Soleil équivalente à la distance Terre-Soleil (Fegley 2000, Lodders 2003). On distingue les éléments réfractaires, dont la température de demi-condensation est supérieure à 1350 Kelvins, des éléments volatils qui incluent les éléments très volatils (T_{C50} inférieure à 500 K) et les éléments modérément volatils (T_{C50} entre 500 et 1 350 K). L'observation des abondances relatives des éléments dans le manteau terrestre en fonction de leur T_{C50} (figure 2) permet de mettre en évidence des groupes d'éléments chimiques qui ont en commun leur affinité pour

les différents réservoirs de la Terre. Les éléments chimiques sont dits lithophiles (Goldschmidt 1937) s'ils ont une affinité pour les roches silicatées telles que celles du manteau. Ainsi, les éléments réfractaires lithophiles présentent des abondances relatives similaires dans la Terre et dans le Système Solaire. Les éléments volatils lithophiles présentent, eux, un appauvrissement qui augmente avec la volatilité, créant une droite de volatilité caractéristique. Tous les autres éléments sont dits sidérophiles et possèdent une affinité préférentielle pour le fer métallique, composant principal du noyau terrestre. Ces éléments sont donc appauvris dans le manteau terrestre par ségrégation dans le noyau terrestre. On distingue les éléments réfractaires sidérophiles des éléments volatils sidérophiles, ces derniers étant doublement appauvris dans le manteau d'une part à cause de leur volatilité et d'autre part en conséquence de leur affinité pour le noyau terrestre. On distingue également les éléments très sidérophiles, qui ont une très forte affinité pour le fer métallique. De nombreuses études ont montré que ces éléments étaient tellement sidérophiles que l'équilibre chimique entre le manteau et le noyau terrestres auraient dû laisser le manteau très appauvri en ces éléments, avec des concentrations extrêmement faibles, environ mille fois plus faibles que les concentrations observées dans des échantillons de manteau. Ces teneurs en éléments très sidérophiles dans le manteau ont par ailleurs permis à ces éléments de migrer dans la croûte continentale où ils sont exploités par l'homme. Ces éléments, dont la présence dans le manteau terrestre ne peut s'expliquer par la différenciation noyau-manteau, ont fait l'objet de nombreuses hypothèses et scénarios afin de réconcilier leurs abondances dans le manteau. Les éléments modérément volatils et sidérophiles (MSVEs) permettent, de par leurs propriétés, d'étudier simultanément les processus liés à la volatilité ainsi que les processus de différenciation, et feront l'objet des travaux de thèse présentés ici.

Les deux sections suivantes sont dédiées aux deux mécanismes majeurs qui ont donné à la Terre la forme, la structure et la composition chimique qui la caractérisent. Il s'agit de l'accrétion de la Terre à partir de matériaux primitifs du Système Solaire, ainsi que sa différenciation en un noyau et un manteau.

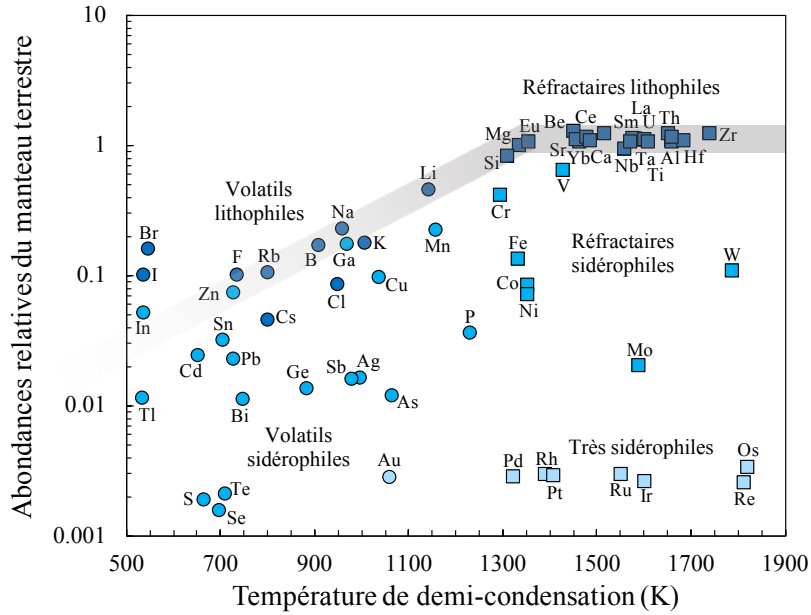


FIGURE 2 – Abondances relatives des éléments chimiques dans le manteau terrestre par rapport à la composition du Système Solaire en fonction des températures de demi-condensation (Clay et al. 2017, Lodders 2003, McDonough 2003). Les éléments réfractaires sont représentés par des carrés et les éléments volatils par des cercles. Les éléments lithophiles se distinguent par un symbole bleu foncé, les éléments sidérophiles sont en bleu clair et les éléments très sidérophiles en bleu pâle. La zone grise met en évidence le domaine des éléments lithophiles et représente la droite d'appauvrissement des éléments volatils. Les abondances relatives sont calculées de la manière suivante : les concentrations estimées de la Terre silicatée sont normalisées à la concentration du magnésium, qui permet de considérer des abondances relatives entre les éléments. Ces abondances sont ensuite normalisées aux abondances dans le Système Solaire, estimées à partir des concentrations chimiques relatives au magnésium mesurées dans les chondrites CI, qui sont des météorites primitives.

0.2 L'accrétion terrestre

0.2.1 Formation du système solaire et de la Terre

L'histoire de la formation de la Terre commence il y a 4,57 milliards d'années par l'effondrement d'un nuage dense et froid de poussière et de gaz, correspondant

à une région dense d'un nuage moléculaire géant (Amelin et al. 2002, Chambers and Halliday 2007, Weissman 2014) similaire à celui présenté sur la figure 3. Le nuage est constitué principalement d'atomes d'hydrogène et d'hélium, mais également de poussière interstellaire incluant d'autres éléments chimiques, vestiges de l'explosion d'étoiles géantes rouges (Dauphas and Chaussidon 2011, Faure and Mensing 2007). Ainsi, un disque de gaz et de poussière est formé et gravite autour du proto-Soleil, dans lequel la matière va migrer vers le centre jusqu'à permettre à la nouvelle étoile de brûler de l'hydrogène. Les vents solaires repoussent ensuite le gaz vers l'extérieur du disque, permettant la condensation de glace (Taylor 2001) et la formation des planètes géantes gazeuses. Les planètes rocheuses sont formées dans un second temps, à partir de matériau sec, rocheux et réfractaire localisé dans les parties internes du Système Solaire, avec probablement une addition de matériaux riches en volatils plus tard dans leur histoire accrétionnelle (Bollard et al. 2017, Schiller et al. 2018) bien que ce point soit très débattu et l'objet même de ces travaux de thèse. La Terre et Vénus auraient été formées en 10 à 100 millions d'années. Dans un premier temps, les forces électrostatiques constituent le moteur de l'agglomération des grains de poussière. Ensuite, l'accrétion des planètes rocheuses est dominée par l'attraction gravitationnelle dès que les éléments accrétés atteignent une taille de 1 à 10 km de diamètre. De tels objets sont appelés planétésimaux (Wetherill and Stewart 1989). La figure 4 représente l'évolution d'une simulation numérique reproduisant la formation des planètes rocheuses (Morbidelli et al. 2012). Les planètes vont ensuite incorporer des embryons planétaires de plus grosse taille, appelés protoplanètes. Selon Chambers (2004), la formation d'une dizaine de ces protoplanètes, de tailles similaires à Mars ou la Lune, serait achevée après 0,1 à 1 Ma. La collision entre des corps d'une telle masse est appelée impact géant (Rubie et al. 2007). Cette dernière phase accrétionnelle a laissé le Système Solaire tel qu'il est observé aujourd'hui, avec quatre planètes rocheuses et quatre planètes gazeuses orbitant autour du Soleil, dont la disposition est présentée sur la figure 5.

La Terre est la plus massive des planètes rocheuses du système solaire, et sa formation implique l'accrétion par gravité d'objets de tailles croissantes. On pense que la dernière étape de sa formation consiste en un impact géant avec une protoplanète de taille comparable à celle de Mars. Cet épisode serait également à l'origine de la formation de la Lune, accrétée à partir des débris expulsés lors de cet impact de grande ampleur, et qui auraient d'abord formé un disque gravitant



FIGURE 3 – Photo de la nébuleuse M42 dans la constellation d'Orion prise par le télescope spatial Hubble. Considéré comme une pouponnière d'étoiles, cette nébuleuse est probablement similaire au nuage moléculaire géant dans lequel le Système Solaire s'est formé. Crédits : NASA/ESA.

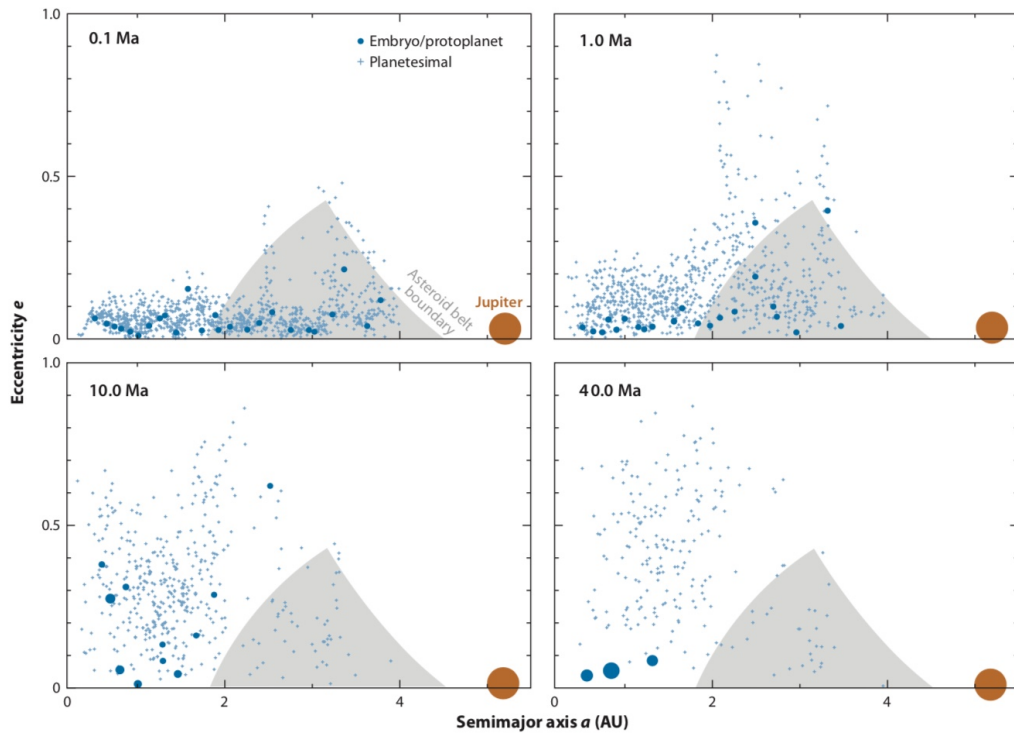


FIGURE 4 – Résultats de simulations numériques modélisant la formation des planètes rocheuses à partir d’un disque de planétésimaux et d’embryons planétaires. Chaque figure montre une vue instantanée du système à un temps donné, avec en abscisse l’axe semi-majeur en AU ou unité astronomique (distance entre la Terre et le Soleil, égale à 150 Mkm), et en ordonnée l’excentricité des orbites des corps représentés. Les tailles des embryons et protoplanètes représentés par les points bleu foncé sont proportionnelles à la racine cubique de leur masse mais ne sont pas à l’échelle par rapport à l’axe des abscisses. Jupiter n’est pas à l’échelle par rapport aux autres corps planétaires. Dans cette simulation, trois planètes rocheuses se forment et la plus grosse a approximativement la masse de la Terre, et seule une petite proportion de la population de planétésimaux est maintenue dans la ceinture d’astéroïdes. Figure extraite de Morbidelli et al. (2012) utilisant des données de O’Brien et al. (2006).

autour de la Terre puis se seraient rapidement accrétés (Canup 2012, Čuk and Stewart 2012, Geiss and Rossi 2013), comme représenté sur la figure 6.

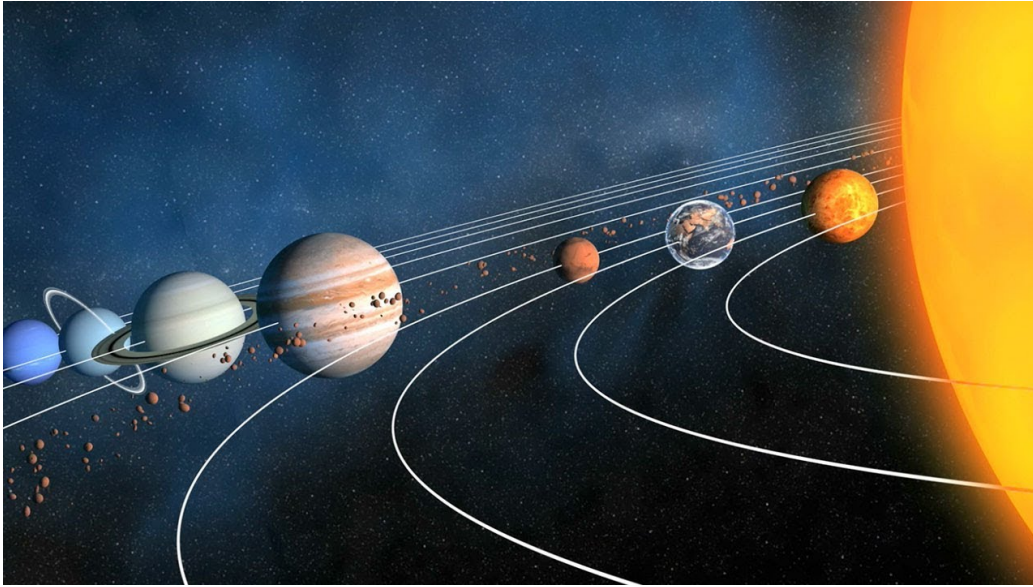


FIGURE 5 – Vue montrant les planètes du Système Solaire telles qu’elles sont observées aujourd’hui. Les échelles ne sont pas respectées. Du Soleil vers le Système Solaire externe il y a : Mercure (trajectoire uniquement), Vénus, Terre, Mars, Jupiter, Saturne, Uranus, Neptune et Pluton (trajectoire seulement). Crédit : NASA.

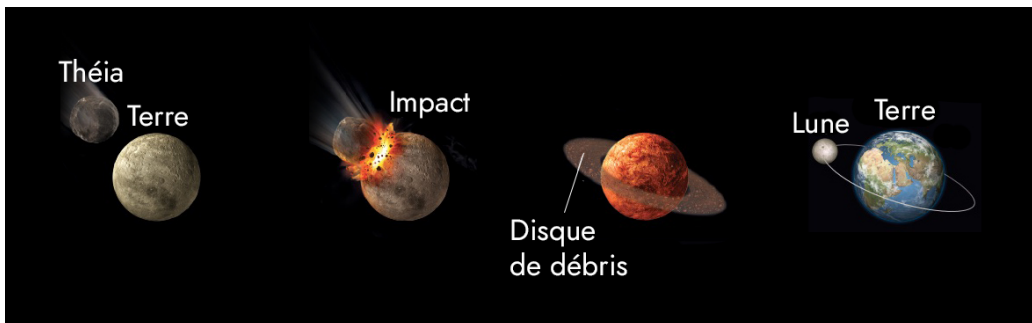


FIGURE 6 – Schéma montrant les principales étapes de la formation de la Lune par impact géant entre la proto-Terre et une planète de la taille de Mars appelée Théia, dont le disque de débris s’accrète pour former la Lune. Adapté de Astronomy magazine par Alexia Schroeder.

0.2.2 Histoire thermique de la Terre

Il est important de considérer l’évolution thermique de la Terre car la formation du noyau nécessite des températures élevées, qui notamment faciliteraient

la formation d'un océan de magma, constituant un mécanisme très efficace de ségrégation du noyau. De plus, les processus thermiques affectant les embryons accrétés pour former la Terre doivent être connus car ils déterminent si la Terre a été formée de matériaux différenciés ou non. (1) La désintégration radioactive de radionucléides à courte période de demi-vie, (2) l'énergie cinétique libérée lors des impacts géants ainsi que (3) la conversion d'énergie gravitationnelle en chaleur lors de la ségrégation du métal à travers le manteau silicaté (Rubie et al. 2007) sont considérés comme les principales sources thermiques entrant en jeu lors de la formation de la Terre. Il a été montré que les collisions entre des corps de tailles inférieures à quelques kilomètres de diamètre ne suffirait pas pour induire leur fusion (Keil et al. 1997). Cependant, la désintégration radioactive de ^{26}Al et ^{60}Fe , avec des demi-vies de 0.73 et 1.5 Ma respectivement (Rubie et al. 2007) pourrait permettre d'atteindre des températures d'environ 1000°C ou plus dans des petits corps, ce qui signifie que le point de fusion de Fe-FeS pourrait être atteint. Des objets déjà différenciés ont donc probablement contribué à l'accrétion terrestre (Greenwood et al. 2005, Yoshino et al. 2003). La fusion de ces petits corps grâce à la désintégration radioactive doit alors avoir lieu lors des phases précoces de la formation du Système Solaire, soit durant le 1^{er} million d'années (Baker et al. 2005). Cependant, l'existence d'astéroïdes indifférenciés tels que Cérès (Thomas et al. 2005) remet en question l'ampleur d'un tel processus, et suggère que la Terre ait été accrétée d'un mélange d'objets différenciés et indifférenciés (Rubie et al. 2007).

Les derniers stades de l'accrétion terrestre sont marqués par des impacts de plus en plus violents, permettant la formation d'un ou plusieurs océans de magma (Benz and Cameron 1990, Melosh 1990, Rubie et al. 2007, Tonks and Melosh 1993). Il a été montré que l'impact lié à l'épisode qui a formé la Lune a potentiellement provoqué la fusion de la Terre dans son ensemble (Cameron 2000, Canup and Asphaug 2001), avec une température moyenne atteignant plusieurs milliers de Kelvins (Rubie et al. 2007). La différenciation pourrait permettre la ségrégation de ^{40}K dans le noyau (Murthy et al. 2003), apportant une source thermique supplémentaire dans le noyau des planètes rocheuses.

0.2.3 Les météorites comme matériau de construction de la Terre

Les météorites sont des objets d'origine extraterrestre qui ont été conservés après leur passage à travers l'atmosphère terrestre. On distingue les chutes (*falls*), dont la chute est observée, des trouvailles (*finds*). Les météorites sont des reliquats de matériaux qui n'ont pas été accrétés aux planètes du Système Solaire. Selon leur texture, les météorites sont classifiées comme différenciées et indifférenciées. Les météorites différenciées ont subi la fusion et la différenciation et sont subdivisées en achondrites, météorites de fer, et météorites mixtes (ou sidérolithes). Les chondrites sont des météorites primitives, provenant d'astéroïdes indifférenciés, et peuvent donc être considérées comme des vestiges du Système Solaire précoce. Elles sont aussi les plus abondantes et représentent 90 % des météorites référencées. Elles sont composées de chondres, de métaux, de sulfures et d'inclusions réfractaires englobés dans une matrice. Les chondres sont des petits objets sphériques, entre quelques centaines de microns et quelques millimètres de diamètre, dont l'agglomération a eu lieu très tôt dans l'histoire du Système Solaire. Les inclusions réfractaires, riches en calcium et aluminium, sont considérées comme les premières phases à s'être condensées dans le Système Solaire et ont été datées à $\sim 4,567$ Ga (Amelin et al. 2002, Bouvier et al. 2007, Bouvier and Wadhwa 2010, Connelly et al. 2012). Trois classes de chondrites peuvent être distinguées en fonction de leur composition chimique et de leur état d'oxydo-réduction : les chondrites ordinaires, les chondrites à enstatite et les chondrites carbonées. Ces classes sont subdivisées en groupes, et les chondrites d'un même groupe proviennent probablement d'un même corps parent.

Les chondrites ordinaires représentent la majorité des météorites trouvées sur Terre (77 % des météorites référencées). En termes d'état d'oxydo-réduction et de teneur en éléments volatils, elles présentent des valeurs intermédiaires entre les chondrites à enstatite, « sèches » et réduites et les chondrites carbonées, oxydées et riches en éléments volatils.

Les chondrites à enstatite sont les météorites les plus réduites d'après l'état des connaissances actuelles. En utilisant le tampon fer-wüstite (iron-wüstite ou IW) qui définit l'équilibre entre du fer métallique et du fer oxydé à un état de valence 2+, elles se situent entre IW-6 et -8 (Fogel et al. 1989). Elles contiennent également

des minéraux spécifiques aux conditions extrêmement réduites (oldhamite CaS et niningérite (Mg,Fe,Mn)S). Leurs caractéristiques principales – pauvres en éléments volatils et réduites – permettent de déterminer leur origine spatiale qui serait relativement proche du Soleil, probablement au niveau de l’orbite de Mercure.

Les chondrites carbonées sont beaucoup plus oxydées, autour de IW-2 et -3 (Righter et al. 2016) par rapport aux chondrites à enstatite, et sont aussi les plus primitives. Les chondrites carbonées, et plus particulièrement les chondrites de type CI (chondrites carbonées appartenant au groupe d’Ivuna), sont les matériaux dont la composition est la plus proche de celle du Soleil. Leur composition chimique s’approche donc de la composition moyenne du Système Solaire, et est généralement considérée comme la composition des matériaux de départ qui ont formé les planètes rocheuses et donc la Terre (Allègre et al. 1995, Anders 1964, Anders and Grevesse 1989, Palme and O’Neill 2014). Elles présentent des abondances relatives similaires à la Terre silicatée pour les éléments lithophiles réfractaires (figure 2). De plus, les similarités entre la signature isotopique de l’hydrogène et de l’azote sur Terre et dans les chondrites carbonées indiquent que ces dernières sont probablement à l’origine de l’eau et des autres éléments volatils sur Terre (Alexander et al. 2012) ainsi que sur la Lune (Saal et al. 2013), bien qu’il ait été récemment montré que les chondrites à enstatite pourraient également avoir apporté l’eau terrestre (Piani et al. 2020). Un message similaire peut être déduit de l’étude des isotopes du silicium, magnésium et calcium dans les chondrites (Armytage et al. 2011, Pringle et al. 2014, Wiechert and Halliday 2007). Toutefois, il a également été proposé que la Terre puisse être accrétée de matériaux issus de plusieurs familles de météorites (Drake and Righter 2002). Les isotopes du silicium ont permis de proposer un modèle d’accrétion terrestre à partir d’un mélange de plusieurs types de chondrites, carbonées et ordinaires (Fitoussi et Bourdon, 2012). Des modèles prenant en compte l’évolution des conditions de pression, de température et de l’état d’oxydo-réduction (fO_2) de la Terre prédisent des scénarios hétérogènes où des matériaux réduits tels que les chondrites à enstatite, s’accrètent dans un premier temps, suivi par l’addition de matériaux de plus en plus oxydés (Cartier et al. 2014, Rubie et al. 2011, 2015, Schonbachler et al. 2010, Wanke and Gold 1981). Cette hypothèse est corroborée par des modèles numériques prédisant la migration des planètes géantes gazeuses vers les parties internes du Système Solaire, apportant des matériaux plus oxydés et riches en éléments volatils (Jacobson and Morbidelli 2014, Morbidelli et al. 2012, Walsh and Morbidelli 2011, Walsh et al. 2012), avant

leur migration vers leurs orbites actuelles. Ce modèle est appelé « Grand Tack » et permettrait d'expliquer la grande diversité chimique observée dans la ceinture d'astéroïdes. D'autre part, la signature isotopique de plusieurs éléments chimiques, tels que le calcium, le chrome, le molybdène, le nickel, l'oxygène et le titane dans la Terre silicatée est similaire à celle des chondrites à enstatite (Burkhardt et al. 2011, Clayton et al. 1984, Dauphas et al. 2014, Mougel et al. 2018, Regelous et al. 2008, Trinquier et al. 2008), permettant de discuter de leur rôle lors de la formation de la Terre. Javoy (1995), Javoy et al. (2010), et Kaminski and Javoy (2013) défendent par ailleurs un modèle d'accrétion de la Terre à partir de chondrites à enstatite uniquement, même si d'autres études ont suggéré qu'un tel matériau n'a pas pu participer significativement à la formation de la Terre (Fitoussi and Bourdon 2012, Savage and Moynier 2013). Dans ces travaux de thèse, l'étude de l'accrétion et la différenciation terrestre par des traceurs géochimiques, dont les abondances actuelles sont héritées des conditions chimiques initiales du système Terre, va permettre d'apporter de nouveaux éléments de réponse concernant la composition des briques élémentaires à l'origine de la Terre.

0.2.4 Le vernis tardif

Le vernis tardif a été invoqué pour la première fois afin d'expliquer les concentrations des éléments très sidérophiles dans le manteau terrestre, tels que les éléments du groupe du platine (O'Neill et al. 1995). En effet, les éléments très sidérophiles ont une très forte affinité pour le noyau terrestre, mais présentent toutefois des abondances relativement élevées dans la Terre silicatée (figure 2). Ces abondances sont estimées à plusieurs ordres de grandeur trop élevées pour être expliquées par une accrétion suivie d'un équilibre noyau-manteau (Chou et al. 1983, Holzheid et al. 2000, Kimura et al. 1974, Mann et al. 2012, Palme and O'Neill 2003). Certaines études suggèrent néanmoins que leur affinité pour le noyau pourrait être amoindrie par les hautes conditions de pression et de température régnant lors de la différenciation (Danielson et al. 2005, Righter and Drake 1997, Rubie et al. 2016). Il a donc été proposé qu'une petite quantité de matériel chondritique, environ 0,5 % de la masse terrestre, ait été accrétée à la Terre après la fin de sa différenciation. Ce vernis tardif est ensuite mélangé au manteau par convection, sans être équilibré avec le noyau qui aurait pour effet de pomper la majorité des élé-

ments très sidérophiles dans le noyau métallique. Un tel scénario a été repris pour expliquer d'autres observables cosmochimiques. Des mesures récentes des isotopes du ruthénium et du sélénium ont estimé qu'une petite quantité de chondrites carbonées a été accrétée après la différenciation terrestre (Fischer-Gödde et al. 2020, Varas-Reus et al. 2019). Un vernis tardif de composition similaire est proposé pour expliquer les rapports de soufre, sélénium et tellure (Wang and Becker 2013). Des calculs de bilan de masse sur des mesures de gaz rare favorisent un vernis tardif plus réduit, inférieur à 0,5 % de la masse terrestre (Dauphas and Marty 2002). Au contraire, des simulations numériques de scénario Grand Tack, liés à la migration des planètes géantes au sein du système solaire, prédisent un vernis tardif de plus grande ampleur (O'Brien et al. 2014). Même si la quantification du vernis tardif mène à des désaccords selon les études, le fait que de nombreuses observables cosmochimiques étudiées à travers diverses méthodes nécessitent un tel processus afin d'être expliquées renforce cette hypothèse.

0.3 La différenciation terrestre

0.3.1 Principe, mécanismes et contraintes temporelles

La différenciation en un noyau et un manteau constitue le moteur principal à l'origine de la structure stratifiée de la Terre. Durant les stades tardifs de la formation de la Terre, la libération d'énergie cinétique et gravitationnelle lors des impacts a probablement induit la fusion d'une grande partie de la surface terrestre, favorisant des stades transitoires ou prolongés d'océan de magma profond recouvrant la Terre (Tonks and Melosh 1993). Le temps de cristallisation d'un tel réservoir de magma serait de l'ordre du millier d'années (Pritchard and Stevenson 2000, Solomatov and Moresi 2000), et pourrait être significativement prolongé par une atmosphère épaisse ou une croûte solide isolante retardant le refroidissement (Spohn and Schubert 1991). Ce processus constitue un mécanisme privilégié pour la ségrégation du noyau de par la différence de densité importante entre le métal liquide et le silicate liquide qui se sépareraient naturellement par gravité à la base de l'océan de magma, comme représenté sur la figure 7. Des études expérimentales ont montré que les abondances en éléments sidérophiles dans le manteau sont le produit d'un équilibre métal-silicate à très haute pression (Mann et al. 2009), com-

patible avec un équilibre dans un contexte d’océan de magma profond. D’autres mécanismes possibles de ségrégation proposés impliquent la percolation ainsi que la migration sous la forme de diapirs et/ou par circulation dans des dikes ou fractures. Ces mécanismes dépendent des propriétés physiques de la Terre primitive. Indépendamment du processus de ségrégation considéré, la migration du métal vers le centre de la Terre aura pour effet la conversion d’énergie potentielle gravitationnelle en chaleur, augmentant la température du noyau de quelques centaines à quelques milliers de degrés (Rubie et al. 2007). La percolation de métal liquide à travers un manteau silicaté cristallisé est possible tant que le liquide reste interconnecté, ce qui dépend de l’angle dièdre ou angle de contact du liquide en contact avec deux solides (Rushmer et al. 2000). Le diapirisme intervient lorsque le métal s’accumule à la base d’un océan de magma, où il peut alors migrer vers le centre de la Terre sous la forme de larges diapirs créés suite à des instabilités gravitationnelles (Karato and Murthy 1997). Le transport de métal liquide par circulation dans des fractures formées dans le manteau encaissant, appelé diking, est considéré comme un mécanisme efficace de ségrégation du métal dans le noyau (Rubie et al. 2007, Rubin 1995). Cependant, contrairement aux processus d’émulsification et de percolation, la migration du métal par diapirisme ou par diking ne permet pas un équilibre chimique total du métal avec l’encaissant silicaté qui l’entoure (Karato and Murthy 1997, Rubie et al. 2007).

La question du *timing* de la différenciation noyau-manteau, étudiée dans de nombreux travaux, peut être abordée à partir de multiples observables cosmochimiques. L’étude des chronomètres Sm-Nd et Lu-Hf (Caro et al. 2005) a montré que l’océan de magma aurait cristallisé dans les premiers 100 Ma de l’histoire de la Terre, en accord avec les données de U-Pb (Wood and Halliday 2010) qui suggèrent une cristallisation complète 80 Ma après le début de l’accrétion. Le système Hf-W est utilisé comme chronomètre (Rubie et al. 2007) grâce aux différences de propriétés chimiques entre le tungstène, élément sidérophile, et l’hafnium qui est lithophile. L’isotope radioactif ^{182}Hf se désintègre en ^{182}W avec une période de demi-vie de 9 millions d’années. La Lune présente une signature en Hf-W impliquant que celle-ci se soit formée environ 50 Ma après la formation du Système Solaire (Thiemens et al. 2019). Il est généralement considéré que la Lune s’est formée à la suite d’un impact géant permettant l’accrétion des 10 derniers pourcents de la masse terrestre, indiquant que l’accrétion et la formation du noyau se sont terminés au plus tôt 50 Ma après le début de l’accrétion. L’avantage du chrono-

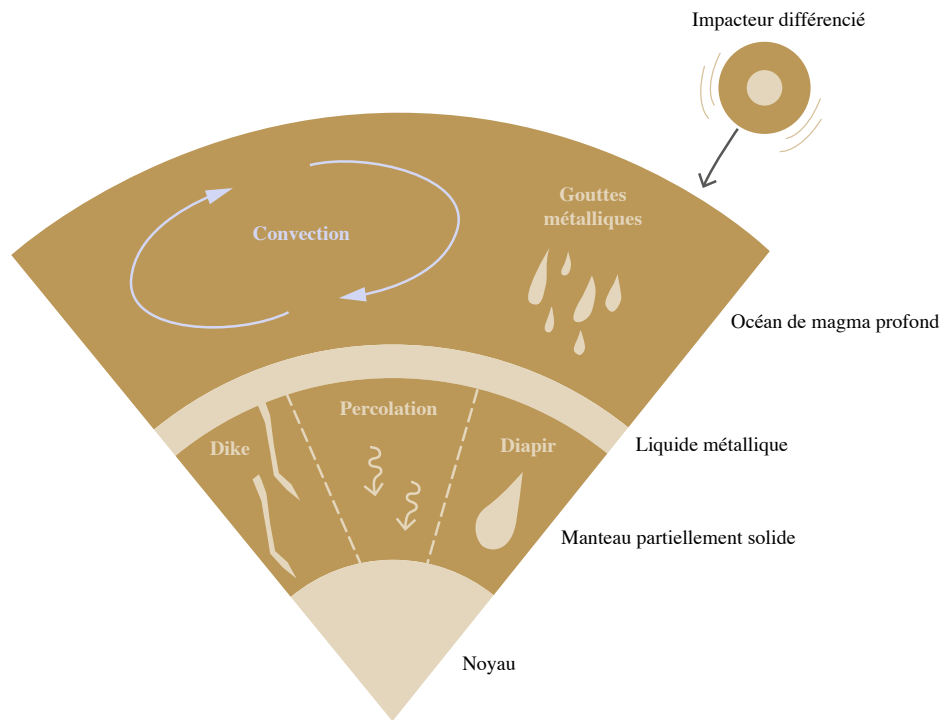


FIGURE 7 – Schéma montrant les différents mécanismes pouvant contribuer à la ségrégation du liquide métallique (en beige) constituant le noyau lors de la différenciation terrestre. Figure : Alexia Schroeder.

mètre Hf-W est que les deux éléments impliqués sont réfractaires, ce qui n'est pas le cas des systèmes U-Pb et Pd-Ag, aussi utilisés pour la datation mais nécessitant de corriger d'éventuelles pertes par volatilisation (Rubie et al. 2007). Les conditions de pression, de température, d'oxydo-réduction et de composition qui déterminent le caractère sidérophile du tungstène ont varié au cours de la différenciation. Il est donc nécessaire de déterminer précisément le comportement sidérophile du W dans un équilibre métal-silicate et l'influence de chaque paramètre (Cottrell et al. 2009b, Wade et al. 2012).

0.3.2 Efficacité de l'équilibration noyau-manteau

L'efficacité de l'équilibration noyau-manteau est une question cruciale car elle a un effet sur l'amplitude de la ségrégation des éléments sidérophiles dans le noyau,

et donc sur les abondances de ces mêmes éléments observées dans le manteau terrestre. Étant donné les conditions extrêmes de pression et de température qui régnaient dans les zones de la Terre où la différenciation a eu lieu, il est difficile de quantifier l'efficacité de la ségrégation noyau-manteau. Bien que la ségrégation du noyau par équilibre dans un océan de magma profond soit considéré comme très efficace (Righter 2005), il a été suggéré que la formation du noyau ait pu être partiellement inefficace, laissant des vestiges de métal dans le manteau silicaté (Jones and Drake 1986, Rubie et al. 2007). En outre, des études proposent même que du métal ait remigré du noyau vers le manteau, ce qui influencerait fortement les abondances en éléments très sidérophiles dans le manteau (Brandon and Walker 2005, Rubie et al. 2007, Walker 2000). Des modèles de dynamique des fluides dans un contexte de mélange turbulent ont montré que les instabilités de Rayleigh-Taylor pourraient émulsifier le métal, permettant l'équilibre métal-silicate (Dahl and Stevenson 2010). Cependant, des embryons planétaires présentant des noyaux de taille supérieure à 10 km ne se désagrègeraient pas complètement suite à leur accréation. En effet, une équilibration chimique totale nécessiterait que le métal se désagrège en fragments de 1 cm à 1 m de diamètre (Rubie et al. 2003). L'équilibration serait donc de moins en moins efficace lors de l'accréation, avec l'augmentation de la taille des embryons accrésés. Des simulations numériques allant dans ce sens montrent que l'équilibration entre les embryons accrésés et le manteau terrestre atteindrait 30 à 80 % (Nimmo et al. 2010), également confirmé par des modèles géochimiques sur le système Hf-W (Rudge et al. 2010). L'équilibration partielle du manteau avec le noyau a également été invoqué comme processus possible expliquant les abondances relativement élevées en éléments très sidérophiles dans le manteau terrestre (Arculus and Delano 1981, Jones and Drake 1986, Walker 2009). Cependant, des simulations numériques ont montré que des mécanismes tels que l'élongation du métal pourraient favoriser l'équilibration chimique jusqu'à atteindre une équilibration totale, même lors de l'accréation d'embryons différenciés de grande taille (Kendall and Melosh 2016, Lherm and Deguen 2018).

0.3.3 Conditions physico-chimiques de la différenciation – Apports de la pétrologie expérimentale

Les éléments réfractaires sidérophiles sont appauvris dans le manteau terrestre par rapport aux éléments réfractaires lithophiles (figure 2) car leur affinité pour le fer métallique aux conditions de la différenciation a eu pour effet de les ségréger préférentiellement dans le noyau de la Terre. L'ampleur de cette ségrégation est dépendante des conditions de pression, température, oxydo-réduction ainsi que de composition auxquelles la différenciation noyau-manteau a eu lieu. La signature chimique des éléments réfractaires sidérophiles dans le manteau est, par conséquent, un enregistrement des conditions physico-chimiques que sont celles de la différenciation terrestre. Les outils développés par la pétrologie expérimentale, dont l'essor au XX^{ème} siècle a suivi celui de la géochimie, permettent de reproduire en laboratoire des conditions extrêmes de pression et de température, afin d'étudier le comportement des minéraux et des éléments chimiques à de telles conditions. Dans ce cadre, des expériences d'équilibre métal-silicate sont menées afin de comprendre et quantifier l'affinité des éléments sidérophiles pour le noyau métallique terrestre. Dans ces expériences, un matériau de départ constitué de métal et de roche est fondu et équilibré à haute pression, jusqu'à atteindre l'équilibre chimique entre métal et silicate. L'expérience est trempée et les phases sont séparées afin de caractériser les concentrations en éléments sidérophiles dans les deux phases, permettant de calculer un coefficient de partage (rapport des concentrations dans le métal et le silicate). La caractérisation du comportement de ces éléments en fonctions des conditions physico-chimiques grâce à la pétrologie expérimentale, permet de résoudre un ou plusieurs ensembles de conditions capables d'expliquer les abondances en éléments sidérophiles observées dans le manteau terrestre. Cette méthode permet donc d'estimer les conditions de pression, de température, d'oxydo-réduction ainsi que de composition qui sont celles de la différenciation terrestre, et considérées comme les conditions régnant à la base d'un océan de magma profond. De nombreuses études focalisées sur le partage élémentaire d'un grand nombre d'éléments réfractaires sidérophiles ont permis d'estimer la pression de la différenciation terrestre à 40-60 GPa (e.g. Bouhifd and Jephcoat 2003, Gessmann and Rubie 2000, Siebert et al. 2012, 2011, Wade and Wood 2005). L'étude du fractionnement isotopique des éléments sidérophiles dans un équilibre métal-silicate apporte des indices supplémentaires sur les conditions de la différenciation, car la signature isotopique de

ces éléments dans le manteau terrestre est également affectée par les interactions noyau-manteau. Il a donc été proposé que la signature isotopique du soufre puisse permettre d'estimer la pression d'équilibration du noyau avec le manteau (Labidi et al. 2016). La température d'équilibration du noyau avec le manteau, bien que débattue, est estimée être proche du liquidus (température à laquelle le dernier solide fond) du manteau (Andrault et al. 2011, Fiquet et al. 2010), à partir de données expérimentales (Gessmann and Rubie 2000, Wade and Wood 2005), c'est-à-dire autour de 2500-3500 K. Le fractionnement isotopique du silicium entre métal et silicate (Moynier et al. 2020) permet d'estimer une température qui tendrait vers la limite basse de cette gamme de température (Hin et al. 2014). L'évolution des conditions oxydo-réductrices lors de la formation du noyau est également sujet à débat. Plusieurs études expérimentales proposent que la différenciation ait débuté dans des conditions réductrices qui auraient ensuite évolué vers des conditions plus oxydantes (e.g. Dalou et al. 2019, Frost et al. 2008, Rubie et al. 2011, Wade and Wood 2005, Wood et al. 2006). Néanmoins, d'autres études montrent au contraire que la différenciation ait pu avoir lieu à des conditions oxydantes évoluant vers des conditions plus réductrices à la fin de l'équilibration noyau-manteau (Righter and Ghiorso 2012, Siebert et al. 2013). La méthode expérimentale décrite dans cette section permet également d'obtenir des informations sur l'efficacité de l'équilibration noyau-manteau (e.g. Dalou et al. 2019, Kempl et al. 2013), détaillée dans la section précédente, ainsi que sur la composition du noyau qui fait l'objet de la section suivante.

0.3.4 Le noyau terrestre

Un alliage de fer et de nickel

Le noyau terrestre représente 32 % de la masse de la Terre. Situé à 2890 km de profondeur, il est impossible de l'étudier par des méthodes directes. Sa découverte, grâce à la sismologie, a permis d'imaginer de nouvelles méthodes pour caractériser physiquement et chimiquement le noyau terrestre. Des expériences analogiques ont permis d'estimer que le noyau de la Terre est principalement constitué de fer (Birch 1964, Brown and McQueen 1986, Jeanloz 1979), ceci étant confirmé par l'observation du champ magnétique terrestre qui est généré par la convection d'un

liquide métallique. Des modèles géochimiques suggèrent également que 5 % de nickel entrent dans la composition du noyau (McDonough 2003, McDonough and Sun 1995). De nombreuses études, basées sur des méthodes expérimentales ainsi que des calculs *ab initio*, ont montré que l'addition de Ni avait très peu d'effet sur les propriétés physiques de l'alliage. Ces propriétés comprennent la densité, la compressibilité et l'élasticité (Asker et al. 2009, Kantor et al. 2007, Lin et al. 2003, Martorell et al. 2013, Wakamatsu et al. 2018). Des études focalisées sur des paramètres chimiques ont également montré l'absence d'effet de la concentration en Ni dans un alliage sur ces paramètres (Fraser and Rammensee 1982, Huang and Badro 2018, Oriani 1953, Zellars et al. 1959), même si deux études isotopiques récentes indiquent l'inverse (Elardo and Shahar 2017, Xia et al. 2019). Cela suggère qu'un alliage de fer et de nickel possède un caractère idéal, c'est-à-dire que ses propriétés physico-chimiques restent inchangées quel que soit le rapport Ni/Fe de l'alliage.

Des éléments sidérophiles

Les éléments sidérophiles ont pour propriété d'avoir une forte affinité pour le fer métallique, et sont donc préférentiellement enrichis dans le noyau et appauvris dans le manteau lors de la différenciation terrestre. Ces éléments étant peu abondants dans le Système Solaire, ils représentent moins de 1 % de la masse du noyau. Néanmoins, leurs propriétés en font des traceurs privilégiés de la différenciation terrestre car leurs abondances dans le manteau sont directement héritées de la ségrégation du noyau. En particulier, les éléments modérément volatils et sidérophiles enregistrent à la fois les processus de formation du noyau et les processus liés à la volatilité. L'étude de leur comportement lors de la différenciation terrestre permet de mieux comprendre l'accrétion des éléments volatils en lien avec la formation du noyau, et constitue l'objet de cette thèse.

Des éléments légers

Dès les années 1950, il est observé, grâce à des études sismologiques, que la densité du noyau terrestre est inférieure à celle du fer pur (Birch 1952, 1964), suggérant la présence d'éléments légers dans le noyau. En effet, comme expliqué précédemment, l'alliage Fe-Ni se comportant de façon idéale, la différence de densité avec le fer pur mesurée est indépendante de la quantité de Ni dans le noyau

et peut entièrement être attribuée à l'incorporation d'éléments légers. La quantité d'éléments légers est estimée à 5-10 % dans le noyau liquide, et 4-5 % dans la graine (Alfè et al. 2002, Anderson and Isaak 2002, Hemley and Mao 2001, Jephcoat and Olson 1987). Les éléments légers pouvant potentiellement entrer dans la composition du noyau doivent remplir plusieurs conditions : (1) avoir une masse atomique inférieure à celle du fer, (2) se trouver en abondance suffisante dans la Terre primitive indifférenciée et (3) être soluble dans le fer liquide aux conditions de la différenciation (Allègre et al. 1995). L'oxygène, le silicium, le soufre, le carbone et l'hydrogène remplissent ces conditions. Le budget en éléments légers du noyau est probablement une combinaison d'un ou plusieurs de ces éléments. L'identification de ces éléments passe par la mise en évidence d'un mécanisme permettant d'intégrer un élément léger dans le noyau ainsi que la réconciliation des contraintes apportées par la minéralogie expérimentale avec celles de la sismologie (densité et vitesses sismiques). La capacité d'un élément à être intégré dans le noyau est dépendant des conditions de pression, de température, d'oxydo-réduction ainsi que des compositions chimiques des deux réservoirs qui s'équilibrent. Ces conditions peuvent être reproduites en laboratoire dans des expériences à haute pression et haute température afin de caractériser le comportement des éléments légers lors de la différenciation terrestre. Les conditions d'oxydation ont un rôle primordial car il a été montré qu'à haute température, le silicium est susceptible de former un alliage avec le fer sous des conditions réductrices alors que des conditions oxydantes favoriseraient la solubilisation de l'oxygène dans le métal (Badro et al. 2015). Certains modèles favorisent l'oxygène comme élément léger dominant dans le noyau (Badro et al. 2015, Frost et al. 2010, Ringwood 1977, Rubie et al. 2004, Siebert et al. 2013), alors que d'autres sont en faveur du silicium (Allègre et al. 1995, Fischer et al. 2015, Gessmann et al. 2001, Rubie et al. 2011, Ziegler et al. 2010). Le carbone a été estimé à 0.2 à 1 poids pourcent (*wt.%*) dans le noyau (McDonough 2003, Wood et al. 2013). L'étude de l'hydrogène comme potentiel élément léger dans le noyau terrestre est très difficile à cause de sa volatilité extrême, mais pourrait contribuer jusqu'à environ 1 *wt.%* du noyau (Clesi et al. 2018, Fukai and Akimoto 1983, Thompson et al. 2018, Umemoto and Hirose 2015). La quantité de soufre dans le noyau terrestre est estimée à environ 2 *wt.%* dans de nombreuses études (Badro et al. 2014, Boujibar et al. 2014, Dreibus and Palme 1996, Mahan et al. 2018a, McDonough 2003, Morard et al. 2013, Suer et al. 2017). Le soufre pourrait avoir eu un rôle crucial lors de la différenciation terrestre. En effet O'Neill (1991)

propose la formation d'un « *Hadean matte* », liquide sulfuré riche en éléments volatils, formé à la limite noyau-manteau durant les dernières phases de l'accrétion puis incorporé au noyau. La ségrégation d'un tel liquide constitue un mécanisme supplémentaire permettant d'inclure des éléments légers et des éléments ayant une forte affinité pour le soufre (éléments dits chalcophiles) dans le noyau. Wood et al. (2014) montrent expérimentalement, pour une sélection d'éléments sidérophiles, qu'il existe une corrélation entre l'appauvrissement dans le manteau de ces éléments et leurs coefficients de partage entre silicate et sulfure à l'état liquide. Ils montrent également une absence de corrélation de ces appauvrissements avec les coefficients de partage entre silicate et fer liquides, renforçant cette hypothèse de ségrégation dans un liquide sulfuré, en accord avec d'autres études expérimentales (Righter et al. 2019, Wood et al. 2008). Dans les travaux présentés ici, l'effet du soufre sur le comportement des éléments étudiés dans le contexte de la formation du noyau a été quantifié et permet d'apporter des contraintes supplémentaires sur la quantité de soufre dans le noyau.

Le partage entre métal et silicate des éléments sidérophiles est influencé par la présence d'éléments légers (Li and Agee 2001, Mann et al. 2009, Tuff et al. 2011, Wade et al. 2012). Il est donc important de connaître la composition du noyau terrestre car elle permet de préciser les conditions de partage entre métal et silicate des éléments sidérophiles, mais aussi de déterminer la composition de la Terre totale (*bulk composition*), ainsi que la structure et la dynamique du noyau terrestre.

0.4 Accrétion des éléments volatils

0.4.1 Signature des éléments volatils dans la Terre silicatée

L'origine des éléments volatils, qui sont des éléments essentiels au développement de la vie sur Terre, est débattue. L'appauvrissement en éléments volatils observé sur Terre est également mal compris. Il pourrait être dû à :

- (1) une perte par volatilisation syn- ou post-accrétion de la Terre
- (2) une condensation incomplète de la nébuleuse solaire.

La perte par volatilisation modifie la composition isotopique des éléments chimiques car les isotopes les plus légers sont plus facilement volatilisés que les isotopes lourds. De nombreuses études rapportent une absence d'enrichissement en isotopes lourds d'éléments modérément volatils du manteau terrestre relativement aux chondrites. En particulier, le potassium (Humayun and Clayton 1995, Tuller-Ross et al. 2019, Wang and Jacobsen 2016), le rubidium (Pringle and Moynier 2017), le sélénium (Varas-Reus et al. 2019) et le zinc (Luck et al. 2005, Pringle et al. 2017, Sossi et al. 2017) ne semblent pas enrichis en isotopes lourds dans le manteau terrestre par rapport aux chondrites, constituant un argument pour l'absence de perte volatile lors de la formation de la Terre par évaporation. De plus, le rapport Mn/Na, utilisé pour tracer les processus de volatilisation post-nébulaires, est identique dans la Terre et les chondrites, ce qui suggère une perte volatile très limitée pendant et après l'accrétion terrestre (O'Neill and Palme 2008, Siebert et al. 2018). Cependant, de petits fractionnements isotopiques ont été observés pour le magnésium (Hin et al. 2017), et le silicium (Pringle et al. 2014, Young et al. 2019) suggérant que la volatilisation ait pu avoir un effet sur la signature isotopique terrestre. La Lune et d'autres corps différenciés du Système Solaire sont, au contraire, fractionnés isotopiquement dans de nombreux systèmes élémentaires (Boyce et al. 2015, Kato et al. 2015, Pringle and Moynier 2017, Pringle et al. 2014, Sharp et al. 2010, Wang and Jacobsen 2016, Wang et al. 2019), montrant que la Lune a subi un appauvrissement significatif en éléments volatils par volatilisation.

0.4.2 Les scénarios d'accrétion

Cette étude a pour objet l'accrétion des éléments volatils sur Terre, la nature des matériaux accrétés, ainsi que la différenciation noyau-manteau. Plusieurs scénarios ont été proposés pour expliquer la signature chimique des éléments volatils observée dans le manteau terrestre :

(1) La Terre a pu être formée à partir de matériaux majoritairement dépourvus d'éléments volatils dans un contexte de *dry accretion*. Ce scénario est corroboré par le fait que le Système Solaire ait probablement été trop chaud lors de la formation de la Terre pour permettre la condensation des éléments volatils (Albarède 2009, Peslier et al. 2017). Dans ce cas, les éléments volatils sont apportés après la différenciation terrestre, sous la forme d'un vernis tardif (Albarède et al. 2013,

O'Neill 1991, Rubie et al. 2011). Un tel vernis tardif a été estimé à environ 0,5 % de la masse de la Terre à partir de modèles basés sur les abondances en gaz rares (Dauphas and Marty 2002), et pourrait provenir de l'accrétion de planétésimaux résiduels (Bottke et al. 2010). Des mesures isotopiques récentes de sélénium (Varas-Reus et al. 2019) et de ruthénium (Fischer-Gödde et al. 2020) ont également permis d'estimer la quantité de vernis tardif à 0,15 et 0,3 % respectivement. Les isotopes de l'oxygène indiquent, quant à eux, un vernis tardif plus volumineux, de l'ordre de 4 % (Albarède et al. 2013). Des mesures expérimentales du fractionnement isotopique du thallium entre sulfure et silicate (Fang and Liu 2019) rapportent un fractionnement significatif à 1650°C. La signature chondritique de la BSE est alors interprétée comme héritée d'un vernis tardif, estimé à 2,5 % de la masse terrestre, en accord avec des études de simulation d'impacts (Marchi et al. 2018). Des études expérimentales du comportement d'éléments volatils et sidérophiles lors de la différenciation noyau-manteau ont montré qu'il était impossible d'expliquer les abondances observées dans le manteau terrestre sans accrétion tardive de ces éléments après la fin de la formation du noyau (Ballhaus et al. 2017, 2013). Wang and Becker (2013) rapportent des mesures de soufre, sélénium et tellure suggérant une origine du vernis tardif majoritairement composé de chondrites carbonées, en accord avec d'autres mesures isotopiques d'éléments très volatils (Albarède et al. 2013, Alexander et al. 2012), bien que d'autres modèles proposent plutôt une composition du vernis tardif similaire aux chondrites à entatite (Dauphas 2017).

À l'instar des éléments volatils, le vernis tardif a également été proposé afin d'expliquer les abondances relativement élevées en éléments très sidérophiles présentes dans le manteau terrestre (Holzheid et al. 2000, Mann et al. 2012, O'Neill et al. 1995). Les variations des rapports isotopiques du platine, présentant une signature lourde dans le manteau archéen et chondritique dans le manteau post-archéen (Creech et al. 2017a) suggèrent également l'addition et le mélange d'un vernis tardif après l'ère archéenne. Un message similaire peut être déduit de l'appauvrissement en éléments du groupe du platine observé dans des komatiites (roches volcaniques ultramafiques) datant de l'Archéen précoce et de leur enrichissement dans les komatiites plus récentes (Maier et al. 2009) dû à l'incorporation d'un vernis tardif au manteau. Une ségrégation inefficace du noyau ainsi qu'une diminution de la sidérophilité de ces éléments à haute pression et haute température (e.g. Danielson et al. 2005, Richter and Drake 1997, Rubie et al. 2016) ont été également proposés pour expliquer les abondances des éléments très sidérophiles, et une

combinaison de ces trois mécanismes est probablement responsable des abondances observées (Walker 2009). L'étude des éléments très sidérophiles apporte donc des preuves supplémentaires en faveur de l'existence d'un vernis tardif, qui est l'un des mécanismes proposés pour expliquer l'accrétion des éléments volatils.

(2) Dans un second scénario possible, la Terre a été accrétée de matériaux partiellement appauvris en éléments volatils tels que les chondrites. Ensuite, la différenciation redistribue les éléments chimiques entre le noyau et le manteau, en fonction de leurs affinités pour le liquide métallique (Righter et al. 2017b, Wood and Halliday 2010). Dans ce scénario appelé *wet accretion*, les éléments volatils sont apportés pendant les phases principales de l'accrétion terrestre, au même titre que tous les autres éléments chimiques. Les abondances relatives et rapports isotopiques d'éléments très volatils, et en particulier les rapports H/C et C/N de la Terre sont en accord avec un tel scénario (Halliday 2013). Ce scénario est supporté par des études expérimentales du comportement d'éléments volatils et sidérophiles dans un équilibre métal-silicate suggérant que les abondances observées dans le manteau terrestre peuvent être expliquées par la distribution de ces éléments entre noyau et manteau à haute pression et haute température (Righter et al. 2017a, b), possiblement associé à un mécanisme tardif de ségrégation dans un liquide sulfuré (Righter et al. 2018, 2019). En particulier, une étude focalisée sur l'antimoine conclut que les abondances mesurées dans les manteaux de la Terre et de la Lune peuvent être expliquées par la différenciation noyau-manteau (Righter et al. 2009). De tels modèles nécessitent une différenciation dans des conditions initiales réduites et prennent en compte l'effet des abondances en éléments légers dans le noyau sur les coefficients de partage et nécessitent une certaine composition chimique du noyau pour fonctionner (e.g. 10,2 % Si, 2 % S et 1,1 % C dans Righter et al. 2017a). Une étude du comportement du plomb entre métal et silicate a également permis d'établir que l'abondance en plomb dans le manteau est cohérente avec un équilibre noyau-manteau (Wood and Halliday 2010).

(3) Un troisième scénario intermédiaire consiste en une accrétion hétérogène de la Terre, où les éléments volatils seraient ajoutés majoritairement durant les dernières phases de l'accrétion et de la différenciation terrestre, comme représenté sur la figure 8. Cette accrétion tardive ne doit pas être confondue avec un vernis tardif, qui arrive lui, après que la différenciation soit terminée. Dans ce scénario, l'apport tardif des éléments volatils peut être synchrone de l'épisode de formation

de Lune, sous la forme d'un impact géant, comme suggéré par les abondances en éléments chalcophiles dans le manteau terrestre, et en particulier le tellure (Yi et al. 2000), qui indiquent que la ségrégation de ces éléments dans le noyau s'est probablement poursuivie après la formation de la Lune. L'étude des isotopes du rubidium supporte également un tel scénario dans lequel l'accrétion des éléments volatils est corrélée avec l'impact géant qui a formé la Lune (Budde et al. 2019) et les derniers stades de l'équilibre noyau-manteau, environ 110 Ma après la formation du Système Solaire (Nebel et al. 2011). Des études récentes ont proposé que les éléments volatils proviennent de matériel de composition chondritique (CI) correspondant à environ 10 à 15 % de la masse de la Terre accrété tardivement lors des phases principales d'accrétion (Braukmüller et al. 2019). Des études expérimentales à très haute pression (46 à 91 GPa) sur le comportement d'éléments volatils et sidérophiles lors de la différenciation tels que le soufre (Suer et al. 2017), le zinc (Mahan et al. 2018b) et le cuivre (Mahan et al. 2018a) ont montré que les abondances observées ne peuvent être expliquées que par une accrétion tardive des éléments volatils, dans les derniers stades de l'accrétion terrestre. Ces études, menées à des conditions directement pertinentes pour la différenciation terrestre, mènent à des conclusions similaires à d'autres études menées à plus basses pressions (e.g. Ballhaus et al. 2017), renforçant la pertinence de l'extrapolation des données à basse pression afin d'adresser cette problématique. Ce scénario d'accrétion hétérogène est également supporté par des études focalisées sur des éléments très volatils tels que les gaz rares (Marty 2012) ou les halogènes (Clay et al. 2017). Le système isotopique Pd-Ag dans le manteau terrestre (Schonbachler et al. 2010) suggère également une évolution des compositions en éléments volatils lors de l'accrétion terrestre. De plus, le comportement du molybdène et du tungstène, qui sont des éléments réfractaires et sidérophiles, déterminé expérimentalement, a montré que les abondances de tels éléments sont reproduites uniquement si le budget terrestre en soufre est accrété dans les derniers 20 % de la formation de la Terre (Wade et al. 2012), en accord avec l'étude expérimentale du rapport C/S de la Terre (Li et al. 2016). Ce scénario pourrait donc également être associé à la formation d'un liquide sulfuré riche en éléments volatils, appelé *Hadean matte* (O'Neill 1991, Rubie et al. 2016, Savage et al. 2015, Schonbachler et al. 2010), qui s'équilibre à la base de l'océan de magma puis se mélange au noyau. Enfin, des simulations numériques ont montré que la migration des planètes géantes (Gomes et al. 2005) a pu entraîner du matériel riche en éléments volatils provenant du Système Solaire

externe (Morbidelli et al. 2012, Raymond et al. 2006) vers les zones internes où les planètes rocheuses sont formées. Ce matériel se serait accrété tardivement et aurait une composition similaire aux chondrites carbonées (Budde et al. 2019, Charnoz et al. 2019, O'Brien et al. 2018, Schiller et al. 2018). Ce scénario est donc validé par une large gamme de méthodes scientifiques, comprenant des études géochimiques et cosmochimiques isotopiques, des études de pétrologie expérimentale ainsi que des simulations numériques d'astrophysique.

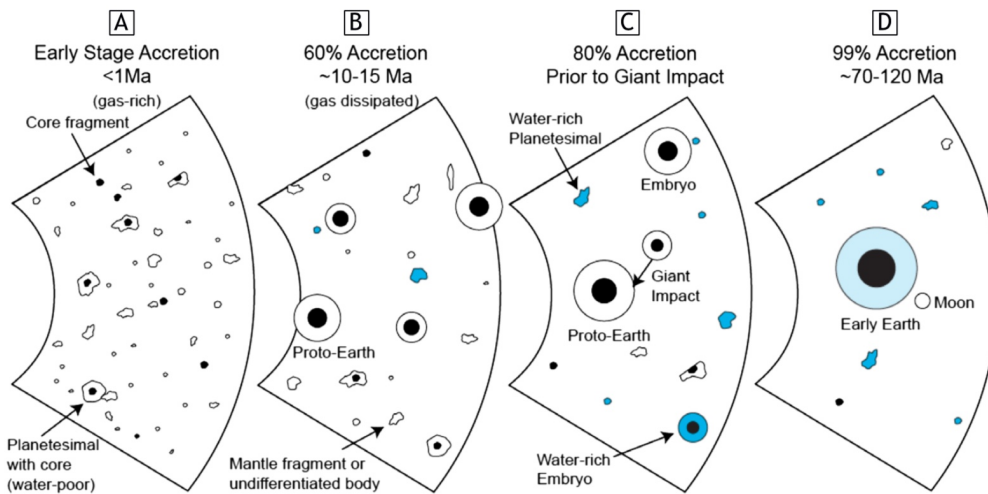


FIGURE 8 – Schéma de l'évolution de l'accrétion des éléments volatils au cours de la formation de la Terre. Dans ce scénario hétérogène, la Terre et ses composants sont pauvres en volatils durant les stades précoces. Les premiers apports significatifs d'éléments volatils arrivent lorsque la Terre possède déjà 60 à 80 % de sa masse totale. Les stades d'accrétions tardifs sont marqués par l'accrétion de corps riches en éléments volatils (représentés en bleu). Figure extraite de Peslier et al. (2017).

Les scénarios (1) et (3) impliquent que les stades précoces de l'accrétion terrestre aient produit une proto-Terre appauvrie en éléments volatils. Cette hypothèse peut être testée par l'étude de systèmes radiogéniques dans lesquels l'élément père et l'élément fils ont des températures de condensation différentes, tels que les systèmes ^{53}Mn - ^{53}Cr , ^{107}Pd - ^{107}Ag , ^{87}Rb - ^{87}Sr , ^{238}U - ^{206}Pb et ^{235}U - ^{207}Pb . Parmi ces systèmes, les systèmes de désintégration à courte durée de demi-vie établissent définitivement leurs signatures dans les 10 à 30 premiers millions d'années, apportant des informations sur les stades très précoces du Système Solaire. Dans le système

^{53}Mn - ^{53}Cr , la composition isotopique en Cr de la Terre silicatée est appauvrie en ^{53}Cr par rapport aux chondrites (e.g. Qin et al. 2010, Trinquier et al. 2008), suggérant que l'élément volatile ^{53}Mn , parent de l'isotope ^{53}Cr , ait été perdu très tôt, dans les premiers 2 Ma suivant la formation du Système Solaire. Un message similaire peut être déduit de l'étude du système ^{87}Rb - ^{87}Sr (Carlson et al. 2015, Halliday and Porcelli 2001, Hans et al. 2013, Nebel et al. 2011, Schonbachler et al. 2010). De plus, l'existence de la ligne des glaces, correspondant à la distance au Soleil au-delà de laquelle les espèces volatiles existent sous forme condensée dans le disque proto-solaire, indique que la Terre se soit formée dans une zone pauvre en éléments volatils (e.g. O'Brien et al. 2014, Raymond et al. 2006).

0.4.3 Une méthode expérimentale

L'étude du comportement chimique, dans un équilibre métal-silicate, des éléments qui sont à la fois volatils et sidérophiles, peut aider à discriminer ces trois scénarios en isolant l'effet des processus liés à la sidérophilie des processus liés à la volatilité. Les éléments modérément volatils et sidérophiles (MSVEs) sont appauvris dans le manteau terrestre comparé aux éléments volatils lithophiles (figure 2) à cause de leur ségrégation dans le noyau (Lodders 2003, Wasson et al. 1988, Wood et al. 2019). Afin de déterminer l'effet de la différenciation sur l'appauvrissement observé, le comportement des MSVEs peut être étudié expérimentalement (e.g. Ballhaus et al. 2017, Blanchard et al. 2015, Corgne et al. 2008, Mahan et al. 2018a, b, 2017, Righter et al. 2017a, b, Siebert et al. 2011, Steenstra et al. 2019, 2017, 2016, Suer et al. 2017). La quantification de l'affinité des MSVEs avec le métal relativement au silicate dans des expériences reproduisant les conditions de la formation du noyau permettent de décorrélérer les effets de la différenciation de ceux des processus liés à la volatilité, et de prédire le comportement de ces éléments dans le cadre des trois scénarios présentés précédemment. La comparaison de ces résultats à des observables géochimiques permet de proposer un ou plusieurs scénarios d'accrétion permettant d'expliquer les signatures chimiques des éléments volatils dans le manteau terrestre.

0.5 Objectifs de la thèse

Les travaux menés dans cette thèse ont pour objectif d’apporter des éléments améliorant la compréhension des conditions d’accrétion et de différenciation de la Terre, et en particulier de l’accrétion des éléments volatils. Les éléments chimiques d’intérêt ont fait l’objet d’expérimentation à haute pression et haute température afin de quantifier leurs affinités élémentaires et isotopiques pour le noyau terrestre par rapport au manteau.

Dans le **chapitre 1**, les méthodes expérimentales et analytiques utilisées dans ces travaux de thèse sont détaillées. Les presses piston-cylindre et multi-enclume ont été utilisées pour mener les expériences. Nous décrivons ces instruments et leur fonctionnement, les spécificités des expériences menées, ainsi que la préparation des échantillons produits lors de ces expériences en vue de les analyser. En particulier, le protocole développé pour la sélection et la préparation des échantillons expérimentaux pour des mesures isotopiques est détaillé. Les multiples instruments d’analyse utilisés pour caractériser les échantillons sont présentés.

Le **chapitre 2** est dédié à la thermodynamique des équilibres métal-silicate à haute pression et haute température. Le formalisme présenté permet d’extraire, à partir des résultats expérimentaux, des paramètres permettant de décrire le comportement des éléments étudiés dans un équilibre métal-silicate en fonction des conditions de pression, de température, de fugacité de l’oxygène (fO_2) et de composition des phases.

Les paramètres ainsi déterminés permettent de reconstruire le coefficient de partage et le facteur de fractionnement isotopique entre métal et silicate des éléments étudiés dans des conditions précises. C’est l’objet du **chapitre 3**, dédié à la modélisation numérique de la distribution des éléments chimiques ou des isotopes lors de la formation du noyau. Ces modèles permettent de tester différents scénarios et de comparer leurs résultats avec les observables géochimiques.

Au **chapitre 4**, nous présentons une étude systématique du partage et du fractionnement isotopique de l’étain entre métal et silicate. Les effets de pression, de température, de fO_2 , de la concentration en soufre dans le métal et de la composition du silicate sur le comportement de l’étain sont quantifiés et permettent de modéliser plusieurs scénarios d’accrétion de l’étain. Nous discutons de la capacité

de ces différents scénarios à expliquer les abondances observables dans la Terre silicatée, et également du rôle du soufre dans de tels scénarios. Les résultats de fractionnement isotopique en lien avec les compositions isotopiques des chondrites, permettent de placer des contraintes supplémentaires et indépendantes sur le scénario d'accrétion le plus adéquat ainsi que sur la nature des matériaux à l'origine des éléments volatils sur Terre. Cette étude est présentée telle que soumise au journal *Geochimica et Cosmochimica Acta*.

Le **chapitre 5** constitue une seconde étude systématique du partage métal-silicate de quatre éléments modérément volatils et sidérophiles : le cadmium, le bismuth, l'antimoine et le thallium. L'étude inclut la détermination des effets de pression, de température, de fO_2 et de la concentration en soufre dans le métal sur le coefficient de partage de ces éléments chimiques. Les modèles numériques de formation du noyau basé sur les résultats expérimentaux permettent notamment de discuter le *timing* de l'accrétion des éléments volatils, la nécessité d'un vernis tardif pour expliquer les abondances observées, ainsi que l'efficacité de l'équilibration noyau-manteau. Cette étude a fait l'objet d'une soumission au journal *Geochimica et Cosmochimica Acta*.

Une troisième application, présentée au **chapitre 6**, propose une étude de l'effet de la concentration en nickel dans le métal sur le facteur de fractionnement isotopique du fer entre métal et silicate. Contrairement à une autre étude publiée récemment, aucun effet significatif du nickel sur le fractionnement isotopique n'est mesuré sur une large gamme de concentrations en nickel (0 à 70 %) à 1873 K et 2 GPa. Une série temporelle est réalisée et 4 matériaux de capsule différents sont testés. Les implications de cette étude incluent les causes de la variabilité des signatures isotopiques en fer dans le Système Solaire interne, ainsi que l'idéalité chimique des alliages de fer et de nickel.

Le **chapitre 7** a pour objectif de synthétiser ces travaux de thèse et de conclure. Y sont également présentés des perspectives de futurs travaux.

Experimental and analytical methods

In order to answer the questions previously raised in the introduction section, samples were synthesised using high-pressure and high-temperature techniques in an attempt to simulate core–mantle equilibration in laboratory facilities. In such experiments, a powder mixture of metal and silicate was heated, melted and left to equilibrate. The quenched experiments presented a coalesced metal sphere surrounded by a silicate melt. The isotopic and chemical abundances of the elements of interest were subsequently measured in both phases of the samples to characterise their elemental and isotopic behaviour under such conditions. A total of 58 piston cylinder and 15 multianvil experiments were performed as part of this PhD thesis. Analytical methods include scanning electron microscopy (SEM), electron probe microanalysis (EPMA), laser-ablation inductively-coupled-plasma mass-spectrometry (LA-ICPMS) and multi-collector inductively-coupled-plasma mass-spectrometry (MC-ICPMS).

1.1 Experimental methods

1.1.1 Starting materials

Starting materials used in both piston cylinder and multianvil experiments were produced using the same method. Silicate powders and metal powders were selected, weighed, and combined together in an agate mortar where they were dry crushed for about 10 minutes until the mixture was homogeneous and well combined.

The silicate portion takes roughly 70 *wt.%* of the starting material and is composed of a crushed natural MORB or natural peridotite. Designed as an analogue of the mantle, the basaltic composition is preferred over pyrolite because its melting point is much lower (liquidus attained at 1673 K at 2 GPa for MORB and 2073 K for pyrolite, Herzberg and Zhang 1996, Yasuda et al. 1994). Furthermore, the use of MgO capsules to contain the starting material induces a diffusion of MgO in the silicate during the experiment, which helps to obtain a MgO concentration in the silicate more relevant to the Earth's mantle (~ 40 *wt.%* versus ~ 8 *wt.%* in MORBs).

The metal phase is made of pure Fe (Fe 99.9% ©Alfa Aesar) or a mixture of half pure Fe and half iron sulphide (FeS 99.99% ©Alfa Aesar). This second metal phase is used for experiments designed to constrain the effect of S on the partitioning and/or isotopic fractionation of the element(s) of interest. The metal phase is doped with percent levels of one or several elements of interests (i.e. Sn, Cd, Bi, Sb, and Tl) as pure metal or pure oxide powders. The amount of these elements added into each starting material is carefully chosen by considering several factors: (1) after equilibrium is achieved in an experiment, the element's concentration in the silicate especially needs to be suitable for analytical measurements (i.e. above EPMA or LA-ICPMS detection limit and/or in sufficient amounts for isotope measurement by MC-ICPMS), meaning that if an element is very siderophile, its doping level must be increased accordingly with the aim of getting sufficient amounts in the silicate (2) when incorporated in a Fe alloy, some elements studied here, especially Sn, have the property of lowering the melting point of the metallic alloy. Therefore, when sufficiently doped in Sn, experiments can be used to investigate

lower temperature conditions at which the metal would not be completely melted otherwise, hence widening the range of temperatures of the experiments. (3) Although studying several elements of interest saves a lot of time, energy and cost, it should be noted that such siderophile elements may interact with each other and have an effect on their respective partition coefficients between metal and silicate, which is why replicate experiments containing only one element of interest must be carried to confirm the absence of effect of other elements on their behaviour.

In chapter 6 where the effect of Ni on Fe isotopic fractionation factor between metal and silicate is studied, the metal portion of the starting material is composed of pure Fe and pure Ni with varying Ni proportions.

1.1.2 Piston cylinder experiments

A piston cylinder apparatus is used to generate pressure by compressing a sample assembly, placed inside a pressure vessel. It involves one or two hydraulic rams powered by a pump in order to compress the sample. It also allows samples to reach high temperatures using a resistance furnace around the sample.

As part of this PhD work, 58 experiments were performed with a 150-tons end-loaded piston cylinder press at the Institut Physique du Globe de Paris (IPGP). The end-load ram is used to strengthen the pressure vessel and reach higher pressures. Uncertainties on pressure and temperature are estimated to be around 0.1 GPa and 50 K (Siebert et al. 2011). Pressure calibration of the apparatus was performed using the alumina concentration in orthopyroxene in equilibrium with pyrope in a MgO–Al₂O₃–SiO₂ system (Perkins and Newton 1981). The friction coefficients reported by McDade et al. (2002) were compared and found to be identical to the coefficients measured during the calibration of the apparatus, allowing similar corrections to be applied for friction loss for several traditionally used assembly materials.

All experiments were performed in 1/2" cell assemblies at 1 to 2 GPa and from 1773 to 2273 K (table 1.1). The outer part of the cylindrical assembly is composed of a pressure medium, made of either talc-pyrex for experiments below 1900 K or compressed BaCO₃ for experiments above 1900 K. The purpose of this piece is to transfer the pressure to the inner parts of the assembly while insulating

them from the surrounding cylinder. Inside the pressure media sits a cylindrical graphite furnace designed to heat the sample when an electric current is injected in it (figure 1.1). The capsule containing the packed starting material is placed in the center of the assembly—where the heating is the most efficient—using two MgO spacers above and below the capsule. The upper spacer is drilled vertically in its center, allowing to place a type D ($W_{97}Re_3/W_{75}Re_{25}$) thermocouple contained in a 4-hole alumina sleeve just above the capsule lid. The thermocouple is composed of two wires of slightly different compositions that are in contact with one another at the top of the capsule. The Seebeck effect refers to the relationship between the gradient of voltage (∇V) measured in this open circuit and the gradient in temperature (∇T) which are directly proportional:

$$\nabla V = -S(T) \cdot \nabla T \quad (1.1)$$

where $S(T)$ is a temperature-dependent material property called the Seebeck coefficient. This simple technique allows to monitor the temperature of the sample during the experiment.

Capsule materials include crushable magnesium oxide (MgO), boron nitride (BN), graphite (C), and single-crystal magnesium oxide (MgO single-crystal or MgO SC). Each capsule material has advantages and downsides, so testing several materials in the same project helps to detect any experimental bias induced by interactions between the sample and the capsule.

Experimental procedure

Prior to the run, a capsule of chosen material is filled with starting material and packed. The capsule is placed inside an assembly (Siebert et al. 2011). The assembly is wrapped in a lead foil in order to minimise friction forces as well as facilitate the extraction of the assembly from the device when the experiment is complete. The assembly is placed in the pressure vessel of the apparatus, which is made of tungsten carbide. A steel and pyrophyllite plug is placed directly above the assembly to ensure electrical contact between the apparatus and the graphite furnace surrounding the encapsulated sample. In order to apply the chosen pressure to the sample, the two hydraulic cylinders are activated in the correct order. First, the pressure vessel is compressed by the end-load hydraulic cylinder or external

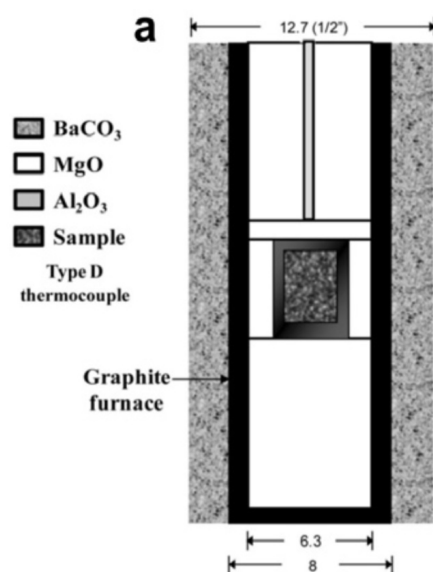


Figure 1.1 – Standard piston-cylinder 1/2" assembly used in this study, with pressure medium made of BaCO₃. Figure from Siebert et al. (2011).

hydraulic cylinder. Once a pressure of 4000 psi is applied to maintain the pressure vessel and the other components, the sample hydraulic cylinder can be operated in order to compress the sample with the piston that sits below it, until the desired pressure is reached. The heating of the sample is achieved by injecting an electric current into the graphite furnace, using Joule heating. Monitoring of the sample by a thermocouple allows the chosen temperature to be reached by adjusting the electric power. A cold-water system, circulating in a top plate and a bottom plate, cools the apparatus parts made of tungsten carbide, preventing them from being damaged. The duration of each run is chosen carefully with respect to the temperature in order to reach elemental and isotopic equilibrium between molten metal and silicate melt whilst minimising the chemical reactions with the capsule (Corgne et al. 2008, Siebert et al. 2011, Thibault and Walter 1995). Samples are quenched by terminating the electrical current. Representative pieces of metal and silicate are mechanically selected under magnifying glass, mounted in resin and carefully polished for SEM observation and EPMA and LA-ICPMS measurement, or dissolved in acid for MC-ICPMS measurement.

1.1.3 Multianvil experiments

The 6–8 Kawai type multianvil system (Kawai and Endo 1970, Kawai et al. 1973) is composed of a hydraulic press in which six tool-steel outer-anvils are used to transfer pressure to eight tungsten carbide cubic inner-anvils. The pressure is then transferred to the assembly through truncations located at the wedges of each tungsten carbide cube, forming an inner octahedral cavity where an assembly containing the sample can be placed. In principle, multianvil presses can generate pressures from 3 to 30 GPa and temperatures up to 3000 K. The bulk of the experiments performed in multianvil presses have been performed using the 5000-ton Zwick/Voggenreiter press or the 1000-ton Hymag press at Bayerisches Geoinstitut (University of Bayreuth). Pressure calibration of both presses were performed using the transition of Bi (I–II and III–V) (Lloyd 1971), the quartz–coesite transition (Bohlen and Boettcher 1982), the coesite–sishovite transition (Yagi and Akimoto 1976) and the olivine– γ -spinel transformation in fayalite (Yagi et al. 1987). More details specific to the calibration of the two presses mentioned here can be found in Rubie (1999) and Frost et al. (2004). Pressure and temperature uncertainties are estimated to 1 GPa and 100 K (e.g. Woodland and Angel 1997, Woodland and O’Neill 1993). Temperature gradients were measured and estimated to be less than 50 K across the sample (Frost et al. 2004, Rubie 1999). Such gradients can be lowered by using a stepped LaCrO_3 heater and in the case of this study, by the superliquidus temperature conditions applied to the sample that are allowing convection processes to homogenise chemically and physically the sample.

In this study, experiments were performed from 7 to 20 GPa and from 1973 to 2573 K (table 1.1). The pressure media consisted of an octahedron made of MgO and 5% Cr_2O_3 , with 18 or 25 mm edges. Pressure was applied with cubic tungsten carbide anvils with 15, 11 and 8 mm truncations (25/15, 18/11 and 18/8 configurations, figure 1.2). The octahedron contains a cylindrical cavity lined with ZrO_2 to ensure thermal insulation. A stepped LaCrO_3 heater was placed inside the assembly. This heater is used to minimise temperature gradients (Rubie 1999). Each assembly was fired at 1000°C for an hour prior to insertion of the encapsulated sample. The starting material was poured in a single-crystal MgO capsule in order to minimise possible interactions between the capsule and the sample, especially at high temperature. The sample was placed between two cylindrical MgO spacers

situated above and below the capsule. The upper MgO spacer is drilled to allow the insertion of the thermocouple contained in a 4-hole alumina sleeve. The emerging wires are enclosed in alumina sleeves and Cu coils in order to protect them during the experiment. A Mo ring and a Mo disk were inserted at the top and bottom parts of the assembly respectively, to ensure electrical contact with the heater. A small piece of pyrophyllite was placed into the top Mo ring, above the thermocouple, prior to cementation of the exterior of the assembly to secure all pieces together.

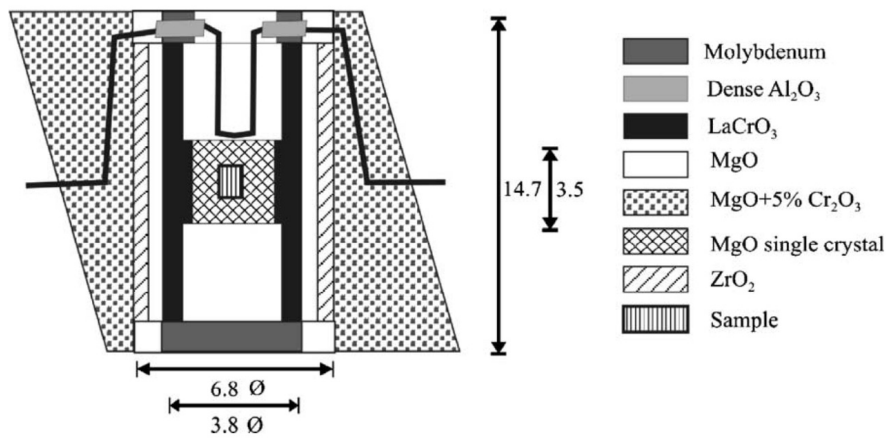


Figure 1.2 – Standard assembly with 18/8 configuration. Figure from Frost et al. (2004).

Experimental procedure

Pyrophyllite gaskets were placed on the inner-anvils around the wedge truncations to accommodate for the friction between the inner-anvils and the assembly. The tungsten carbide cubes were covered in Teflon tape and carboard in order to maintain the gaskets in place. The assembly was loaded in the octahedral cavity formed by the inner-anvils, which were subsequently covered by epoxy sheets ensuring minimal friction with the outer-anvils during experiment run. Pieces of copper foil were placed through the epoxy sheets on the two inner-anvil faces where electrical contact towards the assembly is needed. The sample temperature was monitored using a type D (W₉₇Re₃/W₇₅Re₂₅) thermocouple. Pressure was increased over 200 to 280 minutes. Sample heating was executed by injecting electrical current into the LaCrO₃ furnace in steps of 200 K until reaching ~1800 K.

At this point the temperature was increased more rapidly. The sample was kept at constant chosen temperature for the desired time duration—with the prospect of fully melting the sample and achieving chemical equilibrium between metal and silicate—and subsequently quenched by terminating electrical power. The decompression was operated overnight during 850–1000 minutes.

1.1.4 Sample preparation

Mounted samples

Representative pieces of metal and silicate phases from each experiment were mechanically chosen with great care under optical microscope (x8 magnification). They were mounted in a 2-component acrylic polymerising resin and left to cure at 2 bars for 1 hour. The resulting mountings were polished with silicon carbide paper first and secondly with diamond liquids of decreasing size until obtaining a 1 μm polishing. Samples were carbon coated prior to SEM/EPMA analysis.

Samples for wet chemistry

Metal and silicate phases produced by experiments designed to determine isotopic fractionation factors were carefully selected under magnifying glass (x8). Clean representative pieces of metal were put aside. Selection of the silicate for wet chemistry is critical because the silicate is depleted in the siderophile elements of interest relative to the metal and to the bulk of the material, so more material is needed. Moreover, secondary metals present in the silicate must be avoided in order to measure the isotopic composition of the silicate, free of metal contamination. Therefore, the selection process for silicate requires more precision and fineness. In order to pick representative clean silicate pieces, parts (1) located near the capsule, (2) from the outskirts of the metal phase or (3) containing secondary metal beads were discarded. For each experiment, the silicate phase went through 2 to 3 steps of sorting under the microscope to ensure optimal cleanliness of the selected pieces. This mechanical selection was appropriate for glassy silicates (see figure 1.3i), however, removal of all secondary metals was impossible with partially crystallised silicates from MgO encapsulated experiments (see figures 1.3g and h).

Elemental and stable isotopic fractionations of siderophile elements

Table 1.1 – Experimental parameters for all experiments performed for the three studies presented in chapters 4, 5 and 6.

| # | Run | Project | Apparatus | Date | Assembly | Silicate | Metal | Dopant | P (GPa) | T (K) | Capsule | Pressure medium | t (min) | Notes |
|----|-------|-----------|-----------|------------|----------|----------|--------|----------------------|---------|-------|---------|-------------------|---------|--------|
| 1 | E257 | Sn | Elmo | 07/02/2017 | 1/2" | MORB | Fe | Sn | 2 | 1696 | BN | Talc-pyrex | 30 | |
| 2 | E258 | Sn | Elmo | 08/02/2017 | 1/2" | MORB | Fe,FeS | Sn | 2 | 1696 | BN | Talc-pyrex | 30 | |
| 3 | E259 | Sn | Elmo | 14/02/2017 | 1/2" | MORB | Fe,FeS | Sn | 2 | 1796 | BN | Talc-pyrex | 15 | |
| 4 | E260 | Sn | Elmo | 17/02/2017 | 1/2" | MORB | Fe | Sn | 2 | 1796 | BN | Talc-pyrex | 15 | |
| 5 | E263 | Sn | Elmo | 28/02/2017 | 1/2" | HPLG | Fe,FeS | Sn | 2 | – | BN | Talc-pyrex | 0 | Failed |
| 6 | E264 | Sn | Elmo | 01/03/2017 | 1/2" | HPLG | Fe,FeS | Sn | 2 | 1500 | BN | Talc-pyrex | 60 | |
| 7 | E265 | Sn | Elmo | 07/03/2017 | 1/2" | MORB | Fe,FeS | Sn | 2 | 2296 | BN | BaCO ₃ | 1.5 | |
| 8 | E266 | Sn | Elmo | 20/03/2017 | 1/2" | HPLG | Fe,FeS | Sn | 2 | 1796 | BN | Talc-pyrex | 15 | |
| 9 | E267 | Sn | Elmo | 22/03/2017 | 1/2" | MORB | Fe | Sn | 2 | 2296 | BN | BaCO ₃ | 3 | |
| 10 | E268 | Sn | Elmo | 24/03/2017 | 1/2" | MORB | Fe | Sn | 2 | 1823 | BN | Talc-pyrex | 15 | |
| 11 | E269 | Fe-Ni | Elmo | 28/03/2017 | 1/2" | MORB | Fe,Ni | – | 1 | 1873 | MgO | Talc-pyrex | 15 | |
| 12 | E270 | Fe-Ni | Elmo | 28/03/2017 | 1/2" | MORB | Fe,Ni | – | 1 | 1873 | MgO | Talc-pyrex | 15 | |
| 13 | E271 | Fe-Ni | Elmo | 29/03/2017 | 1/2" | MORB | Fe,Ni | – | 1 | 1873 | MgO | Talc-pyrex | 60 | |
| 14 | E272 | Sn | Elmo | 04/04/2017 | 1/2" | MORB | Fe | Sn | 2 | 2296 | MgO | BaCO ₃ | 2 | |
| 15 | E273 | Sn | Elmo | 05/04/2017 | 1/2" | MORB | Fe | Sn | 2 | 2100 | MgO | BaCO ₃ | 5 | |
| 16 | E274 | Sn | Elmo | 07/04/2017 | 1/2" | MORB | Fe | Sn,Si | 2 | 1700 | MgO | Talc-pyrex | 30 | |
| 17 | E275 | Sn | Elmo | 07/04/2017 | 1/2" | MORB | Fe | Sn,Si | 2 | 1700 | MgO | Talc-pyrex | 30 | |
| 18 | E276 | Fe-Ni | Elmo | 15/05/2017 | 1/2" | MORB | Fe,Ni | – | 1 | 1873 | MgO | Talc-pyrex | 15 | |
| 19 | E290 | Sn | Elmo | 08/09/2017 | 1/2" | MORB | Fe,FeS | Sn | 2 | 1873 | BN | Talc-pyrex | 10 | |
| 20 | E291 | Sn | Elmo | 13/09/2017 | 1/2" | MORB | Fe | Sn,Cu | 2 | 2200 | BN | BaCO ₃ | 3 | |
| 21 | E292 | Sn | Elmo | 18/09/2017 | 1/2" | MORB | Fe | Sn | 2 | 1950 | BN | BaCO ₃ | 10 | |
| 22 | CM21 | Sn | Elmo | 27/09/2017 | 1/2" | MORB | Fe | Sn,Cu | 10.5 | – | MgO | MgO | 1 | Failed |
| 23 | E294 | Sn | Elmo | 29/09/2017 | 1/2" | MORB | Fe | Sn,Cu | 2 | 2025 | BN | BaCO ₃ | 8 | |
| 24 | E295 | Sn | Elmo | 04/10/2017 | 1/2" | KLBI | Fe | Sn,Cu | 2 | 2200 | BN | BaCO ₃ | 3 | |
| 25 | E296 | Sn | Elmo | 10/10/2017 | 1/2" | KLBI | Fe | Sn,Cu | 2 | 2293 | BN | BaCO ₃ | 2 | |
| 26 | E297 | Sn | Elmo | 16/10/2017 | 1/2" | MORB | Fe | Sn,Si | 2 | 1700 | BN | Talc-pyrex | 30 | |
| 27 | E298 | Fe-Ni | Elmo | 18/10/2017 | 1/2" | MORB | Fe,Ni | – | 2 | 1873 | MgO | Talc-pyrex | 15 | |
| 28 | E302 | Fe-Ni | Elmo | 27/10/2017 | 1/2" | MORB | Fe,Ni | – | 2 | 1873 | MgO | Talc-pyrex | 15 | |
| 29 | E317 | Volatiles | Elmo | 23/03/2018 | 1/2" | MORB | Fe | Sn,Cu,In,Cd,Bi,Sb,Tl | 2 | 1873 | MgO | Talc-pyrex | 5 | |
| 30 | Z1820 | Volatiles | Zwick | 03/04/2018 | 25/15 | MORB | Fe,FeS | Sn,Cu,In,Cd,Bi,Sb,Tl | 7 | 1979 | MgO SC | MgO | 10 | |
| 31 | H4735 | Volatiles | Hymag | 04/04/2018 | 18/11 | MORB | Fe,FeS | Sn,Cu,In,Cd,Bi,Sb,Tl | 10 | 2273 | MgO SC | MgO | 5 | |
| 32 | Z1821 | Volatiles | Zwick | 05/04/2018 | 25/15 | MORB | Fe | Sn,Cu,In,Cd,Bi,Sb,Tl | 7 | 2023 | MgO SC | MgO | 1 | |
| 33 | Z1822 | Volatiles | Zwick | 06/04/2018 | 18/11 | MORB | Fe | Sn,Cu,In,Cd,Bi,Sb,Tl | 14 | – | MgO SC | MgO | 0 | Failed |
| 34 | Z1823 | Volatiles | Zwick | 07/04/2018 | 18/11 | MORB | Fe | Sn,Cu,In,Cd,Bi,Sb,Tl | 14 | 2573 | MgO SC | MgO | 1 | |
| 35 | Z1824 | Volatiles | Zwick | 08/04/2018 | 18/8 | MORB | Fe | Sn,Cu,In,Cd,Bi,Sb,Tl | 18 | 2473 | MgO SC | MgO | 4 | |
| 36 | Z1825 | Volatiles | Zwick | 09/04/2018 | 18/8 | MORB | Fe,FeS | Sn,Cu,In,Cd,Bi,Sb,Tl | 18 | 2473 | MgO SC | MgO | 4 | |
| 37 | E318 | Fe-Ni | Elmo | 09/05/2018 | 1/2" | MORB | Fe,Ni | – | 2 | 1873 | MgO SC | Talc-pyrex | 15 | |
| 38 | E320 | Fe-Ni | Elmo | 02/06/2018 | 1/2" | MORB | Fe,Ni | – | 2 | 1823 | BN | Talc-pyrex | 2 | |
| 39 | E321 | Fe-Ni | Elmo | 05/06/2018 | 1/2" | MORB | Fe,Ni | – | 2 | 1873 | BN | Talc-pyrex | 15 | |

CHAPTER 1. Experimental and analytical methods

Table 1.1 (*continued*)

| # | Run | Project | Apparatus | Date | Assembly | Silicate | Metal | Dopant | P (GPa) | T (K) | Capsule | Pressure medium | t (min) | Notes |
|----|-------|-----------|-----------|------------|----------|----------|--------|----------------------|---------|-------|---------|-------------------|---------|--------|
| 40 | E322 | Fe-Ni | Elmo | 29/06/2018 | 1/2" | MORB | Fe,Ni | – | 2 | 1873 | MgO | Talc-pyrex | 15 | |
| 41 | E323 | Fe-Ni | Elmo | 09/07/2018 | 1/2" | MORB | Fe,Ni | – | 2 | 1873 | BN | Talc-pyrex | 3 | |
| 42 | E324 | Fe-Ni | Elmo | 11/07/2018 | 1/2" | MORB | Fe,Ni | – | 2 | 1873 | MgO | Talc-pyrex | 3 | |
| 43 | E325 | Fe-Ni | Elmo | 26/07/2018 | 1/2" | MORB | Fe,Ni | – | 2 | 1873 | MgO | Talc-pyrex | 3 | |
| 44 | H4950 | Volatiles | Hymag | 24/02/2019 | 18/11 | MORB | Fe | Sn,Cu,In,Cd,Bi,Sb,Tl | 12 | 2273 | MgO SC | MgO | 5 | |
| 45 | Z1956 | Volatiles | Zwick | 25/02/2019 | 18/8 | MORB | Fe | Sn,Cu,In,Cd,Bi,Sb,Tl | 20 | 2573 | MgO SC | MgO | 1.3 | |
| 46 | H495* | Volatiles | Hymag | 26/02/2019 | 18/11 | MORB | Fe,FeS | Sn,Cu,In,Cd,Bi,Sb,Tl | 12 | – | MgO SC | MgO | – | Failed |
| 47 | Z1957 | Volatiles | Zwick | 26/02/2019 | 18/8 | MORB | Fe,FeS | Sn,Cu,In,Cd,Bi,Sb,Tl | 20 | 2573 | MgO SC | MgO | 1.3 | |
| 48 | H4951 | Volatiles | Hymag | 27/02/2019 | 18/11 | MORB | Fe | Sn,Cu,In,Cd,Bi,Sb,Tl | 14 | 2373 | MgO SC | MgO | 2 | |
| 49 | H4952 | Volatiles | Hymag | 28/02/2019 | 18/11 | MORB | Fe,FeS | Sn,Cu,In,Cd,Bi,Sb,Tl | 12 | 2373 | MgO SC | MgO | 2 | |
| 50 | Z1959 | Volatiles | Zwick | 29/02/2019 | 18/11 | MORB | Fe | Sn,Cu,In,Cd,Bi,Sb,Tl | 16 | 2473 | MgO SC | MgO | 2 | |
| 51 | E342 | Volatiles | Elmo | 12/04/2019 | 1/2" | MORB | Fe | Sn,Cu,In,Cd,Bi,Sb,Tl | 2 | 1773 | MgO | Talc-pyrex | 15 | |
| 52 | E345 | Volatiles | Elmo | 18/04/2019 | 1/2" | MORB | Fe | Sn,Cu,In,Cd,Bi,Sb,Tl | 2 | 2273 | MgO | BaCO ₃ | 1 | |
| 53 | E369 | Volatiles | Elmo | 05/12/2019 | 1/2" | MORB | Fe | Sn,Cu,In,Cd,Bi,Sb,Tl | 2 | 1773 | MgO | Talc-pyrex | – | Failed |
| 54 | E370 | Volatiles | Elmo | 07/12/2019 | 1/2" | MORB | Fe | Sn,Cu,In,Cd,Bi,Sb,Tl | 2 | 1773 | MgO | Talc-pyrex | 30 | |
| 55 | E372 | Volatiles | Elmo | 13/12/2019 | 1/2" | MORB | Fe,FeS | Sn,Cu,In,Cd,Bi,Sb,Tl | 2 | 1773 | MgO | Talc-pyrex | 30 | |
| 56 | E373 | Fe-Ni | Elmo | 17/12/2019 | 1/2" | MORB | Fe,Ni | – | 2 | 1873 | MgO SC | Talc-pyrex | 15 | |
| 57 | E375 | Fe-Ni | Elmo | 19/12/2019 | 1/2" | MORB | Fe,Ni | – | 2 | 1873 | MgO SC | Talc-pyrex | 5 | |
| 58 | E376 | Fe-Ni | Elmo | 27/12/2019 | 1/2" | MORB | Fe,Ni | – | 2 | 1873 | MgO SC | Talc-pyrex | 30 | |
| 59 | E377 | Fe-Ni | Elmo | 03/01/2020 | 1/2" | MORB | Fe,Ni | – | 2 | 1873 | MgO SC | Talc-pyrex | 30 | |
| 60 | E378 | Fe-Ni | Elmo | 03/01/2020 | 1/2" | MORB | Fe,Ni | – | 2 | 1873 | MgO SC | Talc-pyrex | 30 | |
| 61 | E379 | Fe-Ni | Elmo | 06/01/2020 | 1/2" | MORB | Fe,Ni | – | 2 | 1873 | MgO SC | Talc-pyrex | 30 | |
| 62 | E380 | Fe-Ni | Elmo | 06/01/2020 | 1/2" | MORB | Fe,Ni | – | 2 | 1873 | MgO SC | Talc-pyrex | 30 | |
| 63 | E381 | Fe-Ni | Elmo | 07/01/2020 | 1/2" | MORB | Fe,Ni | – | 2 | 1873 | C | Talc-pyrex | 30 | |
| 64 | E382 | Fe-Ni | Elmo | 07/01/2020 | 1/2" | MORB | Fe,Ni | – | 2 | 1873 | MgO SC | Talc-pyrex | 60 | |
| 65 | E396 | Volatiles | Elmo | 12/02/2020 | 1/2" | MORB | Fe,FeS | Sn,Cu,In,Cd,Bi,Sb,Tl | 2 | 1873 | MgO | Talc-pyrex | 5 | |
| 66 | E397 | Volatiles | Elmo | 12/02/2020 | 1/2" | MORB | Fe,FeS | Sn,Cu,In,Cd,Bi,Sb,Tl | 2 | 1773 | MgO | Talc-pyrex | 15 | |

Therefore, all silicate samples underwent a second step of selection based on the magnetic properties of the metal phase. First, mechanically selected silicate phases were roughly crushed in order to separate as much as possible the potential metal pieces remaining from the silicate. A magnet was used to isolate any metal parts left in the sample, which was subsequently observed under the microscope. Note that if the silicate was not crushed prior to magnetic purification, the discarded metals contained in bigger silicate pieces could lower the volume of sample below the required volume for isotopic measurement. The purified silicate samples were thoroughly observed under the microscope after each magnetic separation which was repeated until no material was isolated by the magnet from the sample. The clean silicate pieces were then finely crushed to facilitate their digestion in acid for elemental purification and subsequent MC-ICPMS analysis.

1.2 Analytical methods

1.2.1 Electron beam-based analytical methods

Multiple analytical tools including scanning electron microscopy (SEM) and electron probe microanalysis (EPMA) are based on the same operating principle. Electrons are excited and emitted by a source, and subsequently focused by electromagnetic lenses under vacuum towards a sample. Electrons can (1) interact with the sample and bounce back (backscatter electron imaging), (2) produce secondary electrons forced out of the sample (secondary electron imaging), (3) induce the emission of X-ray (energy dispersive X-ray, EDX). Although EDX provides rather qualitative compositional information, X-rays can be separated using crystal diffraction, such that the sensor collects one wavelength (wavelength dispersive X-ray spectroscopy, WDS). This last technique, used in electron probe microanalysers (EPMA), provides high resolution quantitative compositional information. Each electron type is received by specific sensors corresponding to the different techniques mentioned above.

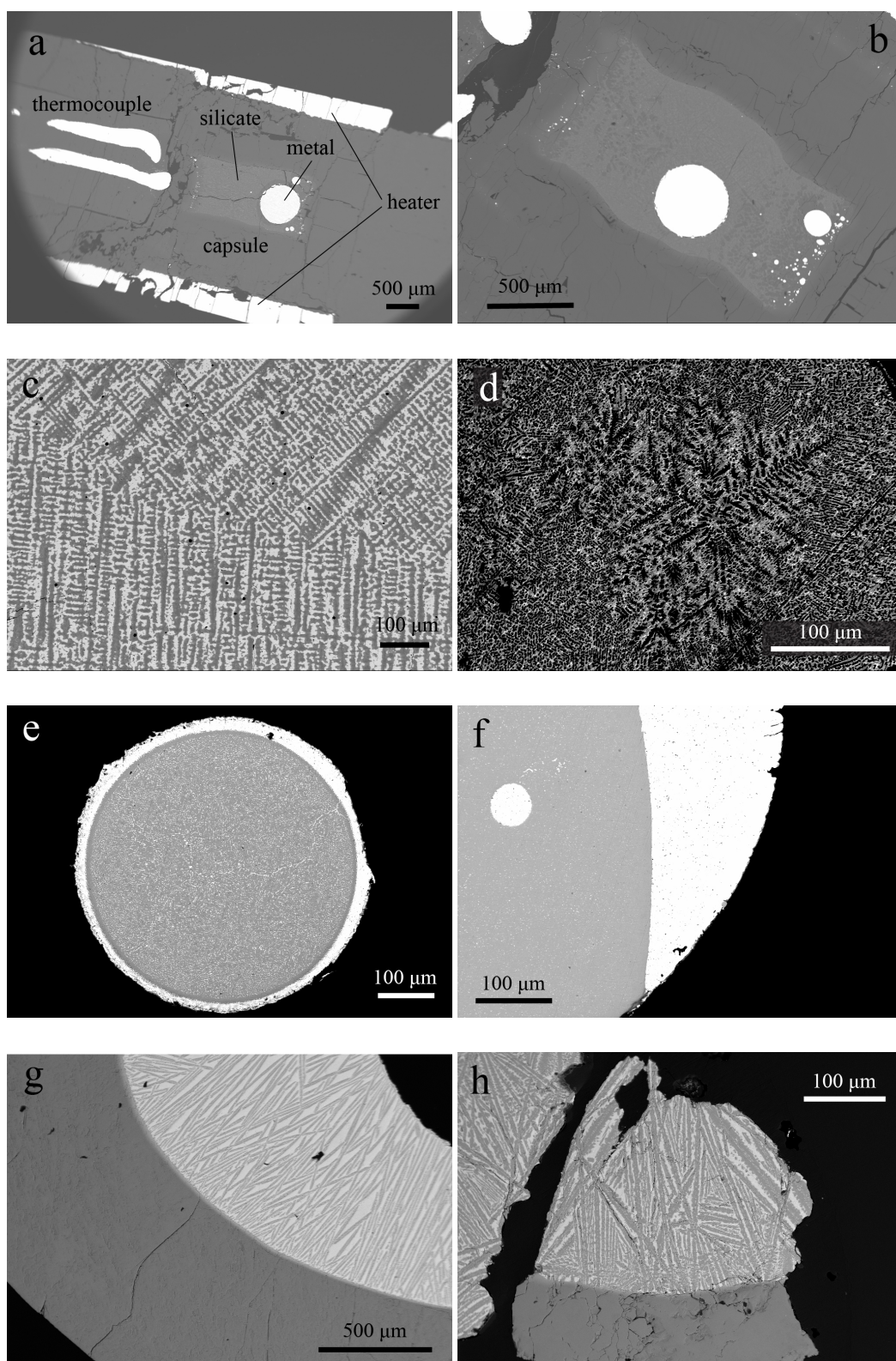
Scanning electron microscopy (SEM)

Scanning electron microscopy produces images of a sample by focusing an electron beam on the surface. Secondary electrons are emitted by atoms excited by the electrons from the beam and detected with a secondary electron detector, and provide morphological and topographical details of the surface of the sample with a resolution of a nanometer. Backscattered electrons are high-energy electrons sourced from the electron beam that are reflected out of the sample as a result of elastic scattering interactions with the sample's atoms. They are monitored by dedicated backscattered electron detectors positioned above the sample, around the electron beam. Heavy elements backscatter electrons with more force, creating an electron flux that will appear brighter on the electron image, hence designated as "electron dense". Using this principle, backscatter electron imaging is used to detect differences in chemical composition across a sample, through differences in contrast on the image.

In this experimental study, after performance of the experiment itself, a critical step is to provide evidence of equilibrium achievement in order for the sample to be exploitable and representative of equilibrated metal and silicate. SEM observation was therefore systematically used to observe representative pieces of each phase of experiments to check that (1) the sample was fully molten during the experiment and (2) that each phase was chemically homogeneous. The combination of the two provides preliminary and necessary arguments in favour of equilibrium achievement during the experiment.

SEM observation is also useful to detect other structures often present in piston cylinder or multianvil metal–silicate equilibrium experiments. The metal phases usually present fine quench textures (figures 1.3c, d), and therefore require the use of rasters instead of points of measurement in order to obtain an average composition (see EPMA section below). However, larger heterogeneities could be present in the metal, as displayed in figures 1.3e and f. They are the result of the formation of two immiscible metal liquids in a Fe–Sn–Si system, designed to explore the effect of more reducing conditions on Sn partitioning (see chapter 4). Due to the impossibility of determining the partitioning of the element of interest between metal and silicate in such a case, these experiments were discarded from the study.

Elemental and stable isotopic fractionations of siderophile elements



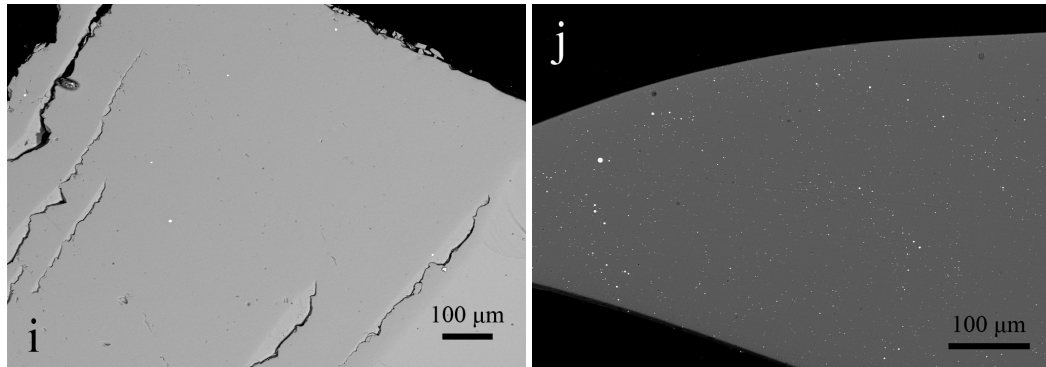


Figure 1.3 – Backscattered electron images from typical metal–silicate experiment run products. **a.** Image of multianvil experiment H4950 (12 GPa, 2273 K), longitudinal cross-section of the cylindrical assembly with visible sample, surrounding capsule, dense furnace and dense metallic thermocouple to the left. **b.** Image of Z1956 (20 GPa, 2573 K), with visible capsule and sample, with deformation of the sample compared to image a. due to higher pressure. **c.** Image of E257 (2 GPa, 1700 K) presenting typical quench texture from the metal phase. **d.** Image of E266 (2 GPa, 1800 K) showing dendritic quench texture in the metal phase. **e.** Image of E274 (2 GPa, 1700 K) metal sphere presenting two immiscible metal phases. **f.** Image of E275 (2 GPa, 1700 K) metal phase with two immiscible metal liquids, preventing correct assessment of the metal bulk composition and therefore metal–silicate fractionation of studied elements. Experiments from d. and e. were discarded from the dataset of this study. **g.** Image of silicate phase with surrounding capsule of E373 (2 GPa, 1873 K) run in single-crystal MgO capsule, and presenting skeletal crystals of olivine due to MgO enrichment from capsule interaction. This image shows a typical clean sample–capsule boundary with reaction limited to the first 30 μm of the capsule permitted by the use of single-crystal MgO. **h.** Image of silicate phase of E273 (2 GPa, 2100 K) run in crushable MgO capsule inducing diffusion of MgO in the silicate with skeletal olivine crystals and. **i.** Image of E268 (2 GPa, 1823 K) silicate phase with glassy texture typical of BN capsule. **j.** Image of E275 (2 GPa, 1700 K) silicate with glassy texture and numerous metal “nuggets” in the silicate, preventing proper compositional characterisation of the silicate. This experiment was discarded from the dataset.

Silicate phases usually present glassy textures as a consequence of the rapid cooling of the experiments upon quenching. Most silicate phases contain a small amount of nano- to micro-size metal spheres (figure 1.3j) referred to as “nuggets”

(e.g. Ertel et al. 2001) that can be attributed to the quench process (e.g. Cottrell and Walker 2006), insolubility due to oversaturation especially at reducing fO_2 conditions (e.g. Bennett et al. 2014) or to incomplete segregation of the metal in the main sphere. Experimental studies have demonstrated that experiments carried out at high acceleration (1450g), by centrifuging the experimental set up, presented clean silicate melts compared to static analogous experiments (Médard et al. 2015). Although the origin of such metal nuggets is still debated, they were considered as artefacts in this study and avoided to the best of our ability for EPMA, LA-ICPMS and MC-ICPMS analysis. The silicate displayed on figure 1.3j presents an overabundance of metal nuggets and the corresponding experiment was therefore discarded from the dataset. MgO encapsulated experiments present MgO enrichment from the capsule, inducing skeletal quenched olivine crystals in the silicate (figure 1.3g, h), producing localised heterogeneities that were also averaged by the use of raster measurements during EPMA and a 90- μm beam size during LA-ICPMS analysis. Secondary metal spheres were often observed near the capsule (e.g. figure 1.3b) due to surface tension properties of such capsule boundary, and were estimated to represent 10% or less of the metal mass of an experiment. These metal spheres were routinely analysed and found to have identical composition to the main metal sphere.

Electron probe microanalysis

All EPMA measurements from this work were performed using a CAMECA SX Five electron microprobe (CAMPARIS, Université Pierre et Marie Curie). Samples were polished and mounted, and evenly carbon coated prior to analysis. A selection of major and trace elements was resolved in both metal and silicate phases using an accelerating voltage of 15 keV and a beam current of 300 nA. Counting times were chosen as follows: 10-20 s for major and 20-90 s for trace elements. To prevent heterogeneities induced by quench textures (e.g. figure 1.3c) or partially crystallised textures (e.g. figure 1.3g) from affecting the measurements, 30 μm rasters were used instead of points to improve the analytical statistics. A large number of 15 to 50 analysis were performed on each phase to ensure statistical relevance of the average concentrations. No compositional zonation was found across the samples presented in this study, advocating for equilibrium achievement.

Standards used in major elements analysis are diopside for SiO_2 , MgO and CaO ; orthopyroxene for K_2O and Al_2O_3 ; Fe_2O_3 for iron oxide; albite for Na_2O ; FeS_2 for S in the silicate and an alloy of Mn and Ti for TiO_2 . For the metallic phase, Fe_2O_3 was used for Fe and O, FeS_2 for sulfur, diopside for Si. For Cd and Bi, metallic Cd and Bi were used as standards, and stibnite (Sb_2S_3) was used for Sb. A Sn oxide standard (SnO_2) was used for Sn measurements. An in-house standard of Tl_2O_3 was made from Tl_2O_3 powder and used to resolve the Tl concentrations in metals and silicates.

1.2.2 Laser-ablation inductively-coupled-plasma mass-spectrometry—LA-ICPMS

LA-ICPMS measurements were performed on the silicate phases of the experiments of this study in order to resolve the concentration of elements of interest depleted in the silicate near or below EPMA detection limits. Laser ablation analysis were performed using an Element XR high-resolution mass spectrometer (Université de Brest) coupled to a 193 nm Compex Pro 102 Coherent Laser system set to a $15\text{J}/\text{cm}^2$ output and a 10 Hz frequency. A $90\text{-}\mu\text{m}$ beam was used to vaporise a significant amount of sample, and 3 to 8 measurements were performed and averaged on each sample. The ablated particles were carried by a helium flux and mixed with argon before entering the plasma. Calibration was performed using Mg concentrations previously determined by EPMA as internal standardisation. Standard interpolations by measurement of glass standards NIST610, NIST612 and NIST614 were used for external standardisation of the data. The data quality is also certified by the repeated analyses of natural basaltic glass standards BIR-1, BCR-2 and BHVO-2.

LA-ICPMS measurements presented in this study were performed using both low ($m/\Delta m=200$) and medium resolution ($m/\Delta m=400$) modes. Each analysis was done as a single spot and lasted 90 seconds with the first 10 seconds of background acquisition (gas blank). Standards were measured twice each (all 6 standards) at the beginning and end of a sequence (i.e. 6 standards measured at least 4 times each day).

1.2.3 Multi-collector inductively-coupled-plasma mass-spectrometry—MC-ICPMS

Sample preparation and purification

In order to avoid interferences in the mass spectrometer, samples need to be chemically purified prior to isotopic analysis. All laboratory work described in this section was performed at the Institut de Physique du Globe de Paris in a class-100 clean room with class-10 laminar flow hoods. The samples were dissolved into acid in order to proceed with the separation technique. The acids used in this work were distilled from BASF Selectipur[®] AR grade acids (69% HNO₃; 37% HCl). All dilutions used ultra-pure (18.2 MΩ cm purity) Milli-Q water. All disposable components (pipette tips, columns and test tubes) and beakers were refluxed in 30% concentrated HNO₃ for 3-5 days, with 2-3 cycles for beakers. Prior to digestion, the samples were weighed in order to obtain approximately 1 mg of the element of interest, and placed in pre-cleaned Savillex Teflon PFA beakers. Crushed silicates were digested in a 1:3 solution of HF:HNO₃ and metals were dissolved in 6 N HCl. The closed beakers were placed on a hotplate at 100°C for 12 hours until full digestion. All samples were dried and silicates were further digested in aqua regia on a hot plate at 150°C in order to remove any residual fluoride complex, and dried down again.

Tin purification Tin was chemically separated from other elements present in the samples using the ion exchange chromatography technique described in Creech et al. (2017b). Since this technique has a relatively low yield of 13 to 66% of Sn recovered from the purification process for geological samples (Creech et al. 2017b), the double spike technique was used in order to correct for all mass-dependent fractionation possibly associated with the loss of Sn during processing of the samples. An amount of double-spike solution was added to the samples after digestion such that the resulting solution contains 39.77% of Sn from the double-spike and 60.23% of Sn from the sample. The double-spike technique has been applied to a variety of isotope systems (e.g. Pb, Cr, Mo, Cd, Pt; Anbar et al. 2001, Compston and Oversby 1969, Creech et al. 2014, Schmitt et al. 2009, Schoenberg et al. 2008) as it has several advantages compared to a sample-standard bracketing method, where

a standard is measured between each sample in order to correct for instrumental mass bias drift. By using the double-spike approach, it is possible to correct for mass-dependent isotope fractionation occurring during chemical purification or mass spectrometry analysis, as well as to accurately determine concentrations and isotopic composition from a single analysis.

All samples were dissolved in 2 mL of 0.5 N HCl. Samples were purified using 1 mL of Eichrom TRU resin. The resin was cleaned and conditioned before loading the sample. The matrix was eluted in order to collect the Sn cut alone by following the steps described in table 1.2. A small volume of 10 N HCl was placed in each clean beaker before Sn collection in order to avoid the formation of insoluble compounds that could precipitate from the Sn-HNO₃ solution. The Sn cuts were subsequently dried and redissolved in 0.5 N HCl in order to obtain a 100 ppm solution for mass spectrometer analysis.

Table 1.2 – Elution scheme for Sn purification (Creech et al. 2017b)

| Step | Eluent | Volume (mL) |
|----------------|------------------------|-------------|
| Cleaning | 0.5 N HCl | 4 |
| Cleaning | H ₂ O | 4 |
| Cleaning | 0.5 N HNO ₃ | 4 |
| Cleaning | H ₂ O | 4 |
| Cleaning | 0.5 N HNO ₃ | 4 |
| Cleaning | H ₂ O | 4 |
| Conditioning | 0.5 N HCl | 4 |
| Sample load | 0.5 N HCl | 2 |
| Matrix elution | 0.5 N HCl | 4 |
| Matrix elution | 0.25 N HCl | 4 |
| Matrix elution | 0.25 N HCl | 3 |
| Sn collection | 0.5 N HNO ₃ | 4 |
| Sn collection | 0.5 N HNO ₃ | 3 |
| Sn collection | 0.5 N HNO ₃ | 3 |

Iron purification All samples from the study presented in chapter 6 with-
 stood Fe purification in order to determine their Fe isotope compositions. Iron
 was chemically separated by performing anion exchange chromatography using Bio-
 Rad AG1-X8 resin (200–400 mesh i.e. 0.038–0.075 mm bead diameter) in 0.4 x 7
 cm Teflon columns (Sossi et al. 2015) loaded with 1 mL of resin. Samples were dis-
 solved in 6 N HCl prior to loading on a previously cleaned and conditioned resin.
 Iron cuts were collected after matrix elution following the procedure detailed in
 table 1.3, and subsequently dried down to be redissolved in 0.5 N HNO₃.

Table 1.3 – Elution scheme for Fe purification (Sossi et al. 2015).

| Step | Eluent | Volume (mL) |
|----------------|----------------------|-------------|
| Cleaning | 3 N HNO ₃ | 5 |
| Cleaning | H ₂ O | 5 |
| Cleaning | 6 N HCl | 5 |
| Conditioning | 6 N HCl | 5 |
| Sample load | 6 N HCl | 0.5 |
| Matrix elution | 6 N HCl | 11 |
| Fe collection | 0.5 N HCl | 3 |

MC-ICPMS measurements

Multi-collector inductively-coupled-plasma mass-spectrometry separates isotopes based on the mass to charge ratio of charged particles in order to discriminate between isotopes of the same element and measure isotopic ratios. The sample is ionised using an inductively-coupled-plasma source, producing positively charged particles that are accelerated and focused in order to be sent through a magnetic field. Ions with different m/z are separated according to their differential magnetic deflection. Lighter cations undergo a larger relative magnetic pull and their path is therefore more curved. At a fixed charge, accelerating voltage and magnetic field, the radius of curvature is proportional to the square root of the ion's mass. It is thus possible to precisely discriminate between different isotopes, using the collectors, here Faraday cups, which are receiving the accelerated ions of a given mass as an electric charge, and converting to counts per seconds.

All isotopic measurements of this work were performed using a Thermo-Scientific Neptune Plus multi-collector inductively-coupled-plasma mass-spectrometer housed at the Institut de Physique du Globe de Paris, France.

Tin isotope measurements Tin isotopes measurements were performed following the method described in Creech et al. (2017b). All sample and standard solutions were diluted such as to obtain Sn concentrations of 100 ng.mL^{-1} in 0.5

N HCl. An ESI Apex-HF desolvator was used as introduction system with a 100 $\mu\text{g}\cdot\text{min}^{-1}$ PFA nebuliser. The Neptune Plus was used in low resolution mode. Faraday cups were used to collect ion beams at ^{116}Sn , ^{117}Sn , ^{118}Sn , ^{119}Sn , ^{120}Sn , ^{121}Sb , ^{122}Sn , ^{123}Sb and ^{124}Sn with all Sn channels connected to amplifiers with $10^{11} \Omega$ resistors. Further details about the instrumental operating conditions and parameters are published in Creech et al. (2017b). Samples were analysed during 412 s, with a consumption of 70 ng of Sn per analysis. Blanks were <1 ng. Baselines were measured on peak during 14 minutes between each analysis and the last 120 seconds were used as the actual baseline and subtracted from the following analysis. We employed the Sn_IPGP standard as reference (ICP standard PlasmaCal 1000 $\mu\text{g}\cdot\text{mL}^{-1}$ Sn ICP std in 20 % HCl, lot #SC9202950). Reference materials and samples for which published data was available were measured in the same sequence as the samples. Data reduction process was performed using Isospike (www.isospike.org; Creech and Paul 2015). Column processed double-spiked standard was measured along with the double-spiked samples, allowing to correct for any mass-dependent fractionation that may occur during chemical purification and mass spectrometry analysis. Using this technique, the internal precision of the standard solution was estimated at ca. 0.013 ‰ per amu with a reproducibility of ca. $\pm 0.023\%$ (2 s.d.) on $\delta^{122/118}\text{Sn}$. For geological samples, repeated measurements of BCR-2 were used to estimate an external reproducibility of $\pm 0.016\%$ (2 s.d.) per amu (Creech et al. 2017b). Tin isotopic results are presented using the delta notation, relative to Sn_IPGP:

$$\delta^{122/118}\text{Sn}_{\text{sample}} = \left(\frac{\left(\frac{^{122}\text{Sn}}{^{118}\text{Sn}}\right)_{\text{sample}}}{\left(\frac{^{122}\text{Sn}}{^{118}\text{Sn}}\right)_{\text{Sn_IPGP}}} - 1 \right) \cdot 1000 \quad (1.2)$$

Iron isotope measurements Iron isotopic compositions were measured following the method described in Sossi et al. (2015), using the Neptune Plus in medium resolution mode. The cups were configured as to collect ^{54}Fe , ^{56}Fe , ^{57}Fe , ^{60}Ni , ^{61}Ni and ^{53}Cr . Chromium was used to correct for any ^{54}Cr interference on ^{54}Fe , even though chromatographic separation was shown to be very efficient, meaning insignificant correction. All sample and standard solutions were diluted in 4 ppm Fe 0.5 N HNO_3 solutions, and spiked with 8 ppm of Ni. The $^{61}\text{Ni}/^{60}\text{Ni}$ ratios measured in all samples were used as internal standardisation to correct for mass bias effects. A solution of IRMM-014 was used for external standardisation of

the sample measurements and IRMM-014 analysis performed in between samples (sample-standard bracketing) were used to calculate the ratios and deltas presented in this study like so:

$$\delta^{56/54}\text{Fe}_{\text{sample}} = \left(\frac{\left(\frac{^{56}\text{Fe}}{^{54}\text{Fe}}\right)_{\text{sample}}}{\left(\frac{^{56}\text{Fe}}{^{54}\text{Fe}}\right)_{\text{IRMM-014}}} - 1 \right) \cdot 1000 \quad (1.3)$$

Thermodynamics of metal–silicate equilibria

The previous chapter focused on the description of experimental and analytical techniques used in this PhD work in order to measure partition coefficients and isotopic fractionation factors between metal and silicate in controlled experiments. This chapter aims at portraying the formalism of metal–silicate equilibrium thermodynamics used in order to describe the partitioning and isotopic fractionation of elements as empirical laws inferred from experimental data. Precise determination of regression coefficients allows to describe thermodynamically the behaviour of elements of interest in a metal–silicate equilibrium as a function of temperature, pressure, oxygen fugacity and composition. This step is required in order to extrapolate the partitioning and isotopic fractionation to conditions that are relevant to Earth’s differentiation.

2.1 Achievement of elemental and isotopic equilibria

Achievement of full equilibration between metal and silicate is critical for accurate characterisation and parameterisation of the behaviour of the studied elements at equilibrium conditions. Sufficient time durations allowing complete fusion and equilibration of the sample, as well as thorough petrographic characterisation

showing homogeneous phase segregation, were achieved in this study. Our data also present overarching trends that can be described thermodynamically, thus providing further evidence of equilibrium.

2.1.1 Elemental equilibrium

Equilibrium achievement of a given element in an experiment is determined by the diffusion rate of the element in the phases involved, and can be calculated through the length of diffusion l , which is a function of a diffusion coefficient D and time of diffusion t :

$$l = 2 \cdot \sqrt{D \cdot t} \quad (2.1)$$

Diffusion coefficients for major elements in liquid silicate between 1800 and 2800 K and 15 to 25 GPa have been estimated to be between 10 and 1000 $\mu\text{m}^2 \cdot \text{s}^{-1}$ (Walker and Agee 1989). Experimental studies of Ni, Co and Fe partitioning involving time series as well as reversal experiments demonstrated that equilibrium is reached within 5 seconds at 5 GPa and 2300 K (Thibault and Walter 1995). A similar message is delivered by Gessmann and Rubie (1998), where Ni and Co were equilibrated between liquid metal and solid magnesiowüstite within 1 minute at 9 GPa and 2473 K. Therefore, siderophile element diffusion coefficients are larger than 10 $\mu\text{m}^2 \cdot \text{s}^{-1}$ at such conditions. Elemental equilibrium achievement is also supported by demonstration of chemical homogeneity of the two phases, using both SEM observations and EPMA measurements.

2.1.2 Isotopic equilibrium

Although elemental equilibrium was demonstrated to be achieved within a few seconds at 2300 K (Thibault and Walter 1995), such equilibration times cannot be extrapolated to isotopic equilibrium because their diffusion rates are driven by distinct chemical potentials (van der Laan et al. 1994, Lesher 1990). Most studies investigating isotopic fractionation between metal and silicate for a variety of elements use time durations of the same order of magnitude as partitioning studies, i.e. from a few minutes to ~ 2 h (Hin et al. 2013, 2014, Poitrasson et al. 2009, Xia et al. 2019). This is due to the fact that the superliquidus conditions applied to the system are ensuring high diffusion rates applied to short diffusion

distances. The convection mechanism occurring inside the capsule helps to mix and homogenise the sample, decreasing the time duration needed for equilibrium achievement. Finely crushed and homogeneous starting materials are also favoring an efficient diffusion when melted. On the other hand, the presence of one solid phase in the system would significantly slow down the diffusion rate.

Experimental measurement of isotopic fractionation factors between metal and silicate also requires the experimental enclosure to form a closed system, preventing volatile loss at such high temperatures. An open system would certainly be associated to a mass-dependent kinetic isotopic fractionation by preferential loss of light isotopes of the element of interest relative to heavier isotopes that would more easily remain in the system. This would result in non-equilibrium conditions. In that respect, the choice of capsule needs to be carefully addressed with the prospect of ensuring an experimental closed system. For the experiments designed in this study, metal capsules are excluded as they would react with the metal phase in which the element of interest would be diffused. Graphite capsules have been used in numerous metal–silicate isotope fractionation experimental studies (e.g. Elardo and Shahar 2017) and have shown to endure relatively long durations at high temperature, allowing equilibrium achievement. However, the use of such capsules induces significant carbon diffusion into the system, with several *wt.%* of C in the metal phases (i.e. ~ 5 *wt.%* at 2123 K, Elardo and Shahar 2017). Such a metal composition may not be relevant to core composition, and as light elements such as C, S, Si and O can have an effect on the fractionation behaviour of siderophile elements between metal and silicate, graphite capsules were not favoured in this study. Instead we used capsules made of boron nitride (BN), crushable MgO and single-crystal MgO for isotope fractionation experiments (see chapters 4 and 6). BN capsules have been shown to induce more reducing conditions in the system (Labidi et al. 2016, Shahar et al. 2015), which can be useful to investigate reducing conditions and widen the range of fO_2 investigated. However, the diffusion of boron in the silicate, up to ~ 10 *wt.%*, is not relevant to the mantle composition and needs confirmation from experiments with different capsule materials that boron does not affect the partitioning (see chapter 4). Although MgO tends to diffuse into the silicate melt during experimentation, the use of MORB in the starting mixture yields MgO concentrations in the final silicate run products that are relevant to mantle concentrations. Single-crystal MgO capsules show promising results in the case study on Fe presented in this work (chapter 6), with the element

of interest being detected only in the first 30 μm of the capsule interior and with concentrations below 5 *wt.%* in this limited volume (see figure 6.3).

As well as for elemental equilibrium, compositionally homogeneous phases are a good indication that the phases were fully molten, allowing isotopic equilibrium achievement. In order to provide solid evidence that equilibrium conditions were reached, two methods are typically used: time series and the “three-isotope method”.

Time series

Numerous studies rely on time series in order to demonstrate equilibrium achievement of metal–silicate isotope fractionation experiments (e.g. Hin et al. 2013, Mahan et al. 2017). It is based on the assumption that if the isotopic distribution between the phases present in the system does not evolve with time, equilibrium ought to be reached. Together with carefully chosen time durations and thorough petrological and chemical studies of the run products, this method has been widely assumed to be sufficient to demonstrate equilibrium achievement (e.g. Hin et al. 2013, 2014, 2012, Labidi et al. 2016, Poitrasson et al. 2009, Roskosz et al. 2006, Seegers et al. 2019, Xia et al. 2019). Such method was favoured in this study and an example is presented on figure 2.1 for Sn isotopic fractionation time series (full study in chapter 4). On this figure, S-free experiments present no dependency of their isotopic fractionation factor with the time duration of the experiment over a range from 2 to 30 minutes, advocating for equilibrium achievement.

Three-isotope method

The three-isotope method (Criss et al. 1987, Matsuhisa et al. 1978, Northrop and Clayton 1966) has been used to extrapolate isotopic compositions of a series of unequilibrated experiments to their equilibrium isotope compositions in order to obtain equilibrium fractionation factors. This is possible because the rates of reaction, when sufficiently close to equilibrium, are linear functions of the departures from equilibrium (DeGroot and Mazur 1962). Applied to the systems described here, it stipulates that rates of isotope exchange can be expected to be linear functions of isotope ratios from the equilibrium fractionation factor (Shahar and

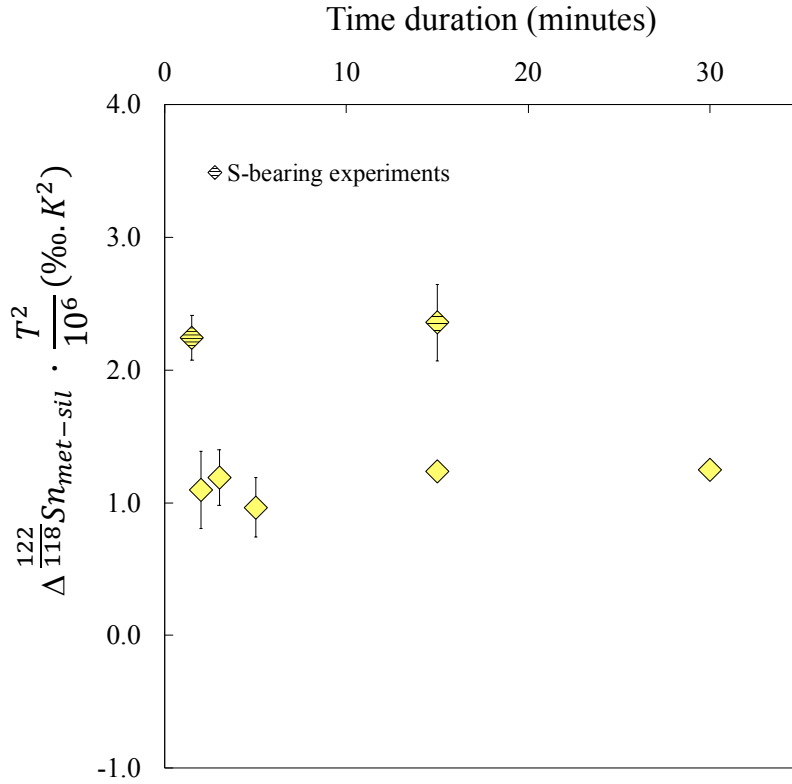


Figure 2.1 – Results from time series for Sn isotopic fractionation factors between metal and silicate. As experiments were carried at different temperature, fractionation factors were corrected for the $1/T^2$ dependency of mass-dependent equilibrium fractionation factors (Urey 1947). Although S-bearing experiments show enhanced metal–silicate fractionation, both S-bearing and S-free groups present consistent isotopic fractionation over a range of time durations from 1 to 30 minutes, allowing demonstration of isotopic equilibrium achievement.

Young 2020). This method is based on the addition of an isotope spike to one of the reactants. As shown on figure 2.2, the addition of isotope spike is shifting the isotopic composition of the spiked reactant and therefore equilibrated phases away from the terrestrial fractionation line (TFL) in a three-isotope plot. The isotopic compositions of equilibrated phases as well as the bulk system plot on a secondary fractionation line, parallel to the TFL, at equilibrium conditions. This method has demonstrated promising results at (a) demonstrating equilibrium achievement, especially at lower temperatures, where kinetics are slower but the isotopic fraction-

ations are predicted to be higher (Urey 1947). (b) It also allows to verify that the system remained closed with respect to mass exchange throughout an experiment (Shahar and Young 2020, Shahar et al. 2008).

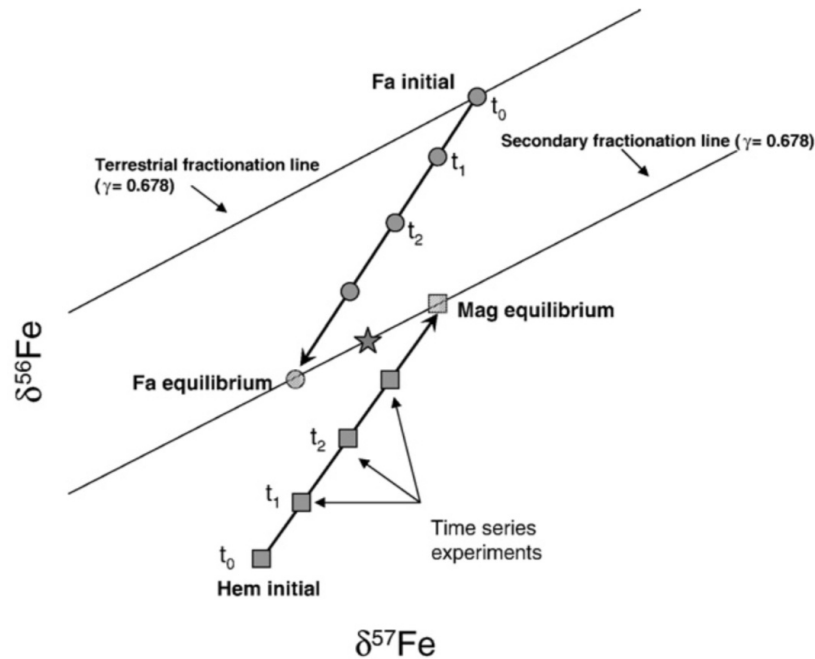


Figure 2.2 – Schematic diagram of the three-isotope method applied to a study on Fe isotope fractionation between fayalite and magnetite. In this example, the hematite initial material was added a ^{54}Fe spike, driving the equilibrated phases and bulk system (star symbol) away from the terrestrial fractionation line (TFL) in a $\delta^{56/54}\text{Fe}$ versus $\delta^{57/54}\text{Fe}$ diagram. The equilibrated phases plot on a secondary fractionation line parallel to the TFL at equilibrium conditions. Figure from Shahar et al. (2008)

Bao et al. (2015) reported that the equilibrium fractionation factor influences the rate of reaction, leading to unequal fractional approaches to equilibrium for the two isotope ratios involved in the three-isotope system, although Shahar and Young (2020) advocate for this effect to be negligible, especially at high temperature. Lazar et al. (2012) also demonstrated experimentally for Ni that such effect was not detectable. Therefore, this method is particularly useful to demonstrate that the system remained closed throughout the experiment. Such closed system demonstration can also be produced by recalculating the bulk isotopic composition

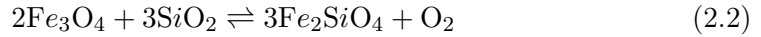
of the experiment based on measured compositions of metal and silicate phases of each experiment, and compare this recalculated bulk composition to the measured bulk composition analysed from the starting material, which is the method favoured in this study.

2.2 Oxygen fugacity

In the experimental systems studied in this work, the redox conditions are quantified by the oxygen fugacity (fO_2) (Eugster and Wones 1962). In a closed system at thermodynamic equilibrium, the oxidation state is characterised by the bulk amount of oxygen inside the system. The oxygen fugacity can be quantified by the oxygen partial pressure. However, if a system does not contain oxygen, oxygen fugacity is defined as the partial pressure of gaseous state oxygen in a virtual infinite reservoir at equilibrium with the system. As free oxygen does not exist at high pressure (Frost 1991) because it is entirely incorporated to mineral phases, this case applies to the systems studied here. Oxygen fugacity is therefore used in order to express the redox state of the system during metal–silicate reactions at high pressure and high temperature.

Oxygen fugacity is traditionally reported relatively to a buffer, composed of pure phases, defining a reference oxygen fugacity at a given temperature. In terrestrial systems studied here, where the focus is made on equilibrium between the core and the mantle, iron oxidation states are used in order to record the redox state of a system. Iron can be found at three different oxidation states on Earth: metallic Fe^0 , as present in the core (Stixrude and Brown 1998), Fe^{2+} , the main iron state found in the mantle (Wood 1991) and Fe^{3+} , present in the crust and hydrosphere along with Fe^{2+} (Frost 1991). The prevalence of an oxidation state over others is the product of the redox conditions that prevailed during the formation of a reservoir. The oxidation conditions of a system determine the stability of oxidised mineral species. As such, a buffer is defined by a chemical reaction at equilibrium.

(1) The **fayalite–magnetite–quartz buffer** (FMQ) is often used to study the upper mantle and corresponds to the following reaction:



(2) The **iron–wüstite buffer** (IW) is more appropriate to the study of core–mantle equilibrium:



The expression of oxygen fugacity with respect to the iron–wüstite buffer is derived from the equilibrium constant of the reaction above. As Fe represents 85 *wt.%* of the core and 8 *wt.%* of the mantle, it can be assumed that Fe behaves ideally in the core–mantle system, meaning that the activity a_i can be approximated by the mole fraction X_i , such that:

$$\Delta IW = 2 \cdot \log \frac{X_{\text{FeO}}^{\text{silicate}}}{X_{\text{Fe}}^{\text{metal}}} \quad (2.4)$$

This expression was used to calculate oxygen fugacities from all experiments reported in this study.

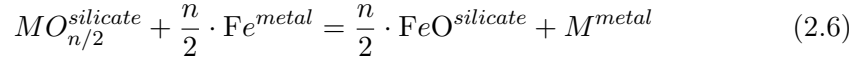
2.3 Thermodynamic description of metal–silicate equilibria

Experiments designed and performed in this work aimed at recording the elemental distribution of elements at metal–silicate equilibrium conditions. The distribution of an element M of valence state n between metal and silicate at equilibrium conditions can be expressed with the partition coefficient defined by:

$$D_M = \frac{X_M^{\text{metal}}}{X_{M\text{O}_{n/2}}^{\text{silicate}}} \quad (2.5)$$

where X_i are the mole fractions of element M and its oxide in the metal and silicate phases respectively. When D_M is >1 , M has more affinity for the metal and is considered siderophile whereas with $D_M < 1$, M is more abundant in the silicate

phase and presents a lithophile behaviour. The mole fractions are computed from mass concentrations measured in each phase by EPMA or LA-ICPMS following the method described in chapter 1. The behaviour of M at equilibrium between metal and silicate can also be expressed from a chemical exchange redox reaction (Wade and Wood 2005):



Experimental systems of this study sustain constant pressure and temperature conditions throughout the run and as such, the energetic evolution of the system is best described by Gibbs free energy. Gibbs free energy G is a thermodynamic potential that evolves in a thermodynamic system at constant P, T conditions such that the equilibrium state is reached when G is minimal. It governs the direction of a reaction at a given set of physical conditions. Gibbs free energy depends on pressure, temperature and chemical composition (n_i):

$$dG = \left. \frac{\partial G}{\partial T} \right|_{P, n_i} dT + \left. \frac{\partial G}{\partial P} \right|_{T, n_i} dP + \sum_{i=1}^k \left. \frac{\partial G}{\partial n_i} \right|_{P, T} dn_i \quad (2.7)$$

The chemical potential μ_i is defined as the partial derivative of Gibbs free energy as a function of composition and represents the variation of energy of a thermodynamic system inferred by the variation of the amount of a component i at constant pressure and temperature:

$$\mu_i = \left. \frac{\partial G}{\partial n_i} \right|_{P, T} \quad (2.8)$$

Here we assume that experiments of this study were carried at constant pressure and temperature. Therefore, the variation of Gibbs free energy is equal to the variation of chemical potential of the reaction, such that:

$$\Delta_r G = \Delta_r \mu \quad (2.9)$$

Applied to reaction in equation 2.6 describing the reaction studied in the experiments, the thermodynamic equilibrium is defined by:

$$\frac{n}{2} \cdot \mu_{Fe}^{metal} + \mu_{MO_{n/2}}^{silicate} = \mu_{M}^{metal} + \frac{n}{2} \cdot \mu_{FeO}^{silicate} \quad (2.10)$$

At equilibrium conditions, the variation of the chemical potential is zero and equals to the sum of the potentials of the reagents subtracted to the sum of the potentials of the reactants, such that:

$$\Delta_r\mu = \left(\mu_{M^{metal}} + \frac{n}{2} \cdot \mu_{FeO^{silicate}} \right) - \left(\frac{n}{2} \cdot \mu_{Fe^{metal}} + \mu_{MO_{n/2}^{silicate}} \right) = 0 \quad (2.11)$$

Thermodynamic activity a of a species i can be defined with the following equation:

$$\mu_i - \mu_i^0 = R \cdot T \cdot \log a_i \quad (2.12)$$

with μ_i^0 the chemical potential at reference state, R the universal gas constant, and T the temperature. The activity of a species represents an “effective concentration” in a mixture and can be measured as the difference between the chemical potential of such species in a mixture and at reference state. Equation 2.11 becomes:

$$\begin{aligned} \Delta_r\mu = & (\mu_{M^{metal}}^0 + R \cdot T \cdot \log a_{M^{metal}}) \\ & + \frac{n}{2} \cdot (\mu_{FeO^{silicate}}^0 + R \cdot T \cdot \log a_{FeO^{silicate}}) \\ & - \frac{n}{2} \cdot (\mu_{Fe^{metal}}^0 + R \cdot T \cdot \log a_{Fe^{metal}}) \\ & + (\mu_{MO_{n/2}^{silicate}}^0 + R \cdot T \cdot \log a_{MO_{n/2}^{silicate}}) = 0 \end{aligned} \quad (2.13)$$

$$\begin{aligned} \Delta_r\mu = & (\mu_{M^{metal}}^0 + \frac{n}{2} \cdot \mu_{FeO^{silicate}}^0 - \frac{n}{2} \cdot \mu_{Fe^{metal}}^0 - \mu_{MO_{n/2}^{silicate}}^0) \\ & + R \cdot T \cdot \log \frac{(a_{FeO}^{silicate})^{n/2} \cdot a_M^{metal}}{a_{MO_{n/2}}^{silicate} \cdot (a_{Fe}^{metal})^{n/2}} \end{aligned} \quad (2.14)$$

$$\Delta_r\mu = \Delta_r\mu^0 + R \cdot T \cdot \log \frac{(a_{FeO}^{silicate})^{n/2} \cdot a_M^{metal}}{a_{MO_{n/2}}^{silicate} \cdot (a_{Fe}^{metal})^{n/2}} \quad (2.15)$$

At thermodynamic equilibrium, $\Delta_r\mu = 0$ (equation 2.11) and $\Delta_r\mu^0 = \Delta_rG^0$ (equation 2.9) with Δ_rG^0 the standard Gibbs free energy of the reaction. Therefore, at constant pressure and temperature conditions:

$$\Delta_rG^0 + R \cdot T \cdot \log \frac{(a_{FeO}^{silicate})^{n/2} \cdot a_M^{metal}}{a_{MO_{n/2}}^{silicate} \cdot (a_{Fe}^{metal})^{n/2}} = 0 \quad (2.16)$$

The equilibrium constant K of reaction from equation 2.6 can be introduced here:

$$\Delta_r G^0 + R \cdot T \cdot \log K = 0 \quad (2.17)$$

$$\log K = \frac{\Delta_r G_{P,T}^0}{R \cdot T} \quad (2.18)$$

The standard Gibbs free energy of the reaction can be expressed as:

$$\Delta_r G_{P,T}^0 = \Delta_r H^0 - T \cdot \Delta_r S^0 + P \cdot \Delta_r V^0 \quad (2.19)$$

with H the enthalpy of the system, S the entropy and V the volume. Therefore:

$$\log K = -\frac{\Delta_r H^0}{R \cdot T} + \frac{\Delta_r S^0}{R} - \frac{P \cdot \Delta_r V^0}{R \cdot T} \quad (2.20)$$

This equation can be written as follows (e.g. Righter and Drake 1999, Wade and Wood 2005):

$$\log K = a + b \cdot \frac{1}{T} + c \cdot \frac{P}{T} \quad (2.21)$$

with $a = -\frac{\Delta_r S^0}{R}$, $b = \frac{\Delta_r H^0}{R}$ and $c = -\frac{\Delta_r V^0}{R}$.

In order to use such an expression of the equilibrium constant, a few assumptions are made. The enthalpy, entropy and volume of the system are considered to be independent of pressure and temperature during the reaction. As such, a , b and c can be applied to the range of pressures and temperatures investigated. This approach has limitations as it was suggested for Ni and Co that the term c is pressure dependent between 0 and 25 GPa (Kegler et al. 2008). This could be due to the changes of coordination of these elements in the silicate phase as pressure increases, with enhanced pressure effect observed at lower pressure. However, such a difference is not necessarily observed between low and high pressure experiments. In this study, the partitioning of the elements of interests was studied over a broad range of pressure, from 2 to 20 GPa, allowing precise characterisation of the pressure effect. The exchange coefficient K is defined as the equilibrium constant of the reaction (equation 2.6):

$$K = \frac{(a_{\text{FeO}}^{\text{silicate}})^{n/2} \cdot a_M^{\text{metal}}}{a_{\text{MO}_{n/2}}^{\text{silicate}} \cdot (a_{\text{Fe}}^{\text{metal}})^{n/2}} \quad (2.22)$$

where a_i are the activities of the different components, such that at constant P, T: $a_i = \gamma_i \cdot X_i$, where γ_i is the activity coefficient and X_i is the mole fraction. In an ideal solution: $a_i = X_i$ and $\gamma_i = 1$.

$$\log K = \log \frac{(X_{\text{FeO}}^{\text{silicate}})^{n/2} \cdot X_M^{\text{metal}}}{X_{\text{MO}_{n/2}}^{\text{silicate}} \cdot (X_{\text{Fe}}^{\text{metal}})^{n/2}} + \log \frac{\gamma_M^{\text{metal}}}{(\gamma_{\text{Fe}}^{\text{metal}})^{n/2}} + \log \frac{(\gamma_{\text{FeO}}^{\text{silicate}})^{n/2}}{\gamma_{\text{MO}_{n/2}}^{\text{silicate}}} \quad (2.23)$$

$$\log K = \log \frac{D_M}{(D_{\text{Fe}})^{n/2}} + \log \frac{\gamma_M^{\text{metal}}}{(\gamma_{\text{Fe}}^{\text{metal}})^{n/2}} + \log \frac{(\gamma_{\text{FeO}}^{\text{silicate}})^{n/2}}{\gamma_{\text{MO}_{n/2}}^{\text{silicate}}} \quad (2.24)$$

$$\log K = \log K_d^M + \log \frac{\gamma_M^{\text{metal}}}{(\gamma_{\text{Fe}}^{\text{metal}})^{n/2}} + \log \frac{(\gamma_{\text{FeO}}^{\text{silicate}})^{n/2}}{\gamma_{\text{MO}_{n/2}}^{\text{silicate}}} \quad (2.25)$$

In this expression of $\log K$, the partition coefficient of M is normalised by the partition coefficient of Fe, which is directly related to $f\text{O}_2$ computed with respect to the iron-wüstite buffer (equation 2.4). This means that such an expression allows to quantify the partitioning of element M independently of $f\text{O}_2$, simplifying the study of the effect of other parameters such as pressure, temperature and composition. The term $\log K_d^M$ is defined as $\log \frac{D_M}{(D_{\text{Fe}})^{n/2}}$ and can be computed for each experiment from molar concentrations of M and Fe in the metal and silicate phases, assessed from mass concentrations measured by EPMA and LA-ICPMS (method in chapter 1). A comparison of $\log D_{\text{Sn}}$ and $\log K_d^{\text{Sn}}$ parameters are displayed on figure 2.3 as a function of temperature, showing a clear trend in the case of $\log K_d^{\text{Sn}}$ (figure 2.3b), but obscured by the $f\text{O}_2$ effect in the plot presenting $\log D_{\text{Sn}}$ (figure 2.3a) for the same set of experiments. $\log D_{\text{Sn}}$ as a function of $f\text{O}_2$ for the same dataset is presented on figure 2.4a. The calculation of $\log D$ and $\log K_d$ parameters from experimental data allows to parameterise the partitioning of the element of interest. Valence states and activity coefficients γ_i are required in order to compute regression parameters a , b and c from experimental data.

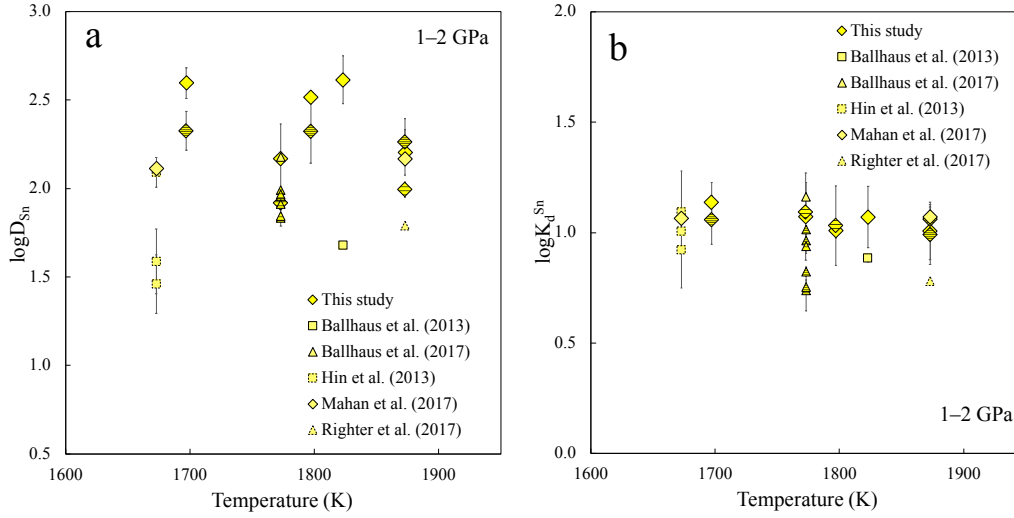


Figure 2.3 – Comparison of the $\log D$ and $\log K_d$ exchange coefficients for the same dataset of Sn partitioning experiments. Experiments represented on both plots were carried at 1–2 GPa and S-rich experiments correspond to symbols with a horizontal-line pattern. No effect of S on Sn partitioning is detected for this range of pressures and temperatures. **a.** $\log D_{Sn}$ as a function of temperature. Since the effect of oxygen fugacity (visible on figure 2.4a for the same dataset) is not corrected, no clear trend can be detected. **b.** $\log K_d^{Sn}$ as a function of temperature for the same set of experiments as figure a. $\log K_d$ is defined as the log of the ratio of D_{Sn} on D_{Fe} (equations 2.24 and 2.25), and as such, provides a quantification of the partitioning corrected for the effect of fO_2 , allowing to resolve clear trends, with here a slight negative effect of temperature on Sn partitioning.

2.3.1 Valence state determination

In order to exploit the thermodynamic metal–silicate formalism mentioned above to parameterise the partitioning of M measured in controlled experiments, accurate determination of the valence state of M in silicate melts is necessary. Several methods can be used to assess the valence state of the studied elements:

- (1) It can be demonstrated that $\log D_M$ is a function of $\frac{n}{4} \cdot \log fO_2$, allowing

to calculate the valence state n from experimental data:

$$\log D_M = -\frac{n}{4} \cdot \log fO_2 - \log K + \frac{\gamma_{MO_{n/2}}^{silicate}}{\gamma_M^{metal}} \quad (2.26)$$

Ideally, such method is permitted by a sufficient number of experiments with similar pressure, temperature and composition over a sufficient range of fO_2 , i.e. ~ 2 log units (Siebert et al. 2011). In this work, such valence demonstration was performed for Sn (figure 2.4a, see also chapter 4) and Cd (figure 2.4b, see also chapter 5). Such

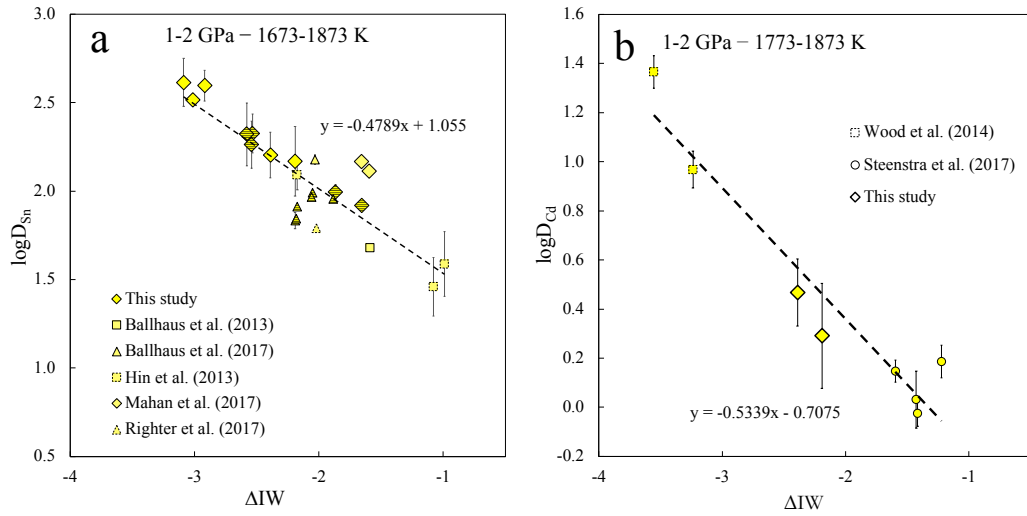


Figure 2.4 – Experimental determination of the valence state of elements by assessment of the slope in a $\log D_{Sn}$ vs ΔIW diagram. The slope equals to $\frac{n}{4}$ (equation 2.26). For Sn (figure a) and Cd (figure b), the slope formed by experiments from this study and from literature of similar pressure, temperature and composition is ~ 0.5 which corresponds to a $2+$ oxidation state.

demonstration is not always accessible due to scarcity of data and/or insufficient oxygen fugacity range. This is the case for Bi, Sb and Tl studied in chapter 5.

(2) K-edge X-ray absorption near-edge structure (XANES) spectrum is an appropriate tool to analyse the structure of silicate melts and determine the coordination of an element of interest at chosen P, T, and fO_2 conditions. XANES spectroscopy allows to quantify the valence state of an element with high precision (e.g. 0.01 precision on $Fe^{3+}/\Sigma Fe$, Cottrell et al. 2009a; 0.015 precision on $Cr^{2+}/\Sigma Cr$, Berry and O’Neill 2004). Such technique is particularly well suited for

studying isotropic materials such as glasses or cubic mesh crystals.

2.3.2 Activity coefficients

The activity of a chemical species in a phase is equal to the mole fraction multiplied by the activity coefficient:

$$a_i = \gamma_i \cdot X_i \quad (2.27)$$

The activity coefficient of a chemical species represents the energetic deviation from ideal behaviour in a solution. An ideal solution is defined by equal interactions between each pair of chemical species, which means that the properties of the solutions can be expressed directly by using concentrations of each species. Therefore, the activity coefficient is used to accommodate deviation from ideality by adjusting the concentrations of chemical species involved.

Two laws can be used to describe the behaviour of chemical species in a solution:

(a) **Raoult's law** states that the activity of each component in an ideal solution of liquids is equal to the vapour pressure of the pure component multiplied by its mole fraction in the solution. Applied to the solvent of a solution, the vapour pressure can be neglected, such that:

$$a_i = X_i \quad (2.28)$$

This means that γ_i tends to be equal to 1 ($\gamma_i \rightarrow 1$) when X_i of the solvent also tends towards 1 ($X_i \rightarrow 1$).

(b) **Henry's law** expresses the amount of dissolved gas in a liquid as a function of its partial pressure above the liquid, multiplied by Henry's law constant. Applied to the solutes in our experimental systems, it states that when the solute is infinitely dilute ($X_i \rightarrow 0$), the activity coefficient tends to its standard value ($\gamma_i \rightarrow \gamma_i^0$), which is often approximated to 1 due to a lack of data. As the elements of interest studied in chapters 4 and 5 cannot be considered infinitely dilute, with up to several *wt.%* concentrations in the metal, different approaches were used to establish the activity coefficients, with distinct method for metal and silicate phases.

Activity coefficient in silicate phases

The last term of equation 2.25 represents the effect of the silicate melt composition on the activity of the element M in the silicate. This term includes the effect of each of the oxides present in the silicate melt which cannot be realistically determined experimentally. Traditionally, the empirical parameter nbo/t , defined as the mole ratio of non-bridging oxygens per tetrahedrally coordinated cations (Mysen et al. 1982), is used to represent the variation of the composition of a silicate melt by estimating its degree of polymerisation. The silicate crystal lattice is made of oxide tetrahedra with a certain degree of chemical bond between them. Tetrahedral cations tend to form a polymerised network (e.g. Si, Al) while other elements tend to break Si–O bonds in the silicate structure (e.g. alkali elements), producing non-bridging oxygen atoms that are not bound to any Si or Al atom. Therefore, the non-bridging oxygens per tetrahedral cations ratio varies from 0, with fully polymerised structure, to 4, with fully depolymerised structure and maximal amount of non-bridging oxygen atoms. The nbo/t parameter is computed from the following expression:

$$nbo/t = \frac{2 \cdot X_O - 4 \cdot \sum_{i=1}^N X_i}{\sum_{i=1}^N X_i} \quad (2.29)$$

with X_O the mole fraction of oxygen in the silicate melt, in which are present N tetrahedrally coordinated cations i of mole fraction X_i .

The nbo/t parameter was used in numerous metal–silicate partitioning studies (e.g. Cottrell et al. 2009a, Righter and Drake 1999, Siebert et al. 2011) and was found to have significant effect on partition coefficients in several cases (Chabot and Agee 2003, Jana and Walker 1997, Walter and Thibault 1995). Although such approach was criticised (O'Neill and Eggins 2002), experimental studies have shown that considering the concentrations of each oxide in the silicate did not induce major improvement compared to the nbo/t approach (Righter and Drake 1999). It should be noted that at upper mantle conditions, the coordination environment in silicate transitions from tetrahedra to octahedra, making the nbo/t parameter irrelevant above ~ 25 GPa.

Chapter 4 of this study is dedicated to characterising the behaviour of Sn in a metal silicate. In this experimental application, two distinct silicates were used in order to study the effect of the silicate melt composition on Sn partitioning: a

natural MORB with nbo/t of ~ 1 in BN capsules, and a KLB1 natural peridotite with nbo/t of ~ 3 in BN capsules. The exchange coefficient $\log K_d^{Sn}$ presents no dependence on nbo/t parameter as shown on figure 2.5 for a group of experiments at 2 GPa and 1700–1800 K. This absence of effect of the silicate melt structure agrees with predictions of limited effect of the silicate melt on the equilibrium constant, especially for low—below 4+—valence state elements (Wade and Wood 2005). For this reason, the activity coefficient in the silicate melt was neglected in both applications presented in this work (chapters 4 and 5).

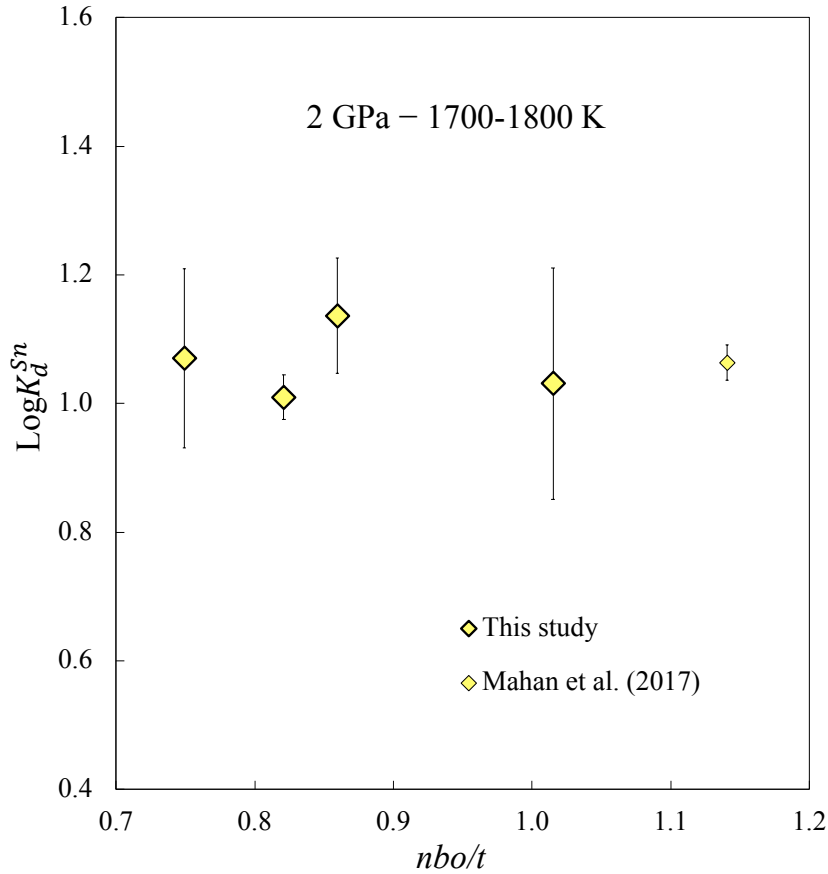


Figure 2.5 – Exchange coefficient $\log K_d^{Sn}$ as a function of nbo/t for Sn experiments carried at 2 GPa between 1700 and 1800 K with ΔIW from -1.6 to -3.0.

Activity coefficient in metal phases

As the activity coefficients of FeO and $MO_{n/2}$ in the silicate melt were neglected in this study, the expression of $\log K_d$ can be simplified as follows:

$$\log K_d = a + b \cdot \frac{1}{T} + c \cdot \frac{P}{T} - \log \frac{\gamma_M^{metal}}{(\gamma_{Fe}^{metal})^{n/2}} \quad (2.30)$$

However, the presence in the metal of major components such as Si, O, S and C have shown to interact strongly with trace elements and induce measurable effects on partitioning (Jana and Walker 1997, Tuff et al. 2011, Wood et al. 2014). Therefore, activity coefficients in the metal can be significant and need to be assessed. Understanding and predicting the physical and chemical properties induced by the chemical composition of metal alloys also has crucial applications in the metallurgy field. In that respect, numerous studies have been carried since the 1950s in order to characterise these properties as a function of composition and physical conditions. The interaction parameter approach was established by (Wagner 1952) to that purpose. The interaction parameter is derived from the Taylor series expression of $\log \gamma_i$ and is defined as follows:

$$\varepsilon_i^i = \left. \frac{\partial \log \gamma_i}{\partial X_i} \right|_{X_i=0} \quad (2.31)$$

$$\varepsilon_i^j = \left. \frac{\partial \log \gamma_i}{\partial X_j} \right|_{X_j=0} \quad (2.32)$$

The interaction parameter translates the effect of the presence of an element j on the activity of an element i . It is negative when the presence of element i is favoured by j , and positive when the effect is opposite. Therefore:

$$\log \gamma_i = \log \gamma_i^0 + \sum_{j=2}^N \varepsilon_i^j \cdot X_j \quad (2.33)$$

This formalism is relevant for extremely dilute solutions, and it was demonstrated that such relation was only valid for a very narrow range of composition. In this study, the formalism proposed by Ma (2001) was preferred for its ability to apply to both dilute and non-dilute systems involving strong interactions between the components. Numerous experimental partitioning studies have favoured this approach Corgne et al. (2008), Fischer et al. (2015), Ricolleau et al. (2011), Siebert

et al. (2013), Wade and Wood (2005). Such formalism is based on the same definition of interaction parameter ε , but its expression is modified as to apply to more concentrated solutions. A large number of interaction parameters covering a wide chemical range was reported by the metallurgy community in the Steelmaking Data Sourcebook (J.S.P.S. 1988). All parameters ε_i^j and γ_i^0 are reported at a reference temperature of 1873 K, and can be extrapolated from the following linear relationships:

$$\varepsilon_i^j(T) = \varepsilon_i^j(T^0) \cdot \frac{T^0}{T} \quad (2.34)$$

$$\log \gamma_i^0(T) = \log \gamma_i^0(T^0) \cdot \frac{T^0}{T} \quad (2.35)$$

In Ma (2001), interaction parameters for the solvent (i.e. Fe) and N solutes i are expressed as follows:

$$\begin{aligned} \log \gamma_{\text{Fe}} = & \sum_{i=2}^N \varepsilon_i^i (X_i + \log(1 - X_i)) \\ & - \sum_{j=2}^{N-1} \sum_{k=j+1}^N \varepsilon_j^k X_j X_k \left(1 + \frac{\log(1 - X_j)}{X_j} + \frac{\log(1 - X_k)}{X_k} \right) \\ & + \sum_{i=2}^N \sum_{\substack{k=2 \\ (k \neq i)}}^N \varepsilon_i^k X_i X_k \left(1 + \frac{\log(1 - X_k)}{X_k} - \frac{1}{1 - X_i} \right) \\ & + \frac{1}{2} \sum_{j=2}^{N-1} \sum_{k=j+1}^N \varepsilon_j^k X_j^2 X_k^2 \left(\frac{1}{1 - X_j} + \frac{1}{1 - X_k} - 1 \right) \\ & - \sum_{i=2}^N \sum_{\substack{k=2 \\ (k \neq i)}}^N \varepsilon_i^k X_i^2 X_k^2 \left(\frac{1}{1 - X_i} + \frac{1}{1 - X_k} + \frac{X_i}{2(1 - X_i)^2} - 1 \right) \end{aligned} \quad (2.36)$$

$$\begin{aligned} \log \gamma_i = & \log \gamma_{\text{Fe}} + \log \gamma_i^0 - \varepsilon_i^i \log(1 - X_i) \\ & - \sum_{\substack{k=2 \\ (k \neq i)}}^N \varepsilon_i^k X_k \left(1 + \frac{\log(1 - X_k)}{X_k} - \frac{1}{1 - X_i} \right) \\ & + \sum_{\substack{k=2 \\ (k \neq i)}}^N \varepsilon_i^k X_k^2 X_i \left(\frac{1}{1 - X_i} + \frac{1}{1 - X_k} + \frac{X_i}{2(1 - X_i)^2} - 1 \right) \end{aligned} \quad (2.37)$$

In the case studies proposed in this work, an element M is equilibrated between silicate melt and melted iron or melted sulphide, such that the elements considered

in the metal phase are Fe, M and S. Calculation of interaction parameters from equations 2.36 and 2.37 (Ma 2001) allows to express the exchange coefficient as follows:

$$\begin{aligned}
 \log K_d &= \log \frac{D_M}{(D_{Fe})^{n/2}} \\
 &= a + b \cdot \frac{1}{T} + c \cdot \frac{P}{T} - \log \gamma_M^0 + \varepsilon_M^M \cdot \log(1 - X_M) + \varepsilon_M^S \cdot \log(1 - X_S) \\
 &\quad + \left(\frac{n}{2} - 1\right) \cdot \varepsilon_S^S \cdot (X_S + \log(1 - X_S))
 \end{aligned} \tag{2.38}$$

In the studies reported in chapters 4 and 5, the constants a , b and c were computed using the least-squares multivariate linear regression method from exchange coefficients of experiments from these studies and associated literature with a metal devoid of light elements that could have an effect on the partitioning of M (i.e. S, Si and C). Interactions between minor/trace elements in the metal were neglected, based on their low abundances in the system. Sulfur-bearing experiments data was used to compute the interaction parameter ε_M^S using equation 2.38. In the case of Sn (chapter 4), ε_{Sn}^{Sn} and γ_{Sn}^0 are equal to -0.29 and 0.95 respectively at 1873 K (J.S.P.S. 1988), but for Cd, Bi, Sb and Tl (chapter 5) the parameters were fitted to the experimental dataset due to a lack of available estimates. For ε_S^S , the value of -5.66 at 1873 K was applied (J.S.P.S. 1988).

2.4 Isotopic equilibrium thermodynamics

Equilibrium mass dependent isotope fractionation decreases as a function of the square of temperature (Bigeleisen and Mayer 1947, Urey 1947). The isotopic fractionation factor of an element M can be approximated as:

$$\Delta^{h/l} M_{metal-silicate} \propto \left(\frac{\Delta m_{h-l}}{m_h \cdot m_l} \cdot \frac{\delta F_{metal-silicate}}{T^2} \right) \cdot 1000 \tag{2.39}$$

where m_h and m_l are the atomic masses of heavy isotope hM and light isotope lM respectively, Δm the isotopic mass difference, $\delta F_{metal-silicate}$ the difference in force constants between the bonds of the isotopes in the metal and silicate phases, and T the temperature in K. Traditionally, the experimental data is fitted to the

square of temperature by computing coefficient a such that:

$$\Delta^{h/l}M_{metal-silicate} = a \cdot \frac{1}{T^2} \quad (2.40)$$

Mass-dependent equilibrium isotope fractionation is a function of mass, temperature, and bonding environment. The heavy isotopes are usually preferentially concentrated in phases with stiffer bonds, which form around atoms with the lowest coordination and highest valence state. For elements that change coordination number across the range of conditions that are relevant to planetary differentiation, such as Mo, varying oxygen fugacity allows to investigate a possible effect on isotope fractionation (Hin et al. 2013).

Since the bonding environment is sensitive to pressure, the question of the potential effect of pressure on equilibrium isotopic fractionation is valid. However, very few studies report metal–silicate isotopic fractionation data for a broad range of pressures. This is due to the fact that higher pressure experimentation yields a volume of sample that is critically small in order to measure isotopic composition of both phases by MC-ICPMS. Shahar et al. (2011) and Poitrasson et al. (2009) reported no difference between experiments carried at 1 and 7 GPa, for Si and Fe metal–silicate isotopic fractionation respectively, suggesting limited or absence of pressure effect on metal–silicate equilibrium isotope fractionation. However, a study based on theoretical calculations on Fe isotopic fractionation reported that Fe could fractionate significantly at core-mantle boundary conditions on Earth (Polyakov 2009), implying a possible effect of pressure.

Core formation modelling

3.1 Background principles and recent advances

Core formation models are based on the regression coefficients computed from experimental data, using the thermodynamic formalism presented in the previous chapter in order to recalculate the partitioning of an element between core and mantle during planetary accretion and subsequent differentiation. Combined with experimental determination of siderophile elements at metal–silicate equilibrium conditions, core formation models are used to determine the scenarios that best reproduce the observed abundances of siderophile elements in the Earth’s mantle. Therefore, numerous pieces of evidence were reported regarding the physical and chemical conditions of the Earth’s formation and differentiation. For instance, the average pressure of equilibration of the core with the mantle was estimated around 40–60 GPa (e.g. Bouhifd and Jephcoat 2003, Gessmann and Rubie 2000, Siebert et al. 2012, 2011, Wade and Wood 2005). Core formation model results also contribute to resolve the composition in light elements of the core (e.g. Badro et al. 2015, Rubie et al. 2011, Tuff et al. 2011, Wade and Wood 2005), as well as the evolution of oxidation conditions in the mantle (e.g. Frost et al. 2008, Rubie et al. 2011, Siebert et al. 2013, 2011, Tuff et al. 2011), and the efficiency of core segregation (e.g. Rubie et al. 2011, Suer et al. 2017). In addition, such models can be applied to elements that are both volatile and siderophile in order to resolve the conditions of accretion of volatile elements (e.g. Ballhaus et al. 2017, Mahan et al. 2018a, b, Suer et al. 2017).

In this study, a multi-stage continuous core formation model was written by the author in Matlab, in which a series of N impactors are accreted and equilibrated with the proto-Earth. In all calculations presented in this chapter, the core is assumed to represent $f = 32.3\%$ of the mass of the Earth, as well as all proto-Earths' cores and embryos' cores involved (Ricolleau et al. 2011, Siebert et al. 2012, 2013, Wade and Wood 2005). All impactors are referred to as embryos regardless of their size, and designated by the letter e in all equations.

3.2 Apparent core–mantle partitioning

Final partition coefficients determined by core formation modelling for the Earth were compared to estimations of the apparent core–mantle partition coefficients for each element of interest to resolve one or a variety of accretion and differentiation scenarios that can realistically explain the abundances of such elements in the Earth's mantle. Estimations of apparent partition coefficients were calculated based on natural abundances measured in the bulk silicate Earth (BSE) and in primitive meteorites (i.e. CI chondrites). Each moderately volatile and siderophile (MSVE) element studied in this work, i.e. Sn, Cd, Bi, Sb and Tl, was assumed to have been accreted in relative abundance identical to that of a lithophile element of similar volatility. Therefore, the additional depletion of the MSVE with respect to the canonical volatile trend is attributed to its segregation into the core. To quantify such depletion, each MSVE was paired with the lithophile element of closest condensation temperature and the difference in relative abundance between the two elements of each pair was converted into core abundance. On figure 3.1 are displayed relative abundances of elements in the Earth's mantle as a function of 50% condensation temperatures for two different estimates (Lodders 2003, Wood et al. 2019). These two estimates yield different lithophile reference elements for Cd, Bi and Sb, which changes slightly the core/BSE estimate. Two values were therefore provided as a consequence of consideration of both condensation temperature estimates (table 3.1). Recent high-precision measurements on carbonaceous chondrites (Braukmüller et al. 2019) showed that relative abundances of chondrites and the BSE present a “hockey stick” pattern with constant relative abundances for elements of condensation temperature between 500 and 750 K, forming the plateau part of the pattern. Because Sn, Cd, Bi and Tl sit on this plateau part, a third

estimation from Braukmüller et al. (2019) was also considered (table 3.1). A range including all three estimates was used as a “target” for core formation models.

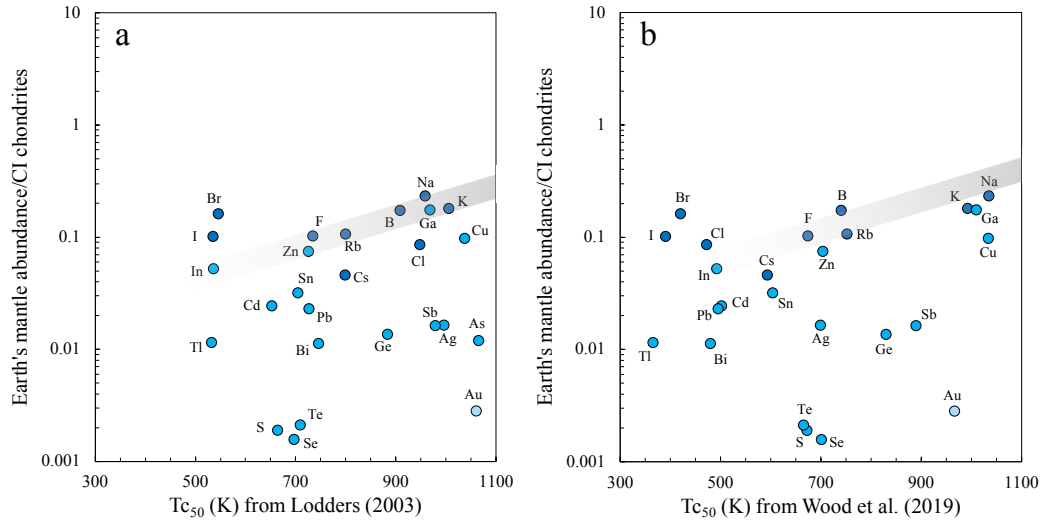


Figure 3.1 – Relative abundances of volatile and moderately volatile elements in the bulk silicate Earth with respect to CI chondrite abundances (McDonough 2003) as a function of two different estimates of 50% condensation temperatures: **a.** from Lodders (2003), **b.** from Wood et al. (2019).

CHAPTER 3. Core formation modelling

Table 3.1 – Compilation of apparent partition coefficients inferred from CI and BSE measurements.

| MSVE | Sn | Cd | Bi | Sb | Tl |
|------------------------------|-------------------|------------------|------------------|-------------------|------------------|
| T_{50} (K) ^a | 704 | 652 | 746 | 979 | 532 |
| T_{50} (K) ^b | 604 | 502 | 480 | 890 | 365 |
| BSE (ppb) | 138 ^d | 64 ^d | 5 ^d | 12 ^d | 3.5 ^e |
| ± | 30 | 19 | 2.5 | 4 | 1.4 |
| CI (ppb) | 1680 ^a | 675 ^a | 110 ^a | 152 ^a | 143 ^a |
| ± | 40 | 6 | 3 | 9 | 2 |
| Core/BSE ^a | 8.6 | 7.1 | 17.2 | 11.8 | 19.2 |
| ± | 4.7 | 4.4 | 11.7 | 4.1 | 18.6 |
| Lithophile reference element | F ^{a,d} | F ^{a,d} | F ^{a,d} | Na ^{a,d} | I ^f |
| Core/BSE ^b | 8.6 | 2.6 | 7.6 | 11.1 | 19.2 |
| ± | 4.7 | 2.6 | 6.4 | 3.9 | 18.6 |
| Lithophile reference element | F ^{a,d} | Cl ^f | Cl ^f | K ^{a,d} | I ^f |
| Core/BSE ^c | 3.2 | 8.6 | 15 | – | 14 |
| Range | 3.2–13.3 | 0–11.5 | 1.2–28.9 | 7.2–15.9 | 0.6–37.8 |

^aLodders (2003); ^bWood et al. (2019); ^cBraukmüller et al. (2019); ^dPalme and O’Neill (2003); ^eMcDonough and Sun (1995); ^fClay et al. (2017)

3.3 Multi-stage continuous core formation models

In the model, Earth's accretion was discretised in N steps. At each step i , an embryo of mass m_i is incorporated to the proto-Earth and equilibrated with its core and mantle at conditions assumed to be that of a deep magma ocean. Equation 2.38 in chapter 2 was restructured in order to restore $\log D_M$:

$$\begin{aligned} \log D_M = & a + b \cdot \frac{1}{T} + c \cdot \frac{P}{T} - \log \gamma_M^0 + \varepsilon_M^M \cdot \log(1 - X_M) + \varepsilon_M^S \cdot \log(1 - X_S) \\ & + \left(\frac{n}{2} - 1\right) \cdot \varepsilon_S^S \cdot (X_S + \log(1 - X_S)) - \log \frac{X_{\text{FeO}}}{X_{\text{Fe}}} \end{aligned} \quad (3.1)$$

All errors on the models presented in this chapter were propagated from error percentages on the computed regression coefficients as follows:

$$\sigma_{\log D_M} = \sqrt{\left(\frac{\sigma_a}{a}\right)^2 + \left(\frac{\sigma_b}{b \cdot T}\right)^2 + \left(\frac{\sigma_c \cdot P}{c \cdot T}\right)^2 + \left(\frac{\sigma_{\varepsilon_M^S} \cdot 1873 \cdot \log(1 - X_S)}{\varepsilon_M^S \cdot T}\right)^2} \quad (3.2)$$

As metal–silicate partition coefficients depend on pressure, temperature, oxygen fugacity and composition, all these parameters are set in order to reconstruct the partitioning of an element M across the accretion and differentiation of the Earth.

3.3.1 Model parameters

Pressure

High-pressure diamond anvil cell metal–silicate partitioning experiments for Ni and Co have shown that the natural mantle abundances correspond to an equilibration pressure of ~ 50 GPa, corresponding to ca. 40% of the mantle's depth (Siebert et al. 2012). In the core formation models presented in this chapter, the equilibration pressure was therefore set at 40% of the proto-Earth's mantle at each step, corresponding to the base of a deep magma ocean. At each incremental step

i , the pressure of equilibration P_i is given by:

$$P_i = 0.4 \cdot P_{final} \cdot m_i^{2/3} \quad (3.3)$$

with P_{final} the pressure at the center of present-day core–mantle boundary, equal to 135.6 GPa and therefore yielding a final P_i of ca. 54 GPa, and m_i the accreted mass fraction at step i .

Temperature

The temperature of equilibration at the base of a deep magma ocean was chosen based on the mantle liquidus. The following equation corresponds to the arithmetic mean of the mantle liquidus estimated by Andrault et al. (2011) and by Fiquet et al. (2010) expressed as a function of pressure, and was used to recalculate the temperature of equilibration at each step:

$$T_i = \frac{1}{2} \cdot \left(2022 + 54.21 \cdot P_i - 0.34 \cdot P_i^2 + 9.0747 \cdot 10^{-4} \cdot P_i^3 + 1940 \cdot \left(\frac{P_i}{29} + 1 \right)^{1/1.9} \right) \quad (3.4)$$

This equation yields a final temperature of equilibration of 3740 K, in agreement with other experimental estimates (e.g. Gessmann and Rubie 2000, Wade and Wood 2005).

Oxygen fugacity

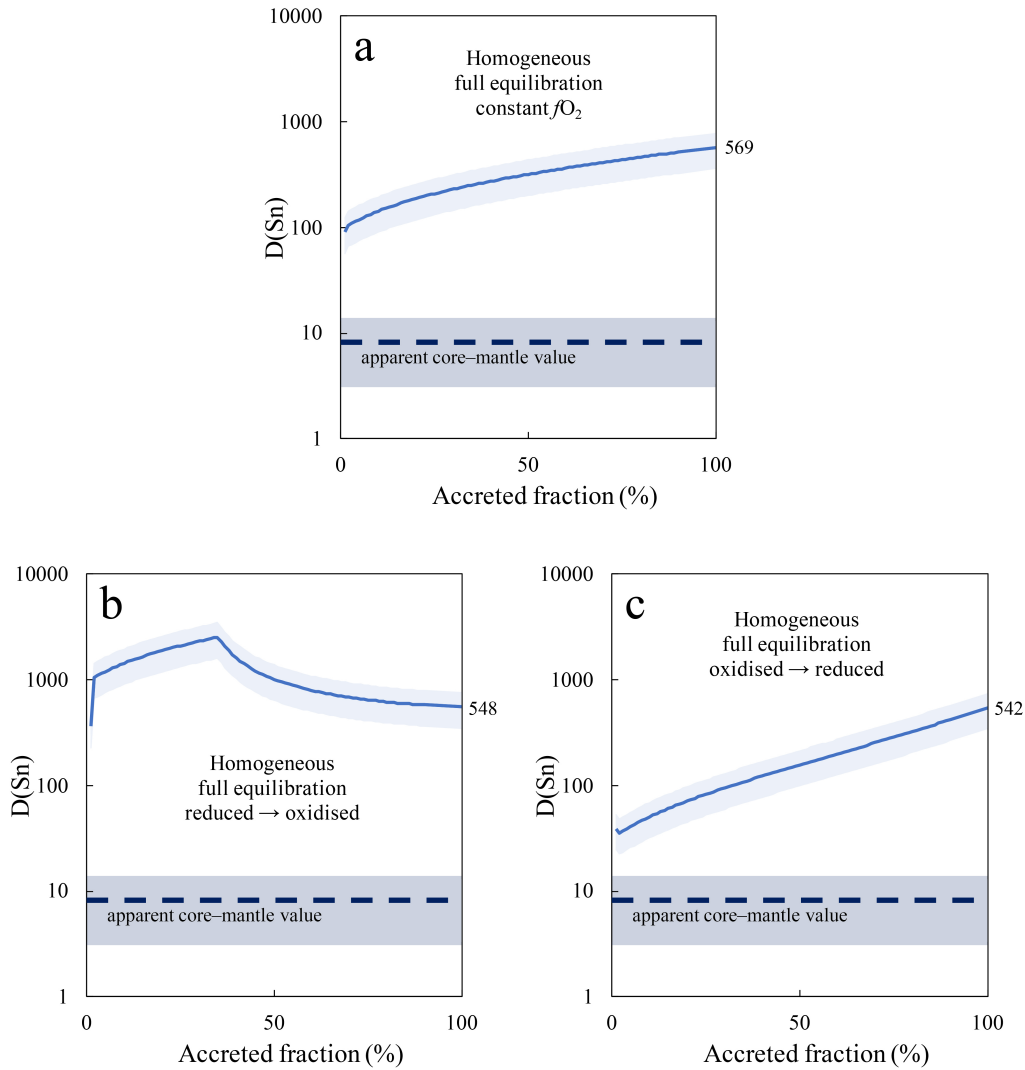


Figure 3.2 – Effect of oxidation conditions of the Earth on Sn partitioning between core and mantle in a homogeneous core formation model with full equilibration. **a.** Reconstruction of Sn partition coefficient with constant $f\text{O}_2$ equal to the present-day value of IW-2.3. **b.** Reconstruction of Sn partition coefficient with reduced conditions (IW-4.3) evolving towards more oxidised conditions during the accretion and differentiation (Siebert et al. 2013). **c.** Reconstruction of Sn partition coefficient with oxidised conditions (IW-1.35) evolving towards more reducing conditions during the accretion, as modelled in Siebert et al. (2013).

The evolution of redox conditions operating upon differentiation of the Earth is a debated topic and a wide range of possible pathways have been argued for. Earth has been proposed to be highly reduced during its early stages with evolution towards more oxidised conditions at later stages based on numerous experimental studies on siderophile elements (Frost et al. 2008, Rubie et al. 2011, Wade and Wood 2005, Wood et al. 2006). On the contrary, other studies suggested that the Earth evolved from oxidising to more reduced conditions (Righter and Ghiorso 2012, Siebert et al. 2013). On figure 3.2, three different fO_2 evolution scenarios are presented, with little implications on the final partition coefficient of Sn in a homogeneous model with full equilibration. All models presented in this study were computed at constant fO_2 of IW-2.3, corresponding to the present-day value, for all steps of the accretion.

Accretion pathway

An accretion pathway was defined as a sequence of accreted embryos with sizes corresponding to 0.01, 0.1, 1, 10, 15 and 20% of the Earth's mass. Models of thermal evolution of small planetary bodies have shown that radioactive decay of short-lived nuclides such as ^{26}Al and ^{60}Fe could have induced temperature allowing differentiation in ~ 30 km bodies (Rubie et al. 2007, Yoshino et al. 2003). This implies that differentiated bodies have probably contributed significantly to the accretion of the Earth. However, the existence of asteroids that are presently undifferentiated such as Ceres (Thomas et al. 2005) shows that the extent of such a process was limited. The Earth probably accreted from a mixture of differentiated and undifferentiated bodies (Rubie et al. 2007). For the sake of simplicity, all embryos were assumed to be differentiated in the models presented here.

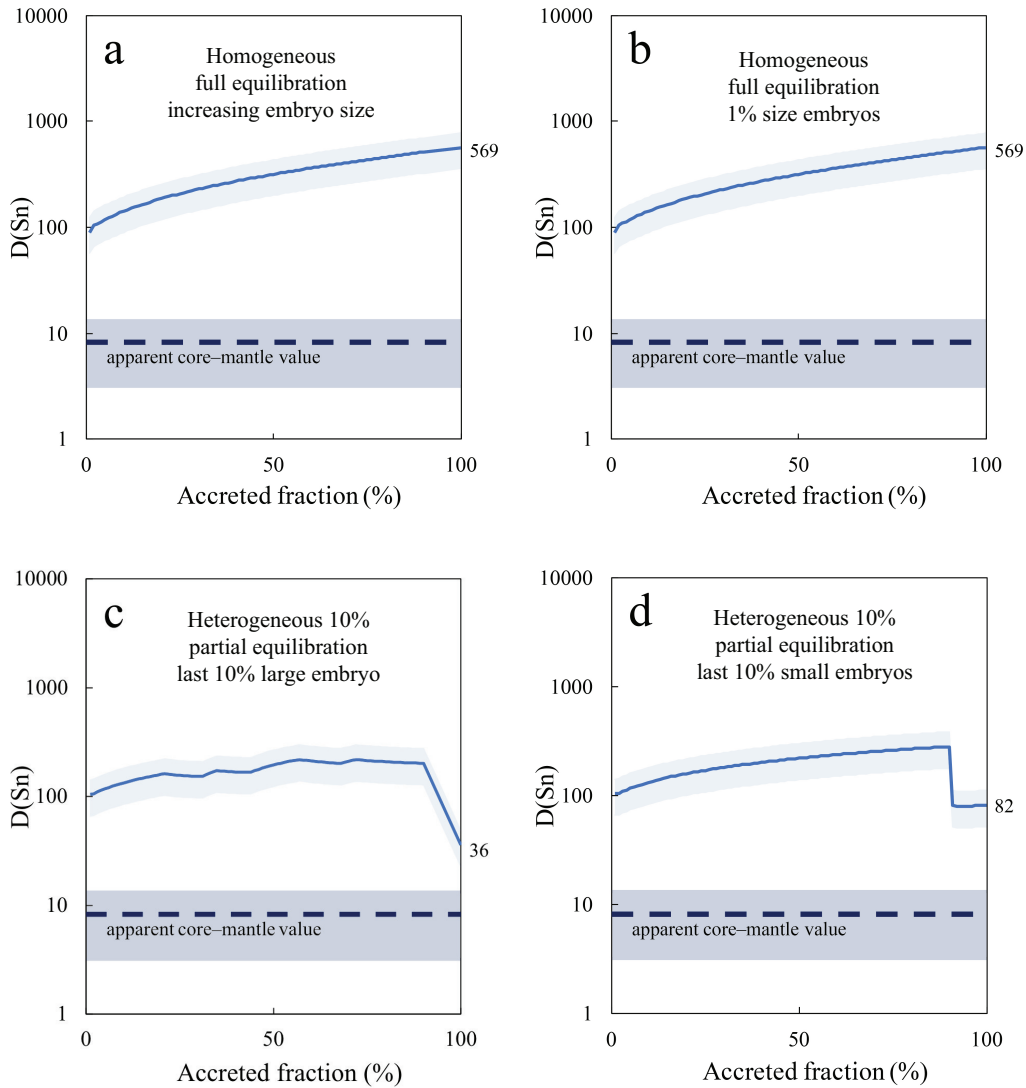


Figure 3.3 – Influence of the accretion pathway of the models for two different accretion scenarios in the case of Sn partitioning. **a.** Reconstruction of Sn partitioning in a scenario of homogeneous accretion with full equilibration using the accretion pathway favoured in this study. **b.** Reconstruction of Sn partitioning in the same scenario as a., with homogeneous accretion and full equilibration, using only embryos of 1% size of the Earth. **c.** Reconstruction of Sn partitioning in a heterogeneous scenario with partial equilibration, where the Sn budget of the Earth is largely brought in the last 10% of Earth’s accretion, as a 10% mass giant impact, using the accretion pathway preferred in this study. **d.** Reconstruction of Sn partitioning in the same heterogeneous scenario as c., with partial equilibration, but with an accretion pathway composed of 0.1%-size embryos in the first 90% of the accretion and with accretion of the last 10% as 1%-size embryos, leading to a higher final D_{Sn} . Therefore, in this study, a final large impactor is necessary to explain the observed Sn abundances in the mantle (full study in chapter 4).

The accretion sequence favoured in the models of this study was written such that the first 60% of the Earth were mostly built from embryos of mass $<1\%$ of the Earth's mass. From 60 to 80–90%, embryos of 1% of the total mass were accreted, and the accretion was completed by a last giant embryo of 10 to 20% of the Earth's mass, corresponding to a giant impact. For models computing a full equilibration of the embryos with the proto-Earth, no difference is detected when the accretion pathway is changed (figure 3.3a and b). However, when a more complex accretion scenario involving partial equilibration is modelled, the accretion pathway has an effect on the outcome of the model (figure 3.3c and d). This is due to the fact that partial equilibration models are sensitive to the size of the accreted embryos (see Equilibration efficiency section below).

Late veneer

The effect of a chondritic late veneer on the final partitioning was systematically investigated for each MSVE studied. The late veneer is modelled as to add a chosen amount of chondritic material to the Earth's mantle with an absence of equilibration with the core. For most elements, such a late veneer did not change significantly the final partition coefficient, accounting for only $\sim 10\%$ of the mantle's budget. However, in the case of Bi, which was found to be very siderophile at high pressure, a 0.5 *wt.%* chondritic late veneer was required in order to account for the relatively high abundances measured in the Earth's mantle (figure 3.4 and see chapter 5). This late addition of chondritic material after core formation ceased is supported in numerous studies regarding HSE abundances (Holzheid et al. 2000, Mann et al. 2012, O'Neill et al. 1995). Recent Pt isotopic measurements also found evidence of such a late veneer to explain variations between pre-convection Archean rocks and present-day mantle Pt isotopic compositions (Creech et al. 2017a). Such scenario is consistent with other numerous cosmochemical studies (e.g. Fischer-Gödde et al. 2020, Varas-Reus et al. 2019, Wang and Becker 2013).

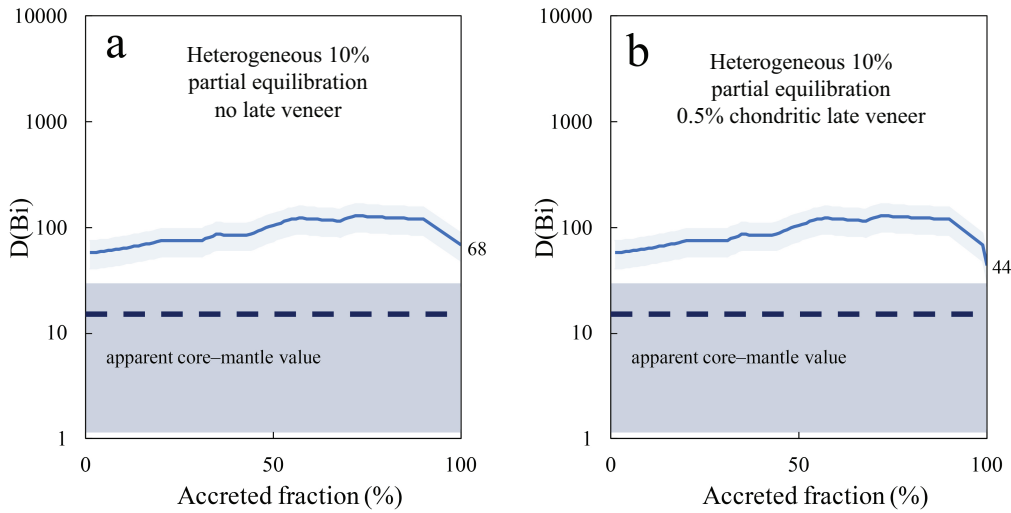


Figure 3.4 – Effect of the addition of a 0.5 mass % late veneer on Bi partitioning in a heterogeneous scenario where the volatiles are accreted in the last 10% of the accretion with partial equilibration. **a.** Reconstruction of Bi partition coefficient with no late veneer addition. **b.** Reconstruction of Bi partitioning with a 0.5% late veneer.

Sulfur abundance

Several MSVEs behaviour studied in this work have shown to be sensitive to the S content of the metal phase upon equilibration. The estimate of 1.9 *wt.%* of S in the core was used (McDonough 2003) as it agrees well with other experimental studies (Mahan et al. 2018b, Rubie et al. 2011, Suer et al. 2017). In the study on Sn partitioning presented in chapter 4 of this thesis, the S content is estimated to be ca. 3 *wt.%* to account for Sn abundance in the Earth’s mantle, which is within error of previously mentioned estimates. This estimate is also consistent with mineral physics studies (Badro et al. 2015, Morard et al. 2013) studying the physical properties (e.g. density, elastic properties) of (Fe,S) alloys.

Moderately siderophile and volatile element abundance

The bulk MSVE abundance of the Earth was calculated from the same BSE and core concentrations estimates used to compute the apparent core–mantle partition coefficient. This allows consistency between the input and the output of the model. When the model matches the apparent core–mantle value, the final concentrations in the core and the mantle of the modelled Earth are identical to estimates presented in table 3.1.

3.3.2 Equilibration efficiency

Several studies proposed that the equilibration of the core with the mantle may not be total, as such a process would help retain HSE elements in the mantle and account for their relatively high abundances in the Earth’s mantle (Arculus and Delano 1981, Jones and Drake 1986, Walker 2009). Based on Hf–W and U–Pb systems and siderophile elements abundances, geochemical models predict a degree of equilibration around 36% (Rudge et al. 2010). Metal–silicate partitioning studies including S (Suer et al. 2017), Sn (chapter 4 of this study), Bi and Tl (chapter 5 of this study) also support partial equilibration over full equilibration to account for these elements’ abundances. Rubie et al. (2003) propose that for larger accreted embryos, the metal is required to break down to fragment of 1 cm to 1 m in order to obtain efficient equilibration between core and mantle. A similar message is delivered from Deguen et al. (2014) reporting fluid dynamics experiments suggesting that larger impactors are decreasing equilibration efficiency. Therefore, two different methods were used in order to model a partial equilibration in this study. At each step of the accretion, the partition coefficient of the proto-Earth D_M and of the accreted embryo D_M^e are calculated using the equation 3.1.

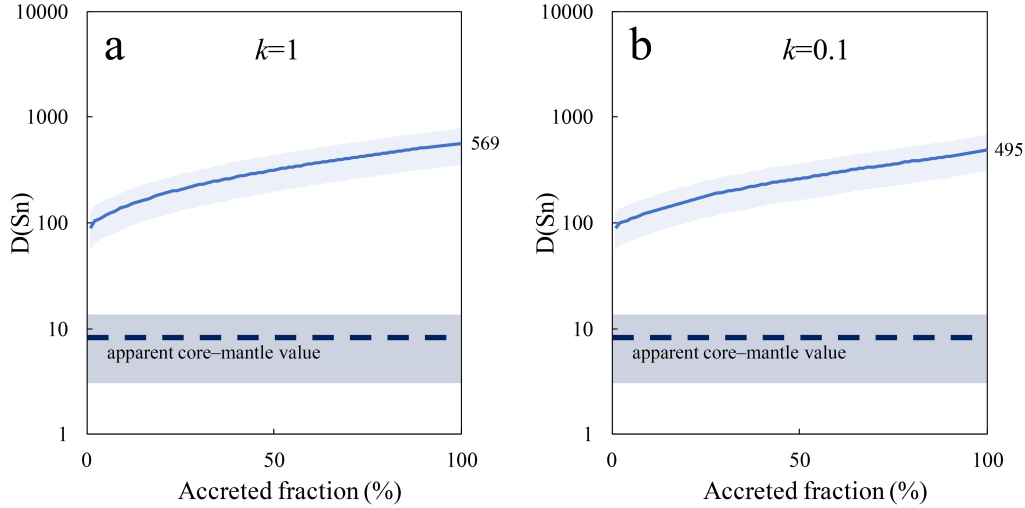
Parameter k formalism

Figure 3.5 – Effect of the variation of the k parameter on the partition coefficient of Sn in a homogeneous core formation model. **a.** Core formation model reconstructing Sn partition coefficient for a homogeneous accretion and $k = 1$ (full equilibration). **b.** Core formation model reconstructing Sn partition coefficient for a homogeneous accretion and $k = 0.1$.

In a first approach, the mantle and core concentrations at each step are computed by taking into account that the fraction k of the core of the accreted embryo is equilibrated with the mantle. When $k = 1$, the equilibration process is fully achieved. When $k \neq 1$, the fraction $1 - k$ of the embryo's core merges directly into the proto Earth's core. In such case, the abundance of M in the core at step i equals to the abundance at step $i - 1$ plus the amount of M in the fraction of the embryo that merges directly into the core, plus the amount of M from the fraction of the embryo's core that equilibrates with the mantle but ends up into the core by equilibration process. The abundance of M in the mantle at step i corresponds to the mantle abundance at step $i - 1$ plus the amount from the mantle of the accreted embryo, plus the amount from the part of the core of the embryo that equilibrated with the mantle and was subsequently segregated in the mantle.

Considering simple mass balance relations:

$$(C_{bulk}^M)_i^e = f \cdot (C_{core}^M)_i^e + (1 - f) \cdot (C_{mantle}^M)_i^e \quad (3.5)$$

$$(C_{bulk}^M)_i = f \cdot (C_{core}^M)_{i-1} + (1 - f) \cdot (C_{mantle}^M)_{i-1} + F_i^e \cdot (C_{bulk}^M)_i^e \quad (3.6)$$

with:

$$D_{M_i}^e = \frac{(C_{core}^M)_i^e}{(C_{mantle}^M)_i^e} \quad (3.7)$$

and:

$$D_{M_i} = \frac{(C_{core}^M)_i}{(C_{mantle}^M)_i} \quad (3.8)$$

The concentrations of element M in the core and in the mantle can therefore be computed at each step, using the following equations:

$$(C_{mantle}^M)_i = \frac{F_{i-1}(1-f)(C_{mantle}^M)_{i-1} + F_i^e \frac{((1-f)+fkD_{M_i}^e)(C_{bulk}^M)_i^e}{(1-f)+fD_{M_i}^e}}{F_i(1-f) + F_i^e fkD_{M_i}} \quad (3.9)$$

$$(C_{core}^M)_i = \frac{F_{i-1}f(C_{core}^M)_{i-1} + F_i^e f(1-k) \frac{D_{M_i}^e (C_{bulk}^M)_i^e}{fD_{M_i}^e + (1-f)} + F_i^e fkD_{M_i} (C_{mantle}^M)_i}{F_i f} \quad (3.10)$$

with $(C_{mantle}^M)_i$ and $(C_{core}^M)_i$ the abundances of element M at step i of the accretion in the mantle and the core respectively. F_i represents the total accreted fraction of material at step i , and F_i^e is the incremental fraction of material accreted at step i . $(C_{bulk}^M)_i^e$ is the bulk abundance of element M in the accreted embryo at step i . $D_{M_i}^e$ is the partition coefficient of element M between core and mantle in the embryo accreted, and D_{M_i} the partition coefficient of M in the proto-Earth accreted at step i . f is the mass fraction of core/total body used both for the proto-Earth and the accreted embryos. It is possible to vary k in order to test multiple partial equilibration scenarios but: (1) varying k does not change significantly the outcome of the models, as presented on figure 3.5 where varying k from 1 to 0.1 for the same scenario only lowers the final partition coefficient by 13%. (2) Secondly, contrary to the other formalism presented below, testing random values for k is not backed by any physics significance.

Parameter ε formalism

Fluid dynamics analog experiments have shown that in order for full equilibration to be achieved, metal from the differentiated embryos need to break down to small droplets to be properly segregated to the core, which is less likely for bigger impactors. This effect can be calculated with the equilibration efficiency ε (Deguen et al. 2014) which quantifies the fraction of silicate and metal that equilibrate during metal segregation down to the core, preventing full equilibration. Parameter ε replaces k in equations 3.9 and 3.10, and is calculated as follows:

$$\varepsilon_i = \frac{k}{1 + \frac{D_{M_i}}{\Delta_i}} \quad (3.11)$$

where k is the fraction of the core of the embryo equilibrating with the mantle of the proto-Earth, D_{M_i} the partition coefficient between metal and silicate of element M at equilibration conditions of step i , and Δ_i the metal diffusion, corresponding to the ratio between the mass of equilibrated silicates and the mass of equilibrated metal, which is expressed as follows:

$$\Delta = \frac{\rho_{silicate}}{\rho_{metal}} \cdot \left(\left(1 + \alpha \cdot \frac{z}{r_0} \right)^3 - 1 \right) \quad (3.12)$$

where ρ are the densities, α the entrainment coefficient, z the position of the center of mass and r_0 the initial radius of the embryo's core.

Two examples where ε was used to model partial equilibration are shown on figure 3.6, where it appears that using such formalism lowers significantly the partitioning compared to using only k parameter (figure 3.5). However, varying k when using ε formalism does not affect significantly the results, with little difference between ε and $k = 0.8$ (figure 3.6a) and ε and $k = 0.5$ (figure 3.6b). Therefore, for all models in this study using the ε formalism, we took $k = 0.5$. In the two cases presented in figures 3.6a and b, the average of ε values are 0.059 and 0.037 respectively, with ε equal to 0.0018 and 0.0011 respectively by the end of accretion.

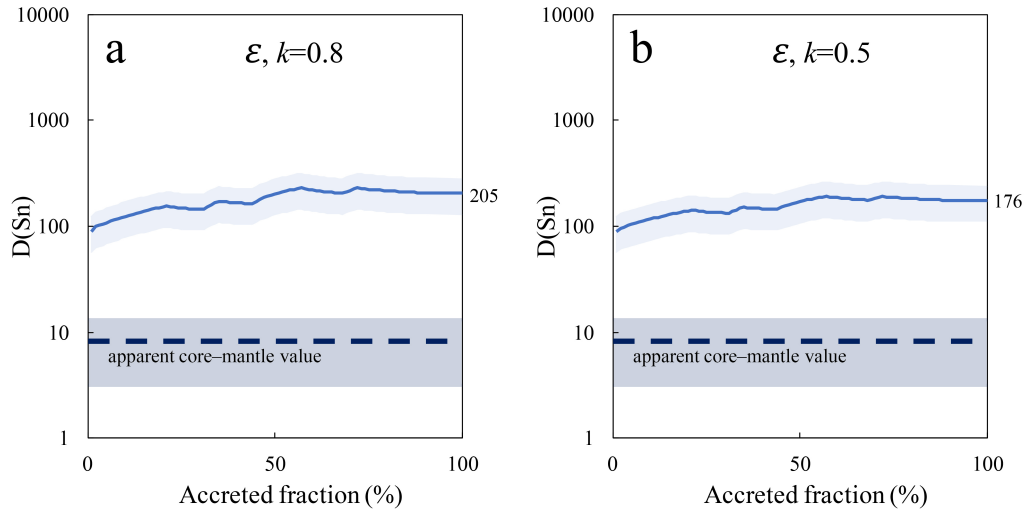


Figure 3.6 – Modelling of partial equilibration with ε formalism developed by Deguen et al. (2014). The scenario presented on both plots corresponds to the same scenario of homogeneous accretion as on figure 3.5. **a.** Reconstruction of Sn partitioning with partial equilibration using ε and with $k = 0.8$. **b.** Reconstruction of Sn partitioning using ε and $k = 0.5$.

For most MSVEs studied in this work (i.e. Sn, Bi and Tl), the use of such formalism is necessary in order for the models to match the apparent core–mantle values. Without such modelling of partial equilibration, no models are able to reconcile our experimental data with observed abundances of these MSVEs in the Earth’s mantle, which is an interesting result on its own. It means that experimental data from this study strongly supports partial equilibration over full equilibration during core formation (see chapters 4 and 5).

3.3.3 Compositionally homogeneous versus heterogeneous accretion scenarios

Since most mantle abundances of MSVEs studied here could not be accounted for by a homogeneous accretion (i.e. Sn, Bi and Sb)—even with partial equilibration modelled from the formalism detailed above as well as the addition of a late veneer—other scenarios were tested. In agreement with numerous studies (e.g. Braukmüller et al. 2019, Mahan et al. 2018a, b, Suer et al. 2017, Wade et al. 2012),

scenarios involving the accretion of the Earth's budget in volatile elements in the last stages of the planet's formation, as a large embryo representing 10 to 20% of the Earth's mass was modelled. In such scenarios, the volatiles budget is concentrated in one last large embryo, which is predicted to equilibrate less efficiently than smaller embryos (see section on the equilibration efficiency). As a result, MSVEs are more easily retained in the mantle in this scenario, allowing to match the observed abundances in the present-day mantle for Sn, Sb and Bi. In the models computed in this study, no other scenario is able to reconcile the mantle abundances with the experimentally measured siderophile behaviours of these 3 elements.

In practice, the last embryo is modelled as to contain the entirety of the MSVEs and S budgets of the Earth, determined using the same estimates as apparent core–mantle values (see section on apparent core–mantle partition coefficients). During the early stages of the accretion, the concentrations applied in the model correspond to one thousandth of the bulk Earth concentration, in order to compute a partition coefficient without affecting the budget of both proto-Earth's reservoirs.

As a result, the partition coefficient is efficiently lowered in models of heterogeneous accretion (figures 3.7c and d) compared to homogeneous accretion scenarios with both full equilibration (figure 3.7a) and partial equilibration (figure 3.7b). For all MSVEs studied in this work, we find that such a scenario of late delivery of the volatile elements in the last 10 to 20% of the main phases of the Earth's accretion is compatible with observed abundances. Moreover, for Sn, Bi, and Sb, this scenario is found necessary in order to account for the relatively high abundances measured in the Earth's mantle, based on experimental determination of their partitioning behaviour at metal–silicate equilibrium. More details on these results and subsequent discussion can be found in chapters 4 and 5.

3.3.4 Predicting isotopic fractionation factors

In chapter 4 focusing on Sn partitioning and isotopic fractionation during core formation, the Sn isotopic composition of the core and the mantle was reconstructed in the models during accretion in order to predict the isotopic composition of the Earth's mantle for a given accretion scenario and a given building material

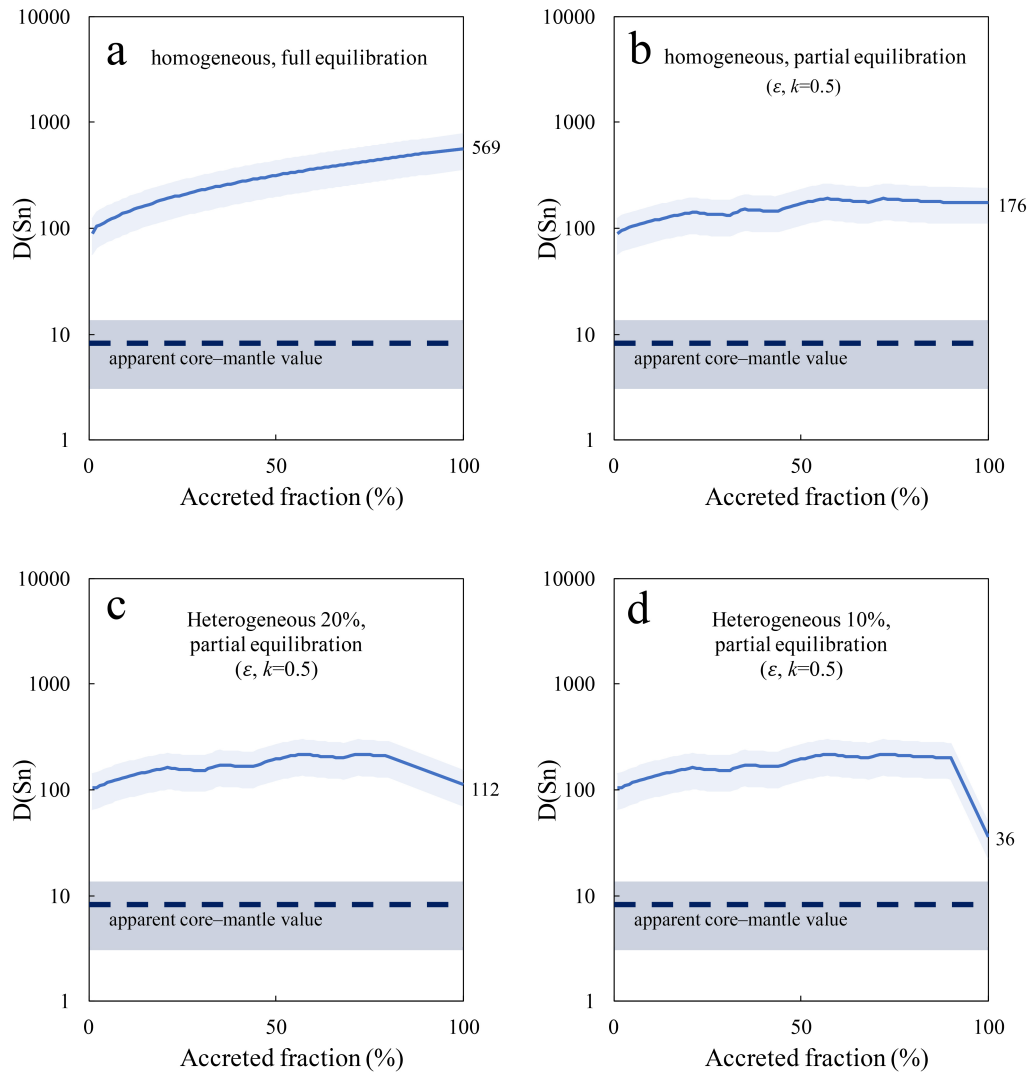


Figure 3.7 – Multiple core formation models reconstructing Sn partition coefficient between core and mantle through Earth’s accretion. **a.** Model of a homogeneous scenario with full equilibration. **b.** Model of a homogeneous scenario with partial equilibration. **c.** Model of a heterogeneous scenario where all the volatile elements are brought in the last 20% of the accretion, with partial equilibration. **d.** Model of a heterogeneous scenario with a volatile delivery in the last 10% of the Earth’s accretion, with partial equilibration.

characterised by its Sn isotopic composition (i.e. enstatite, ordinary and carbonaceous chondrites). The predicted isotopic compositions were compared to the BSE Sn isotopic composition. In such models, the isotopic equilibration was assumed to follow the same efficiency as the elemental equilibration.

Assuming the following:

$$\delta^{118/122}\text{Sn}_{\text{bulk}_i} = f \cdot (C_{\text{core}}^{\text{Sn}})_i \cdot \delta^{118/122}\text{Sn}_{\text{core}_i} + (1 - f) \cdot (C_{\text{mantle}}^{\text{Sn}})_i \cdot \delta^{118/122}\text{Sn}_{\text{mantle}_i} \quad (3.13)$$

and:

$$\Delta^{118/122}\text{Sn}_{\text{core-mantle}_i} = \delta^{118/122}\text{Sn}_{\text{core}_i} - \delta^{118/122}\text{Sn}_{\text{mantle}_i} \quad (3.14)$$

At each step i , the mantle isotopic composition was recalculated using the following equation:

$$\delta^{118/122}\text{Sn}_{\text{mantle}_i} = \frac{\delta^{118/122}\text{Sn}_{\text{bulk}_i} - f \cdot (C_{\text{core}}^{\text{Sn}})_i \cdot \Delta^{118/122}\text{Sn}_{\text{core-mantle}_i}}{f \cdot (C_{\text{core}}^{\text{Sn}})_i - (1 - f) \cdot (C_{\text{mantle}}^{\text{Sn}})_i} \quad (3.15)$$

with $\Delta^{118/122}\text{Sn}_{\text{core-mantle}_i} = \frac{1.18 \cdot 10^6}{T^2}$.

In order to compute partial equilibration isotopic models, the concentrations were replaced by isotopic ratios multiplied by the concentrations in equation 3.9 and 3.10.

3.4 Model limitations and future improvements

Core formation models from this study cumulate uncertainties from the experimental protocol (uncertainty on the temperature, pressure, possible artefacts), and from the parameterisation process (errors on the regression coefficients) and therefore yield significant uncertainty. Moreover, a lot of assumptions and approximations on various parameters are required in order to compute such models. A selection of these are detailed and discussed in this section.

3.4.1 Continuous core formation

In the models presented in this work, core segregation was modeled in a context of deep magma ocean continuously over the course of the accretion, which is an assumption. Earth may have gone through one or several transient or prolonged stages of deep magma oceans covering the Earth towards the end of the accretion, induced by giant impact (Rubie et al. 2007, Tonks and Melosh 1993). In particular, the Moon-forming impact may even have induced the melting of the entire Earth (Cameron 2000, Canup and Asphaug 2001). However, there is no evidence that such deep magma ocean was constantly active during the entirety of the accretion and differentiation process. In further models, a differentiation regime composed of active stages of core formation in a context of deep magma ocean interspersed with inactive stages, modelling periods of full crystallisation of the Earth's mantle, could be tested.

3.4.2 Fully differentiated impactors

As mentioned previously, the Earth probably accreted from a mixture of differentiated (e.g. Greenwood et al. 2005, Taylor and Norman 1990) and undifferentiated bodies (e.g. Thomas et al. 2005). In that regard, the models presented are too simplistic as they only consider differentiated embryos, and could be improved by setting a fraction of undifferentiated embryos amongst the accreted bodies. Such proportion could evolve as the accretion progresses since the larger embryos accreted towards the end of the Earth's formation are more likely to be already differentiated.

Moreover, as pointed out by Rubie et al. (2016), core formation models usually do not consider the material that is ejected and lost upon impact of the embryo to the proto-planet. The effect of such process could be significant if preferential collisional erosion occurs in sufficient magnitude as to induce compositional fractionation (e.g. O'Neill and Palme 2008).

3.4.3 Mole fractions versus mass fractions

The partition coefficients derived from experiments and subsequently parameterised are expressed as a mole fraction ratio, and are also reconstructed as such by core formation models. However, when operating mass balance calculations involving the two main reservoirs of the Earth, certain parameters are more conveniently expressed as mass fractions. The core to body ratio, f , used in equations 3.9 and 3.10, corresponds to a mass ratio. The modelling of the late veneer also uses a mass fraction approximation. Although such assumptions may not affect significantly the outcome of the models (Wade et al. 2012), a more unified model using only mass fractions could be constructed and used for future work. The results of such models could then be presented as the evolution of the mantle abundance in *wt.%* of the element of interest across the accretion process, with the target value being the observed mantle abundance also in *wt.%*. This would simplify the presentation of the results to the reader, by using direct geochemical observables as reference.

Tracing Earth's volatile delivery with Sn

This first study aims at bringing new elements of answer regarding the timing and origin of volatile elements on Earth by using the methods described in the three previous chapters, namely (1) measurement of the Sn partitioning and isotopic fractionation between metal and silicate in controlled experiments, (2) thorough parameterisation of the effects of pressure, temperature, oxygen fugacity and composition and (3) subsequent core formation modelling in order to reconcile experimental results with observed abundances by one or a variety of accretion scenarios. This study is presented as submitted to be peer reviewed by *Geochimica et Cosmochimica acta* journal. All research work presented in the study was done by the author of this thesis, under proper supervision. Piston cylinder experiments were performed under the supervision of Brandon Mahan and Julien Siebert. Multianvil experiments were operated as part of two DMG Core Facility Program proposals at Bayerisches Geoinstitut (University of Bayreuth) with help from Ingrid Blanchard and Julien Siebert, and with technical support from Svyatoslav Shcheka. Tin isotopic measurements were executed by the author, under the supervision of John B. Creech and Frédéric Moynier. Lastly, thermodynamic parameterisation and core formation modelling were operated by the author on Matlab with guidance and advice from Julien Siebert.

Tracing Earth's volatile delivery with Sn

E. Kubik^{1,*}, J. Siebert^{1,2}, B. Mahan¹, J.B. Creech¹, I. Blanchard³, S. Shcheka³, A. Agranier⁴, F. Moynier¹.

¹Université de Paris, Institut de Physique du Globe de Paris, CNRS, 1 Rue Jussieu, 75005 Paris, France.

²Institut Universitaire de France, Paris, France.

³Bayerisches Geoinstitut, University of Bayreuth, Germany.

⁴Institut Universitaire Européen de la Mer, Université de Brest, France.

*kubik@ipgp.fr

Abstract

Earth's accretion history for volatile elements, and the origin of their depletions with respect to the Sun and primitive meteorites, continue to be debated. The two most extreme scenarios propose either that volatile elements were delivered during the main phases of Earth's accretion and differentiation, or that the Earth accreted from materials largely devoid of volatiles with late addition of volatile-rich material after core formation ceased. Experiments evaluating the effect of metal–silicate equilibrium on the chemical and isotopic distribution of elements that are both volatile and siderophile during core formation can be used to distinguish between these scenarios. Tin is a moderately volatile and siderophile element which is only depleted by a factor of 5 in the mantle with respect to lithophile elements of similar volatility. Its metal–silicate partitioning behavior is poorly constrained, and therefore the effect of core–mantle equilibration on the abundance of Sn in the mantle is presently unclear. Moreover, Sn isotopic composition in natural samples (i.e. terrestrial rocks, chondrites) can provide independent and complementary constraints on the origin of Earth's mantle volatiles, but this first requires the determination of Sn isotopic fractionation during core–mantle equilibration. In this work, we have performed a series of high-pressure and high-temperature experiments in a piston cylinder press and in multi-anvil apparatus from 2 to 20 GPa and 1700 to 2573 K, and systematically investigated the relative influence of temperature, pressure, oxygen fugacity, and metal and silicate compo-

sition on the metal–silicate partitioning behavior of Sn. Our results indicate that Sn siderophility noticeably decreases with increasing temperature and S content of the liquid metal but increases dramatically with pressure. These results can be used to characterise the conditions of Earth’s formation. A resolvable isotopic fractionation factor between metal and silicate was also measured on these experiments indicating that core–mantle equilibrium temperatures (~ 3000 K) could potentially generate a Sn isotopic composition of the mantle lighter than the core by 150–200 ppm per amu. Core formation modelling shows that the reduced depletion of Sn in the bulk silicate Earth can only be produced if volatiles were added late in the accretion history, namely during the last 10% of Earth’s accretion, and possibly involving equilibration with a sulfide “matte” that segregated to the core. Consequently, a final core containing roughly 2 to 4 *wt.%* S is required. Furthermore, modelling of the final Sn isotopic composition of the BSE argues for a late Sn accretion delivery on Earth during the last stages of core formation with carbonaceous chondrite-like material as the most likely source of volatiles.

Introduction

The habitability of Earth depends intrinsically on the presence of volatile elements, and therefore the timing and origin of volatile elements delivery to Earth is a key question yet to be answered. Volatile elements are depleted in terrestrial planets compared to the Sun’s photosphere according to their condensation temperature (Palme and O’Neill 2014). The two most extreme mechanisms that could explain this depletion are (1) a loss of volatile elements by syn- and post-accretion volatilisation processes, or (2) a depletion of volatile elements within the accreted material that formed the terrestrial planets due to incomplete condensation in the solar nebula (Albarède 2009).

A lack of K (Bloom et al. 2020, Humayun and Clayton 1995, Tuller-Ross et al. 2019, Wang and Jacobsen 2016), Rb (Nebel et al. 2011, Pringle et al. 2017) and Zn (Luck et al. 2005, Pringle et al. 2017, Sossi et al. 2017) heavy isotope enrichment in the Earth’s mantle compared to primitive meteorites has been used as evidence for the absence of volatile loss by evaporation during Earth’s formation. Furthermore, the Mn/Na ratio, which is a tracer of post-nebular volatilisation, is roughly chon-

drift in the Earth, suggesting limited volatile loss during or after Earth’s accretion (O’Neill and Palme 2008, Siebert et al. 2018). However, it should be noted that small isotopic fractionations observed for Mg (Hin et al. 2017) and Si (e.g. Pringle et al. 2014, Young et al. 2019) have been used as argument that volatilisation may play a role in establishing the composition of the Earth. The same is not true for the Moon and some other differentiated terrestrial bodies, which are markedly enriched in the heavy isotopes of numerous elements (Boyce et al. 2015, Kato et al. 2015, Pringle and Moynier 2017, Pringle et al. 2014, Sharp et al. 2010, Wang et al. 2019), or light isotopes for certain elements (e.g. Cr, Sn, Sossi et al. 2018, Wang et al. 2019), lending credence to the widely-held view that volatilisation during Moon formation and evolution resulted in isotopic fractionation. This study focuses on the accretion of volatile elements during Earth’s formation, the nature of its building blocks, and subsequent core–mantle differentiation. Several accretion scenarios could produce the observed volatile elements pattern of the Earth:

(1) The Earth formed from material largely devoid of volatile elements, a.k.a. “dry accretion”. This scenario is supported by the fact that the solar system temperature during the main phases of Earth’s accretion may be too high to allow the condensation of those elements (Albarède 2009). In this case, volatiles are brought after the planet’s differentiation ceased around 100 million years after the solar system formation, as the so-called late veneer (Albarède et al. 2013, Budde et al. 2019, Dauphas 2017, O’Neill 1991).

(2) In a second possible scenario, the Earth is accreted from material partially depleted in volatile elements, such as chondrites or their components (e.g. chondrules). The subsequent differentiation redistributes the elements according to their siderophile behaviour between core and mantle (Righter et al. 2017b, Wood and Halliday 2010) or are lost by evaporation (Hin et al. 2017, Norris and Wood 2017, Pringle et al. 2014). In this case, volatiles are mostly brought during the main phases of the planet’s accretion.

(3) A third and intermediate scenario consists of the heterogeneous accretion of the planet, where the volatile elements are mainly brought during the last phases of accretion and differentiation (and being all but absent prior to this). It has been recently proposed that volatile elements on Earth come from 10 to 15 *wt.%* of CI-like material brought in the later part of the main phases of Earth’s accretion (Braukmüller et al. 2019, Mahan et al. 2018a, b). Volatiles are accreted rapidly and

late, possibly associated with the formation of the so-called Hadean matte (O'Neill 1991, Savage et al. 2015, Schonbachler et al. 2010), a sulfur- and volatile-rich liquid that settles at the core–mantle boundary and subsequently mixes into the core.

The study of the partitioning and isotopic behavior of elements that are both volatile and siderophile can help discriminate between these three scenarios by isolating the effect of siderophile processes, such as the Earth's differentiation, from the effect of volatile processes.

Moderately siderophile and volatile elements (MSVEs) are depleted in the Earth's mantle compared to lithophile volatile elements, presumably due to their segregation into the core, and as a consequence they do not follow the canonical volatility trend pattern (Lodders 2003, Wasson et al. 1988, Wood et al. 2019). A way to infer the effect of differentiation on the observed volatile depletion is to experimentally study the behaviour of MSVEs during such processes (e.g. Ballhaus et al. 2017, Blanchard et al. 2015, Corgne et al. 2008, Mahan et al. 2018a, b, 2017, Righter et al. 2017b, Siebert et al. 2011, Steenstra et al. 2019, 2017, 2016, Suer et al. 2017). The behaviour of MSVEs at core formation conditions in controlled experiments, and their comparison to geochemical observables, helps to deconvolve the effects of differentiation and volatile-related processes from one another. Two different approaches—elemental, and isotopic—can be used to investigate such behaviour.

The elemental behaviour of MSVEs can be experimentally characterised in a metal–silicate equilibrium, wherein partition coefficients are measured to express the MSVE fractionation between the metal and silicate phases. Comprehensive parameterisations of metal–silicate partitioning constrain the effects of temperature, pressure, fO_2 , metal and silicate composition, and includes the influence of capsule material (Siebert et al. 2011).

Numerous recent studies investigate the metal–silicate isotopic fractionation of elements (e.g. Bourdon et al. 2018, Burkhardt et al. 2014, Creech et al. 2017c, Mahan et al. 2017, Savage et al. 2015). In such studies, experimental metal–silicate fractionations of a given element are often compared to the isotopic composition of the bulk silicate Earth (BSE) and primitive meteorites to assess whether the siderophile element abundance in the Earth's mantle can be explained by the accretion and differentiation of primitive material from the solar system. Measurements

of the isotopic fractionation provide a second and independent constraint on the timing and origin of the volatile accretion relative to the Earth’s differentiation, and likewise comparison to the BSE and primitive meteorites provide insights into dominant redistribution processes and source materials.

Combining elemental and isotopic observations from experiments is thus a particularly robust approach, where parameterisations of elemental and isotopic fractionations between metal and silicate can be used as input in core formation models. In such models, the partitioning and isotopic fractionation can be reconstructed at each step of the Earth’s accretion, taking into account the evolving pressure and temperature conditions, allowing to test different accretion scenarios and address questions regarding the formation and differentiation of terrestrial planets (e.g. Blanchard et al. 2015, Bourdon et al. 2018, Rubie et al. 2011, Rudge et al. 2010, Wade and Wood 2005). In particular, this approach has allowed to determine the pressure, temperature and oxygen fugacity conditions of core formation (Wade and Wood 2005). The results of those models can then be compared to natural observations and used to discriminate between accretion scenarios.

In this study we have comprehensively characterised Sn partitioning and isotopic fractionation in metal–silicate equilibrium. Tin is a moderately siderophile and moderately volatile element with a condensation temperature of 704 K (Lodders 2003) recently reappraised to 604 K according to Wood et al. (2019). As such, Sn abundance in the Earth’s mantle is affected by both core–mantle differentiation and by volatile processes, which makes it a good tracer of volatile accretion. Tin’s depletion in Earth’s primitive mantle by a factor of 5 is very small compared to the depletion expected from its siderophile behaviour at low pressure and low temperature. For example, Sn’s metal–silicate partitioning at low P, T conditions is very close to that of S, however, Sn is less depleted in the Earth’s mantle than S by a factor of 20 (Palme and O’Neill 2014, Wood et al. 2006). By characterising Sn partitioning at the conditions of the Earth’s accretion, it is possible to constrain possible accretion pathways that can lead to this perceived overabundance. Unlike previous studies reporting Sn metal–silicate partitioning results as part of an ensemble and/or at lower pressures (Ballhaus et al. 2017, 2013, Capobianco et al. 1999, Righter and Drake 2000, Righter et al. 2017b, 2019, 2010, Vogel et al. 2018), this study is entirely dedicated to Sn. By focusing explicitly on Sn and its partitioning at higher P, T conditions than previously explored, we provide com-

prehensive constraints on its partitioning as a function of thermodynamic variables. Partitioning results from 30 novel metal–silicate experiments have been combined with literature data for parameterisation of Sn partitioning at PT conditions that encompass that during Earth’s core–mantle differentiation, and this has been input into models of Sn partitioning at plausible core formation conditions.

Tin has 10 stable isotopes with masses ranging from 112 to 124. The most abundant are ^{120}Sn (32.6 %), ^{118}Sn (24.2 %) and ^{116}Sn (14.5 %). The observation of Sn isotopic fractionation during igneous processes (Badullovich et al. 2017, Wang et al. 2019) is a good indicator that it might also fractionate between molten metal and silicate. For now, no data exist on Sn isotopic fractionation in this context. Recent data from Creech and Moynier (2019) report Sn isotopic compositions for a selection of ordinary, enstatite and carbonaceous chondrites. These three chondrite types show distinct average Sn isotopic compositions, with average $\delta^{122/118}\text{Sn}$ (permil variation of the $^{122}\text{Sn}/^{118}\text{Sn}$ ratio relative to the Sn_IPGP standard) of $-0.29\pm 0.44\text{‰}$, $0.12\pm 0.28\text{‰}$ and $0.47\pm 0.12\text{‰}$ respectively. Furthermore, an overlap between the carbonaceous chondrites measurements and the BSE, which has a $\delta^{122/118}\text{Sn}$ equal to $0.49\pm 0.11\text{‰}$, is observed. Therefore, comparing the isotopic fractionation of Sn as a consequence of metal–silicate differentiation to the Sn isotopic composition of chondrites may help discriminate between possible source materials for Earth’s volatiles. Furthermore, it has recently been shown that the silicate Moon is enriched in the lighter isotopes of Sn compared to the silicate Earth as the result of volatility processes (Wang et al. 2019). As it has been suggested that most of the missing lunar Sn may be alternatively be stored in its core (Steenstra et al. 2016), it is important to test whether part of the light isotope enrichment of the lunar mantle may reflect metal–silicate fractionation. It should be noted that Sn fractionation during volatilisation processes has been evidenced both from low temperature experimental study (She et al. 2020) and natural sample measurements (Creech and Moynier 2019).

Experimental and analytical methods

Further details on experimental and analytical methods can be found in the supplementary materials.

Table 4.1 – Starting material compositions

| Starting material | Silicate phase | | | | Metallic phase | | |
|-------------------|----------------|------|----|-------|----------------|----|--------------------|
| | MORB | KLB1 | Sn | Fe | FeS | Cu | Tl, In, Cd, Bi, Sb |
| A | 70% | | 8% | 22% | | | |
| B | 70% | | 4% | 26% | | | |
| C | 70% | | 4% | 13% | 13% | | |
| D | 70% | | 4% | 25% | | 1% | |
| E | | 70% | 4% | 25% | | 1% | |
| F | 70% | | 2% | 30% | | 1% | 1% of each |
| G | 70% | | 2% | 13.5% | 16.5% | 1% | 1% of each |

Starting materials

Seven mixtures composed of homogenised metallic and silicate powders were used to conduct the 30 high-pressure and high-temperature experiments of this study. The different compositions of the metallic and silicate phases were used to experimentally assess their effect on partitioning and isotopic fractionations (table 4.1). The material was Sn-doped from 2 to 8 *wt.%* using Putratronic pure 99.8% powder to ensure sufficient Sn concentration in the silicate for electron microprobe measurement. Three additional experiments were doped with 2, 5 and 10 *wt.%* of Si in order to investigate the effect of Si on Sn partitioning and widen the range of fO_2 of this study.

Piston cylinder experiments

Eighteen experiments were performed using a 150-tons end-loaded piston cylinder apparatus at the Institut Physique du Globe de Paris (IPGP). All piston cylinder experiments conducted in this study were performed at 2 GPa and from 1696 to 2296 K (table 4.2). Those conditions allowed the fusion of the material and the chemical equilibrium between metal and silicate. Two capsule materials were tested, boron nitride and magnesium oxide, in order to study the interaction processes that could occur during the experiment. The metal and silicate were

separated after each experiment and sufficient material from each phase was prepared for both elemental and isotopic analysis. Clean pieces were carefully selected mechanically under magnifying glass.

Multianvil experiments

Twelve additional experiments were performed at Bayerisches Geoinstitut using a 5000-ton Zwick and a 1000-ton Hymag multianvil apparatus from 7 to 20 GPa. The starting material was contained in a single-crystal MgO capsule and lid. During the experiment, the sample temperature was monitored using a $W_{97}Re_3/W_{75}Re_{25}$ type D thermocouple. All experimental parameters are summarised in table 4.2.

Electron microprobe analysis

Pieces of metal and silicate from each experiment were selected, and mounted in a resin and polished. Those pieces were then carbon coated and analysed with the CAMPARIS laboratory CAMECA SX Five electron microprobe (Université Pierre et Marie Curie) in order to resolve a selection of major and trace elements in both metal and silicate phases (table 4.2). In order to avoid any effect of the quench textures obtained in the experiments on the microprobe analysis, especially in the metal parts, rasters of 30 μm were used instead of points. No zonations were found across the samples in any experiment, which proves that equilibrium was achieved.

Laser-ablation ICPMS measurements

In the higher pressure experiments, the depletion of Sn in the silicate fraction of the samples resulted in concentrations below detection limits of EPMA analysis. Instead, LA-ICPMS measurements were performed at the University of Brest in order to obtain Sn concentrations in the silicate phases of multianvil experiments. Ablation was conducted using a 193 nm Compex Pro 102 Coherent Laser Ablation System coupled to an Element XR high-resolution mass spectrometer. Data accuracy was ensured via internal calibrations, using Mg concentrations previously measured by EPMA, and by standard interpolations using glass standards

NIST610, NIST612 and NIST614.

Sample preparation and dissolution

Metallic and silicate phases stemming from piston cylinder experiments were separated mechanically and crushed. The eventual metallic pieces contaminating the silicate were removed magnetically. Silicate samples were dissolved using a common HF-HNO₃ method: crushed silicates were digested in a 1:3 solution of HF:HNO₃. Metals were dissolved in 6 N HCl. The samples in closed Teflon bombs were heated on a hotplate at 100°C. Samples were double-spiked using the method described in Creech et al. (2017b) by addition of a double-spike solution in the sample beaker following proportions of 39.77% double-spike Sn and 60.23% Sn from the sample.

Chemical purification of Sn

Tin was chemically separated from the rest of the sample prior to its mass spectrometer analysis to avoid interferences using the ion exchange chromatography technique described in Creech et al. (2017b). Biorad columns containing 1 mL of Eichrom TRU resin were used. Tin cuts were then recovered in 10 mL of 0.5 N HNO₃. This chemical process is executed in order to recover a Sn cut containing about 1 μ g of Sn. Each Sn cut was then dried and redissolved into 0.5 N HCl for a concentration of ca. 100 ng.mL⁻¹ for mass spectrometer analysis.

Mass spectrometry and data reduction

Tin isotope measurements were performed using a Neptune Plus MC-ICPMS (IPGP, Paris) following the method described in Creech et al. (2017b). Samples were analysed during 412 s, inducing a consumption of 70 ng of Sn per analysis. Blanks were <1 ng and two natural samples were measured along with our samples and found to reproduce values published previously (Creech and Moynier 2019; see supplementary information). All isotope data reduction was performed using Isospike (www.isospike.org; Creech and Paul 2015).

Results

Petrography

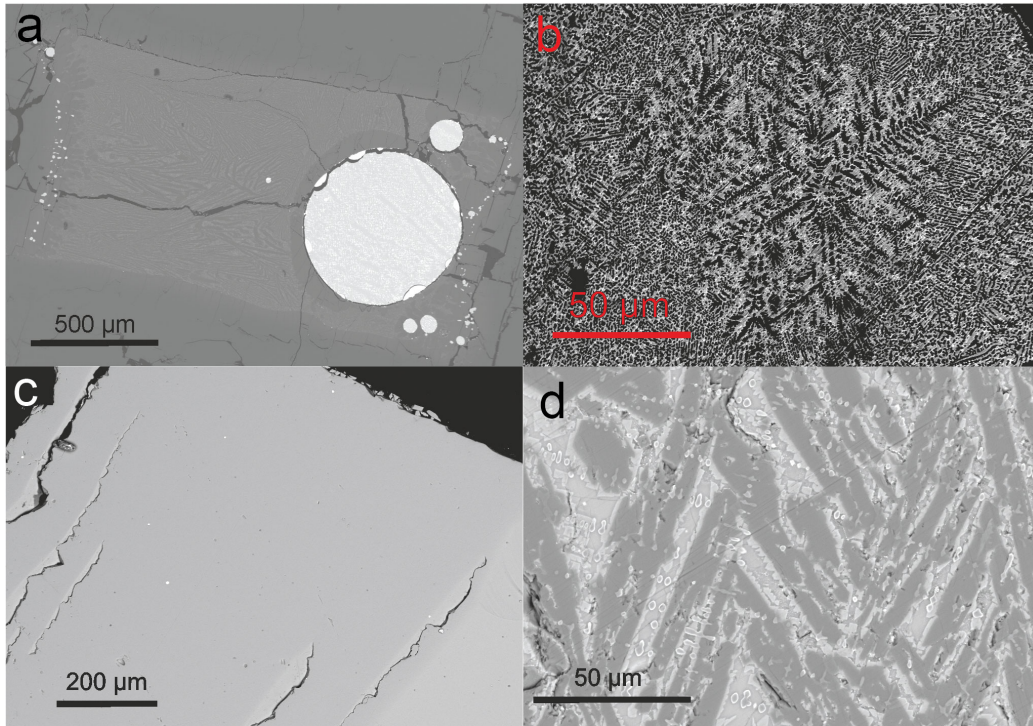


Figure 4.1 – Back-scattered electron images from typical multianvil and piston cylinder run products. **a.** Image of H4950 multianvil experiment (12 GPa, 2273 K). The average composition of both phases are measured with 30 μm rasters on the electron microprobe, and a 90 μm beam size for laser ablation in order to homogenize quench textures in the metal and in the silicate that correspond to local chemical heterogeneities. **b.** Image of metal phase (piston cylinder, 2 GPa, 1797 K) showing dendritic quench texture. **c.** Image of silicate phase of run 268 (piston cylinder, 2 GPa, 1823 K) typical of low temperature, boron nitride encapsulated runs showing clean glass with a few $\sim 1 \mu\text{m}$ metal nuggets. **d.** Image of silicate phase of run 272 (piston cylinder, 2 GPa, 2296 K) showing typical quench textures for high temperature MgO-encapsulated experiments with dendritic olivine crystals and interstitial pyroxenite glass (brighter gray).

In each experiment, the superliquidus temperature allowed the metal to coalesce into a single metal sphere, measuring about 1 mm in the piston cylinder experiments and 500 μm in multianvil experiments (figure 4.1a). This sphere was surrounded by the silicate part of the sample, which sometimes contained several other much smaller metal spheres (figure 4.1a). All silicate phases were glassy (figure 4.1c) except for the higher temperature MgO encapsulated experiments, in which MgO diffusion led to crystallisation of olivine and pyroxene (figure 4.1d). The metallic phases have quench textures (figure 4.1b). Those primary petrographic observations indicate that the starting material was fully molten in all the experiments, allowing the equilibrium to be achieved. Si-doped experiments present several immiscible phases in the metal part and some metal contamination in the silicate as micro- and nano-nuggets and were therefore discarded from this study.

Elemental compositions

All elemental data from EPMA and LA-ICPMS are presented in table 4.2. The MgO content of the silicate phases of the experiments, from 6.5 *wt.%* to 41.8 *wt.%*, is a function of the experimental temperature since the MgO introduction from the capsule to the sample is favored at higher temperatures. This content is inferior to 30 *wt.%* in boron nitride encapsulated experiments. The SiO₂ content ranges from 30.1 *wt.%* to 52 *wt.%*. Tin concentration varies from 100 to 4000 ppm. The metallic phases of the experiments are dominated by Fe. The S content varies from 0 to 17.4 *wt.%*. Tin concentration ranges from 3.3 to 23 *wt.%*. Both silicate and metallic phases are compositionally homogeneous at the scale of EPMA analyses. Oxygen fugacity is calculated as follows, relative to the iron-wüstite (IW) buffer:

$$\Delta IW = 2 \cdot \log \frac{X_{\text{FeO}}^{\text{silicate}}}{X_{\text{Fe}}^{\text{metal}}} \quad (4.1)$$

ΔIW varies from -3.38 to -1.6 in the experiments (table 4.2).

Metal–silicate Sn partitioning

Tin metal–silicate partitioning can be written as a chemical exchange redox reaction:



where n is the valence of Sn. The valence of Sn was determined for the range of $f\text{O}_2$ in our experiments and is demonstrated in figure 4.2, where Sn partitioning is plotted as a function of $f\text{O}_2$. The slope of the regression line presented here corresponds to $n/4$ (Siebert et al. 2011) and is shown to be 0.5 in this study. Therefore, this allows precise determination of a valence state of 2+ for Sn in the experiments of this study and associated literature data (e.g. Vogel et al. 2018; 2+). However, it is noted that this result is in contradiction with the Sn valence state reported from Richter et al. (2019). Further XANES study is needed to fully resolve the Sn valence state in silicate melts. As a 2+ valence state is currently the most harmonious, herein this value is used for further calculations and modelling. The metal–silicate partition coefficient corresponds to the ratio of molar concentrations:

$$D_{\text{Sn}} = \frac{X_{\text{Sn}}^{\text{metal}}}{X_{\text{SnO}}^{\text{silicate}}} \quad (4.3)$$

The equilibrium constant associated with the redox reaction 4.2 is:

$$K = \frac{a_{\text{FeO}}^{\text{silicate}} \cdot a_{\text{Sn}}^{\text{metal}}}{a_{\text{SnO}}^{\text{silicate}} \cdot a_{\text{Fe}}^{\text{metal}}} \quad (4.4)$$

where a is the activity of the different components, and $a = \gamma_i \cdot x_i$, where γ_i is the activity coefficient and x_i is the mole fraction:

$$\log K = \log \frac{x_{\text{FeO}}^{\text{silicate}} \cdot x_{\text{Sn}}^{\text{metal}}}{x_{\text{SnO}}^{\text{silicate}} \cdot x_{\text{Fe}}^{\text{metal}}} + \log \frac{\gamma_{\text{Sn}}^{\text{metal}}}{\gamma_{\text{Fe}}^{\text{metal}}} + \log \frac{\gamma_{\text{FeO}}^{\text{silicate}}}{\gamma_{\text{SnO}}^{\text{silicate}}} \quad (4.5)$$

The influence of silicate melt composition is represented by the last term of this equation. In our experiments, two different silicate compositions were used, MORB and peridotite, and no difference in partitioning was found between experiments run in similar conditions. To further investigate this effect, the *nbo/t* parameter, corresponding to the molar ratio of non-bridging oxygens per tetrahedrally coordinated cation, was calculated (table 4.2), and found to have no effect on Sn

CHAPTER 4. Tracing Earth's volatile delivery with Sn

Table 4.2 – Main parameters of all experiments, average major and trace element compositions of metal and silicate phases by EPMA and LA-ICPMS and isotopic compositions by MC-ICPMS. Errors correspond to 1 standard deviation σ .

| Experiment | E257 | E258 | E259 | E260 | E265 | E267 | E268 | E272 | E273 |
|--|--------------|--------------|--------------|--------------|-------------------|-------------------|--------------|-------------------|-------------------|
| Starting material | A | C | C | A | C | A | B | B | B |
| Pressure (GPa) | 2 | 2 | 2 | 2 | 2 | 2 | 2 | 2 | 2 |
| Temperature (K) | 1696 | 1696 | 1796 | 1796 | 2296 | 2296 | 1823 | 2296 | 2100 |
| Duration (min) | 30 | 30 | 15 | 15 | 1.5 | 3 | 15 | 2 | 5 |
| Pressure media | Talc-pyrex | Talc-pyrex | Talc-pyrex | Talc-pyrex | BaCO ₃ | BaCO ₃ | Talc-pyrex | BaCO ₃ | BaCO ₃ |
| Capsule | BN | BN | BN | BN | BN | BN | BN | MgO | MgO |
| Silicate composition (oxide wt.%) | | | | | | | | | |
| n | 40 | 30 | 25 | 24 | 19 | 6 | 26 | 67 | 71 |
| SiO ₂ | 51.36 ± 0.42 | 49.96 ± 0.32 | 50.14 ± 0.26 | 51.74 ± 0.55 | 45.58 ± 1.42 | 46.23 ± 0.43 | 52.06 ± 0.69 | 34.54 ± 0.33 | 33.79 ± 0.24 |
| Al ₂ O ₃ | 15.87 ± 0.13 | 15.48 ± 0.04 | 15.47 ± 0.06 | 16.05 ± 0.09 | 14.28 ± 0.30 | 14.24 ± 0.21 | 16.12 ± 0.26 | 8.49 ± 0.44 | 11.50 ± 0.32 |
| CaO | 10.21 ± 0.13 | 9.97 ± 0.08 | 9.93 ± 0.04 | 10.43 ± 0.11 | 9.36 ± 0.11 | 9.20 ± 0.10 | 9.09 ± 0.99 | 5.69 ± 0.36 | 8.56 ± 0.45 |
| MgO | 8.37 ± 0.05 | 8.14 ± 0.02 | 8.05 ± 0.05 | 8.58 ± 0.03 | 7.21 ± 0.13 | 7.03 ± 0.11 | 8.15 ± 0.08 | 41.81 ± 0.87 | 32.94 ± 1.09 |
| FeO | 3.99 ± 0.18 | 4.91 ± 0.14 | 4.73 ± 0.29 | 3.59 ± 0.18 | 4.20 ± 1.14 | 5.03 ± 0.10 | 3.50 ± 0.28 | 5.76 ± 0.16 | 7.61 ± 0.21 |
| B ₂ O ₃ | 3.84 ± 0.25 | 5.56 ± 0.11 | 5.60 ± 0.14 | 3.20 ± 0.16 | 12.99 ± 4.39 | 10.89 ± 1.69 | 3.08 ± 0.52 | 0.09 ± 0.02 | 0.02 ± 0.01 |
| Na ₂ O | 2.94 ± 0.04 | 2.75 ± 0.03 | 2.90 ± 0.03 | 3.34 ± 0.02 | 2.80 ± 0.95 | 2.81 ± 0.08 | 3.47 ± 0.06 | 1.77 ± 0.17 | 2.86 ± 0.20 |
| TiO ₂ | 1.76 ± 0.04 | 1.72 ± 0.02 | 1.70 ± 0.02 | 1.78 ± 0.02 | 1.48 ± 0.05 | 1.45 ± 0.06 | 1.74 ± 0.05 | 0.98 ± 0.06 | 1.36 ± 0.06 |
| K ₂ O | 0.68 ± 0.01 | 0.66 ± 0.01 | 0.67 ± 0.01 | 0.72 ± 0.01 | 0.65 ± 0.10 | 0.67 ± 0.02 | 0.66 ± 0.07 | 0.42 ± 0.04 | 0.65 ± 0.04 |
| P ₂ O ₅ | 0.13 ± 0.01 | 0.13 ± 0.01 | 0.13 ± 0.003 | 0.14 ± 0.01 | 0.05 ± 0.048 | 0.11 ± 0.01 | 0.14 ± 0.02 | 0.13 ± 0.01 | 0.20 ± 0.01 |
| SnO ₂ | 0.08 ± 0.02 | 0.06 ± 0.02 | 0.06 ± 0.02 | 0.10 ± 0.01 | 0.08 ± 0.03 | 0.36 ± 0.01 | 0.03 ± 0.01 | 0.10 ± 0.01 | 0.20 ± 0.01 |
| SO ₂ | 0.01 ± 0.003 | 0.04 ± 0.01 | 0.06 ± 0.03 | 0.01 ± 0.002 | 0.17 ± 0.08 | 0.03 ± 0.004 | 0.01 ± 0.003 | 0.04 ± 0.002 | 0.04 ± 0.002 |
| N | | | | | 0.57 ± 0.89 | 0.91 ± 0.33 | N.D. | N.D. | N.D. |
| Total | 99.23 ± 0.74 | 99.38 ± 0.25 | 99.43 ± 0.32 | 99.67 ± 0.55 | 99.41 ± 4.76 | 98.96 ± 1.60 | 98.05 ± 1.68 | 99.82 ± 0.08 | 99.74 ± 0.08 |
| Metal composition (wt.%) | | | | | | | | | |
| n | 23 | 31 | 27 | 29 | 22 | 23 | 21 | 31 | 33 |
| Fe | 72.31 ± 0.19 | 69.76 ± 0.12 | 69.69 ± 0.09 | 72.40 ± 0.22 | 72.10 ± 0.28 | 73.11 ± 0.17 | 85.47 ± 0.19 | 85.01 ± 0.26 | 85.56 ± 0.18 |
| Sn | 23.12 ± 0.17 | 10.99 ± 0.10 | 10.45 ± 0.11 | 23.12 ± 0.23 | 9.16 ± 0.33 | 21.87 ± 0.14 | 11.37 ± 0.14 | 12.33 ± 0.18 | 12.14 ± 0.15 |
| P | 0.23 ± 0.01 | 0.15 ± 0.00 | 0.16 ± 0.01 | 0.24 ± 0.00 | 0.24 ± 0.01 | 0.29 ± 0.02 | 0.25 ± 0.01 | 0.15 ± 0.01 | 0.12 ± 0.00 |
| S | 0.22 ± 0.01 | 16.12 ± 0.14 | 15.46 ± 0.12 | 0.24 ± 0.01 | 14.48 ± 0.32 | 0.26 ± 0.03 | 0.24 ± 0.02 | 0.23 ± 0.02 | 0.23 ± 0.02 |
| Si | 0.03 ± 0.01 | 0.01 ± 0.001 | 0.01 ± 0.001 | 0.04 ± 0.01 | 0.01 ± 0.001 | 0.10 ± 0.05 | 0.09 ± 0.00 | 0.03 ± 0.01 | 0.01 ± 0.001 |
| O | | | | | 0.82 ± 0.50 | 0.02 ± 0.01 | N.D. | 0.65 ± 0.06 | 0.45 ± 0.03 |
| B | | | | | 0.01 ± 0.01 | N.D. | 0.04 ± 0.01 | N.D. | N.D. |
| N | | | | | 0.08 ± 0.07 | 0.31 ± 0.03 | N.D. | N.D. | N.D. |
| Ti | | | | | 0.004 ± 0.001 | 0.01 ± 0.00 | 0.01 ± 0.00 | 0.01 ± 0.002 | 0.005 ± 0.001 |
| Mg | | | | | | | | 0.07 ± 0.004 | 0.07 ± 0.001 |
| Total | 95.65 ± 0.07 | 96.86 ± 0.06 | 95.74 ± 0.08 | 96.00 ± 0.08 | 96.39 ± 0.27 | 95.80 ± 0.08 | 97.33 ± 0.10 | 98.28 ± 0.10 | 98.40 ± 0.06 |
| D_{Sn} | 394 ± 79 | 211 ± 53 | 209 ± 86 | 328 ± 21 | 128 ± 44 | 86 ± 3 | 411 ± 128 | 182 ± 15 | 91 ± 6 |
| $\log K_d^{Sn}$ | 1.14 ± 0.09 | 1.06 ± 0.11 | 1.03 ± 0.18 | 1.01 ± 0.04 | 0.74 ± 0.19 | 0.56 ± 0.02 | 1.07 ± 0.14 | 0.90 ± 0.04 | 0.73 ± 0.03 |
| ΔIW | -2.92 | -2.53 | -2.58 | -3.01 | -2.73 | -2.75 | -3.09 | -2.73 | -2.47 |
| nbo/t | 0.86 | 1.02 | 1.02 | 0.82 | 1.67 | 1.49 | 0.75 | 3.11 | 2.53 |
| Metal and silicate isotopic compositions (‰) | | | | | | | | | |
| $\delta^{122/118}Sn_{silicate}$ | -0.18 ± 0.01 | | -0.38 ± 0.03 | -0.21 ± 0.01 | -0.26 ± 0.01 | 0.06 ± 0.01 | 0.09 ± 0.01 | 0.10 ± 0.02 | 0.12 ± 0.01 |
| $\delta^{122/118}Sn_{metal}$ | 0.26 ± 0.02 | | 0.35 ± 0.06 | 0.18 ± 0.01 | 0.16 ± 0.02 | 0.29 ± 0.03 | 0.20 ± 0.03 | 0.30 ± 0.04 | 0.34 ± 0.04 |
| $\Delta^{122/118}Sn_{met-sil}$ | 0.43 ± 0.02 | | 0.73 ± 0.09 | 0.38 ± 0.02 | 0.43 ± 0.03 | 0.23 ± 0.04 | 0.10 ± 0.04 | 0.21 ± 0.06 | 0.22 ± 0.05 |

Elemental and stable isotopic fractionations of siderophile elements

Table 4.2 (*continued*)

| Experiment | E290 | E291 | E292 | E294 | E295 | E296 |
|-----------------------------------|---------------|-------------------|-------------------|-------------------|-------------------|-------------------|
| Starting material | C | D | B | D | E | E |
| Pressure (GPa) | 2 | 2 | 2 | 2 | 2 | 2 |
| Temperature (K) | 1873 | 2200 | 1950 | 2025 | 2200 | 2293 |
| Duration (min) | 10 | 3 | 10 | 8 | 3 | 2 |
| Pressure media | Talc-pyrex | BaCO ₃ |
| Capsule | BN | BN | BN | BN | BN | BN |
| Silicate composition (oxide wt.%) | | | | | | |
| n | 40 | 30 | 25 | 24 | 19 | 6 |
| SiO ₂ | 49.62 ± 0.47 | 48.67 ± 1.19 | 49.35 ± 0.86 | 48.81 ± 0.54 | 45.34 ± 0.30 | 43.70 ± 0.67 |
| Al ₂ O ₃ | 15.68 ± 0.16 | 14.59 ± 0.42 | 14.69 ± 0.31 | 14.63 ± 0.15 | 5.29 ± 0.10 | 5.49 ± 0.13 |
| CaO | 9.80 ± 0.09 | 11.89 ± 0.28 | 11.99 ± 0.12 | 11.99 ± 0.11 | 4.05 ± 0.03 | 3.96 ± 0.07 |
| MgO | 8.11 ± 0.11 | 8.09 ± 0.26 | 8.26 ± 0.09 | 8.15 ± 0.10 | 34.68 ± 0.29 | 34.64 ± 0.37 |
| FeO | 4.70 ± 0.25 | 5.15 ± 0.19 | 4.37 ± 0.43 | 3.79 ± 0.14 | 3.00 ± 0.15 | 3.12 ± 0.20 |
| B ₂ O ₃ | 3.84 ± 0.25 | 5.56 ± 0.11 | 5.60 ± 0.14 | 3.20 ± 0.16 | 12.99 ± 4.39 | 10.89 ± 1.69 |
| Na ₂ O | 3.19 ± 0.41 | 2.18 ± 0.08 | 2.18 ± 0.06 | 2.18 ± 0.12 | 0.42 ± 0.06 | 0.41 ± 0.04 |
| TiO ₂ | 1.74 ± 0.09 | 0.97 ± 0.08 | 1.03 ± 0.08 | 0.97 ± 0.07 | 0.17 ± 0.03 | 0.17 ± 0.06 |
| K ₂ O | 0.61 ± 0.03 | 0.17 ± 0.01 | 0.17 ± 0.01 | 0.17 ± 0.02 | 0.03 ± 0.01 | 0.04 ± 0.01 |
| P ₂ O ₅ | 0.11 ± 0.03 | 0.15 ± 0.03 | 0.13 ± 0.04 | 0.11 ± 0.04 | 0.03 ± 0.03 | 0.02 ± 0.02 |
| SnO ₂ | 0.06 ± 0.02 | 0.08 ± 0.01 | 0.05 ± 0.01 | 0.06 ± 0.01 | 0.03 ± 0.01 | 0.04 ± 0.01 |
| SO ₂ | 0.08 ± 0.03 | 0.03 ± 0.02 | 0.02 ± 0.02 | 0.02 ± 0.01 | 0.01 ± 0.01 | 0.01 ± 0.01 |
| N ₂ O | 1.05 ± 0.35 | 2.10 ± 0.85 | 0.75 ± 0.52 | 1.55 ± 0.30 | 3.41 ± 0.62 | 3.50 ± 1.08 |
| CuO | | 0.07 ± 0.01 | | 0.04 ± 0.01 | 0.07 ± 0.01 | 0.07 ± 0.01 |
| Total | 98.05 ± 1.59 | 97.91 ± 1.68 | 95.34 ± 2.17 | 96.06 ± 1.43 | 106.53 ± 2.27 | 104.77 ± 1.45 |
| Metal composition (wt.%) | | | | | | |
| n | 15 | 12 | 13 | 16 | 15 | 16 |
| Fe | 70.67 ± 0.15 | 81.00 ± 0.66 | 84.60 ± 0.51 | 81.76 ± 0.48 | 80.10 ± 0.63 | 80.71 ± 0.41 |
| Sn | 10.36 ± 0.14 | 11.71 ± 0.48 | 11.68 ± 0.39 | 10.30 ± 0.51 | 9.18 ± 0.41 | 9.57 ± 0.32 |
| P | 0.14 ± 0.01 | 0.13 ± 0.01 | 0.12 ± 0.01 | 0.13 ± 0.01 | 0.01 ± 0.003 | 0.01 ± 0.002 |
| S | 17.19 ± 0.21 | 0.36 ± 0.07 | 0.32 ± 0.04 | 0.36 ± 0.05 | 0.01 ± 0.002 | 0.01 ± 0.003 |
| Si | 0.02 ± 0.003 | 0.40 ± 0.02 | 0.25 ± 0.02 | 0.38 ± 0.06 | 0.54 ± 0.12 | 0.39 ± 0.13 |
| O | 0.52 ± 0.05 | 0.21 ± 0.02 | 0.14 ± 0.02 | 0.06 ± 0.01 | 0.12 ± 0.02 | 0.08 ± 0.01 |
| Ti | 0.03 ± 0.01 | 0.01 ± 0.002 | 0.01 ± 0.002 | 0.01 ± 0.004 | 0.01 ± 0.002 | 0.01 ± 0.002 |
| Mg | 0.01 ± 0.003 | 0.01 ± 0.003 | 0.01 ± 0.004 | 0.03 ± 0.01 | 0.01 ± 0.003 | 0.01 ± 0.003 |
| Cu | 0.045 ± 0.011 | 4.28 ± 0.21 | 0.05 ± 0.01 | 2.29 ± 0.09 | 4.02 ± 0.20 | 3.55 ± 0.08 |
| Total | 98.95 ± 0.11 | 98.11 ± 0.10 | 97.17 ± 0.17 | 96.17 ± 0.58 | 93.98 ± 0.12 | 94.30 ± 0.11 |
| D_{Sn} | 183 ± 56 | 192 ± 26 | 299 ± 39 | 215 ± 33 | 470 ± 80 | 414 ± 73 |
| $\log K_d^{Sn}$ | 0.99 ± 0.13 | 0.92 ± 0.06 | 1.04 ± 0.07 | 0.84 ± 0.07 | 0.98 ± 0.11 | 0.93 ± 0.08 |
| ΔIW | -2.54 | -2.72 | -2.86 | -2.99 | -3.38 | -3.38 |
| nbo/t | 0.85 | 0.98 | 0.85 | 0.93 | 3.16 | 3.53 |

CHAPTER 4. Tracing Earth's volatile delivery with Sn

Table 4.2 (*continued*)

| Experiment | E317 | E342 | E345 | H4735 | H4950 | H4951 | H4952 | E396 | E397 |
|-----------------------------------|--------------|---------------|-------------------|------------------------------------|------------------------------------|------------------------------------|------------------------------------|---------------|---------------|
| Starting material | F | F | F | G | F | F | G | G | G |
| Pressure (GPa) | 2 | 2 | 2 | 10 | 12 | 14 | 12 | 2 | 2 |
| Temperature (K) | 1873 | 1773 | 2273 | 2273 | 2273 | 2373 | 2373 | 1873 | 1773 |
| Duration (min) | 5 | 15 | 1 | 5 | 5 | 2 | 2 | 5 | 15 |
| Pressure media | Talc-pyrex | Talc-pyrex | BaCO ₃ | MgO+Cr ₂ O ₃ | Talc-pyrex | Talc-pyrex |
| Capsule | MgO | MgO | MgO | MgO SC | MgO SC | MgO SC | MgO SC | MgO | MgO |
| Silicate composition (oxide wt.%) | | | | | | | | | |
| n | 21 | 18 | 25 | 30 | 13 | 14 | 10 | 13 | 29 |
| SiO ₂ | 40.05 ± 0.46 | 41.14 ± 0.26 | 30.15 ± 0.51 | 37.66 ± 0.20 | 38.57 ± 0.16 | 37.99 ± 0.32 | 36.54 ± 0.54 | 41.44 ± 1.43 | 39.79 ± 0.19 |
| Al ₂ O ₃ | 10.66 ± 1.12 | 10.00 ± 1.23 | 8.26 ± 0.15 | 9.24 ± 0.15 | 9.10 ± 0.25 | 10.16 ± 0.17 | 8.27 ± 0.13 | 10.06 ± 0.76 | 12.56 ± 0.31 |
| CaO | 8.54 ± 0.96 | 7.94 ± 1.05 | 7.60 ± 0.15 | 8.60 ± 0.18 | 9.22 ± 0.19 | 9.26 ± 0.23 | 8.66 ± 0.28 | 7.65 ± 0.70 | 10.15 ± 0.31 |
| MgO | 29.35 ± 2.56 | 27.88 ± 2.97 | 28.59 ± 0.84 | 34.31 ± 0.31 | 35.71 ± 0.36 | 34.74 ± 0.42 | 37.06 ± 0.60 | 24.58 ± 1.02 | 20.12 ± 0.75 |
| FeO | 8.26 ± 0.25 | 10.11 ± 0.12 | 11.66 ± 0.24 | 7.09 ± 0.10 | 5.67 ± 0.13 | 5.95 ± 0.09 | 7.41 ± 0.09 | 10.64 ± 0.86 | 13.39 ± 0.10 |
| Na ₂ O | 1.85 ± 0.22 | 1.53 ± 0.21 | 1.15 ± 0.03 | 0.78 ± 0.02 | 1.18 ± 0.05 | 1.22 ± 0.04 | 1.01 ± 0.04 | 2.06 ± 0.13 | 1.99 ± 0.05 |
| TiO ₂ | 0.71 ± 0.08 | 0.68 ± 0.09 | 0.46 ± 0.01 | 0.72 ± 0.03 | 0.70 ± 0.03 | 0.73 ± 0.03 | 0.71 ± 0.03 | 0.69 ± 0.07 | 0.88 ± 0.03 |
| K ₂ O | 0.20 ± 0.02 | 0.15 ± 0.02 | 0.15 ± 0.003 | 0.16 ± 0.01 | 0.13 ± 0.01 | 0.14 ± 0.01 | 0.09 ± 0.01 | 0.20 ± 0.02 | 0.17 ± 0.003 |
| P ₂ O ₅ | 0.01 ± 0.001 | 0.02 ± 0.002 | 0.06 ± 0.003 | 0.06 ± 0.003 | 0.01 ± 0.000 | 0.01 ± 0.001 | 0.07 ± 0.003 | 0.07 ± 0.006 | 0.09 ± 0.001 |
| SO ₂ | 0.01 ± 0.001 | 0.01 ± 0.001 | 0.05 ± 0.003 | 0.12 ± 0.01 | 0.008 ± 0.001 | 0.01 ± 0.001 | 0.55 ± 0.04 | 0.18 ± 0.02 | 0.24 ± 0.01 |
| SnO | | | | | | | | 0.07 ± 0.006 | 0.08 ± 0.003 |
| Total | 99.99 ± 0.31 | 99.74 ± 0.28 | 88.61 ± 0.51 | 99.30 ± 0.17 | 100.89 ± 0.12 | 100.76 ± 0.13 | 101.30 ± 0.26 | 98.18 ± 0.36 | 100.08 ± 0.50 |
| Sn (ppm) | 268 ± 80 | 300 ± 136 | 1146 ± 226 | 1008 ± 100 | 222 ± 19 | 188 ± 26 | 2106 ± 146 | | |
| Metal composition (wt.%) | | | | | | | | | |
| n | 23 | 31 | 27 | 29 | 22 | 23 | 21 | 31 | 33 |
| Fe | 31 | 27 | 25 | 28 | 14 | 11 | 15 | 12 | 14 |
| Fe | 87.58 ± 0.26 | 86.76 ± 0.64 | 89.51 ± 0.16 | 64.91 ± 0.35 | 80.66 ± 0.61 | 80.73 ± 0.72 | 60.63 ± 0.60 | 62.80 ± 1.26 | 63.33 ± 0.55 |
| Sn | 3.82 ± 0.05 | 3.86 ± 0.03 | 3.43 ± 0.06 | 5.29 ± 0.06 | 5.08 ± 0.11 | 4.55 ± 0.05 | 5.21 ± 0.07 | 5.33 ± 0.21 | 5.20 ± 0.13 |
| P | 0.08 ± 0.004 | 0.09 ± 0.004 | 0.001 ± 0.000 | 0.01 ± 0.001 | 0.09 ± 0.004 | 0.11 ± 0.004 | 0.010 ± 0.002 | 0.02 ± 0.004 | 0.02 ± 0.002 |
| S | 0.24 ± 0.01 | 0.24 ± 0.01 | 0.10 ± 0.01 | 16.15 ± 0.14 | 0.26 ± 0.01 | 0.29 ± 0.02 | 19.98 ± 0.26 | 10.31 ± 0.40 | 11.08 ± 0.23 |
| Si | 0.02 ± 0.002 | 0.01 ± 0.002 | 0.01 ± 0.001 | 0.01 ± 0.002 | 0.04 ± 0.01 | 0.02 ± 0.004 | 0.02 ± 0.001 | 0.01 ± 0.004 | 0.03 ± 0.03 |
| O | 0.01 ± 0.01 | 0.16 ± 0.04 | N.D. | 1.32 ± 0.13 | 0.19 ± 0.03 | 0.17 ± 0.05 | 1.41 ± 0.27 | 0.42 ± 0.07 | 0.55 ± 0.05 |
| Ti | N.D. | 0.004 ± 0.001 | 0.003 ± 0.001 | N.D. | 0.008 ± 0.002 | N.D. | N.D. | 0.002 ± 0.001 | 0.003 ± 0.001 |
| Mg | 0.14 ± 0.002 | 0.14 ± 0.002 | 0.15 ± 0.004 | 0.10 ± 0.00 | 0.13 ± 0.004 | 0.13 ± 0.004 | 0.08 ± 0.001 | 0.09 ± 0.007 | 0.09 ± 0.006 |
| Total | 98.74 ± 0.22 | 99.10 ± 0.55 | 97.71 ± 0.15 | 98.25 ± 0.26 | 98.08 ± 0.50 | 98.24 ± 0.66 | 97.26 ± 0.18 | 92.68 ± 0.49 | 94.06 ± 0.17 |
| D_{Sn} | 159 ± 47 | 147 ± 67 | 30 ± 6 | 53 ± 5 | 279 ± 24 | 292 ± 41 | 25 ± 2 | 98 ± 10 | 83 ± 4 |
| $\log K_d^{Sn}$ | 1.01 ± 0.13 | 1.07 ± 0.20 | 0.48 ± 0.09 | 0.64 ± 0.04 | 1.09 ± 0.04 | 1.14 ± 0.06 | 0.37 ± 0.03 | 1.06 ± 0.06 | 1.09 ± 0.02 |
| ΔIW | -2.39 | -2.19 | -2.01 | -2.17 | -2.71 | -2.66 | -2.07 | -1.87 | -1.65 |
| nbo/t | 2.88 | 2.76 | 3.64 | 3.24 | 3.27 | 3.23 | 3.60 | 2.63 | 2.60 |

Elemental and stable isotopic fractionations of siderophile elements

Table 4.2 (*continued*)

| Experiment | Z1820 | Z1821 | Z1823 | Z1824 | Z1825 | Z1956 | Z1957 | Z1959 |
|-----------------------------------|------------------------------------|------------------------------------|------------------------------------|------------------------------------|------------------------------------|------------------------------------|------------------------------------|------------------------------------|
| Starting material | G | F | F | F | G | F | G | F |
| Pressure (GPa) | 7 | 7 | 14 | 18 | 18 | 20 | 20 | 16 |
| Temperature (K) | 1979 | 2023 | 2573 | 2473 | 2473 | 2573 | 2573 | 2473 |
| Duration (min) | 10 | 1 | 1 | 4 | 4 | 1 | 1 | 1 |
| Pressure media | MgO+Cr ₂ O ₃ |
| Capsule | MgO SC |
| Silicate composition (oxide wt.%) | | | | | | | | |
| n | 13 | 19 | 13 | 9 | 22 | 15 | 13 | 15 |
| SiO ₂ | 35.29 ± 0.90 | 48.54 ± 1.04 | 39.39 ± 0.55 | 44.82 ± 0.35 | 39.16 ± 0.16 | 39.45 ± 0.68 | 39.90 ± 0.34 | 37.78 ± 0.43 |
| Al ₂ O ₃ | 9.72 ± 1.25 | 12.07 ± 0.58 | 9.09 ± 0.29 | 14.12 ± 0.95 | 8.83 ± 0.14 | 9.32 ± 0.07 | 8.93 ± 0.07 | 9.73 ± 0.11 |
| CaO | 6.96 ± 0.99 | 12.33 ± 0.41 | 9.10 ± 0.45 | 10.32 ± 0.07 | 9.69 ± 0.10 | 9.36 ± 0.26 | 9.48 ± 0.21 | 8.98 ± 0.24 |
| MgO | 35.89 ± 1.86 | 15.35 ± 0.30 | 35.61 ± 0.91 | 23.44 ± 0.37 | 30.42 ± 0.18 | 33.36 ± 0.97 | 31.53 ± 0.51 | 36.88 ± 0.68 |
| FeO | 9.98 ± 0.26 | 8.45 ± 0.54 | 5.99 ± 0.12 | 4.86 ± 0.45 | 7.79 ± 0.07 | 6.15 ± 0.14 | 6.52 ± 0.11 | 5.93 ± 0.12 |
| Na ₂ O | 0.69 ± 0.11 | 1.75 ± 0.14 | 1.16 ± 0.04 | 1.00 ± 0.16 | 1.06 ± 0.03 | 1.34 ± 0.03 | 1.26 ± 0.03 | 1.11 ± 0.03 |
| TiO ₂ | 0.70 ± 0.10 | 0.78 ± 0.08 | 0.68 ± 0.04 | 0.77 ± 0.07 | 0.82 ± 0.03 | 0.72 ± 0.02 | 0.67 ± 0.04 | 0.73 ± 0.02 |
| K ₂ O | 0.22 ± 0.03 | 0.10 ± 0.02 | 0.14 ± 0.01 | 0.11 ± 0.02 | 0.14 ± 0.01 | 0.15 ± 0.01 | 0.12 ± 0.005 | 0.12 ± 0.01 |
| P ₂ O ₅ | 0.08 ± 0.01 | 0.02 ± 0.005 | 0.01 ± 0.000 | 0.01 ± 0.001 | 0.09 ± 0.02 | 0.01 ± 0.000 | 0.04 ± 0.002 | 0.01 ± 0.000 |
| SO ₂ | 0.16 ± 0.02 | 0.005 ± 0.001 | 0.006 ± 0.001 | 0.002 ± 0.001 | 0.11 ± 0.01 | 0.01 ± 0.001 | 0.27 ± 0.01 | 0.008 ± 0.001 |
| Total | 100.10 ± 0.60 | 100.03 ± 0.98 | 101.73 ± 0.21 | 100.22 ± 0.21 | 99.99 ± 0.26 | 100.56 ± 0.18 | 99.99 ± 0.16 | 101.88 ± 0.11 |
| Sn (ppm) | 1385 ± 65 | 368 ± 151 | 272 ± 8 | 208 ± 20 | 2497 ± 258 | 259 ± 72 | 2407 ± 415 | 250 ± 34 |
| Metal composition (wt.%) | | | | | | | | |
| n | 10 | 18 | 39 | 33 | 43 | 19 | 16 | 9 |
| Fe | 59.99 ± 1.32 | 87.00 ± 0.60 | 78.02 ± 0.50 | 78.77 ± 0.35 | 63.29 ± 0.35 | 78.26 ± 0.82 | 62.90 ± 0.82 | 76.38 ± 5.09 |
| Sn | 4.65 ± 0.26 | 4.80 ± 0.11 | 5.58 ± 0.09 | 4.92 ± 0.05 | 6.35 ± 0.19 | 4.19 ± 0.31 | 6.60 ± 0.23 | 4.24 ± 0.36 |
| P | 0.001 ± 0.000 | 0.17 ± 0.04 | 0.08 ± 0.005 | 0.06 ± 0.005 | 0.01 ± 0.001 | 0.09 ± 0.01 | 0.03 ± 0.01 | 0.06 ± 0.01 |
| S | 17.90 ± 0.44 | 0.32 ± 0.05 | 0.31 ± 0.01 | 0.23 ± 0.006 | 15.91 ± 0.22 | 0.30 ± 0.02 | 16.73 ± 0.69 | 0.23 ± 0.02 |
| Si | 0.03 ± 0.001 | N.D. | 0.05 ± 0.01 | 0.04 ± 0.005 | 0.04 ± 0.01 | 0.23 ± 0.06 | 0.01 ± 0.01 | 0.04 ± 0.006 |
| O | 1.97 ± 0.18 | 0.19 ± 0.06 | 1.25 ± 0.14 | 0.99 ± 0.13 | 1.55 ± 0.11 | 0.36 ± 0.07 | 1.17 ± 0.35 | 0.38 ± 0.10 |
| Ti | N.D. | N.D. | N.D. | N.D. | N.D. | 0.003 ± 0.001 | N.D. | N.D. |
| Mg | 0.09 ± 0.003 | 0.23 ± 0.06 | 0.18 ± 0.03 | 0.13 ± 0.01 | 0.11 ± 0.02 | 0.12 ± 0.004 | 0.41 ± 0.33 | 0.12 ± 0.01 |
| Total | 98.17 ± 0.13 | 99.99 ± 0.68 | 98.15 ± 0.28 | 98.03 ± 0.13 | 98.07 ± 0.18 | 98.48 ± 0.32 | 96.85 ± 0.33 | 98.55 ± 0.43 |
| D_{Sn} | 34 ± 3 | 142 ± 58 | 247 ± 9 | 268 ± 25 | 26 ± 3 | 197 ± 56 | 28 ± 5 | 214 ± 34 |
| $\log K_d^{Sn}$ | 0.64 ± 0.04 | 1.00 ± 0.18 | 1.09 ± 0.02 | 1.05 ± 0.06 | 0.38 ± 0.05 | 0.99 ± 0.13 | 0.34 ± 0.08 | 1.01 ± 0.08 |
| ΔIW | -1.80 | -2.30 | -2.61 | -2.76 | -2.06 | -2.61 | -2.22 | -2.65 |
| nbo/t | 3.51 | 1.94 | 3.22 | 2.24 | 3.07 | 3.11 | 3.03 | 3.37 |

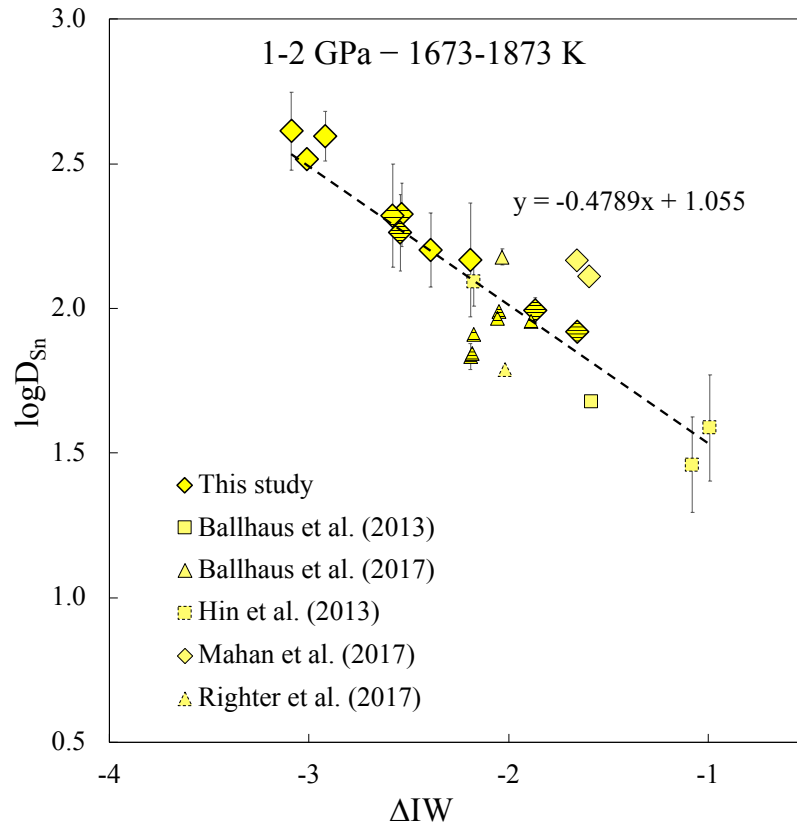


Figure 4.2 – Partition coefficient $\log D_{\text{Sn}}$ as a function of oxygen fugacity ΔIW calculated relatively to iron-wüstite (equation 4.1) for all experiments between 1 and 2 GPa and 1673–1873 K of this study and data compiled from the literature (Ballhaus et al. 2017, 2013, Hin et al. 2013, Mahan et al. 2017, Righter et al. 2017b). Errors correspond to 1 standard deviation (σ) and were propagated from EPMA and LA-ICPMS measurements of this study and from the literature. The variation in partition coefficient over a significant interval of fO_2 allows accurate determination of the valence state of Sn. In fact, it can be demonstrated that $\log D_{\text{Sn}}$ is a function of $n/4 \log fO_2$ (Siebert et al. 2011). With the slope of the regression line shown on this figure equal to 0.5, we demonstrate that Sn has a valence of 2+ over a range of more than 2 fO_2 log units. Experiments containing more than 1 mol% of S in the metal part are represented with a horizontal lines pattern. They were included in this figure because in this study we find that S has no effect on Sn partitioning at 1–2 GPa.

partitioning for groups of experiments that share similar conditions. Furthermore,

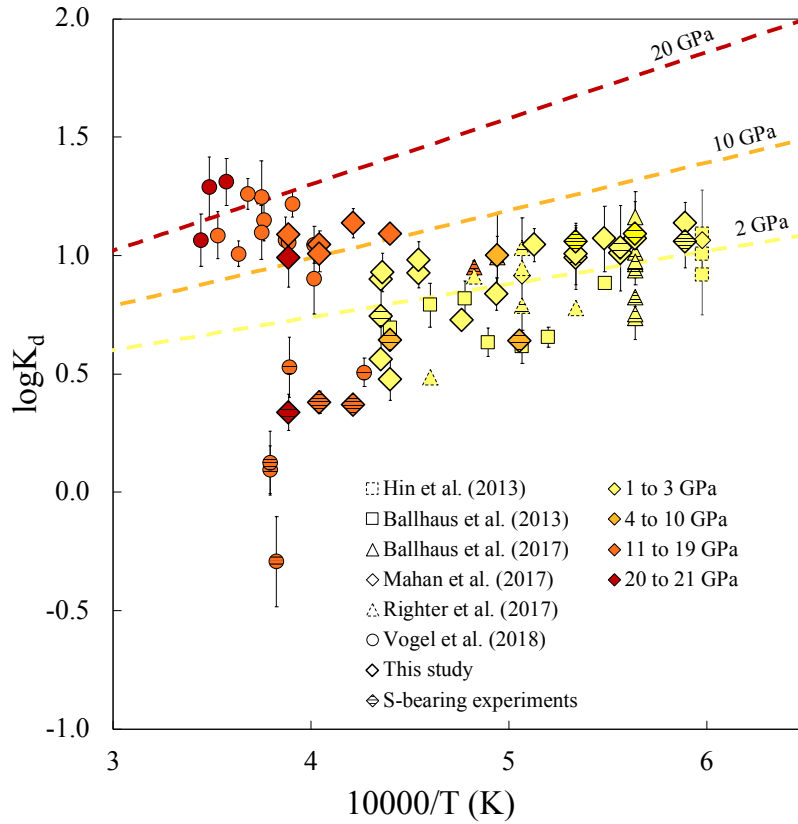


Figure 4.3 – Exchange coefficient $\log K_d^{Sn}$ plotted as a function of reciprocal temperature for all experiments of this study and data compiled from the literature (Ballhaus et al. 2017, 2013, Hin et al. 2013, Mahan et al. 2017, Righter et al. 2017b, Vogel et al. 2018). Errors correspond to 1 standard deviation (σ) and were propagated from EPMA and LA-ICPMS measurements of this study and from the literature. Experiments containing more than 1 mol% of S in the metal part are represented with a horizontal lines pattern. All experiments are color-coded according to their pressure: 1–3 GPa in yellow, 4–10 GPa in orange, 10–19 GPa in light red, >19 GPa in dark red. Multilinear regression fits are also displayed at IW-2 in several conditions: 2 GPa, 10 GPa, and 20 GPa with no S in the metal. Sn partitioning is affected by temperature, Sn becoming less siderophile as the temperature increases. Pressure has a positive and strong effect on the partition coefficient. Sulfur also presents a notable effect on $\log K_d^{Sn}$ which tends to lower the partitioning as the S content of the metal phase increases above 4 GPa.

it is demonstrated that elements with low valence states are very little affected by the structure and composition of the melt (Siebert et al. 2011). For Sn, having

a valence state of 2+ and showing no difference in partitioning for the different silicate compositions tested, the effect of the silicate composition is not further investigated in this study and is considered negligible. The $\log K$ is simplified as follows:

$$\log K = \log \frac{x_{\text{FeO}}^{\text{silicate}} \cdot x_{\text{Sn}}^{\text{metal}}}{x_{\text{SnO}}^{\text{silicate}} \cdot x_{\text{Fe}}^{\text{metal}}} + \log \frac{\gamma_{\text{Sn}}^{\text{metal}}}{\gamma_{\text{Fe}}^{\text{metal}}} \quad (4.6)$$

$$\log K = \log K_d^{\text{Sn}} + \log \frac{\gamma_{\text{Sn}}^{\text{metal}}}{\gamma_{\text{Fe}}^{\text{metal}}} \quad (4.7)$$

The equilibrium constant $\log K_d^{\text{Sn}}$ is used to compare the partitioning of different experiments with different oxygen fugacities. The $\log K_d^{\text{Sn}}$ is equal to the partition coefficient of Sn divided by that of Fe, allowing to normalise the partitioning with $f\text{O}_2$:

$$\log K_d^{\text{Sn}} = \log \frac{x_{\text{FeO}}^{\text{silicate}} \cdot x_{\text{Sn}}^{\text{metal}}}{x_{\text{SnO}}^{\text{silicate}} \cdot x_{\text{Fe}}^{\text{metal}}} = \log \frac{D_{\text{Sn}}}{D_{\text{Fe}}} \quad (4.8)$$

The partitioning represented by the exchange coefficient $\log K_d^{\text{Sn}}$ is displayed in figure 4.3 as a function of reciprocal temperature. The $\log K_d^{\text{Sn}}$ varies from 0.41 to 1.40 in this study. No difference in $\log K_d^{\text{Sn}}$ was detected between the BN encapsulated experiments and those in MgO for similar pressure and temperature conditions. The group of experiments from 1 to 3 GPa, represented in yellow, contains experiments doped with 2 and 8 *wt.*% of Sn and three experiments from Mahan et al. (2017) are doped with 16 *wt.*% Sn, which appears not to affect the Sn partitioning. This group of low pressure experiments shows a slight dependence of the partitioning to temperature, which results in Sn behaving less siderophile at higher temperatures. The higher pressure experiments present enhanced Sn siderophility, which indicates a marked effect of pressure on Sn partitioning. Amongst the low pressure experiments (1 to 3 GPa), no difference in Sn partitioning is observed between S-bearing experiments and experiments from which the metal is devoid of S. On the other hand, experiments from 4 to 21 GPa display a strong decrease of Sn partitioning in S-bearing experiments compared to experiments of similar pressures which are devoid of S in their metal. The presence of a significant amount of S in the metal makes Sn less siderophile above 4 GPa.

Isotopic compositions

All isotopic data collected via MC-ICPMS analysis are presented in table 4.2. Results are expressed using the delta notation as $\delta^{122/118}\text{Sn}$ which represents the difference in per mil of the $^{122}\text{Sn}/^{118}\text{Sn}$ ratio of the sample relative to the standard Sn_IPGP. In the silicate phases of the experiments, $\delta^{122/118}\text{Sn}$ Sn ranges from -0.38 to 0.12, and from 0.16 to 0.35 in the metal fraction. Metal is found to be enriched in Sn heavier isotopes in all experiments. The bulk $\delta^{122/118}\text{Sn}$ of each experiment is calculated and found to be on average 0.25 ± 0.07 (1sd).

Metal–silicate Sn isotopic fractionation

The isotopic fractionation factor is calculated for each experiment as follows:

$$\Delta^{122/118}\text{Sn}_{\text{metal-silicate}} = \delta^{122/118}\text{Sn}_{\text{metal}} - \delta^{122/118}\text{Sn}_{\text{silicate}} \quad (4.9)$$

Tin isotopic fractionation factors $\Delta^{122/118}\text{Sn}_{\text{metal-silicate}}$ are positive for all experiments and range from 0.10 to 0.73.

Discussion

Equilibrium conditions

Elemental and isotopic equilibrium between metal and silicate is crucial for accurate characterisation of Sn’s behaviour in such conditions. Petrographic observation of the experiment run products of this study show no compositional zoning in either metal or silicate (figure 4.1). The time duration of experiments was chosen according to the temperature of the run and in agreement with previous studies (Corgne et al. 2008, Mahan et al. 2017, Siebert et al. 2011) that report time series experiments at superliquidus conditions and evince equilibrium achievement after few tens of seconds.

Tin metal–silicate partitioning and Earth accretion

Thermodynamic parameterisation

The thermodynamic formalism shown above (equation 4.6) can be restructured as follows:

$$\log K_d = a + b \cdot \frac{1}{T} + c \cdot \frac{P}{T} - \log \frac{\gamma_{\text{Sn}}^{\text{metal}}}{\gamma_{\text{Fe}}^{\text{metal}}} \quad (4.10)$$

K_d values were calculated using electron microprobe and LA-ICPMS measurements for each experiments. The values of a , b and c were computed using the least-squares multivariate linear regression using results from experiments with no S in the metal from this study and from previous studies (Ballhaus et al. 2017, 2013, Hin et al. 2013, Mahan et al. 2017, Righter et al. 2017b, Vogel et al. 2018):

$$\log K_{\text{Sn}} = 0.18 \pm 0.20 + 1236 \pm 363 \cdot \frac{1}{T} + 77.9 \pm 13 \cdot \frac{P}{T} \quad (4.11)$$

The regression lines shown in figure 4.3 were computed using the calculated regression parameters. S-bearing experiments were used to calculate the interaction parameter:

$$\log K - \log K_d = \log \frac{\gamma_{\text{Sn}}^{\text{metal}}}{\gamma_{\text{Fe}}^{\text{metal}}} \quad (4.12)$$

The activity coefficients $\gamma_{\text{Sn}}^{metal}$ and $\gamma_{\text{Fe}}^{metal}$ were computed using the interaction parameter approach developed by Ma (2001):

$$\log K_d = \log \frac{D_{\text{Sn}}}{D_{\text{Fe}}} = a + b \cdot \frac{1}{T} + c \cdot \frac{P}{T} - \log \gamma_{\text{Sn}}^0 + \varepsilon_{\text{Sn}}^{\text{Sn}} \cdot \log(1 - x_{\text{Sn}}) + \varepsilon_{\text{Sn}}^{\text{S}} \cdot \log(1 - x_{\text{S}}) \quad (4.13)$$

where $\varepsilon_{\text{Sn}}^i$ represents interaction parameters and γ_{Sn}^0 the activity coefficient of Sn. $\varepsilon_{\text{Sn}}^{\text{S}}$ is the interaction parameter representing the effect of the presence of S on Sn activity. $\varepsilon_{\text{Sn}}^{\text{S}}$ is a function of pressure, temperature, S and Sn concentrations. $\varepsilon_{\text{Sn}}^{\text{Sn}}$ and γ_{Sn}^0 are equal to -0.29 and 0.95 respectively at 1873 K (J.S.P.S. 1988). $\varepsilon_{\text{Sn}}^{\text{S}}$ was fitted to the experimental dataset and found to be equal to 5.8 ± 0.38 . Values of $\log K$ for all experiments of the dataset are shown in figure 4.4. This expression of Sn metal–silicate partitioning only displays the effect of pressure and temperature. S-bearing experiments show similar partitioning to experiments that are devoid of this element.

Core formation models

Core formation models are used in order to recalculate the partition coefficient of an element at each incremental step of Earth’s accretion (Rubie et al. 2015, Rudge et al. 2010, Wade and Wood 2005). The final coefficient obtained can then be compared to the observed partition coefficient determined for the Earth. This method allows to test multiple accretion scenarios and assess whether those scenarios can realistically explain the observed concentration of an element in the Earth’s mantle.

In this study, the experimentally calculated regression parameters were used to model the evolution of Sn partitioning during several scenarios of Earth’s accretion using the following equation:

$$\log D_{\text{Sn}} = a + b \cdot \frac{1}{T} + c \cdot \frac{P}{T} + \varepsilon_{\text{Sn}}^{\text{S}0} \cdot \frac{1873}{T} \cdot \log(1 - x_{\text{S}}) - \log \frac{x_{\text{FeO}}}{x_{\text{Fe}}} \quad (4.14)$$

$\varepsilon_{\text{Sn}}^{\text{Sn}}$ and γ_{Sn}^0 found in equation 4.13 simplify here because Sn is very dilute in the materials considered in our models. In those models, the differentiation is occurring in a continuous way over Earth’s accretion (Wade and Wood 2005). The pressure and temperature conditions, which are those of the base of a deep magma ocean

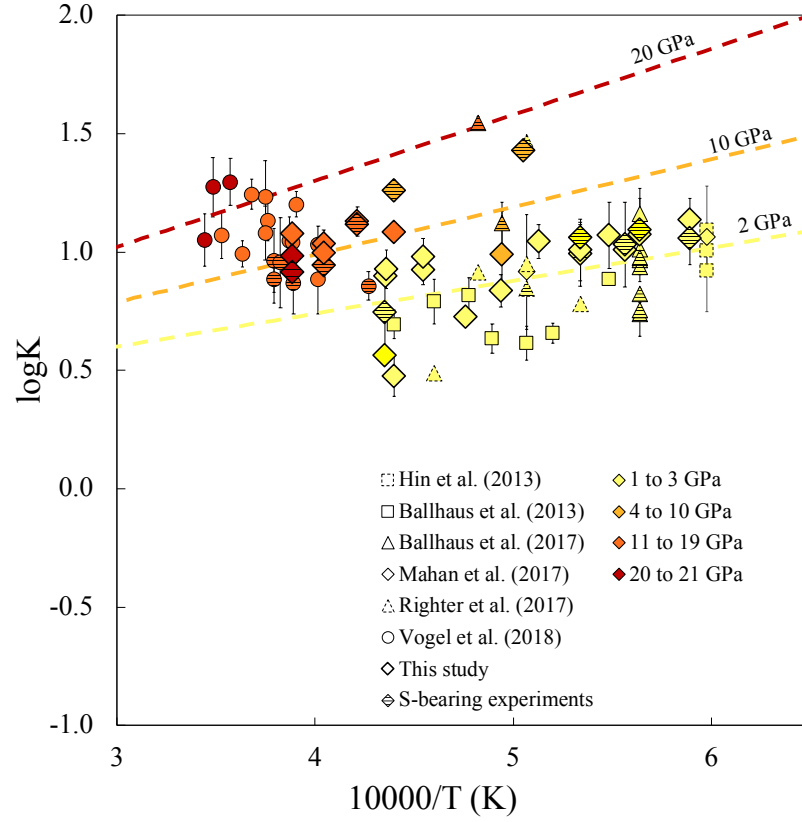


Figure 4.4 – $\log K$ determined experimentally as a function of reciprocal temperature for all experiments of this study and data compiled from the literature (Ballhaus et al. 2017, 2013, Hin et al. 2013, Mahan et al. 2017, Richter et al. 2017b, Vogel et al. 2018). Errors correspond to 1 standard deviation σ and were propagated from EPMA and LA-ICPMS measurements of this study and from the literature. Experiments containing more than 1 mol% of S in the metal are represented with a horizontal lines pattern. All experiments are color-coded according to their pressure: 1–3 GPa in yellow, 4–10 GPa in orange, 11–19 GPa in light red, >19 GPa in dark red. Multilinear regression fits are also displayed at IW-2 in several conditions: 2 GPa, 10 GPa, and 20 GPa with no S in the metal. $\log K$ being defined as $a + b \cdot \frac{1}{T} + c \cdot \frac{P}{T}$, this figure displays the effect of pressure and temperature alone on Sn partitioning between metal and silicate.

are then evolving over the course of the accretion (see supplementary information). Several degrees of equilibration between core and mantle were tested. The parameter k represents the fraction of the core of the accreted embryo that equilibrates

with the mantle of the proto-Earth. A full equilibration is modeled with k equal to 1, and lowering k allows to model a partial equilibration. The formalism proposed by Deguen et al. (2014) was used to model the efficiency of the equilibration with more precision with parameter ε which represents the equilibration efficiency based on k , and other considerations such as the mass of silicate that is dragged towards the core along with the metal when metal segregation occurs, preventing full equilibration. All full equilibration models presented here use $k = 1$ and all partial equilibration models use an ε with $k = 0.5$. Results of homogeneous core formation models are presented in figure 4.5a. The model computed in the case of partial equilibration shows a lower final partitioning coefficient than the one with full equilibration but none of the two models can be reconciled with the Sn partitioning coefficient of Earth, which is estimated as 8.5 ± 5 (see supplementary information) based on the apparent depletion of Sn relative to the canonical volatility curve (Lodders 2003, Palme and O'Neill 2014).

A heterogeneous accretion scenario was also considered in order to investigate the effect on Sn partitioning of a delivery of all the volatiles in the later part of the main phases of Earth's accretion as proposed in previous studies (Braukmüller et al. 2019, Suer et al. 2017) (figure 4.5b). The computation of the delivery of Earth's volatile elements, including Sn and S in the last 10 to 20% of accretion generated a final Sn partitioning that is significantly lower than in the homogeneous accretion scenario, mainly due to the effect of a higher concentration of S which makes Sn less siderophile, combined with a partial equilibration of the impactors' cores with the Earth's mantle. With a scenario of volatile delivery in the last 20% of accretion, the final D_{Sn} is still an order of magnitude higher than the observed partitioning. When the volatile budget of the Earth was concentrated in the last 10% of accretion, lower partition coefficients were obtained (56 ± 14 with full equilibration and 42 ± 11 in the case of partial equilibration). The reason for this is that most of the S and Sn budget of the Earth are concentrated in one last embryo in the model which therefore has a high S core content which helps to put a lot of Sn in the mantle of this embryo. When accreted, this 10 *wt.%* embryo's mantle merges with the Earth's mantle, lowering the final D_{Sn} of the planet. Since the S content in the core of the Earth was found to have such a large influence on Sn partitioning in the Earth, this parameter was varied in figure 4.6 from 1.8 *wt.%*—which is the value proposed in literature from cosmochemical estimates (McDonough 2003)—to 4 *wt.%*, computed with a volatile delivery in the last 10% of the accretion using

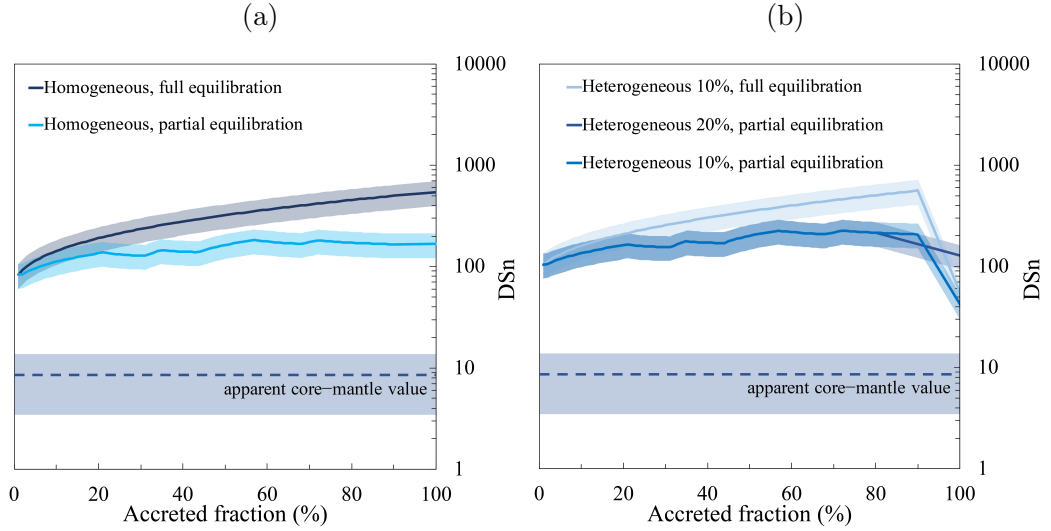


Figure 4.5 – Evolution of D_{Sn} during Earth’s accretion computed from core formation models with full and partial equilibration and 1.8 *wt.*% S in the core of the final Earth. **a.** Tin partitioning with continuous and homogeneous core formation models with full and partial equilibration. For partial equilibration, ε was computed with $k = 0.5$. The final D_{Sn} displayed for Earth are respectively 544 ± 145 and 167 ± 45 . The use of an ε is lowering significantly the partitioning of Sn, but the final values are too high to be compared to the observed Sn partitioning on Earth (8.56 ± 5.07), shown as a dotted line on the figure. **b.** Tin partitioning as a function of the percentage of accreted Earth computed from continuous heterogeneous core formation models in which all the Sn and S were brought in the last 20% or in the last 10% of Earth’s accretion in order to simulate a late accretion stage. The obtained final D_{Sn} are lower than in the scenario presented in a.: 128 ± 34 for the dark blue curve which represents a 20% late accretion stage with partial equilibration, 55 ± 15 for the light blue curve corresponding to a 10% late accretion stage with full equilibration, and 42 ± 11 for the blue curve which shows a 10% late accretion stage with partial equilibration, using an ε with $k = 0.5$. The partitioning is still distinct from the observed value shown in dotted line (8.56 ± 5.07). In those models we used a succession of planetesimals of different sizes to be accreted at each steps: 0.1, 1, 10 and 20 *wt.*% of the Earth’s total mass. In calculations considering a partial equilibration, the partition coefficients are sensitive to the size of the accreted embryos which is why we observe variations on the curve at stages where there is a change of the size of accreted bodies.

an equilibration efficiency parameter ε with $k = 0.5$. We find that with 2.5–3.5 wt.% of S in the core, the observed Sn partitioning coefficient for this accretion scenario matches the observed value (figure 4.6). Although there is no consensus on the exact S content of the core, the 2.5–3.5% found in this study are in good agreement within error with cosmochemical estimates (McDonough 2003), recent partitioning studies at comparable P and T conditions (Mahan et al. 2018b, Suer et al. 2017), and mineral physics studies (Badro et al. 2014, Morard et al. 2013). Other light elements are thought to present significant abundances in the Earth’s core such as O, C and Si (e.g. Allègre et al. 1995, Ringwood 1977) and could have an effect on Sn partitioning. The effect of Si is not included in our parameterisation for the reasons mentioned above, but it should be noted that the interaction parameter predicted by Righter et al. (2019) would influence the parameterisation and further models and conclusions of this study.

Tin metal–silicate isotopic fractionation

Mass-dependent equilibrium fractionation of isotopes decreases as a function of the reciprocal square of temperature (Urey 1947):

$$\Delta^{122/118}\text{Sn}_{\text{metal-silicate}} = a \cdot \frac{1}{T^2} \quad (4.15)$$

Using the dataset of this study displayed on figure 4.7, parameter a is found to be equal to $1.18 \cdot 10^6 \pm 0.05 \cdot 10^6 K^{-2}$. S-bearing experiments show higher Sn isotopic fractionation than the rest of the dataset and are therefore excluded for parameterisation considering their unrealistic S content compared to natural systems. More S-bearing experiments are needed to properly parameterise this effect. No difference in isotopic fractionation is detected between experiments performed in BN capsules and those in MgO capsules. A significant Sn metal–silicate isotopic fractionation was measured from the experimental dataset of this study. This result seems to be in disagreement with the rather small difference in between the β -factors of pure α -Sn and SnO-bearing silicates reported from recent nuclear resonant inelastic X-ray scattering (NRIXS) measurements (Roskosz et al. 2020). This argues against a measurable Sn isotopic fractionation during core formation. However, such conclusions were reached on samples that are not geochemically relevant (i.e. quenched glasses, pure Sn solid metal) at room pressure and further NRIXS measurements

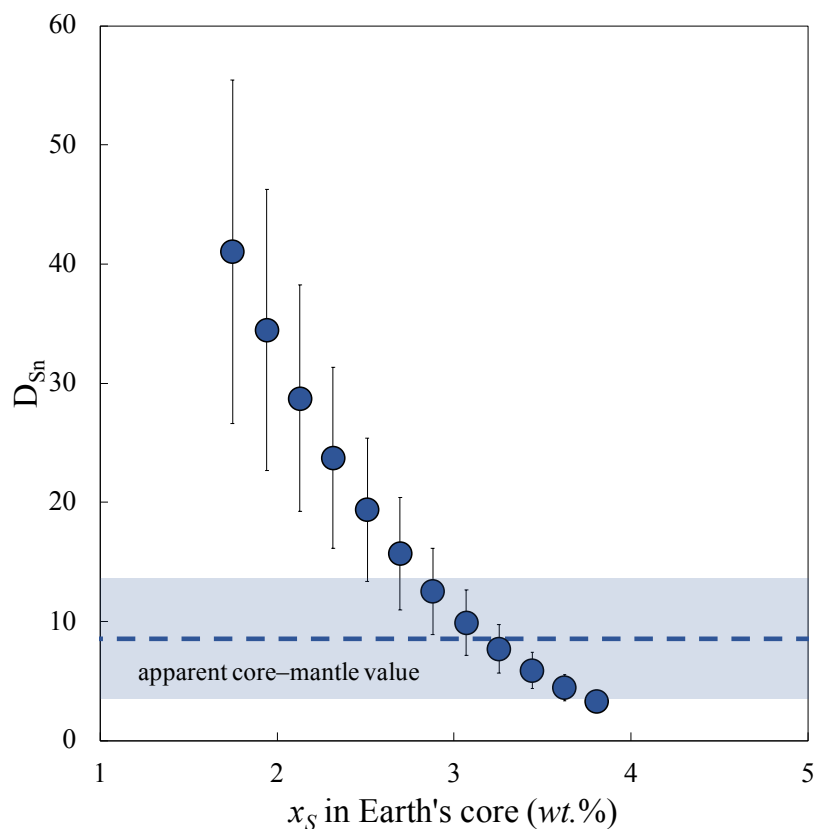


Figure 4.6 – Heterogeneous partial equilibration core formation models. The final D_{Sn} is plotted for a range of different S concentrations that are forced into the Earth's core. D_{Sn} is computed in the case of a late accretion of Sn and S in the last 10% of Earth's formation, using an ε and with $k = 0.5$. In this calculation the bulk S content of the accreted embryos are entered as input and the x_S in the cores of the embryos and Earth are computed using multilinear regression equation from Rose-Weston et al. (2009) which describes the experimentally determined behavior of S in a metal-silicate equilibrium. It shows that if there is 3 wt.% of S in the Earth's core, the apparent partitioning of Sn, plotted as a blue dotted line, can be perfectly reconciled with the computed partitioning inferred from experimental data.

need to be carried out to confirm this potential discrepancy with the present work. The parameterisation of this fractionation with temperature variation indicates that at conditions relevant for Earth core-mantle equilibrium ($\sim 3000\text{K}$), the resultant mantle could be isotopically lighter than the core by $150\text{--}200 \pm 17$ ppm per amu. Although a lot of isotopic systems predict an enrichment of the mantle in

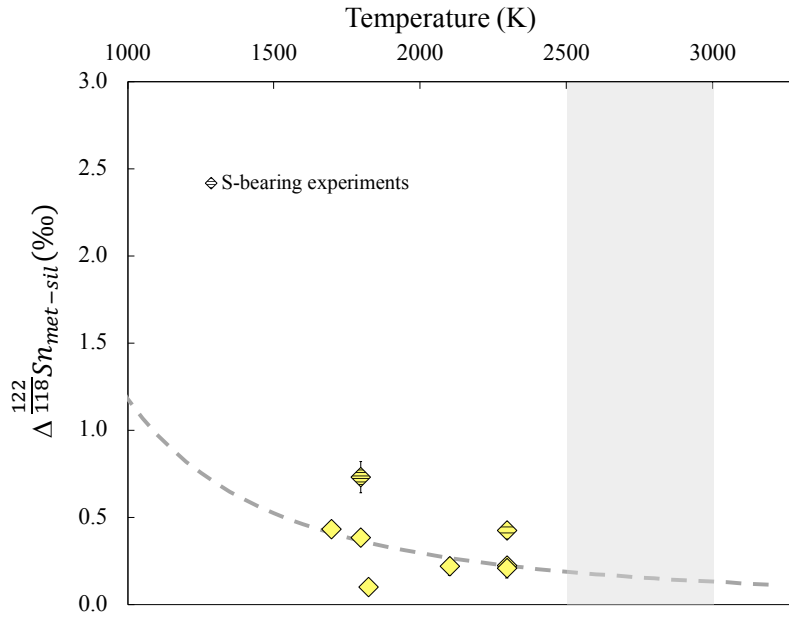


Figure 4.7 – Sn isotope fractionation between metal and silicate from a selection of piston cylinder experiments at 2 GPa as a function of the equilibrium temperature of those experiments. This fractionation is a function of $\frac{1}{T^2}$ Urey (1947) as represented by the grey dashed regression. A fractionation between 0.10 and 0.73‰ is observed. S-bearing experiments, represented with a horizontal lines pattern, seem to present a higher fractionation of Sn isotopes between metal and silicate. The grey zone corresponds to temperatures that are relevant to the conditions of core–mantle differentiation in a deep magma ocean on Earth. The interpolation of the regression based on experimental data at such temperatures shows that isotopic fractionation could be observed in the conditions of Earth’s differentiation.

heavy isotopes (e.g. Mo, Si, Hin et al. 2013, 2014), it is not unusual to detect a light isotope enrichment in the silicate part (e.g. S, Fe, Ni, Elardo and Shahar 2017, Guignard et al. 2020, Labidi et al. 2016, Shahar et al. 2015). Recent measurements of Sn isotopic compositions of chondrites by Creech and Moynier (2019) show an overlap between the carbonaceous chondrites composition and that of the primitive mantle measured by Badullovich et al. (2017). This overlap could be the result of two scenarios: (1) The Sn budget of the Earth did not equilibrate with the core, either through the addition of an unequilibrated late veneer, and/or a low rate of partial equilibration between core and mantle; or (2) the temperature

during core–mantle differentiation was higher than 4000 K, preventing detectable Sn isotopic fractionation to occur, as suggested by recent work by Olson and Sharp (2018). In this second case, the Sn isotopic signature of the BSE would match the signature of its building blocks, which would then only match that of carbonaceous chondrites (and not enstatite or ordinary chondrites, see figure 4.8), in agreement with other cosmochemical observables (Braukmüller et al. 2019, Marty 2012, O’Neill 1991). The experimentally parameterised Sn isotopic partitioning in a metal–silicate equilibrium was used as input in an isotopic core formation model in order to test different accretion scenarios, where ordinary, enstatite and carbonaceous chondrites were considered as potential sources for the Earth’s volatiles (figure 4.8). The conditions of the models match those of the elemental core formation models discussed in the previous section. During metal–silicate equilibration, the metal is preferentially enriched in the heavier isotopes of Sn whereas the silicate is enriched in Sn lighter isotopes. In the computed models, the Sn isotopic composition of one of the three types of chondrites was used as the bulk Sn isotopic composition of the Earth (ordinary: $-0.29 \pm 0.44\text{‰}$, enstatite: $0.12 \pm 0.28\text{‰}$ and carbonaceous: $0.47 \pm 0.12\text{‰}$, Creech and Moynier 2019). The mantle and core isotopic compositions were then calculated both in the case of a homogeneous accretion and an heterogeneous accretion where the volatiles were brought in the last 10% of Earth’s accreted mass. After core–mantle equilibration, the computed isotopic composition was shifted towards lighter values for the mantle compared to the bulk, as expected (figure 4.8). The ordinary and enstatite chondrites, of which the average Sn isotopic composition is significantly lighter than the BSE, show computed mantle values for Sn isotopes that are even lighter, from $-0.60 \pm 0.05\text{‰}$ to $-0.08 \pm 0.04\text{‰}$, which are incompatible with the BSE ($0.49 \pm 0.11\text{‰}$, Badullovich et al. 2017). On the other hand, results for carbonaceous chondrites isotopic core formation models show good agreement with Sn isotopic composition of the BSE. The dispersion of Sn isotopic compositions within this group of chondrites is displayed on figure 4.8. Our computed Sn isotopic BSE composition in the case of heterogeneous accretion, which is $0.37 \pm 0.04\text{‰}$, plots within error of the BSE isotopic composition. The observed BSE Sn isotopic composition could be explained by the same scenario as the observed Sn abundance in the BSE without the need to invoke other processes (i.e. volatilisation processes). In this scenario, carbonaceous chondrite-like material appears to be the most likely source of volatile elements on Earth according to our Sn isotope dataset. Wang et al. (2019) propose an estimate

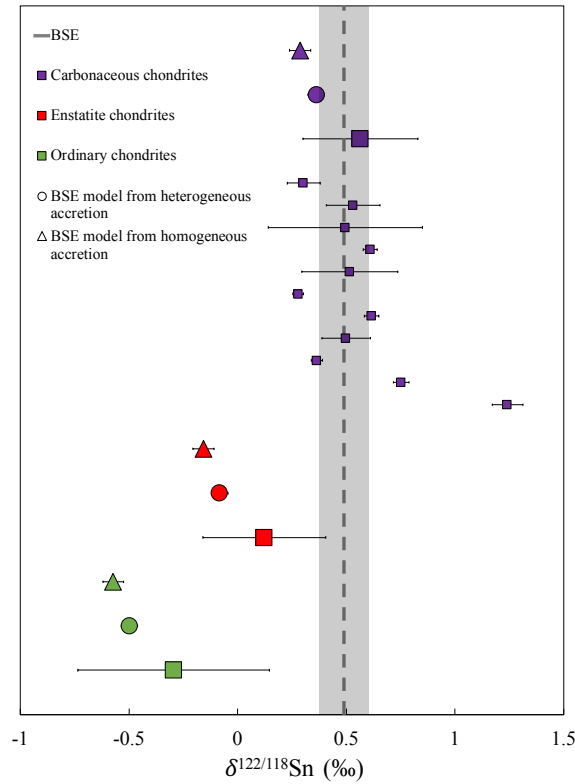


Figure 4.8 – Isotopic compositions of core formation models computed for different types of possible building materials compared to the BSE value (Badullovich et al. 2017) in dashed line with uncertainty in gray. Average isotopic compositions of carbonaceous chondrites (purple), enstatite chondrites (red) and ordinary chondrites (green) from Creech and Moynier (2019) are plotted as large squares and displaying standard deviations between single meteorites measurements. Individual measurements of carbonaceous chondrites are represented as small purple squares. Multiple isotopic core formation models were computed using each of the average chondrites $\delta^{122/118}\text{Sn}$ as the isotopic composition of Earth’s building blocks. For each chondrite type, a homogeneous accretion model with an ε and $k = 0.5$ was calculated and represented as a triangle. A heterogeneous model where all the volatiles were brought in the last 10% of Earth’s accretion, considering an ε value and $k = 0.5$, is represented as a circle. Error bars of the models correspond to the propagation of uncertainty on the regression parameter. The isotopic composition of carbonaceous chondrites overlap with that of the BSE. The modeled $\delta^{122/118}\text{Sn}$ of the BSE are lower than the $\delta^{122/118}\text{Sn}$ from the chosen building block because the heavier isotopes of Sn tend to go preferentially into the core. Models based on carbonaceous chondrite isotopic compositions are closer to the BSE than for other potential source materials. Moreover, individual Sn isotopic measurements of carbonaceous chondrites (small purple squares) overlap with that of the BSE (with notable dispersion), and both overlap with the heterogeneous model. Based on this evidence, carbonaceous chondrite-like material appears to be the best potential source of volatile elements on Earth.

of the Bulk Silicate Moon (BSM) of $0.03 \pm 0.02\%$ ($\delta^{122/118}\text{Sn}$ relative to Sn_IPGP) which is significantly lighter than the BSE ($0.49 \pm 0.11\%$). Although the Moon and the Earth share common episodes of their accretion history—namely the giant impact stage—the Moon is clearly volatile depleted compared to the Earth most likely because of volatilisation processes (Boyce et al. 2015, Kato et al. 2015, Pringle and Moynier 2017, Pringle et al. 2014, Sharp et al. 2010, Wang and Jacobsen 2016) or core formation (Steenstra et al. 2016). The light Sn isotopic signature of the BSM is not fully consistent with volatile loss and could be explained by mixing processes between the protolunar disk and the Earth as proposed by Wang et al. (2019), and, as our data suggest, lunar core formation may also have left the silicate fraction of the Moon enriched in the lighter isotopes.

Core formation and Earth’s accretion

A scenario in which the volatile delivery occurs in the last part of the main phases of Earth’s accretion is in agreement with numerous other studies. This last stage could be associated to a sulfur-rich iron liquid that forms and segregates into the core (referred to as the Hadean matte; Rubie et al. 2016). While our study does not necessitate this added complexity, it does not negate its possibility either. Several studies show volatile elements metal–silicate equilibrium data that cannot be reconciled with the observed abundances in the case of a homogeneous accretion scenario. In particular, Suer et al. (2017) and Mahan et al. (2018a, b) report S, Zn and Cu metal–silicate diamond anvil cell experiments at conditions relevant to Earth’s core formation (46 to 91 GPa), and are able to reconcile their data to the observed S, Zn and Cu contents of the present-day mantle with a volatile delivery in the last part of the main phases of the Earth’s accretion, a scenario also supported by Ballhaus et al. (2017). This accretion pathway is not only backed by metal–silicate studies, but isotopic measurements of Pd-Ag and noble gases (Marty 2012, Schonbachler et al. 2010) show that terrestrial isotopic compositions can only be explained by a heterogeneous accretion scenario. A more recent study on halogen abundances and ratios (Clay et al. 2017) corroborates late-stage accretion of volatile-rich planetesimals. Numerical simulations put spatial constraints on this mechanism showing that the source of volatiles on Earth was probably an influx of material from the outer solar system which was delivered late in the planet’s growth

(Morbidelli et al. 2012, Raymond et al. 2006). O’Brien et al. (2018) and Schiller et al. (2018) also state that this late delivery is composed of material originated from beyond the snow line and chemically similar to carbonaceous chondrites.

Carbonaceous chondrites appear to be important terrestrial planet building blocks, and are the most likely source of volatiles on Earth (O’Neill 1991, Schonbachler et al. 2010). Recent work on S, Se and Te measurements (Braukmüller et al. 2019) shows that the most volatile elements are unfractionated from one another in Earth and chondrites, creating a volatile element plateau (or “hockey-stick” pattern). Braukmüller et al. (2019) propose a scenario of delivery of volatiles under the form of 10–15 *wt.%* of CI-like material before core formation ceased (potentially as a giant, Moon-forming impact), in view of the depletion of siderophile and chalcophile volatile elements relative to the observed plateau.

Moreover, though the systematic linkage of water and other volatile species is debatable, the highly volatile elements (e.g. H, N, Kr, Xe) further support volatile delivery via carbonaceous chondrite-like material. For example the D/H ratios of carbonaceous chondrites are consistent with the bulk Earth value (Alexander et al. 2012, Sarafian et al. 2017). The coupled similarity in H and N isotopic compositions between CI chondrites and the bulk Earth also advocates for a carbonaceous chondritic source for volatile elements in the Earth’s mantle (Marty 2012). For heavy noble gases, isotope data obtained on mantle-derived samples also show a chondritic affinity for these noble gases in the silicate portion of Earth (Holland et al. 2009, Péron and Moreira 2018), although some studies suggest that there could be multiple noble gas reservoirs in the deep mantle (Tucker and Mukhopadhyay 2014).

Lastly, recent modelling results of large impact dynamics strongly support the notion that most or all volatiles are retained during Earth’s accretion (Daly and Schultz 2018, Lock and Stewart 2017). A similar message is delivered by Siebert et al. (2018) regarding the chondritic Mn/Na ratio observed on Earth, favoring incomplete accretion in the solar nebula over syn- and post-accretion volatilisation processes to explain the volatile depletion. Taken together, these observations provide a means to retain most or all inherited volatiles during the entire accretionary process.

Assuming that Earth’s Sn budget and isotopic signature has been inherited

from its source material (Creech and Moynier 2019), our results show that any difference in Sn isotope composition and abundances between the BSE and potential building blocks (e.g. carbonaceous chondrites) is largely a consequence of the process of core formation.

Conclusions

Thirty piston cylinder and multianvil press experiments have been performed to characterise the metal–silicate behavior of Sn at high pressure and high temperature. A double approach was used in which both Sn elemental partitioning and Sn isotopic fractionation were measured at metal–silicate equilibrium. Subsequent parameterisation and core formation models show that pressure has a notable positive effect on Sn partitioning that makes the relatively high Sn abundance in the Earth’s mantle largely incompatible with a scenario of homogeneous accretion and associated differentiation. The observed Sn concentration in the BSE can be reconciled with our experimental data only in an accretionary scenario where most of the volatile budget was delivered during the last 10% of the main phases of Earth’s formation. Moreover, around 3 *wt.*% of S in the core are needed to sufficiently lower the modeled partitioning in order to match the observed Sn abundance. Tin isotopes are found to be fractionated at metal–silicate equilibrium, such that the mantle ought to become enriched in the lighter isotopes during core formation. Earth’s building blocks should then be heavier than the bulk silicate Earth value. For ordinary and enstatite chondrite types, the averages of available Sn isotopic compositions are found to be significantly lighter than the BSE estimate, whereas carbonaceous chondrites provide a plausible match. Our isotope data therefore promotes carbonaceous chondrite-like material as the most likely source of Earth’s volatiles.

Acknowledgements

We acknowledge the financial support of the UnivEarthS Labex program at Sorbonne Paris Cité (ANR-10-LABX-0023 and ANR-11-IDEX-0005-02). SEM instruments are supported by IPGP multidisciplinary program PARI, and by Paris-

IdF region SESAME Grant No. 12015908. We thank Stephan Borensztajn for support during SEM observations. We acknowledge and thank the DFG Core Facility Program at Bayerisches Geoinstitut. We thank Bleuenn Guéguen for technical support during LA-ICPMS measurements at IUEM, University of Brest. We also thank Nicolas Wehr for technical support and advice in high-pressure laboratory of IPGP. JS thanks the financial support of the French National Research Agency (ANR Project VolTerre, grant no. ANR-14-CE33-0017-01). FM acknowledges funding from the European Research Council under the H2020 framework program/ERC grant agreement 637503 (Pristine), and the ANR through a *chaire d'excellence* Sorbonne Paris Cité.

Supplementary information

Experimental and analytical methods – supplementary details

Starting materials

For the silicate fraction, a natural MORB and a natural KLB-1 peridotite, were used. All metal fractions were composed of pure powders. The metal phase is made of pure Fe that is mixed with FeS in some experiments in order to investigate the effect of S on Sn metal–silicate fractionation. It was also doped with 1 *wt.%* Cu, Tl, In, Cd, Bi, Sb to assess the effect of the metal composition on Sn partitioning (table 4.1). All compounds from each starting material were weighed, mixed and crushed in an agate mortar to prevent any heterogeneity. The composition of the natural MORB used in our starting materials (in *wt.%*) is given in table 4.3.

Piston cylinder experiments

All experiments were performed in in 1/2" cell assemblies. The duration of each experiment was chosen according to the temperature of the run with the prospect of both reaching elemental and isotopic equilibrium and minimising the chemical reactions with the capsule material which are likely to occur at high

Table 4.3 – Natural MORB composition (*wt.%*)

| Natural MORB | |
|--------------------------------|-------|
| SiO ₂ | 50.22 |
| Al ₂ O ₃ | 15.86 |
| Fe ₂ O ₃ | 10.6 |
| CaO | 10.3 |
| MgO | 7.97 |
| Na ₂ O ₃ | 3.38 |
| TiO ₂ | 1.7 |
| K ₂ O | 0.72 |
| P ₂ O ₅ | 0.3 |
| MnO | 0.2 |

temperature (Corgne et al. 2008, Siebert et al. 2011). Assemblies were composed of a graphite furnace and a BaCO₃ pressure cell for experiments above 1900 K and talc-pyrex pressure cell for lower temperature experiments. Assemblies are fully described in Siebert et al. (2011). During the experiment, the temperature was measured and controlled using a type D thermocouple (W₉₇Re₃/W₇₅Re₂₅) situated axially above the sample touching the lid of the capsule, in a 4-hole alumina sleeve. The sample was quenched by switching off the electrical power when the chosen time duration was over.

Thorough description of the piston cylinder pressure calibration and used assemblies can be found in Siebert et al. (2011). The pressure calibration is using the same principle of phase transitions as detailed below for multianvil pressure calibration.

Multianvil experimentation

MgO octahedra were used as pressure media, with 18 mm edges. Pressure was distributed to the sample in several directions using cubic tungsten carbide

anvils with 11 and 8 mm truncations (18/11 and 18/8 configurations). In order to minimise temperature gradients, a stepped LaCrO_3 heater was used (Rubie 1999).

Pressure calibration for both presses used is described in Rubie (1999) and Frost et al. (2004) and involves using the transition of Bi (I-II and III-V) (Lloyd 1971), the quartz–coesite transition (Bohlen and Boettcher 1982), the coesite–stishovite transition (Yagi and Akimoto 1976) and the fayalite– γ -spinel transition (Yagi et al. 1987). Pressure and temperature uncertainties (e.g. Woodland and Angel 1997, Woodland and O'Neill 1993) are estimated to be 1 GPa and 100°C for temperature. Furthermore, temperature gradients have been shown to be inferior to 100°C across the sample, lowered by the use of a stepped LaCrO_3 heater (Frost et al. 2004, Rubie 1999). Single-crystal MgO capsules were used in all our MAP experiments to ensure the minimum interaction between the capsule and the sample. No further contamination from other parts of experimental assemblies in both PC and MAP experiments were expected nor detected during chemical measurements.

Electron microprobe measurements

Samples were mounted in a resin and polished with silicon carbide paper and then diamond liquid until obtaining a 1 μm polishing before analysis. An accelerating voltage of 15 keV and a beam current of 300 nA were used and the counting times consist of 10–20 s for major elements and 20–90 s for trace elements. Standards used in major elements analysis are diopside for SiO_2 , MgO, CaO; orthopyroxene for K_2O and Al_2O_3 ; Fe_2O_3 for iron oxide; albite for Na_2O ; FeS_2 for S in the silicate and an alloy of Mn and Ti for TiO_2 . For the metallic phase, Fe_2O_3 was used for Fe and O, FeS_2 for S, diopside for Si. Sn detection limit is estimated to ~ 100 ppm and the standard used for Sn was a SnO_2 oxide.

LA-ICPMS measurements

The laser ablation was set up at 15 J/cm^2 output and a 10 Hz laser frequency. 90- μm beam size was used in order to vaporise a significant and therefore statistically relevant amount of sample, providing appropriate estimations for the average compositions of silicate phases. The generated aerosol particles were carried by an helium flux and mixed with argon before entering the plasma. LA-ICPMS mea-

measurements published in this study were performed using both low ($m/\Delta m=200$) and medium resolutions ($m/\Delta m=400$) modes. The Sn concentrations provided in table 4.2 for each experiment consist in an average of 3 to 8 points of 90- μm that were made in each silicate phase. Each analysis was done as a single spot and lasted 90 seconds with the first 10 seconds of background acquisition (gas blank). Standards were measured twice each (all 6 standards) at the beginning and end of a sequence. The data accuracy is ensured by internal calibrations, using Mg concentrations measured by electron microprobe, and by standard interpolations using glass standards NIST610, NIST612 and NIST614. The data quality is also certified by the repeated analyses of natural basaltic glass standards BIR-1, BCR-2 and BHVO-2. The accuracy of Sn concentrations is estimated between 3 and 40% depending of the concentration levels.

MC-ICPMS measurements

Sample preparation The samples were double-spiked because of the low yields of the chemical separation which is about 70% of Sn recovered (Creech et al. 2017b). After addition of the double-spike, the samples were dried, and silicate samples were further digested in aqua regia on a hot plate at 150°C to remove any fluoride complex and dried again. All samples were then dissolved in 2 mL of 0.5 N HCl.

Chemical purification of Sn Biorad columns containing 1 mL of Eichrom TRU resin were cleaned with the following sequence of acids: 4 mL of 0.5 N HCl, 4 mL H₂O, 2x (4 mL 0.5 N HNO₃, 4 mL H₂O). A volume of 4 mL 0.5 N HCl was used to condition the resin for the samples, which was then loaded in 2 mL of 0.5 N HCl. This step was followed by a 4 mL of 0.5 N HCl + 7 mL of 0.25 N HCl rinse.

Mass spectrometry and data reduction Between each analysis, baselines were measured on peak (i.e. on-peak zeros) during 14 min and the last 120 s were used as the actual baseline and subtracted from the following analysis. Measurements of column processed double-spiked standard along with our samples as well as the double-spike added to our samples prior to column separation allowed for

Table 4.4 – Tin isotopic compositions for chondritic samples measured in the same sequence as the samples from this study, compared to results from Creech and Moynier (2019).

| Group | Sample | This study | | | Creech and Moynier (2019) | | |
|-------|----------|-----------------------------|-----------|---|-----------------------------|-----------|---|
| | | $\delta^{122/118}\text{Sn}$ | 2σ | n | $\delta^{122/118}\text{Sn}$ | 2σ | n |
| CV3 | Allende | 0.524 | 0.010 | 3 | 0.499 | 0.111 | 4 |
| EH3 | SAH97096 | 0.420 | 0.035 | 2 | 0.349 | 0.044 | 6 |

correction for any mass-dependent fractionation that may occur during chemical purification and mass-spectrometry analysis. Blanks were $< 1\text{ng}$. Measurements on chondritic samples, for which Sn isotopic compositions have already been published, were performed (table 4.4). Reference isotopic data for Sn does not yet exist to provide means for evidence of accuracy, but the consistency of the measurements presented here demonstrate long-term reproducibility.

Results – parameterisation

List of all experiments used in the regression calculation:

- all experiments from this study
- runs 171, 172, 173 from Mahan et al. (2017)
- runs 3707a, 3718a, 926a, 926b, 3355a, 3355b, 3450a, 822a, 941b, 859b, 865b, 929b, 1062a, 1062b, 1008a, 3367b, 3364b from Vogel et al. (2018)
- A15, A17, A20, A40, A41, A42, A43 from Ballhaus et al. (2013)
- M1600, M1700, M1800, M1900, FeS+1 from Righter et al. (2017b)
- CM1, CM2, CM2.5, CM5, CM6, CM20, CM30, CM32, CM34, CM35, CM36 from Ballhaus et al. (2017)
- RH82, RH97, RH99 from Hin et al. (2013).

Numerical modelling method – supplementary details on core formation models

Equilibrium efficiency Fluid dynamics analog experiments show that in order for full equilibration to happen, metal from impactors needs to break down to small droplets to be segregated in the core properly, which is less efficient for bigger impactors. This effect can be calculated with parameter ε which takes into account the amount of silicate that is dragged along with the metal when metal migration to the core occurs, countering a full equilibration. Although this study favors the formalism by Deguen et al. (2014), numerical simulations have shown that the stretching of metal upon impact in a magma ocean could facilitate equilibrium even for large impactors (Kendall and Melosh 2016, Lherm and Deguen 2018).

Apparent core–mantle partitioning of Sn of the Earth This estimated Sn partitioning of Earth is calculated by assuming that Sn was accreted in similar relative abundance than the lithophile elements of closest condensation temperature (here we chose F, with $T_c=734$ K) and that the difference in abundances between Sn and F is attributed to core formation, allowing the calculation of an estimated partition coefficient. Our estimation is in good agreement both with recent reappraisal of condensation temperatures by Wood et al. (2019) and the recently proposed hockey stick volatile pattern of Braukmüller et al. (2019). This estimated partition coefficient could be overestimated if the Earth-forming materials underwent significant post-nebular volatile loss inducing a reduced amount of Sn in the bulk Earth compared to what is estimated here from CI chondrites. This would in fact reinforce our conclusions in the sense that a late delivery of the volatile elements would be even more necessary to reproduce such a low apparent core–mantle partition coefficient in our models.

Core formation model operation Pressure and temperature were increased as a function of the accreted fraction and oxygen fugacity remained constant. Accretion is modeled in 20, 10, 1, 0.1, and 0.01 increments. Temperatures were fixed following the peridotite liquidus (average between Andraut et al. 2011 and Fiquet et al. 2010). Pressure of equilibrium was set at 40% of the proto-Earth’s mantle di-

ameter at each step (Siebert et al. 2012) corresponding to the base of a deep magma ocean. For each embryo size, the bulk S and Sn content were chosen (set to be that of the bulk Earth computed by McDonough 2003). The D_S is then calculated according to expression given by Rose-Weston et al. (2009) in which experiments were used to parameterise the behavior of S in a metal–silicate equilibrium, which was used in order to assess the S concentration in each embryo’s core. This information is used to compute the D_{Sn} of each embryo type. Starting from a 1 *wt.%* embryo, we accrete embryos one by one of a fixed size that is increasing with time from 0.1 *wt.%* to 20 *wt.%*. For each embryo, the S and Sn content and distribution between core and mantle are known as well as the Sn isotopic composition of the different reservoirs (which depends only on temperature and isotopic composition of the building blocks). This data is used in equations from Rudge et al. (2010) in order to calculate the D_{Sn} of the proto-Earth at each step of the accretion. Proper parameters used in these equations allows to model either full equilibration ($k = 1$) or a partial equilibration by replacing k by the value of parameter ε from Deguen et al. (2014) that propose a more accurate estimation of the efficiency of the equilibrium based on fluid dynamics experiments. No late veneer was added in our core formation models because a 0.5 *wt.%* chondritic late veneer in the Earth’s mantle would account for only 11 ppb out of the 138 ppb ($\sim 8\%$) of Sn measured in the primitive mantle Palme and O’Neill (2014). Such a minor contribution means that the observable Sn partitioning would be 9.5 ± 5 before the later veneer occurred, and 8.5 ± 5 after, and both results are indistinguishable within error.

Earth's volatile accretion as told by Cd, Bi, Sb and Tl core–mantle distribution

This second study focuses on the timing of accretion and origin of volatile elements on Earth and uses the methods previously described applied to Cd, Bi, Sb and Tl partitioning behaviour between core and mantle. The study is constructed as follows: (1) measurement of the partitioning of the elements of interest between metal and silicate in controlled experiments, (2) thorough parameterisation of the effects of pressure, temperature, oxygen fugacity and composition and (3) subsequent core formation modelling in order to reconcile experimental results with observed abundances by one or a variety of accretion scenarios of volatile elements. This study is reported as submitted to be peer reviewed by *Geochimica et Cosmochimica acta* journal. All research work was performed by the author of this thesis, under proper supervision. All piston cylinder experiments were performed by the author, under the supervision of Julien Siebert. Multianvil experiments were operated as part of two DMG Core Facility Program proposals at Bayerisches Geoinstitut (University of Bayreuth) with technical support from Svyatoslav Shcheka. SEM, EPMA and LA-ICPMS measurements were performed by the author. Thermodynamic parameterisation and core formation modelling were operated on Matlab with guidance and advice from Julien Siebert.

Earth’s volatile accretion as told by Cd, Bi, Sb and Tl core–mantle distribution

E. Kubik^{1,*}, J. Siebert^{1,2}, I. Blanchard³, A. Agranier⁴, B. Mahan⁵, F. Moynier¹.

¹Université de Paris, Institut de Physique du Globe de Paris, CNRS, 1 Rue Jussieu, 75005 Paris, France.

²Institut Universitaire de France, Paris, France.

³Bayerisches Geoinstitut, University of Bayreuth.

⁴Institut Universitaire Européen de la Mer, Université de Brest.

⁵James Cook University, Queensland, Australia.

*kubik@ipgp.fr

Abstract

The timing and origin of volatile elements accretion on Earth has been and continues to be key questions, despite intense research scrutiny. Two end-member scenarios are usually proposed in which (1) volatile elements were delivered during the main phase of Earth’s accretion and underwent subsequent core–mantle differentiation, or (2) Earth accreted from largely dry and volatile-depleted material, with late addition of volatile-rich material after differentiation. Studying the behavior of elements that are both volatile and siderophile in a metal–silicate equilibrium can help discriminate between those two scenarios by deconvolving the effect of siderophile processes such as the Earth’s differentiation from the effect of volatile processes. We report high-pressure and high-temperature metal–silicate equilibrium experiments that are used to trace the behavior of four moderately volatile and siderophile elements: Cd, Bi, Sb and Tl. Experiments were performed in piston cylinder and multianvil presses between 2 and 20 GPa, from 1700 to 2600 K, in order to study the partitioning behavior of these elements, including the relative influence of pressure, temperature, oxygen fugacity, and composition. Our results indicate that Cd, Bi, Sb and Tl partitioning coefficients are largely controlled by changes in temperature, pressure and the S content of the metal phase. The pressure effect on Tl and Bi partitioning is measured for the first time and improves significantly the knowledge of Bi and Tl behaviour during core forma-

tion. Core formation modelling was used to reconcile the experimental data with observed abundances for different accretion scenarios. Homogeneous accretion with full core–mantle equilibration induces a massive segregation of Bi, Sb and Tl in the core, preventing reproduction of observed present-day mantle abundances. We find that a scenario in which the volatile elements are accreted in the last 10–20% of the Earth’s accretion is the most suitable accretion process that is able to explain the abundances of Cd, Bi, Sb and Tl in Earth’s mantle. Partial core–mantle equilibration is necessary to reproduce Bi and Tl abundances. A 0.5% chondritic late veneer is supported to account for the Bi abundance measured in the bulk silicate Earth. These observations corroborate a growing wealth of evidence in support of this schematic heterogeneous accretion pathway.

Introduction

The presence of active plate tectonics, liquid ocean and life, make the Earth unique compared to any other terrestrial planets of the solar system. The origin of volatile elements—which are crucial to the development of life on Earth—is a hotly debated topic. The depletion in volatile elements of the Earth’s mantle could be due to (1) a volatile loss by syn- and post-accretional volatilisation, and/or to (2) incomplete condensation of the solar nebula (Albarède 2009).

Volatile loss on Earth has been largely argued against by studies reporting a lack of heavy isotope enrichment in the Earth’s mantle compared to primitive meteorites (Humayun and Clayton 1995, Luck et al. 2005, Pringle and Moynier 2017, Pringle et al. 2017, Sossi et al. 2017, Tuller-Ross et al. 2019, Varas-Reus et al. 2019, Wang and Jacobsen 2016), although small isotopic fractionations reported for Mg (Hin et al. 2017) and Si (e.g. Pringle et al. 2014, Young et al. 2019) suggest volatilisation may have happened. The Mn/Na ratio, which is sensitive to post-nebular volatilisation and is chondritic in the bulk Earth, provides an additional argument for limited volatile loss during or after Earth’s accretion (O’Neill and Palme 2008, Siebert et al. 2018), favoring incomplete condensation of the solar nebula as the main process explaining the volatile depletion on Earth. This study aims at discriminating between several plausible accretion scenarios that could produce the observed volatile elements pattern of the Earth’s mantle:

(1) “Dry accretion”, where the Earth largely accreted from dry material, devoid of volatile elements. The solar system temperature during that period may have been too high to allow the condensation of volatile elements (Albarède 2009), supporting this scenario. The volatiles are brought after core formation ceased, as a late veneer of chondritic composition (Albarède et al. 2013, Budde et al. 2019, Dauphas 2017, O’Neill 1991).

(2) “Wet accretion”, on the other hand, designates an accretion from building blocks that are partially volatile depleted, such as chondritic material(s). The elements are segregated between core and mantle according to their siderophilicity during differentiation, which explains the abundances of elements in the Earth’s mantle (Righter et al. 2017b, Wood and Halliday 2010), potentially associated with volatile loss (Hin et al. 2017, Norris and Wood 2017, Pringle et al. 2014).

(3) In an intermediate scenario, Earth is accreted from compositionally heterogeneous material, and the bulk of its volatile element inventory is brought in the last stages of accretion and differentiation. As proposed by Braukmüller et al. (2019), the volatile elements on Earth could originate from 10 to 15 *wt.%* of CI-like material brought towards the end of the main phases of Earth’s accretion. This stage could have been associated with the formation of a volatile-rich liquid sulfide matte that subsequently mixed into the core (O’Neill 1991, Savage et al. 2015, Schonbachler et al. 2010).

By studying the metal–silicate partitioning behavior of elements that are both volatile and siderophile, the effect of the Earth’s differentiation can be isolated from the effect of volatile processes, helping to discriminate between the three main volatile accretion scenarios.

This study focuses on four moderately siderophile and volatile elements (MSVEs), which are depleted in the Earth’s mantle compared to lithophile volatile elements as a consequence of their segregation into the core during differentiation (Lodders 2003, Wasson et al. 1988, Wood et al. 2019). Experimental studies of MSVE behavior at metal–silicate equilibrium at high pressure and high temperature can be used to characterise the siderophilicity of such elements and infer the effect of differentiation on their observed abundances in the Earth’s mantle (e.g. Ballhaus et al. 2017, Blanchard et al. 2015, Corgne et al. 2008, Mahan et al. 2017, Righter et al. 2017b, Siebert et al. 2011, Steenstra et al. 2019, Suer et al. 2017). Comprehensive

parameterisation of metal–silicate partitioning includes the effect of pressure, temperature, fO_2 , metal and silicate composition. Such parameterisation can be used as input in core formation models, where the partitioning is reconstructed at each step of the Earth’s accretion at the predicted pressure and temperature conditions of the Earth’s differentiation. These models are used to test various accretion scenarios in an attempt to reconcile experimentally determined partitioning behaviors of elements with their observed abundances in the Earth’s mantle (e.g. Blanchard et al. 2015, Rubie et al. 2011, Wade and Wood 2005). The results of those models can then be compared to natural observation and used to isolate the most likely accretion scenarios.

This study is focused on experimental characterisation of the partitioning behavior of Cd, Bi, Sb, and Tl in a metal–silicate equilibrium. These elements are MSVEs with condensation temperatures of 652, 746, 979 and 532 K respectively (Lodders 2003), recently reappraised to 502, 480, 890 and 365 K (Wood et al. 2019) in particular by including recent halogen abundances adjustment (Clay et al. 2017). The fact that they are affected by core–mantle differentiation as well as volatile processes makes them good tracers of volatile accretion. Cadmium metal–silicate partitioning data has been reported in several studies (e.g. Wang et al. 2016, Wood et al. 2014) with very different conclusions, ranging from Cd mantle abundance being fully explained by core formation (Righter et al. 2017b, 2019), to not at all (Ballhaus et al. 2013). This could be the consequence of the scarcity of high-pressure experiments permitting to observe and quantify other operative effects such as pressure. Bismuth and thallium metal–silicate partitioning have never been measured above 3 GPa, meaning that the pressure effect on their partitioning has never been constrained. Bismuth abundance in the bulk silicate Earth (BSE) has been explained based on low-pressure data, to be controlled by core formation (Righter et al. 2017b) possibly associated with segregation in a sulfide matte (Righter et al. 2019), but models including the pressure effect on the Bi partitioning could lead to significantly different conclusions. Also based on low-pressure experiments, Tl abundances in the BSE have been explained by late accretion (Ballhaus et al. 2013) or sulfide segregation (Wood et al. 2014, 2008). However, novel insight on the pressure effect on the Tl partitioning could help refine the associated core formation models. Existing data of Sb partitioning include a majority of experiments below 2 GPa (Steenstra et al. 2017), though some higher-pressure experiments are reported (Vogel et al. 2018), and lead to a variety of proposed

Table 5.1 – Starting material compositions (*wt.%*)

| Starting material | Silicate phase | | Metallic phase | | | |
|-------------------|----------------|-------|----------------|----|------------------------|--|
| | MORB | Fe | FeS | Sn | Cu, Tl, In, Cd, Bi, Sb | |
| A | 70% | 30% | | 2% | 1% of each | |
| B | 70% | 13.5% | 16.5% | 2% | 1% of each | |

scenarios that may explain the Sb abundance in the BSE: core formation alone (Righter et al. 2009, 2017a, b), possibly including equilibration with a sulfide liquid (Wood et al. 2014). Further parameterisation of the Sb partitioning between metal and silicate may help to better understand the processes that produced the observed Sb abundance in the Earth’s mantle.

We report novel partitioning data for 17 experiments performed at high pressure and high temperature. Combined with literature data, they enhance our collective comprehension of the behavior of these elements, in particular by widening the range of pressure investigated in this type of experiments. Subsequent parameterisation was used for extrapolation to conditions relevant to Earth’s differentiation, and has been integrated into core formation models to explore the partitioning behaviour of Cd, Bi, Sb and Tl along a range of plausible volatile accretion trajectories and propose coherent story for the behaviour of these MVSEs during Earth’s accretion.

Experimental and analytical methods

Starting materials

Experiments were prepared with two different starting materials made of metal and silicate powder mixtures (table 5.1). A natural MORB was used as the silicate fraction. The metal fraction was added to the silicate as pure powders of Fe and FeS. The mixture was then doped with elements of interest and all components were combined in an agate mortar after weighing, and the bulk subsequently mixed and crushed together until obtaining a homogeneous mixture.

Piston cylinder experiments

Five experiments were performed with a 150-tons end-loaded piston cylinder press at the Institut Physique du Globe de Paris (IPGP). They were all performed in 1/2" cell assemblies at 2 GPa and from 1773 to 2273 K. The duration of each run was chosen carefully with respect to the temperature in order to reach elemental equilibrium between molten metal and silicate melt while minimising the chemical reactions with the capsule (Corgne et al. 2008, Siebert et al. 2011). Prior to the run, a MgO capsule was filled with starting material and packed, and the capsule was placed inside a talc–pyrex assembly (Siebert et al. 2011). The temperature of the sample was measured during the experiment using a type D thermocouple ($W_{97}Re_3/W_{75}Re_{25}$) previously placed in contact with the lid of the capsule. Samples were quenched by terminating heating. Representative pieces of metal and silicate were mechanically selected under magnifying glass, mounted in resin and carefully polished for scanning electron microscopy (SEM) observation, and electron microprobe (EPMA) and laser ablation (LA-ICPMS) measurements.

Multianvil experiments

Twelve multianvil experiments were performed at Bayerisches Geoinstitut using a 5000-ton Zwick and a 1000-ton Hymag multianvil apparatus from 7 to 20 GPa. Pressure media consisted of MgO octahedra with 18 and 25 mm edges. Cubic tungsten carbide anvils with 15, 11 and 8 mm truncations (25/15, 18/11 and 18/8 configurations) were used to apply pressure to the sample along three primary axes. The starting material was contained in single-crystal MgO capsule and lid. In order to minimise temperature gradients, a stepped $LaCrO_3$ heater was used. During the experiment, the sample temperature was monitored using a type D $W_{97}Re_3/W_{75}Re_{25}$ thermocouple. The experimental conditions are summarised in table 5.2. The whole samples were mounted in resin and polished until exposure of a significant surface of metal and silicate material for SEM, EPMA and LA-ICPMS analysis.

Electron microprobe measurements

EPMA measurements were performed using a CAMECA SX Five electron microprobe (CAMPARIS, Université Pierre et Marie Curie). Polished and mounted samples were evenly carbon coated prior to analysis. A selection of major and trace elements was resolved in both metal and silicate phases (table 5.2) using an accelerating voltage of 15 keV and a beam current of 300 nA. Counting times were chose as follows: 10–20 s for major and 20–90 s for trace elements. To prevent heterogeneities induced by quench textures from affecting the measurements, 30 μm rasters were used instead of points to improve the analytical statistics. No compositional zonation was found across the samples presented in this study, advocating for equilibrium achievement.

Laser-ablation ICPMS measurements

LA-ICPMS measurements were performed on the silicate phases of the experiments of this study in order to constrain the concentration of elements of interest depleted in the silicate below EPMA detection limits (table 5.2). Laser-ablation analysis were performed using an Element XR high-resolution mass spectrometer (Université de Brest) coupled to a 193 nm Compex Pro 102 Coherent Laser system. The laser was set to a 15J/cm² output and a 10 Hz frequency. A 90- μm beam was used to vaporise a significant amount of sample, and 3 to 8 measurements were performed and averaged on each sample (table 5.2). A helium flux was used to carry the ablated particles that were mixed with argon before entering the plasma. Data calibration was computed using both Mg concentrations previously measured by EPMA as internal standardisation and standard interpolations by measurement of silicate standards NIST610, NIST612 and NIST614.

Results

Petrography

Petrological observation of silicate phases shows homogeneous melts presenting skeletal quenched olivine and pyroxene crystals due to reaction with the MgO capsule. Metal phases consist of a single metal sphere with a diameter of roughly 1 mm in piston cylinder runs and 500 μm in multianvil runs. Quench textures can be observed on the sections of these spheres. These petrological observations indicate that the starting material was fully melted at superliquidus temperatures allowing coalescence of the liquid metal and equilibrium achievement.

Elemental compositions

All elemental concentrations from EPMA and LA-ICPMS are presented in table 5.2. In the silicate phase of the experiments, the MgO content ranges from 15.4 to 37 *wt.%* and SiO₂ from 30.2 to 48.5 *wt.%*. The combination of EPMA and LA-ICPMS allowed to measure the wide range of concentrations of the studied elements: 900 to 4000 ppm for Cd, 4 to 200 ppm for Bi, 1 to 1400 ppm for Sb and 600 to 6000 ppm for Tl.

Iron is the main component of the metallic phase with 60 to 90 *wt.%*. The S content ranges from 0.1 to 20 *wt.%*. Concentrations of the elements of interest in Fe-rich phase range well above EPMA detection limits, as follows: 0.03 to 2 *wt.%* for Cd, 0.04 to 3.5 *wt.%* for Bi, 1.8 to 3.5 *wt.%* for Sb and 0.01 to 2.3 *wt.%* for Tl.

Silicate and metallic phases were found compositionally homogeneous after thorough SEM observation and EPMA analyses. Oxygen fugacity, calculated with respect to the iron-wüstite (IW) buffer (equation 5.1), varies from -2.8 to -1.7 in the experiments.

$$\Delta IW = 2 \cdot \log \frac{X_{\text{FeO}}^{\text{silicate}}}{X_{\text{Fe}}^{\text{metal}}} \quad (5.1)$$

CHAPTER 5. Cd, Bi, Sb and Tl core–mantle distribution

Table 5.2 – Main parameters of all experiments, average major and trace element compositions of metal and silicate phases by EPMA and LA-ICPMS. Errors correspond to 1 standard deviation σ .

| Experiment | Z1820 | Z1821 | Z1823 | Z1824 | Z1825 | Z1956 | Z1957 | Z1959 |
|-----------------------------------|------------------------------------|------------------------------------|------------------------------------|------------------------------------|------------------------------------|------------------------------------|------------------------------------|------------------------------------|
| Starting material | B | A | A | A | B | A | B | A |
| Pressure (GPa) | 7 | 7 | 14 | 18 | 18 | 20 | 20 | 16 |
| Temperature (K) | 1979 | 2023 | 2573 | 2473 | 2473 | 2573 | 2573 | 2473 |
| Duration (min) | 10 | 1 | 1 | 4 | 4 | 1 | 1 | 1 |
| Pressure media | MgO+Cr ₂ O ₃ |
| Capsule | MgO SC |
| Silicate composition (oxide wt.%) | | | | | | | | |
| n | 13 | 19 | 13 | 9 | 22 | 15 | 13 | 15 |
| SiO ₂ | 35.29 ± 0.90 | 48.54 ± 1.04 | 39.39 ± 0.55 | 44.82 ± 0.35 | 39.16 ± 0.16 | 39.45 ± 0.68 | 39.90 ± 0.34 | 37.78 ± 0.43 |
| Al ₂ O ₃ | 9.72 ± 1.25 | 12.07 ± 0.58 | 9.09 ± 0.29 | 14.12 ± 0.95 | 8.83 ± 0.14 | 9.32 ± 0.07 | 8.93 ± 0.07 | 9.73 ± 0.11 |
| CaO | 6.96 ± 0.99 | 12.33 ± 0.41 | 9.10 ± 0.45 | 10.32 ± 0.07 | 9.69 ± 0.10 | 9.36 ± 0.26 | 9.48 ± 0.21 | 8.98 ± 0.24 |
| MgO | 35.89 ± 1.86 | 15.35 ± 0.30 | 35.61 ± 0.91 | 23.44 ± 0.37 | 30.42 ± 0.18 | 33.36 ± 0.97 | 31.53 ± 0.51 | 36.88 ± 0.68 |
| FeO | 9.98 ± 0.26 | 8.45 ± 0.54 | 5.99 ± 0.12 | 4.86 ± 0.45 | 7.79 ± 0.07 | 6.15 ± 0.14 | 6.52 ± 0.11 | 5.93 ± 0.12 |
| Na ₂ O | 0.69 ± 0.11 | 1.75 ± 0.14 | 1.16 ± 0.04 | 1.00 ± 0.16 | 1.06 ± 0.03 | 1.34 ± 0.03 | 1.26 ± 0.03 | 1.11 ± 0.03 |
| TiO ₂ | 0.70 ± 0.10 | 0.78 ± 0.08 | 0.68 ± 0.04 | 0.77 ± 0.07 | 0.82 ± 0.03 | 0.72 ± 0.02 | 0.67 ± 0.04 | 0.73 ± 0.02 |
| K ₂ O | 0.22 ± 0.03 | 0.10 ± 0.02 | 0.14 ± 0.01 | 0.11 ± 0.02 | 0.14 ± 0.01 | 0.15 ± 0.01 | 0.12 ± 0.005 | 0.12 ± 0.01 |
| P ₂ O ₅ | 0.08 ± 0.01 | 0.02 ± 0.005 | 0.01 ± 0.000 | 0.01 ± 0.001 | 0.09 ± 0.02 | 0.01 ± 0.000 | 0.04 ± 0.002 | 0.01 ± 0.000 |
| SO ₂ | 0.16 ± 0.02 | 0.01 ± 0.001 | 0.01 ± 0.001 | 0.002 ± 0.001 | 0.11 ± 0.01 | 0.01 ± 0.001 | 0.27 ± 0.01 | 0.01 ± 0.001 |
| Total | 100.10 ± 0.60 | 100.03 ± 0.98 | 101.73 ± 0.21 | 100.22 ± 0.21 | 99.99 ± 0.26 | 100.56 ± 0.18 | 99.99 ± 0.16 | 101.88 ± 0.11 |
| Sn (ppm) | 1385 ± 65 | 368 ± 151 | 272 ± 8 | 208 ± 20 | 2497 ± 258 | 259 ± 72 | 2407 ± 415 | 250 ± 34 |
| Cd (ppm) | 2119 ± 432 | 3761 ± 1037 | 1966 ± 48 | 3673 ± 211 | 3490 ± 250 | 2991 ± 749 | 2564 ± 517 | 2626 ± 50 |
| Bi (ppm) | 35 ± 6 | 126 ± 105 | 52 ± 4 | 50 ± 12 | 157 ± 46 | 54 ± 15 | 183 ± 30 | 64 ± 16 |
| Sb (ppm) | 72 ± 18 | 19 ± 8 | 10 ± 2 | 5 ± 1 | 144 ± 80 | 10 ± 3 | 113 ± 19 | 22 ± 13 |
| Tl (ppm) | 2348 ± 119 | 5875 ± 3597 | 1098 ± 291 | 609 ± 66 | 733 ± 449 | 622 ± 184 | 1133 ± 205 | 841 ± 50 |
| Metal composition (wt.%) | | | | | | | | |
| n | 10 | 18 | 39 | 33 | 43 | 19 | 16 | 9 |
| Fe | 59.99 ± 1.32 | 87.00 ± 0.60 | 78.02 ± 0.50 | 78.77 ± 0.35 | 63.29 ± 0.35 | 78.26 ± 0.82 | 62.90 ± 0.82 | 76.38 ± 5.09 |
| Sn | 4.65 ± 0.26 | 4.80 ± 0.11 | 5.58 ± 0.09 | 4.92 ± 0.05 | 6.35 ± 0.19 | 4.19 ± 0.31 | 6.60 ± 0.23 | 4.24 ± 0.36 |
| P | 0.001 ± 0.000 | 0.17 ± 0.04 | 0.08 ± 0.005 | 0.06 ± 0.005 | 0.01 ± 0.001 | 0.09 ± 0.01 | 0.03 ± 0.01 | 0.06 ± 0.01 |
| S | 17.90 ± 0.44 | 0.32 ± 0.05 | 0.31 ± 0.01 | 0.23 ± 0.01 | 15.91 ± 0.22 | 0.30 ± 0.02 | 16.73 ± 0.69 | 0.23 ± 0.02 |
| Si | 0.03 ± 0.001 | N.D. | 0.05 ± 0.01 | 0.04 ± 0.005 | 0.04 ± 0.01 | 0.23 ± 0.06 | 0.01 ± 0.01 | 0.04 ± 0.01 |
| O | 1.97 ± 0.18 | 0.19 ± 0.06 | 1.25 ± 0.14 | 0.99 ± 0.13 | 1.55 ± 0.11 | 0.36 ± 0.07 | 1.17 ± 0.35 | 0.38 ± 0.10 |
| Ti | N.D. | N.D. | N.D. | N.D. | N.D. | 0.003 ± 0.001 | N.D. | N.D. |
| Mg | 0.09 ± 0.003 | 0.23 ± 0.06 | 0.18 ± 0.03 | 0.13 ± 0.01 | 0.11 ± 0.02 | 0.12 ± 0.004 | 0.41 ± 0.33 | 0.12 ± 0.01 |
| Cd | 1.82 ± 0.28 | 0.35 ± 0.09 | 0.73 ± 0.06 | 0.87 ± 0.05 | 0.58 ± 0.03 | 1.42 ± 0.15 | 0.50 ± 0.07 | 2.01 ± 1.32 |
| Bi | 1.73 ± 0.15 | 0.37 ± 0.12 | 1.66 ± 0.09 | 2.24 ± 0.08 | 2.44 ± 0.19 | 2.26 ± 0.17 | 2.02 ± 0.45 | 3.47 ± 2.07 |
| Sb | 3.01 ± 0.21 | 2.63 ± 0.12 | 3.28 ± 0.06 | 3.25 ± 0.03 | 3.05 ± 0.08 | 4.30 ± 0.34 | 3.47 ± 0.23 | 3.29 ± 0.21 |
| Tl | 1.04 ± 0.11 | 0.32 ± 0.07 | 1.82 ± 0.16 | 1.73 ± 0.09 | 0.01 ± 0.005 | 2.03 ± 0.14 | 0.17 ± 0.07 | 2.26 ± 1.53 |
| Total | 98.17 ± 0.13 | 99.99 ± 0.68 | 98.15 ± 0.28 | 98.03 ± 0.13 | 98.07 ± 0.18 | 98.48 ± 0.32 | 96.85 ± 0.33 | 98.55 ± 0.43 |
| D_{Cd} | 8.8 ± 2.2 | 1.0 ± 0.4 | 4.5 ± 0.4 | 2.7 ± 0.2 | 1.7 ± 0.1 | 5.8 ± 1.6 | 2.0 ± 0.5 | 9.7 ± 6.3 |
| $\log K_d^{Cd}$ | 0.05 ± 0.11 | -1.14 ± 0.16 | -0.65 ± 0.04 | -0.96 ± 0.05 | -0.80 ± 0.04 | -0.54 ± 0.12 | -0.81 ± 0.11 | -0.34 ± 0.29 |
| D_{Bi} | 513 ± 96 | 32 ± 28 | 380 ± 38 | 507 ± 127 | 157 ± 48 | 510 ± 150 | 113 ± 32 | 690 ± 447 |
| $\log K_d^{Bi}$ | 1.36 ± 0.08 | -0.23 ± 0.39 | 0.62 ± 0.04 | 0.63 ± 0.12 | 0.65 ± 0.13 | 0.75 ± 0.13 | 0.39 ± 0.12 | 0.85 ± 0.28 |
| D_{Sb} | 428 ± 109 | 1497 ± 646 | 3870 ± 771 | 6935 ± 1198 | 213 ± 118 | 5146 ± 1676 | 312 ± 56 | 1904 ± 1142 |
| $\log K_d^{Sb}$ | 1.28 ± 0.11 | 1.45 ± 0.19 | 1.63 ± 0.09 | 1.77 ± 0.09 | 0.79 ± 0.24 | 1.76 ± 0.14 | 0.83 ± 0.08 | 1.29 ± 0.26 |
| D_{Tl} | 4.5 ± 0.5 | 0.6 ± 0.4 | 20.0 ± 5.6 | 32.1 ± 3.9 | 0.2 ± 0.1 | 39.6 ± 12.1 | 1.5 ± 0.7 | 33.9 ± 23.1 |
| $\log K_d^{Tl}$ | 0.21 ± 0.05 | -0.81 ± 0.29 | 0.65 ± 0.12 | 0.82 ± 0.07 | -1.28 ± 0.33 | 0.95 ± 0.13 | -0.36 ± 0.20 | 0.87 ± 0.30 |
| ΔIW | -1.80 | -2.30 | -2.61 | -2.76 | -2.06 | -2.61 | -2.22 | -2.65 |

Elemental and stable isotopic fractionations of siderophile elements

Table 5.2 (*continued*)

| Experiment | E317 | E342 | E345 | H4735 | H4950 | H4951 | H4952 | E396 | E397 |
|-----------------------------------|--------------|---------------|-------------------|------------------------------------|------------------------------------|------------------------------------|------------------------------------|---------------|---------------|
| Starting material | A | A | A | B | A | A | B | B | B |
| Pressure (GPa) | 2 | 2 | 2 | 10 | 12 | 14 | 12 | 2 | 2 |
| Temperature (K) | 1873 | 1773 | 2273 | 2273 | 2273 | 2373 | 2373 | 1873 | 1773 |
| Duration (min) | 5 | 15 | 1 | 5 | 5 | 2 | 2 | 5 | 15 |
| Pressure media | Talc-pyrex | Talc-pyrex | BaCO ₃ | MgO+Cr ₂ O ₃ | Talc-pyrex | Talc-pyrex |
| Capsule | MgO | MgO | MgO | MgO SC | MgO SC | MgO SC | MgO SC | MgO | MgO |
| Silicate composition (oxide wt.%) | | | | | | | | | |
| n | 21 | 18 | 25 | 30 | 13 | 14 | 10 | 13 | 29 |
| SiO ₂ | 40.05 ± 0.46 | 41.14 ± 0.26 | 30.15 ± 0.51 | 37.66 ± 0.20 | 38.57 ± 0.16 | 37.99 ± 0.32 | 36.54 ± 0.54 | 41.44 ± 1.43 | 39.79 ± 0.19 |
| Al ₂ O ₃ | 10.66 ± 1.12 | 10.00 ± 1.23 | 8.26 ± 0.15 | 9.24 ± 0.15 | 9.10 ± 0.25 | 10.16 ± 0.17 | 8.27 ± 0.13 | 10.06 ± 0.76 | 12.56 ± 0.31 |
| CaO | 8.54 ± 0.96 | 7.94 ± 1.05 | 7.60 ± 0.15 | 8.60 ± 0.18 | 9.22 ± 0.19 | 9.26 ± 0.23 | 8.66 ± 0.28 | 7.65 ± 0.70 | 10.15 ± 0.31 |
| MgO | 29.35 ± 2.56 | 27.88 ± 2.97 | 28.59 ± 0.84 | 34.31 ± 0.31 | 35.71 ± 0.36 | 34.74 ± 0.42 | 37.06 ± 0.60 | 24.58 ± 1.02 | 20.12 ± 0.75 |
| FeO | 8.26 ± 0.25 | 10.11 ± 0.12 | 11.66 ± 0.24 | 7.09 ± 0.10 | 5.67 ± 0.13 | 5.95 ± 0.09 | 7.41 ± 0.09 | 10.64 ± 0.86 | 13.39 ± 0.10 |
| Na ₂ O | 1.85 ± 0.22 | 1.53 ± 0.21 | 1.15 ± 0.03 | 0.78 ± 0.02 | 1.18 ± 0.05 | 1.22 ± 0.04 | 1.01 ± 0.04 | 2.06 ± 0.13 | 1.99 ± 0.05 |
| TiO ₂ | 0.71 ± 0.08 | 0.68 ± 0.09 | 0.46 ± 0.01 | 0.72 ± 0.03 | 0.70 ± 0.03 | 0.73 ± 0.03 | 0.71 ± 0.03 | 0.69 ± 0.07 | 0.88 ± 0.03 |
| K ₂ O | 0.20 ± 0.02 | 0.15 ± 0.02 | 0.15 ± 0.003 | 0.16 ± 0.01 | 0.13 ± 0.01 | 0.14 ± 0.01 | 0.09 ± 0.01 | 0.20 ± 0.02 | 0.17 ± 0.003 |
| P ₂ O ₅ | 0.01 ± 0.001 | 0.02 ± 0.002 | 0.06 ± 0.003 | 0.06 ± 0.003 | 0.01 ± 0.000 | 0.01 ± 0.001 | 0.07 ± 0.003 | 0.07 ± 0.01 | 0.09 ± 0.001 |
| SO ₂ | 0.01 ± 0.001 | 0.01 ± 0.001 | 0.05 ± 0.003 | 0.12 ± 0.01 | 0.01 ± 0.001 | 0.01 ± 0.001 | 0.55 ± 0.04 | 0.18 ± 0.02 | 0.24 ± 0.01 |
| SuO | | | | | | | | 0.07 ± 0.01 | 0.08 ± 0.003 |
| CdO | | | | | | | | 0.09 ± 0.01 | 0.11 ± 0.003 |
| Bi ₂ O ₃ | | | | | | | | 0.002 ± 0.001 | 0.001 ± 0.000 |
| Sb ₂ O ₃ | | | | | | | | 0.10 ± 0.01 | 0.14 ± 0.005 |
| Tl ₂ O ₃ | | | | | | | | 0.22 ± 0.02 | 0.24 ± 0.01 |
| Total | 99.99 ± 0.31 | 99.74 ± 0.28 | 88.61 ± 0.51 | 99.30 ± 0.17 | 100.89 ± 0.12 | 100.76 ± 0.13 | 101.30 ± 0.26 | 98.18 ± 0.36 | 100.08 ± 0.50 |
| Su (ppm) | 268 ± 80 | 300 ± 136 | 1146 ± 226 | 1008 ± 100 | 222 ± 19 | 188 ± 26 | 2106 ± 146 | | |
| Cd (ppm) | 982 ± 292 | 1677 ± 736 | 1774 ± 545 | 2528 ± 57 | 2621 ± 80 | 2458 ± 113 | 1628 ± 75 | | |
| Bi (ppm) | 4 ± 1 | 4 ± 3 | 140 ± 199 | 29 ± 9 | 59 ± 5 | 46 ± 6 | 114 ± 54 | | |
| Sb (ppm) | 2 ± 1 | 1 ± 1 | 81 ± 81 | 30 ± 8 | 13 ± 2 | 10 ± 1 | 108 ± 55 | | |
| Tl (ppm) | 2282 ± 651 | 3600 ± 1527 | 2401 ± 708 | 702 ± 72 | 1354 ± 141 | 805 ± 90 | 938 ± 88 | | |
| Metal composition (wt.%) | | | | | | | | | |
| n | 31 | 27 | 25 | 28 | 14 | 11 | 15 | 12 | 14 |
| Fe | 87.58 ± 0.26 | 86.76 ± 0.64 | 89.51 ± 0.16 | 64.91 ± 0.35 | 80.66 ± 0.61 | 80.73 ± 0.72 | 60.63 ± 0.60 | 62.80 ± 1.26 | 63.33 ± 0.55 |
| Su | 3.82 ± 0.05 | 3.86 ± 0.03 | 3.43 ± 0.06 | 5.29 ± 0.06 | 5.08 ± 0.11 | 4.55 ± 0.05 | 5.21 ± 0.07 | 5.33 ± 0.21 | 5.20 ± 0.13 |
| P | 0.08 ± 0.004 | 0.09 ± 0.004 | 0.001 ± 0.000 | 0.01 ± 0.001 | 0.09 ± 0.004 | 0.11 ± 0.004 | 0.01 ± 0.002 | 0.02 ± 0.004 | 0.02 ± 0.002 |
| S | 0.24 ± 0.01 | 0.24 ± 0.01 | 0.10 ± 0.01 | 16.15 ± 0.14 | 0.26 ± 0.01 | 0.29 ± 0.02 | 19.98 ± 0.26 | 10.31 ± 0.40 | 11.08 ± 0.23 |
| Si | 0.02 ± 0.002 | 0.01 ± 0.002 | 0.01 ± 0.001 | 0.01 ± 0.002 | 0.04 ± 0.01 | 0.02 ± 0.004 | 0.02 ± 0.001 | 0.01 ± 0.004 | 0.03 ± 0.03 |
| O | 0.01 ± 0.01 | 0.16 ± 0.04 | N.D. | 1.32 ± 0.13 | 0.19 ± 0.03 | 0.17 ± 0.05 | 1.41 ± 0.27 | 0.42 ± 0.07 | 0.55 ± 0.05 |
| Ti | N.D. | 0.004 ± 0.001 | 0.003 ± 0.001 | N.D. | 0.01 ± 0.002 | N.D. | N.D. | 0.002 ± 0.001 | 0.003 ± 0.001 |
| Mg | 0.14 ± 0.002 | 0.14 ± 0.002 | 0.15 ± 0.004 | 0.10 ± 0.00 | 0.13 ± 0.004 | 0.13 ± 0.004 | 0.08 ± 0.001 | 0.09 ± 0.01 | 0.09 ± 0.01 |
| Cd | 0.26 ± 0.03 | 0.29 ± 0.06 | 0.03 ± 0.01 | 1.42 ± 0.05 | 0.82 ± 0.07 | 0.67 ± 0.04 | 0.66 ± 0.05 | 1.77 ± 0.14 | 1.80 ± 0.12 |
| Bi | 0.15 ± 0.03 | 0.33 ± 0.08 | 0.04 ± 0.01 | 1.54 ± 0.17 | 1.38 ± 0.09 | 1.42 ± 0.07 | 1.45 ± 0.25 | 2.08 ± 0.17 | 2.52 ± 0.25 |
| Sb | 2.60 ± 0.03 | 2.71 ± 0.03 | 3.10 ± 0.07 | 3.02 ± 0.05 | 3.54 ± 0.07 | 3.37 ± 0.05 | 1.85 ± 0.02 | 2.94 ± 0.17 | 2.82 ± 0.13 |
| Tl | 0.05 ± 0.01 | 0.09 ± 0.02 | 0.04 ± 0.01 | 0.36 ± 0.02 | 1.18 ± 0.09 | 0.87 ± 0.07 | 0.08 ± 0.04 | 0.39 ± 0.08 | 0.69 ± 0.11 |
| Total | 98.74 ± 0.22 | 99.10 ± 0.55 | 97.71 ± 0.15 | 98.25 ± 0.26 | 98.08 ± 0.50 | 98.24 ± 0.66 | 97.26 ± 0.18 | 92.68 ± 0.49 | 94.06 ± 0.17 |
| D_{Cd} | 2.9 ± 0.9 | 2.0 ± 1.0 | 0.2 ± 0.1 | 5.7 ± 0.3 | 3.8 ± 0.4 | 3.3 ± 0.3 | 4.2 ± 0.4 | 21.4 ± 2.5 | 18.8 ± 1.3 |
| $\log K_d^{Cd}$ | -0.73 ± 0.14 | -0.80 ± 0.21 | -1.72 ± 0.18 | -0.33 ± 0.02 | -0.77 ± 0.04 | -0.81 ± 0.03 | -0.41 ± 0.04 | 0.45 ± 0.06 | 0.49 ± 0.03 |
| D_{Bi} | 450 ± 178 | 907 ± 606 | 3 ± 4 | 537 ± 170 | 287 ± 29 | 374 ± 55 | 131 ± 65 | 1096 ± 428 | 3123 ± 1155 |
| $\log K_d^{Bi}$ | 0.86 ± 0.17 | 1.31 ± 0.29 | -1.02 ± 0.63 | 1.11 ± 0.14 | 0.43 ± 0.05 | 0.58 ± 0.06 | 0.56 ± 0.22 | 1.72 ± 0.17 | 2.32 ± 0.16 |
| D_{Sb} | 13981 ± 5108 | 23454 ± 13100 | 386 ± 386 | 1004 ± 281 | 3211 ± 519 | 4097 ± 478 | 175 ± 88 | 35 ± 4 | 24 ± 1 |
| $\log K_d^{Sb}$ | 2.35 ± 0.16 | 2.73 ± 0.24 | 1.08 ± 0.43 | 1.38 ± 0.12 | 1.48 ± 0.07 | 1.62 ± 0.05 | 0.69 ± 0.22 | 0.23 ± 0.06 | 0.21 ± 0.03 |
| D_{Tl} | 0.3 ± 0.1 | 0.3 ± 0.1 | 0.2 ± 0.1 | 5.1 ± 0.6 | 10.7 ± 1.4 | 0.9 ± 1.8 | 0.9 ± 0.5 | 3.7 ± 0.8 | 5.9 ± 0.9 |
| $\log K_d^{Tl}$ | -1.17 ± 0.14 | -1.08 ± 0.20 | -1.28 ± 0.16 | 0.17 ± 0.05 | 0.35 ± 0.06 | 0.45 ± 0.06 | -0.55 ± 0.21 | 0.13 ± 0.10 | 0.38 ± 0.07 |
| ΔIW | -2.39 | -2.19 | -2.01 | -2.17 | -2.71 | -2.66 | -2.07 | -1.87 | -1.65 |

Metal–silicate partitioning

The distribution of an element M of valence state n between metal and silicate at equilibrium conditions can be expressed with the partition coefficient:

$$D_M = \frac{X_M^{metal}}{X_{MO_{n/2}}^{silicate}} \quad (5.2)$$

where X_i are the mole fractions of element M or its oxide in the metal and silicate phases. The equilibrium of M between metal and silicate can also be represented as a chemical exchange redox reaction:



The exchange coefficient K of this reaction will allow to quantify the partitioning of element M independently of fO_2 , simplifying the study of the effect of other parameters such as pressure, temperature and composition:

$$K = \frac{(a_{FeO}^{silicate})^{n/2} \cdot a_M^{metal}}{a_{MO_{n/2}}^{silicate} \cdot (a_{Fe}^{metal})^{n/2}} \quad (5.4)$$

where a_i are the activities of the different components, such that $a_i = \gamma_i \cdot x_i$, where γ_i is the activity coefficient and x_i is the mole fraction:

$$\log K = \log \frac{(x_{FeO}^{silicate})^{n/2} \cdot x_M^{metal}}{x_{MO_{n/2}}^{silicate} \cdot (x_{Fe}^{metal})^{n/2}} + \log \frac{\gamma_M^{metal}}{(\gamma_{Fe}^{metal})^{n/2}} + \log \frac{(\gamma_{FeO}^{silicate})^{n/2}}{\gamma_{MO_{n/2}}^{silicate}} \quad (5.5)$$

$$\log K = \log \frac{D_M}{(D_{Fe})^{n/2}} + \log \frac{\gamma_M^{metal}}{(\gamma_{Fe}^{metal})^{n/2}} + \log \frac{(\gamma_{FeO}^{silicate})^{n/2}}{\gamma_{MO_{n/2}}^{silicate}} \quad (5.6)$$

$$\log K = \log K_d^M + \log \frac{\gamma_M^{metal}}{(\gamma_{Fe}^{metal})^{n/2}} + \log \frac{(\gamma_{FeO}^{silicate})^{n/2}}{\gamma_{MO_{n/2}}^{silicate}} \quad (5.7)$$

The term K_d^M can be calculated for each experiment as it depends on mole fractions of M and Fe in the metal and silicate phases. The determination of the valence state of M is essential for the calculation of the equilibrium constant and further parameterisation of the partitioning. The preferred valence state for Cd is 2+ in numerous previous studies (Righter et al. 2017b, 2019, Wood et al. 2014). It can be demonstrated that $\log D_M$ is a function of $\frac{n}{4} \log fO_2$, allowing to calculate the

valence state from a selection of experiments that are similar in pressure, temperature and composition over a sufficient range of fO_2 (Siebert et al. 2011). Our data combined with literature data allows to provide such an estimation of the valence state of Cd over more than two log units of fO_2 (figure 5.1). The slope of the regression line is equal to 0.5, which corresponds to a 2+ valence state. The scarcity of the data and insufficient oxygen fugacity range prevents from demonstrating the valence state of Bi, Sb and Tl by the same method as that of Cd on figure 5.1. However, Sb has been studied assuming largely a 3+ valence state (Righter et al. 2009, 2017a, b, Steenstra et al. 2017, Vogel et al. 2018, Wood et al. 2014) which was also favoured in this study. Bismuth partitioning was also parameterised as a trivalent cation in agreement with previous studies (Righter et al. 2017b, 2019), and Tl as a monovalent cation (Wood et al. 2014, 2008). XANES studies are needed in order to quantitatively determine the valence state of these elements in silicate melts.

The partitioning of Cd, Bi, Sb and Tl represented by the exchange coefficient $\log K_d$ defined in equation 5.7 is presented on figure 5.2 as a function of reciprocal temperature. Cadmium partitioning (figure 5.2a) presents no resolvable effect of temperature or pressure. Experiments performed below 19 GPa and containing significant amounts of S in their metal present enhanced $\log K_d$, suggesting a positive effect of S at those conditions. On figure 5.2b which displays $\log K_d^{Bi}$, temperature notably decreases the partitioning and pressure has a strong positive effect on $\log K_d$. A similar pattern is observed from $\log K_d^{Sb}$ (figure 5.2c). Sulfur has a positive effect on Bi partitioning of experiments at 2 GPa whereas S-bearing experiments at higher pressures present similar $\log K_d$ as S-free experiments at comparable conditions. For Sb, all S-bearing experiment present lower partitioning than their S-free analogues, suggesting a negative effect of S. Pressure and temperature both have a strong and positive effect on $\log K_d^{Tl}$ (figure 5.2d). A discrepancy on the S effect can be observed on figure 5.2d where S-bearing low-pressure experiments present higher partitioning than S-free ones whereas above 10 GPa S-bearing experiments present lower partitioning than their S-free analogues.

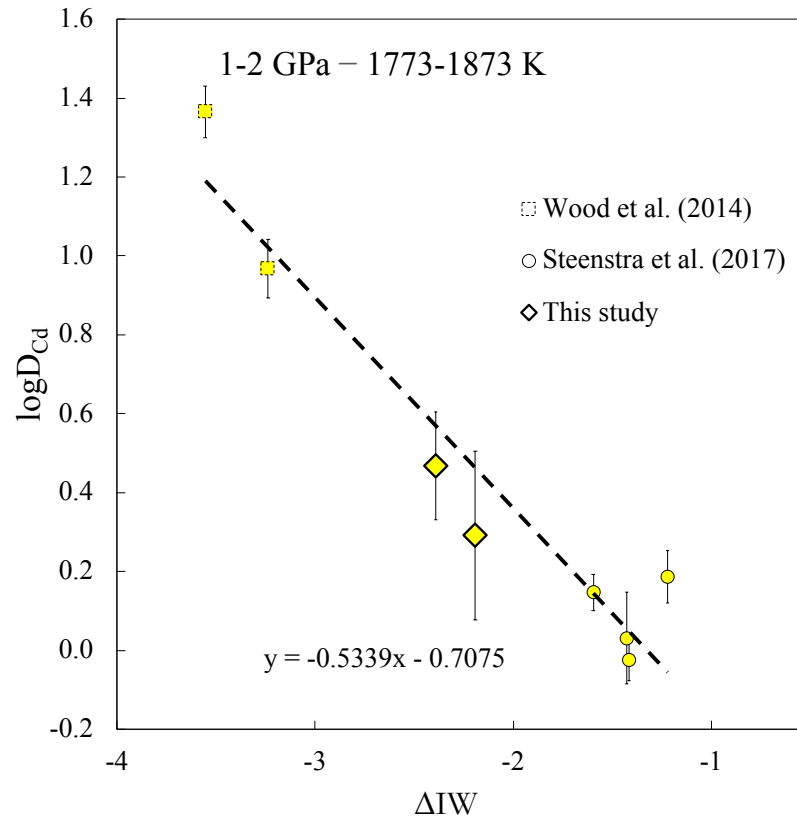


Figure 5.1 – Partition coefficient $\log D_{Cd}$ as a function of oxygen fugacity ΔIW calculated relatively to iron–wüstite (equation 5.1) for all experiments between 1 and 2 GPa and 1773–1873 K of this study and data compiled from the literature (Steenstra et al. 2017, Wood et al. 2014). Errors correspond to 1 standard deviation (σ) and were propagated from EPMA and LA-ICPMS measurements of this study and from the literature. The variation in partition coefficient over a significant interval of fO_2 allows accurate determination of the valence state of Cd. In fact, it can be demonstrated that $\log D_{Cd}$ is a function of $\frac{n}{4} \log fO_2$ (Siebert et al. 2011). With the slope of the regression line shown on this figure equal to 0.5, we demonstrate that Cd has a valence of 2+ over an fO_2 range of more than 2 log units.

Discussion

Equilibrium conditions

Achievement of equilibrium between metal and silicate is critical for accurate characterisation and parameterisation of the studied elements behaviours at 152

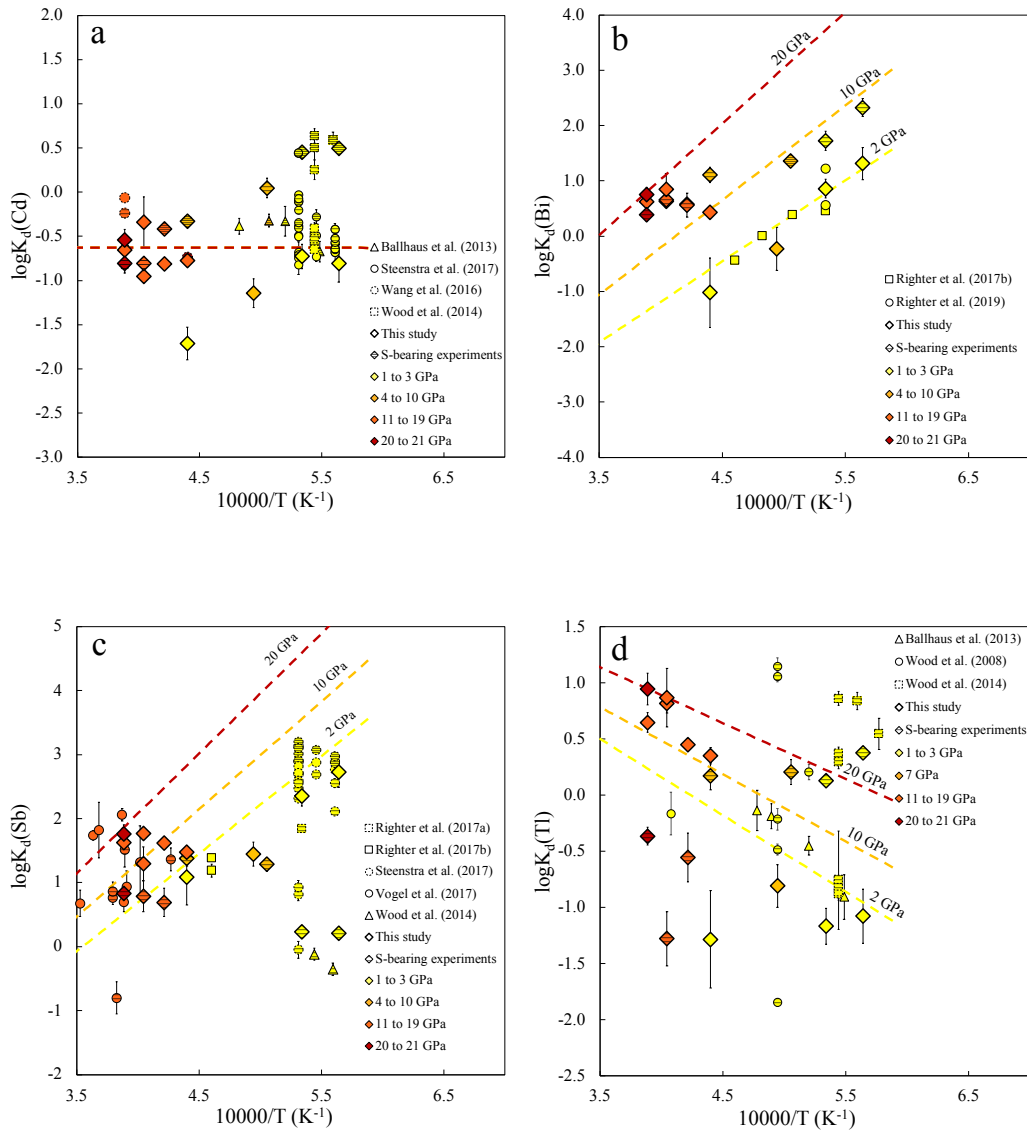


Figure 5.2 – Exchange coefficient $\log K_d$ as a function of reciprocal temperature for Cd, Bi, Sb and Tl and for all experiments of this study and literature data. Errors are 1 standard deviation (σ) propagated from EPMA and LA-ICPMS measurements of this study and from the literature. Experiments holding more than 1 mol% of S in the metal part are differentiated by a horizontal lines pattern. All experiments are color-coded according to their run pressure: 1–3 GPa in yellow, 4–10 GPa in orange, 10–19 GPa in light red, >19 GPa in dark red. Multilinear regression fits are also displayed at IW-2 in the following conditions: 2 GPa, 10 GPa, and 20 GPa with no S in the metal.

such conditions. Sufficient time durations allowing complete fusion of the sample (Thibault and Walter 1995), as well as thorough petrographic characterisation showing homogeneous phase segregation, were achieved in this study. Our data presents overarching trends that can be described thermodynamically, thus providing further evidence of equilibrium.

Metal–silicate partitioning of MSVEs and Earth accretion

Thermodynamic parameterisation

Parameter $\log K_d$ defined in equation 5.7 was calculated for Cd, Bi, Sb and Tl in each experiment and reported in table 5.2 and presented in figure 5.2. The ratio of oxide activity coefficients was neglected as it is predicted to have little effect on the equilibrium constant, especially for low—below 4+—valence state elements (Wade and Wood 2005). $\log K_d$ can be expressed as follows:

$$\log K_d = a + b \cdot \frac{1}{T} + c \cdot \frac{P}{T} - \log \frac{\gamma_M^{metal}}{(\gamma_{Fe}^{metal})^{n/2}} \quad (5.8)$$

The constants a , b and c reported in table 5.3 were computed using the least-squares multivariate linear regression method from measurements on experiments of this study and associated literature with a metal devoid of S, Si and C. These parameters were used to calculate the regression lines displayed in figure 5.2 and 5.3. The interaction parameter was calculated using the partitioning of S-bearing experiments:

$$\log K - \log K_d = \log \frac{\gamma_M^{metal}}{(\gamma_{Fe}^{metal})^{n/2}} \quad (5.9)$$

The activity coefficients γ_M^{metal} and γ_{Fe}^{metal} were deduced using the interaction parameter approach developed by Ma (2001):

$$\begin{aligned} \log K_d = \log \frac{D_M}{(D_{Fe})^{n/2}} = & a + b \cdot \frac{1}{T} + c \cdot \frac{P}{T} - \log \gamma_M^0 + \varepsilon_M^M \cdot \log(1 - x_M) \\ & + \varepsilon_M^S \cdot \log(1 - x_S) + \left(\frac{n}{2} - 1\right) \cdot \varepsilon_S^S \cdot (x_S + \log(1 - x_S)) \end{aligned} \quad (5.10)$$

Table 5.3 – Summary of regression parameters calculated for Cd, Bi, Sb and Tl using experiments of this study and literature data.

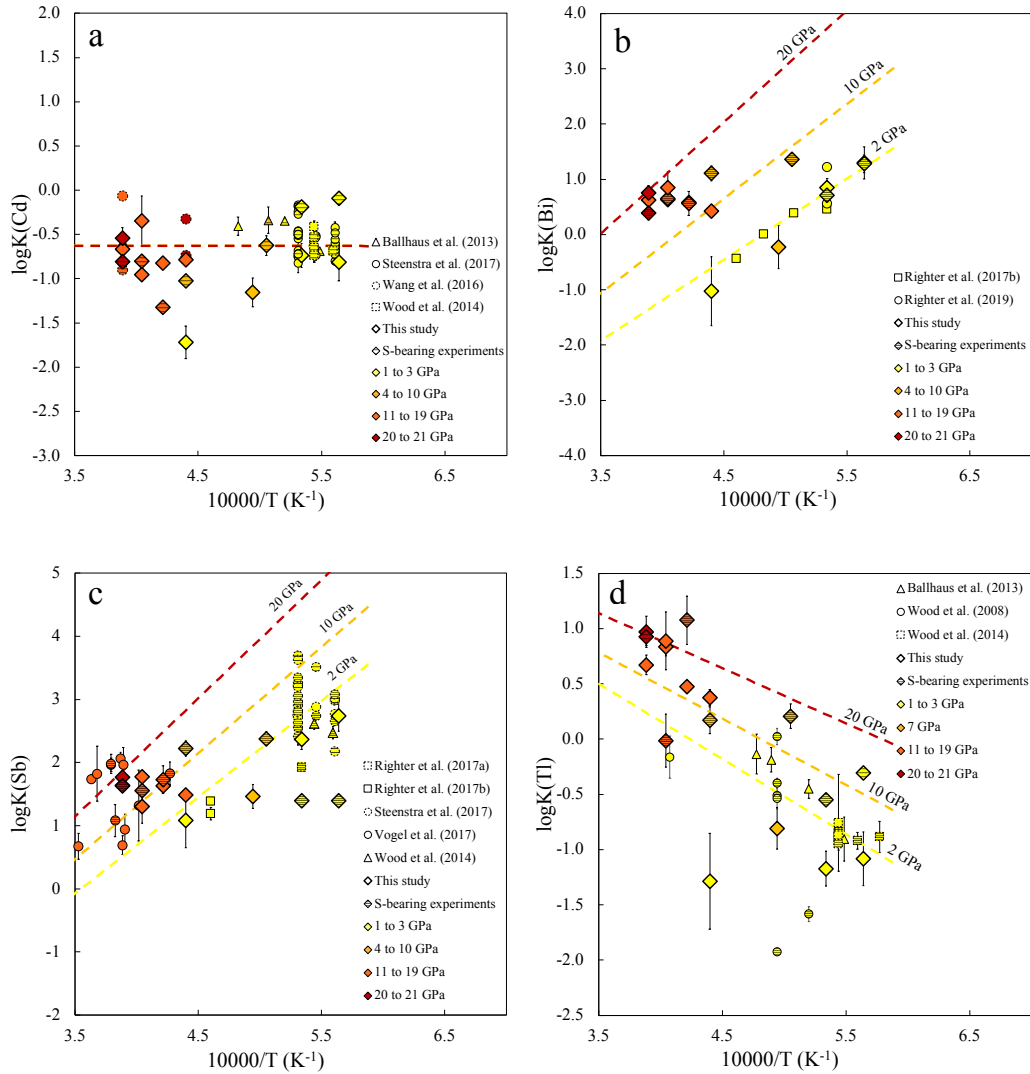
| Parameter | Cd | | Bi | | Sb | | Tl | |
|-------------------|----------------|--------|---------------|--------|--------------|--------|----------------|--------|
| a | -0.63 | ± 0.21 | -7.05 | ± 1.04 | -5.41 | ± 0.99 | 2.88 | ± 0.65 |
| b | – | | 14037 | ± 2020 | 14870 | ± 1745 | -7010 | ± 1200 |
| c | – | | 308 | ± 40 | 193 | ± 61 | 101 | ± 28 |
| ε_M^S | -4.29 | ± 0.27 | -4.11 | ± 1.07 | 10.48 ± 0.66 | | (below 7 GPa) | |
| | (below 18 GPa) | | (below 3 GPa) | | | | (above 10 GPa) | |

where ε_j^i represents interaction parameter of i on j , and γ_M^0 the activity coefficient of M . ε_M^S is the interaction parameter representing the effect of the presence of S on the activity of M . ε_M^S was fitted to the experimental dataset for all four elements using equation 5.10 and reported in table 5.3. Values of $\log K$, calculated for all experiments of the dataset, are shown in figure 5.3. This expression of M metal–silicate partitioning only displays the effect of pressure and temperature. S-bearing experiments are corrected for their S effect and show similar partitioning to experiments of comparable P,T conditions that are devoid of S.

Core formation models

Core formation modelling is used to assess the partition coefficient of an element at each incremental step of a differentiated planetary body’s accretion (Rubie et al. 2015). The intended purpose is to compare the final partition coefficient obtained to the observed partitioning of an element in a planetary body of interest. By testing multiple accretion scenarios and their effects on the distribution of the element of interest, it is possible to propose one or a variety of scenarios that can account for the observed abundance of an element in the mantle of a differentiated planet.

The experimentally computed regression parameters that thermodynamically describe the behavior of Cd, Bi, Sb and Tl in a metal–silicate equilibrium (table



5.3) were used to recalculate the partitioning over the course of Earth's accretion, simulating several different plausible scenarios, using the following equation:

$$\log D_M = \log K_d^M - \frac{n}{2} \cdot \log \frac{x_{\text{FeO}}}{x_{\text{Fe}}} \quad (5.11)$$

We used continuous core formation models (Wade and Wood 2005) in which the evolution of pressure and temperature conditions at the base of a deep magma ocean was reconstructed over the course of the accretion, as a function of the accreted fraction. Planetesimals and differentiated planetary embryos of increasing

Figure 5.3 – $\log K$ determined experimentally as a function of reciprocal temperature for Cd, Bi, Sb and Tl and for all experiments of this study and literature data. Errors correspond to 1 standard deviation (σ) and were propagated from EPMA and LA-ICPMS measurements of this study and from the literature. Experiments holding more than 1 mol% of S in the metal are identified by a horizontal lines pattern. All experiments are color-coded according to their run pressure: 1–3 GPa in yellow, 4–10 GPa in orange, 11–19 GPa in light red, >19 GPa in dark red. Multilinear regression fits are also displayed at IW-2 in the following conditions: 2 GPa, 10 GPa, and 20 GPa with no S in the metal. $\log K$ being defined as $a + b \cdot \frac{1}{T} + c \cdot \frac{P}{T}$, this figure displays the effect of pressure and temperature alone on M partitioning between metal and silicate, meaning that the partitioning is corrected for the effect of S.

sizes are incorporated one by one to form the planet. The f_{O_2} of present-day core–mantle equilibrium was used (IW-2.3) during the accretion for all models. All presented models were computed with 1.9 wt.% of S in the core of the Earth and differentiated embryos, in agreement with multiple estimates (e.g. McDonough 2003, Suer et al. 2017). Parameter k , defined as the fraction of the core of the accreted embryo that equilibrates with the mantle of the proto-Earth, is used to simulate several degrees of equilibration efficiency. Fluid dynamics analog experiments showed that full equilibration of an impactor’s core with the proto-planet’s core necessitates the metal of the impactor’s core to break down to small size droplets and to segregate into the core of the planet, which is less efficient with increasing impactor size. This effect can be modeled using parameter ε (Deguen et al. 2014) which includes the effect of the mass of silicate that is dragged towards the core along with the metal when core segregation occurs, preventing full equilibration. The formalism established by Deguen et al. (2014) was used to model the efficiency of the equilibrium with more accuracy.

Homogeneous models, where the elements involved—Cd, Bi, Sb, Tl and S—are present in the same concentrations in the accreted material over the course of the accretion, were computed for each of the four elements of interest. A heterogeneous accretion scenario was also modeled, in which the delivery of the volatile elements is concentrated in the later part of the main phases of Earth’s accretion, before core segregation ceased, as proposed in recent studies (Braukmüller et al. 2019, Suer et al. 2017). We also tested the possibility of a late veneer, consisting of the late

accretion of a limited amount of chondritic material which may have been brought after core formation ended, and would therefore be mixed in the mantle with no equilibration with the core. The late veneer is a process known best for explaining the platinum group elements abundances in the Earth’s mantle, which are orders of magnitude higher than their predicted abundances by core segregation, given their highly siderophile behavior (e.g. Day et al. 2016, Holzheid et al. 2000).

Results from the core formation models computed in this study (figure 5.4) were compared to estimations of the core–mantle partition coefficient of Cd, Bi, Sb and Tl, which are based on natural samples measurements. For each element, this estimation is calculated by assuming that the MSVE accreted in similar relative abundance to a lithophile element of similar volatility. In this framework, the additional depletion of the MSVE relative to the canonical volatile lithophile trend is attributed to its segregation into the core. As this is a quantitative approach, each element’s depletion can be calculated and used as to estimate the abundance of a given MSVE in the Earth’s core. Combined with the BSE abundance estimates, an apparent core–mantle partition coefficient can be constituted. Each of Cd, Bi, Sb and Tl was paired with the lithophile element of closest condensation temperature (table 5.4). We provide two estimates, one using condensation temperatures T_{50} from Lodders (2003) and a second one using more recent estimates from Wood et al. (2019), which changes the lithophile reference element for Cd, Bi, Sb, and therefore the core/BSE estimation. We also considered the hockey stick volatile pattern proposed by Braukmüller et al. (2019) which affects Cd, Bi and Tl as their condensation temperatures correspond to the plateau part of the pattern. We used a range including all three of these estimates as the apparent core–mantle value, acting as a “target” for our core formation models.

Results from core formation modelling are presented in figure 5.4. The effect of S on partitioning determined experimentally is varying with the pressure of equilibrium (table 5.3). This was taken into account in the models and the S effect was calculated according to the pressure range when necessary. In calculations considering partial equilibration, D_M is sensitive to the size of the accreted embryos which is why we observe variations on the curves at stages where there is a change of the size of accreted bodies. For Cd, Sb and Tl, a late veneer of 0.5% of the Earth’s mass composed of CI material was found to have negligible effect on the modeled partitioning. Such a process would account for only ~ 10 wt.% of the

Elemental and stable isotopic fractionations of siderophile elements

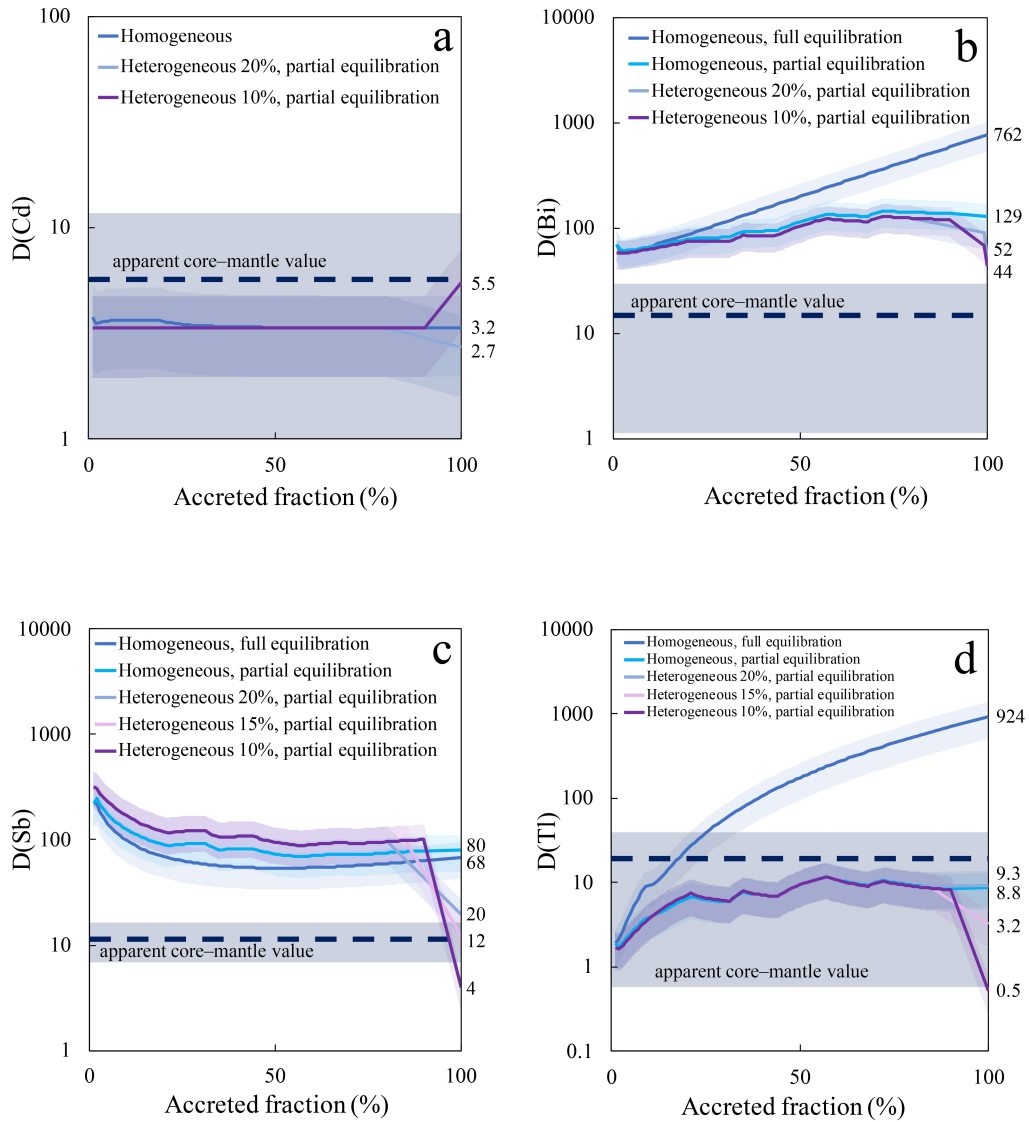
Table 5.4 – Compilation of apparent partition coefficients inferred from CI chondrites and BSE measurements.

| MSVE | Cd | Bi | Sb | Tl |
|----------------------------------|------------------|------------------|-------------------|------------------|
| T ₅₀ (K) ^a | 652 | 746 | 979 | 532 |
| T ₅₀ (K) ^b | 502 | 480 | 890 | 365 |
| BSE (ppb) | 64 ^d | 5 ^d | 12 ^d | 3.5 ^e |
| ± | 19 | 2.5 | 4 | 1.4 |
| CI (ppb) | 675 ^a | 110 ^a | 152 ^a | 143 ^a |
| ± | 6 | 3 | 9 | 2 |
| Core/BSE ^a | 7.1 | 17.2 | 11.8 | 19.2 |
| ± | 4.4 | 11.7 | 4.1 | 18.6 |
| Lithophile reference element | F ^{a,d} | F ^{a,d} | Na ^{a,d} | I ^f |
| Core/BSE ^b | 2.6 | 7.6 | 11.1 | 19.2 |
| ± | 2.6 | 6.4 | 3.9 | 18.6 |
| Lithophile reference element | Cl ^f | Cl ^f | K ^{a,d} | I ^f |
| Core/BSE ^c | 8.6 | 15 | – | 14 |
| Range | 0–11.5 | 1.2–28.9 | 7.2–15.9 | 0.6–37.8 |

^aLodders (2003); ^bWood et al. (2019); ^cBraukmüller et al. (2019); ^dPalme and O’Neill (2003); ^eMcDonough and Sun (1995); ^fClay et al. (2017)

CHAPTER 5. Cd, Bi, Sb and Tl core–mantle distribution

abundance of these elements in the Earth’s mantle, and was therefore not included on the corresponding figures. In the case of Bi, for which a 0.5 wt.% late veneer would raise by 16 wt.% its BSE abundance, the effect is larger and was included in the models presented in figure 5.4b.



Experimental Cd partitioning was found to be independent of pressure and temperature conditions, with a positive effect of S on D_{Cd} reported below 18

Figure 5.4 – Evolution of D_M during Earth’s accretion computed for Cd, Bi, Sb and Tl from core formation models with full and partial equilibration, and homogeneous and heterogeneous scenarios. Apparent core–mantle values are represented as a dark blue zone with its central value as a dashed line. Errors of models are propagated from error percentages on the computed regression coefficients. For all partial equilibration models, ε was computed with $k=0.5$. In calculations involving a partial equilibration, D_M is sensitive to the size of the accreted embryos which is why we observe variations on the curves at stages where there is a change of the size of accreted bodies. All models were computed at constant fO_2 of IW-2.3 and with 1.9 wt.% S in the cores of the Earth and differentiated embryos. **a.** With no pressure and temperature effect, D_{Cd} evolution is the same for homogeneous accretion scenario, whether partial or full equilibration is modeled, with a final partitioning of 3.2 ± 1.4 . The apparent core–mantle value ranges from 0 to 11.5, with all the models computed here being a match to this estimation. However, a heterogeneous scenario with an accretion of the volatiles in the last 10% yields a final D_{Cd} of 5.5 ± 2.3 which is closer to the central estimated value. On the contrary, with a scenario of volatile delivery in the last 20%, the final D_{Cd} is 2.7 ± 1.1 sits further from the central value, due to a different effect of S in the last accreted embryo. **b.** The estimated D_{Bi} of the Earth ranges from 1.3 to 28.9. The reconstructed partitioning for a scenario of full equilibration with compositionally homogeneous accretion is one order of magnitude higher than the observed value, with a final D_{Bi} of 762 ± 225 , and is still significantly higher with a homogeneous scenario with partial equilibration (final $D_{Bi}=129\pm 38$). Two scenarios consider an accretion of the volatiles in the last 10 and 20% of the accretion including a 0.5 wt.% late veneer of CI chondrite-like material and present final D_{Bi} of 44 ± 13 and 52 ± 15 respectively. **c.** In the case of Sb, the scenario of partial equilibration with homogeneous accretion presents a higher final partitioning (80 ± 29) than the full equilibration with homogeneous accretion scenario (68 ± 25) because of the strong negative effect of S which is undermined by a less efficient equilibration. These two scenarios are higher than the apparent core–mantle D_{Sb} which ranges from 7.2 to 15.9. Three heterogeneous scenarios were modeled with an accretion of the volatile elements in the last 10, 15 and 20% of the Earth’s formation and yield final partitioning of respectively 4 ± 1 , 12 ± 4 and 20 ± 7 , the 15% late accretion being the best match to the central observed value. **d.** The apparent core–mantle D_{Tl} value ranges from 0.6 to 37.8. The homogeneous model with full equilibration yields a final D_{Tl} of 924 ± 414 , which is too high to reconcile the experimental data with the observed abundances through this scenario. Using a partial equilibration model allows to match the observed partitioning with the following final D_{Tl} : 8.8 ± 4 for a homogeneous accretion, 3.2 ± 1 for a delivery of volatiles in the last 15% of Earth’s accretion and 9.3 ± 4 for a delivery in the last 20%. A scenario of accretion of the volatiles in the last 10% of the Earth’s accretion presents a final D_{Tl} within error of the target value (0.5 ± 0.2).

GPa. This leads to a full match of all the modeled scenarios with the apparent core–mantle value which ranges from 0 to 11.5 (figure 5.4a), preventing strong arguments in favor of a scenario compared to another. D_{Cd} evolution for a homogeneous accretion leads to a final partitioning of 3.2 ± 1.4 . However, a heterogeneous scenario with an accretion of the volatiles in the last 10% yields a final D_{Cd} of

5.5 ± 2.3 which is closer to the central estimated value. This is due to the fact that the pressure of equilibration in the last accreted embryo, 10% of Earth’s mass, is inferior to 18 GPa, inducing an effect of S that increases the partitioning. On the contrary, with a scenario of volatile delivery in the last 20%, the final accreted embryo is equilibrated at a pressure above 18 GPa, which means that the effect of S is not considered. The final D_{Cd} is 2.7 ± 1.1 and sits further from the central value.

The estimated D_{Bi} of the Earth ranges from 1.2 to 28.9 (table 5.4). The reconstructed partitioning for a scenario of full equilibration with compositionally homogeneous accretion is more than one order of magnitude higher than the observed value, with a final D_{Bi} of 762 ± 225 (figure 5.4b), making this scenario unlikely. A homogeneous scenario with partial equilibration (final $D_{Bi}=129\pm 38$) yields a final partitioning also significantly higher and distinct from the apparent value. It should be noted that a homogeneous accretion with a partial equilibration and a 0.5 *wt.%* late veneer would not meet the upper limit of the estimated core–mantle value with a final D_{Bi} of 63 ± 19 . When considering an accretion of the volatiles in the last 10 and 20% of the accretion including a 0.5 *wt.%* late veneer of CI chondrite-like material, the final D_{Bi} is closer to the observed partitioning, with final D_{Bi} of 44 ± 13 and 52 ± 15 respectively. When using distinct BSE estimate by McDonough (2003) of 2.5 ± 0.75 ppb, the estimated core–mantle partitioning (31 ± 25) is higher and less consistent with the estimate from Braukmüller et al. (2019) but allows for the modeled accretion of the volatile elements in the last 10% with a 0.5% late veneer to reproduce the estimated partitioning within error, with $D_{Bi}=44\pm 13$. Bismuth abundance in the Earth mantle is not well resolved, but by using multiple existing estimates the only scenario in which this abundance can be accounted for involves a heterogeneous accretion of the volatile elements in the last 10% of Earth’s accretion associated to a 0.5 *wt.%* late veneer of chondritic composition.

The core formation models of Sb (figure 5.4c) are unique in the sense that for a homogeneous accretion, the scenario with partial equilibration presents a higher final partitioning (80 ± 29) than with a full equilibration (68 ± 25) because of the strong negative effect of S that is undermined by a less efficient equilibration. These two scenarios are higher than the apparent core–mantle D_{Sb} which ranges from 7 to 16. Three heterogeneous scenarios are presented here with an accretion of

the volatile elements in the last 10, 15 and 20% of the Earth's formation yielding final partition coefficients of respectively 4 ± 1 , 12 ± 4 and 20 ± 7 . The 15% late accretion scenario is the best match to the central observed value and the modeled 20% scenario presents a final D_{Sb} that falls within error of estimated core–mantle value.

The apparent core–mantle D_{Tl} value ranges from 0.6 to 38. A homogeneous model with full equilibration (figure 5.4d) yields a final D_{Tl} of 924 ± 414 , which is significantly higher than the target value, preventing reconciliation of the experimental data with the observed abundances through this scenario. Using a partial equilibration model for the same homogeneous accretion scenario allows to match the observed partitioning with a final D_{Tl} of 8.8 ± 4 . Three heterogeneous accretion models are also presented, with two of them yielding final D_{Tl} within the range of the observed core–mantle value: 3.2 ± 1 for a delivery of volatiles in the last 15% of Earth's accretion and 9.3 ± 4 for a delivery in the last 20%. A scenario of accretion of the volatiles in the last 10% of the Earth's accretion presents a final D_{Tl} lower but within error of the observed value (0.5 ± 0.2).

A homogeneous accretion with full equilibration is only compatible with the observed partitioning in the case of Cd, therefore, such a scenario is not well supported by this study. The apparent core–mantle partition coefficients of Cd and Bi are best reproduced in the case of an accretion of the volatiles in the last 10% of the Earth's accretion with a partial equilibrium, although the Cd models do not allow strong conclusions. The abundances of Sb and Tl in the BSE are best reproduced in a scenario of accretion of the volatile elements in the last 15–20% of Earth's accretion. The abundances of Cd and Tl could also be explained by a homogeneous accretion with partial equilibration. Although Cd, Sb and Tl apparent partitioning can be explained without including a late veneer, no model would fall in the range of the apparent Bi core–mantle value without a 0.5 *wt.*% late veneer, in agreement with previous studies based on different geochemical observables (Holzheid et al. 2000, Médard et al. 2015, Suer et al. 2017). Several scenarios could explain the abundances in the Earth's mantle for most of the elements studied here, however, the most supported scenario includes a partial equilibration and an accretion of the volatile elements in the last 10 to 20% of the Earth's accretion, before core–mantle equilibration ceased, possibly preceded by a 0.5% late veneer composed of CI chondritic material. Such a scenario is also supported by recent studies (Braukmüller

et al. 2019, Mahan et al. 2018a, b, Suer et al. 2017). Lastly, our results advocate for partial equilibration over full equilibration (especially for Bi and Tl) which is a result worth mentioning since the efficiency of the core–mantle equilibration is a debated topic (e.g. Deguen et al. 2014, Kendall and Melosh 2016).

Core formation and Earth’s volatile accretion

A late volatile delivery The experimental study of Cd, Bi, Sb and Tl behavior in a metal–silicate equilibrium and subsequent core formation modelling argues in favor of a scenario of volatile delivery in the last 10 to 20% of the main phases of Earth’s accretion, in agreement with numerous other studies. A late delivery of Tl on Earth is also supported by recent study by Fang and Liu (2019), reporting isotopic fractionation of Tl between metal and silicate and concluding that a late delivery of Tl is needed to explain the chondritic isotopic composition of the BSE. Experimental studies on other volatile and siderophile elements show that a homogeneous accretion scenario would not reconcile the observed abundances of these elements in the BSE. In particular, for S (Suer et al. 2017), Zn (Mahan et al. 2018b) and Cu (Mahan et al. 2018a), experimental data was only reconciled with observables by volatile delivery in the last stages of Earth’s accretion, a scenario also supported by Ballhaus et al. (2017). Amongst these references, metal–silicate diamond anvil cell experiments (Mahan et al. 2018a, b, Suer et al. 2017) at conditions that are directly comparable to those of Earth’s differentiation (46 to 91 GPa) lead to similar conclusions as lower pressure studies (Ballhaus et al. 2017) and strengthens the relevance of low-pressure experiments to address this issue. Experimental results on refractory siderophile elements Mo and W show that the Earth’s mantle abundances are only reproduced if the S budget is accreted in the last 20% of the accretion (Wade et al. 2012). Such a scenario is also supported by experimental study on the C/S ratio of the Earth (Li et al. 2016). The existence of experimental studies focused on highly volatile, moderately volatile and refractory siderophile elements promoting heterogeneous accretion reinforces its possibility, together with non-experimental studies on a variety of isotopic and elemental measurements on elements of various volatility properties. As such, a heterogeneous accretion scenario is also supported by highly-volatile elements studies, such as noble gases (Marty 2012). Isotopic measurements on natural samples on Pd-Ag (Schonbachler et al. 2010) also support such a scenario. Halogens natural abun-

dances and ratios corroborates late-stage accretion of volatile rich planetesimals (Clay et al. 2017). Recent S, Se and Te measurements in chondrites and terrestrial mantle (Braukmüller et al. 2019) show that the volatile trend in Earth and chondrites presents a “hockey-stick” pattern, forming a plateau for the most volatile elements. A scenario of volatile delivery as 10–15 *wt.%* of CI-like material before core formation ceased (potentially as a giant, Moon-forming impact), is proposed to explain the depletion of siderophile and chalcophile volatile elements relative to the observed plateau. This last stage accretion process could be associated to the formation of a S-rich and volatile-rich liquid at the base of the mantle that was subsequently segregated into the core, often referred to as the Hadean matte (Rubie et al. 2016). Lastly, reported numerical simulation studies investigating this late delivery process, indicate that the accreted material may originate from the outer solar system (Morbidelli et al. 2012, Raymond et al. 2006) and may have been triggered by the rapid migration of the giant planets (Gomes et al. 2005). This material would likely have come from beyond the snow line, with a carbonaceous chondrite-like composition (Charnoz et al. 2019, O’Brien et al. 2018, Schiller et al. 2018), recently confirmed by Mo isotopic measurements (Budde et al. 2019).

The late veneer The reconstruction of Bi partitioning by core formation models indicate that a 0.5% late veneer of CI-chondrite composition is necessary to explain the Bi abundance in the Earth’s mantle. The late veneer has first been invoked in order to explain the relatively high concentrations of highly siderophile elements (HSE) such as the platinum group elements in the Earth’s mantle that are impossible to reconcile with their enhanced siderophility (Holzheid et al. 2000, Mann et al. 2012, O’Neill et al. 1995) as well as Pt isotopic composition (Crech et al. 2017a), even if some studies suggest that their siderophility could be lowered by higher PT conditions (e.g. Danielson et al. 2005, Righter and Drake 1997, Rubie et al. 2016). Recent Ru and Se isotopic measurements (Fischer-Gödde et al. 2020, Varas-Reus et al. 2019) estimated a carbonaceous-chondrite-like late veneer of respectively 0.3 and 0.15% of the Earth’s mass. A late veneer of similar composition is also supported by S, Se and Te ratios (Wang and Becker 2013). Mass balance calculations on noble metals and gas yield a small late veneer mass, inferior to 0.5% (Dauphas and Marty 2002). On the other hand, numerical simulation of a Grand Tack scenario linked to the migration of giant planets predicts a more massive late veneer (O’Brien et al. 2014). Although there is a discrepancy on the mass of the

late veneer, numerous studies focusing on various cosmochemical observables and using multiple methods necessitate such a late veneer to explain these observables.

Core–mantle equilibration efficiency We show that Bi and Tl abundances in the Earth’s mantle can only be explained by scenarios implicating a partial equilibration process between core and mantle, also supported by other metal–silicate partitioning studies (e.g. Suer et al. 2017). A low core formation efficiency has also been proposed as a plausible process contributing to the observed high HSE abundances in the BSE (Arculus and Delano 1981, Jones and Drake 1986, Walker 2009). Geochemical models predict that the degree of equilibration during core formation was 36% based on Hf–W, U–Pb and siderophile elements constraints (Rudge et al. 2010). Fluid dynamics experiments by Deguen et al. (2014) suggest that equilibration becomes less efficient as the size of the impactors increases, requiring the metal to break down to fragments of 1 cm to 1 m for efficient chemical equilibration (Rubie et al. 2003). Our experimental data agrees with this quantified process. However, it should be noted that recent numerical simulations provide mechanisms, such as stretching of the metal, that would induce full equilibration even for large differentiated planetesimals accreted to a terrestrial magma ocean (Kendall and Melosh 2016, Lherm and Deguen 2018).

Conclusions

We report metal–silicate partitioning data at high pressure and high temperature for Cd, Bi, Sb and Tl intended to better constrain the behaviour of MSVEs during core formation. Characterisation of such partitioning helps to deconvolve the effect of differentiation from the effect of volatile-related processes on the observed abundances of the studied elements in the BSE, in order to propose a suitable accretion scenario of the volatile elements on Earth. Partition coefficients of Cd, Bi, Sb and Tl are controlled by pressure, temperature, fO^2 and S content of the metal phase. Subsequent core formation modelling shows that each studied MSVE abundance in the Earth’s mantle could be explained by one or several scenarios. A homogeneous accretion with full equilibration is not well supported here, as it would create a deficit of Bi and Tl of roughly an order of magnitude in the Earth’s mantle. The most unifying scenario involves a heterogeneous scenario

where the volatile elements are accreted in the last 10 to 20% of the Earth's accretion, before core segregation ceased. Our study also supports partial equilibration of the mantle with the core during Earth's accretion. Lastly, a 0.5% late veneer of carbonaceous chondrite-like nature is required to account for the Bi abundance observed in Earth's mantle.

Acknowledgements

We acknowledge the financial support of the UnivEarthS Labex program at Sorbonne Paris Cité (ANR-10-LABX-0023 and ANR-11-IDEX-0005-02). SEM instruments are supported by IPGP multidisciplinary program PARI, and by Paris-IdF region SESAME Grant No. 12015908. We thank Stephan Borensztajn for support during SEM observations. We acknowledge and thank the DFG Core Facility Program at Bayerisches Geoinstitut. We thank Bleuenn Guéguen for technical support during LA-ICPMS measurements at IUEM, University of Brest. We also thank Nicolas Wehr for technical support and advice in high-pressure laboratory of IPGP. JS thanks the financial support of the French National Research Agency (ANR Project VolTerre, grant no. ANR-14-CE33-0017-01). FM acknowledges funding from the European Research Council under the H2020 framework program/ERC grant agreement 637503 (Pristine), and the ANR through a *chaire d'excellence* Sorbonne Paris Cité.

Supplementary information

Starting material

Table 5.5 – Composition of the natural t-MORB used in the starting materials (in *wt.%*, Wanless et al. 2015).

| | Natural MORB |
|--------------------------------|--------------|
| SiO ₂ | 51.1 |
| Al ₂ O ₃ | 15.0 |
| FeO | 6.6 |
| CaO | 14.2 |
| MgO | 10.6 |
| Na ₂ O ₃ | 1.3 |
| TiO ₂ | 0.6 |
| K ₂ O | 0.7 |
| P ₂ O ₅ | 0.1 |
| MnO | 0.1 |

Piston cylinder experiments

The five piston cylinder experiments of this study were conducted in talc–pyrex 1/2” cell assemblies at 2 GPa. All experimental parameters are summarised in table 5.2. Uncertainties on pressure and temperature are estimated to be around 0.1 GPa and 50 K (Siebert et al. 2011). Pressure calibration of the apparatus was performed using the alumina concentration in orthopyroxene in equilibrium with pyrope in a MgO–Al₂O₃–SiO₂ system (Perkins and Newton 1981).

Multianvil experiments

Pressure calibration for both presses used is described in Rubie (1999) and Frost et al. (2004) and involves using the transition of Bi (I-II and III-V) (Lloyd 1971), the quartz–coesite transition (Bohlen and Boettcher 1982), the coesite–stishovite transition (Yagi and Akimoto 1976) and the fayalite– γ spinel transition (Yagi et al. 1987). Pressure and temperature uncertainties (e.g. Woodland and Angel 1997, Woodland and O'Neill 1993) are estimated to be 1 GPa and 100°C. Furthermore, temperature gradients have been shown to be inferior to 50°C across the sample, lowered by the use of a stepped LaCrO₃ heater (Frost et al. 2004, Rubie 1999) and by the convection process occurring at superliquidus conditions. Single-crystal MgO capsules were used in all our MAP experiments to ensure the minimum interaction between the capsule and the sample. No further contamination from other parts of experimental assemblies in both PC and MAP experiments were expected nor detected during chemical measurements.

Electron microprobe measurements

Standards used in major elements analysis are diopside for SiO₂, MgO, CaO; orthopyroxene for K₂O and Al₂O₃; Fe₂O₃ for iron oxide; albite for Na₂O; FeS₂ for S in the silicate and an alloy of Mn and Ti for TiO₂. For the metallic phase, Fe₂O₃ was used for Fe and O, FeS₂ for sulfur, diopside for Si. For Cd and Bi, metallic Cd and Bi were used as standards, and stibnite (Sb₂S₃) was used for Sb standardisation. An in-house standard of Tl₂O₃ was made from Tl₂O₃ powder and used to resolve the Tl concentrations in metals and silicates.

Laser-ablation ICPMS measurements

LA-ICPMS measurements published in this study were performed using both low ($m/\Delta m=200$) and medium resolutions ($m/\Delta m=400$) modes. Each analysis was done as a single spot and lasted 90 seconds with the first 10 seconds of background acquisition (gas blank). Standards were measured twice each (all 6 standards) at the beginning and end of a sequence. The data accuracy is ensured by internal calibrations, using Mg concentrations measured by electron microprobe, and by

standard interpolations using glass standards NIST610, NIST612 and NIST614. The data quality is also certified by the repeated analyses of natural basaltic glass standards BIR-1, BCR-2 and BHVO-2.

The effect of nickel on iron isotope fractionation during core formation

In this study, experiments were designed and performed in order to test the effect of the Ni content of the metal on the Fe metal–silicate isotopic fractionation factor, with implications regarding the role of core formation in establishing planetary Fe isotopic signatures as well as Fe–Ni ideality. The piston cylinder experiments were performed by the author with help from Paolo Sossi, Julien Siebert and Mathieu Roskosz. Iron isotopic compositions were measured by the author, under the supervision of Paolo Sossi, Edward Inglis and Frédéric Moynier.

The effect of nickel on iron isotope fractionation during core formation

E. Kubik^{1,*}, P. Sossi¹, J. Siebert^{1,2}, E. Inglis¹, M. Roskosz³, F. Moynier¹.

¹Université de Paris, Institut de Physique du Globe de Paris, CNRS, 1 Rue Jussieu, 75005 Paris, France.

²Institut Universitaire de France, Paris, France.

³IMPMC, CNRS, UMR 7590, Sorbonne Universités, Université Pierre et Marie Curie, Muséum National d'Histoire Naturelle, CP 52, 57 rue Cuvier, Paris F-75231, France.

*kubik@ipgp.fr

Abstract

The iron isotopic composition of planetary mantles of differentiated inner solar system bodies are similar to, or heavier than chondritic meteorites. Core–mantle differentiation is a likely contributor to planetary isotopic fractionation. However, previous metal–silicate experimental work has given contradictory isotopic results, and it was recently suggested that Ni content of the metal may exert a strong control on the Fe isotopic fractionation. Here, we complement existing data with twenty-two novel metal–silicate equilibrium experiments with varying nickel content. We find no statistically resolvable effect of the nickel content of the metallic phase on iron isotopic fractionation over a wide range of Ni concentrations (0 to 70 wt.% in the metal). We also find that diffusion from single-crystal MgO capsules does not affect the Fe isotope composition of the silicate, and that this type of capsule minimises Fe loss, making them well-suited for isotopic fractionation experiments. Our data across all experiments yields an average isotopic fractionation factor $\Delta^{56}\text{Fe}_{\text{metal-silicate}}=0.05\pm 0.11$ (2σ) at 1873 K and between 1–2 GPa, suggesting that no or little isotopic fractionation of iron is expected to occur during core formation at low pressures. As such, our data does not support core formation as the main mechanism causing the observed variability in iron isotope ratios observed between the silicate Earth, Moon, Vesta and other differentiated asteroids. A combination of multiple accretion-related processes—including accretion

from the solar nebula, volatile-depleting events such as giant impacts, and disproportionation of ferrous iron to ferric iron and iron metal in larger bodies—could explain the chondritic compositions of the mantles of Mars and Vesta as well as the heavier signatures in the Earth and the Moon’s mantles. Our results also support the ideality of (Fe,Ni) alloys, previously demonstrated for physical properties but still marginally evidenced for chemical properties.

Introduction

Experimental determination of isotopic fractionation of siderophile elements between metal and silicate is a relatively new method used to investigate various planetary processes. Recorded experimental isotopic fractionations can be compared to natural isotope signatures, providing a powerful tool for interpretation of planetary isotope signatures and refining our knowledge of the history of solar system planetary bodies. In principle, a melted silicate and a melted metal are equilibrated at high pressure and high temperature until elemental and isotopic equilibrium between the two phases is reached. Silicate and metal from each quenched experiment are physically separated and their isotope compositions are determined. Such studies on various siderophile elements can be used to trace the conditions of planetary differentiation—its temperature (Hin et al. 2014), its pressure (Labidi et al. 2016), redox conditions (Dalou et al. 2019), subsequent rehomogenisation mechanisms (Kempl et al. 2013), and the composition of the core (Mahan et al. 2017, Savage et al. 2015, Xia et al. 2019). Such results allow us to isotopically characterise the building blocks that accreted into planetary bodies (Hin et al. 2014), permitting assessment of whether core formation is the main planetary process controlling the abundances and isotope compositions of certain elements. Alternatively, other possible mechanisms such as magmatic differentiation Bonnard et al. (2016) or volatilisation processes (Xia et al. 2019) may be required. Therefore, numerous key questions may be addressed with experimental evidence. However, experimentally-determined isotopic fractionation factors are often in disaccord with one another, namely, Zn (Bridgestock et al. 2014, Mahan et al. 2017, Xia et al. 2019), Si (Hin et al. 2014, Kempl et al. 2013, Shahar et al. 2011, 2009), Ni (Guignard et al. 2020, Lazar et al. 2012), Cu (Savage et al. 2015, Xia et al. 2019). These discrepancies are partially attributable to differences in the

experimental approach. In this respect, replication of such experiments combined with non-experimental determination of core formation isotopic consequences (e.g. Georg et al. 2007, Moynier et al. 2011) can only be beneficial for the general understanding of the conditions of planetary differentiation.

Planetary materials show significant variability in iron isotopic compositions. Ordinary, enstatite and carbonaceous chondrites present an average $\delta^{56}\text{Fe}$ (per mil variation of the $^{56}\text{Fe}/^{54}\text{Fe}$ ratio relative to IRMM-014) of $0.00\pm 0.01\text{‰}$ (2σ) (Craddock and Dauphas 2011). The terrestrial mantle is estimated to have a $\delta^{56}\text{Fe}=0.03\pm 0.02\text{‰}$ (Craddock et al. 2013, Sossi et al. 2016b) while mid-ocean ridge basalts (MORB) are isotopically heavier with average $\delta^{56}\text{Fe}=0.10\pm 0.01\text{‰}$ (Craddock and Dauphas 2011, Craddock et al. 2013, Nebel et al. 2018, Teng et al. 2013). Even accounting for the effect of olivine crystallisation and correcting their iron isotopic composition back to that of a primary melt in equilibrium with mantle peridotite, MORBs define an average $\delta^{56}\text{Fe}=0.07\pm 0.01\text{‰}$ (Nebel et al. 2018, Sossi et al. 2016b) heavier than chondritic meteorites. By contrast, primary melts of the martian and vestan mantles, determined from the SNC (shergottite-nakhitechassignite) and HED (howardite-eucrite-diogenite) groups of meteorites, respectively, have near-chondritic isotopic signatures (Poitrasson et al. 2004, Schoenberg and von Blanckenburg 2006, Sossi et al. 2016b, Wang et al. 2012) whereas angrites are markedly heavier ($\delta^{56}\text{Fe}=0.12\pm 0.04\text{‰}$, $n=7$, Wang et al. 2012). Lunar basalts yield a range of isotopic compositions from near-chondritic to 0.3‰ (Liu et al. 2010, Poitrasson et al. 2004, 2019, Sossi and Moynier 2017, Wang et al. 2015, Weyer et al. 2005), with a similar iron isotope composition of the Moon and Earth's mantles ($\delta^{56}\text{Fe}=0.05\pm 0.03\text{‰}$, Poitrasson et al. 2019, Sossi and Moynier 2017).

Several processes have been proposed to be responsible for this observed variability including (1) volatile loss by vaporisation during the Moon-forming giant impact (Liu et al. 2017, Poitrasson 2007, Poitrasson et al. 2004), (2) accretion from the solar nebula associated with various degrees of nebular or post-nebular Fe loss in planetary building blocks (Sossi et al. 2016a), (3) disproportionation of ferrous iron (Fe^{2+}) into Fe^{3+} and metallic iron by perovskite crystallisation during accretion in bigger planetary bodies such as the Earth (Frost and McCammon 2008, Williams et al. 2012) and (4) core–mantle equilibration related isotopic fractionation at either high (Polyakov 2009) or low pressures (Elardo and Shahaar 2017). Leshner et al. (2020) argued that the upper part of the Earth's core could be enriched

in heavier Fe isotopes by thermodiffusion. If this heavier Fe is, as suggested in the study, transported to the upper mantle by ascending plumes, it could explain the heavy Fe isotopic signature of the BSE (bulk silicate Earth). However, core–mantle equilibration remains the main process that determined the isotopic signatures of the two geological reservoirs since the Earth’s accretion. It is therefore crucial to understand the isotopic behavior of Fe during core–mantle equilibration, which remains debated.

Early experimental work addressing this question did not find any resolvable isotopic fractionation of Fe between metallic and silicate phases over a range of pressures, from 1 to 60 GPa (Poitrasson et al., 2009; Hin et al., 2012; Shahar et al., 2016; Liu et al., 2017), leading to the conclusion that, at the high temperatures required for core formation on telluric bodies (≥ 2000 K, e.g., Righter and Drake 1996), equilibrium isotope fractionation between metal and silicate, which is proportional to $1/T^2$, should be negligible. Although some of the metallic phases investigated contained a small fraction of Ni ($\sim 5\text{--}9$ wt.%) as is relevant to planetary cores, the effect of Ni on iron isotope fractionation was not explicitly investigated prior to the study of Elardo and Shahar (2017). They reported piston cylinder experiments conducted at 2123 K and 1 GPa in which the Ni content of the metal varied between 1 and 26 at.%, and observed a systematic increase of the fractionation factor with Ni, in which $\Delta^{57}\text{F}_{e_{\text{metal-silicate}}} = 0.011(X_{\text{Ni}}, \text{at.}\%) + 0.04$. Thus, the presence of Ni in the metal enhances the Fe isotopic fractionation between metal and silicate leading to the enrichment of the silicate in the lighter Fe isotopes relative to the metal. Because the sense of this fractionation is opposite to that observed in the mantles of differentiated bodies, Elardo and Shahar (2017) invoked significant isotopic fractionation during partial melting to restore the light subchondritic mantle isotopic composition inferred from their experiments to the superchondritic values observed in basaltic achondrites (e.g. Sossi et al. 2016b). Importantly, such an isotopic effect implies that (Fe,Ni) alloys do not mix ideally, which is at odds with the constancy of density, compressibility, and wave velocities of (Fe,Ni) alloys with increasing Ni content (e.g. Badro et al. 2014, Kantor et al. 2007, Lin et al. 2003, Martorell et al. 2013). Moreover, this ideality has been assumed in numerous experimental studies on core formation processes in which the effect of Ni was neglected. Xia et al. (2019) report Zn and Cu metal–silicate isotope fractionation experiments with significant sensitivity to the Ni content of the metal. Positive Ni-induced isotope fractionation were measured for Fe (Elardo

and Shahar 2017), Zn and Cu (Xia et al. 2019), based on less than 10 experiments for each. More experimental results, involving a broader range of Ni contents, are needed to come across a consensus on the existence of an effect of the Ni concentration of an (Fe,Ni) alloy on various chemical and isotopic parameters. Therefore, assessing the iron isotope fractionation between metal and silicate has profound implications for our understanding of core formation processes and for the physical properties of core-forming alloys.

To address this question, twenty-two metal–silicate equilibrium experiments were performed in a piston cylinder apparatus in order to characterise the effect of Ni on the Fe isotopic fractionation. In particular, a wider range of Ni content in the metal (from 0 to 70 *wt.%*) was covered compared to previous work (0 to 25 *wt.%*, Elardo and Shahar 2017).

Method

Experimental method

Mixtures composed of 70 *wt.%* MORB with varying proportions of pure Fe and Ni were prepared by weighing each component and combining them in an agate mortar until complete homogenisation. All experiments were performed in a 150-tons end-loaded piston cylinder apparatus at the Institut Physique du Globe de Paris (IPGP). They were performed at 1 to 2 GPa and at 1873 K in order to induce the fusion and equilibrium between metal and silicate in the system. Four capsule types—boron nitride, crushable MgO, single-crystal MgO and graphite—were tested in order to test their effect on the iron isotopic fractionation.

Sample collection and purification

The metal and silicate were separated mechanically after each experiment. Clean pieces from each phase were selected carefully under magnifying glass. Metal pieces were directly dissolved in 6 N HCl. Silicate samples were sorted in order to select clean pieces devoid of metal bead or capsule material. These pieces were roughly crushed and a magnet was used to collect any last piece of metal that

could remain. The silicate was finely crushed in an agate mortar and digested in a 1:3 solution of HF:HNO₃ in closed Teflon bombs on a hotplate at 100°C. Silicate samples were then dried and further digested in aqua regia on a hot plate at 150°C to remove any residual fluoride complex. They were dried again and dissolved in 6 N HCl for purification. The purification of iron in the samples was performed following the method described in Sossi et al. (2015), by anion exchange chromatography using AG1-X8 (200-400 mesh) and 0.4 x 7 cm Teflon columns. Columns were filled with 1 mL AG1-X8 resin and cleaned with 5 mL 3 N HNO₃, 5 mL H₂O and conditioned with 5 mL 6 N HCl. The samples were subsequently loaded in 0.5 mL of 6 N HCl. The matrix was eluted with 11 mL of 6 N HCl. The Fe cuts were eluted with 3 mL of 0.5 N HCl, and dried to be redissolved in 0.5 N HNO₃. They were diluted to 4 ppm Fe solutions and spiked with 8 ppm of Ni, following the method described in Sossi et al. (2015).

MC-ICPMS measurements

Iron isotopic measurements were performed on a Neptune Plus MC-ICPMS at IPGP (Université de Paris), used in medium resolution mode. The cups were configured as described in Sossi et al. (2015) in order to measure ⁵⁴Fe, ⁵⁶Fe, ⁵⁷Fe, ⁶⁰Ni, ⁶¹Ni and ⁵³Cr used to correct for any ⁵⁴Cr interference on ⁵⁴Fe, even though chromatographic separation was shown to be very efficient, meaning insignificant correction. The ⁶¹Ni/⁶⁰Ni ratios measured in all samples were used to correct for mass bias effects. Measurements of IRMM-014 performed in between samples were used to calculate the ratios and deltas presented in this study.

Evidence of metal–silicate equilibrium

Two methods are typically used in order to assess metal–silicate isotopic equilibrium in high-temperature experiments: time series and the “three-isotope method”. It has been known for a few decades that elemental equilibrium can be reached very quickly in superliquidus conditions metal–silicate experiments (5 seconds at 2300 K, Thibault and Walter 1995). As these diffusion rates cannot necessarily be extrapolated to isotopic exchange rate, several experimental studies report that isotopic exchange can actually be faster than chemical diffusion

while pointing at differences between systems (van der Laan et al. 1994, Leshner 1990). In this context, numerous studies report relatively short equilibration time experiments (e.g. Hin et al. 2013, Shahar et al. 2011). Successful isotopic equilibrium achievement after a few minutes can be explained by the superliquidus temperatures reached, under which the entire sample is melted with multiple equilibration accelerators: (1) diffusion rates are significantly higher at liquid state than in presence of a solid phase, (2) the convection operating inside the capsule has a positive effect on the homogenisation time of the melted sample, (3) homogenisation is additionally favoured by using a finely crushed homogeneous powder as starting material. As such, time series consist of a sufficient method to attest fully equilibrated experiments. In this study specifically, (a) thorough SEM and EDX characterisation of each phase allowed to provide proof that the totality of the sample material was fully molten and (b) resulted in chemically homogeneous phases (see supplementary information). (c) The Fe isotopic fractionation follow a systematic consistent trend permitted by a large dataset of 22 experiments certifying good statistical significance. (d) Repeated time series experiments show no statistically resolvable evolution of the Fe isotopic fractionation factor between 3- and 30-minutes time durations (supplementary figure 6.6), with experiments of 30 minutes and more presenting enhanced variability, with both positive and negative factors and therefore attributed to increased reactions with the capsule (figure 6.1b). Moreover, the results are in agreement with several other studies performed in distinct facilities (Elardo and Shahar 2017, Hin et al. 2012, Liu et al. 2017, Poitrasson et al. 2009; , see figure 6.1a). Such results are also in agreement with numerous pieces of evidence of (Fe,Ni) alloy ideality (Badro et al. 2014, Kantor et al. 2007, Lin et al. 2003, Martorell et al. 2013). With respect to such demonstration of isotopic equilibrium, the three-isotope method was not included in the protocol of this study. Although Cao and Bao (2017) and Bourdon et al. (2018) reported artifacts that could lead to non-linear trajectories, drawing the limits of the method, other studies have demonstrated its promising results (Shahar and Young 2020, Shahar et al. 2008), and in particular its usefulness in verifying that the system remained closed with respect to mass exchange throughout an experiment. Contrary to the present work, the three-isotope method is particularly well suited for subsolidus system where isotopic equilibrium cannot be approached due to the low diffusion rates in solid phases (e.g. Shahar et al. 2008). In this study, the use of MgO single crystal capsules was employed to ensure minimal interaction with the

capsule (see supplementary information). Moreover, the recalculation of the bulk isotope composition of experiments based on measured δ^{56} of each phase by a simple mass balance yields a good reproducibility (on average $\delta^{56}\text{Fe}_{bulk}=0.40\pm 0.08\%$, 1 s.d.) which is a second reason why the three-isotope method is not needed here.

Iron isotopic behavior in metal–silicate equilibrium experiments

Twenty-two metal–silicate equilibrium experiments were performed. Experiments were carried at 1 and 2 GPa and 1873 K in an end-loaded (Bristol-type) piston cylinder press housed at the Institut de Physique du Globe de Paris. The starting mixtures were composed of natural MORB combined with pure Fe and Ni powders. The Ni content of the starting mixture was varied from 0 to 70 *wt.*% of the metal fraction. A number of capsule materials were tested, including crushable MgO, single-crystal MgO, graphite and boron nitride. Run durations were varied between 3 and 60 minutes in order to assess the timescales required to approach isotopic equilibrium. Petrographic observations indicate that the starting material was fully molten in all experiments (see supplementary materials) where the silicate phases were found homogeneous in both composition and texture. The metal coalesced into a discrete ball in all experiments, and subsequent to quenching, was separated mechanically from the silicate phase. All experimental parameters and isotopic measurements are available in table 6.1.

All experiments from this study and literature are presented in figure 6.1a. It should be noted that all experiments from different studies were carried at different temperature conditions (see supplementary figure 6.7 for comparison of experiments corrected for the temperature effect). Our results show no correlation between the Ni content of the metal and the iron isotopic fractionation factor between metal and silicate (figure 6.1b). There is also no resolvable difference between the experiments using the different types of capsules, although from petrographic observations, single-crystal MgO capsules minimise the extent of the reaction between capsule and sample by containing the extent of the interactions within the first 30 μm of the capsule. Measurements on multiple parts of experiment E375 are presented in figure 6.2. This short-duration experiment (5 minutes) exhibits a glassy silicate

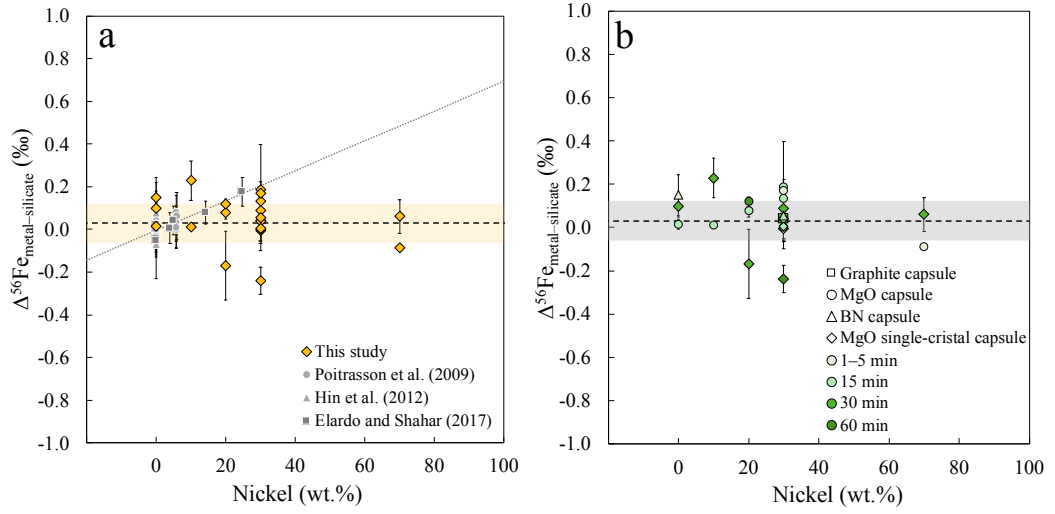


Figure 6.1 – Results of Fe isotopic fractionation in metal–silicate equilibrium experiments. Error bars correspond to 2 standard deviations. **a.** $\Delta^{56}\text{Fe}_{\text{metal-silicate}}$ of all experiments of this study and from literature (Elardo and Shahar 2017, Hin et al. 2012, Poitrasson et al. 2009) as a function of the Ni content of the metallic phase. It should be noted that experiments from other studies were carried at different conditions of P and T than the experiments from this study and the temperature effect was not corrected on this figure. The horizontal dashed line with orange error represents the average of all experiments presented on the graph, i.e. $0.03 \pm 0.09\text{‰}$ (1 s.d.). The dotted line represents the trend of Ni content dependency on Fe isotopic fractionation factor derived from Elardo and Shahar (2017). **b.** $\Delta^{56}\text{Fe}_{\text{metal-silicate}}$ for all experiments of this study. Squares are experiments carried in graphite capsules, circles correspond to the ones in MgO capsules, triangles for experiments using boron nitride capsules and diamonds for experiments carried in single-crystal MgO capsules. Experiments are color coded according to their time durations: pale green for 1–5 minutes, emerald green for 15 minutes, light green for 30 minutes, and dark green for 60 minutes. The horizontal dashed line with grey error represents the average of all experiments presented on graph a., i.e. $0.03 \pm 0.09\text{‰}$ (1 s.d.).

in the center of the capsule and partially crystallised silicate towards the capsule boundary where skeletal olivine crystals grew as a result of MgO enrichment from the capsule. This particular experiment presents a gradient in MgO composition with a decreasing amount of MgO toward the center of the capsule due to its

short time duration. Measurements on these separated parts show no difference in Fe isotopic composition between glass and crystallised silicates which means that MgO diffusion towards the center of the sample does not affect the Fe isotope composition of the silicate. Therefore, in this particular case, MgO capsules are well-suited for isotope fractionation experiments with respect to MgO diffusion. This experiment also presents an isotopic composition of the metal identical to the silicate. The first 30 μm of the capsule containing less than 4 *wt.*% of Fe, however, presents a clear enrichment in light Fe isotopes, even after a few minutes. At such superliquidus temperatures, interactions between the capsule and the sample progress with increasing time duration. Therefore, in the long term, measured isotopic fractionations can be driven by interactions between the capsule and the sample.

Iron isotopic fractionation factors from this study yield an average of $\Delta^{56}\text{Fe}_{\text{metal-silicate}}=0.05\pm 0.11\%$. This means that these results are not significantly different from 0.0%, and no dependence on the Ni content in the metal is detected over a wide range of Ni concentrations.

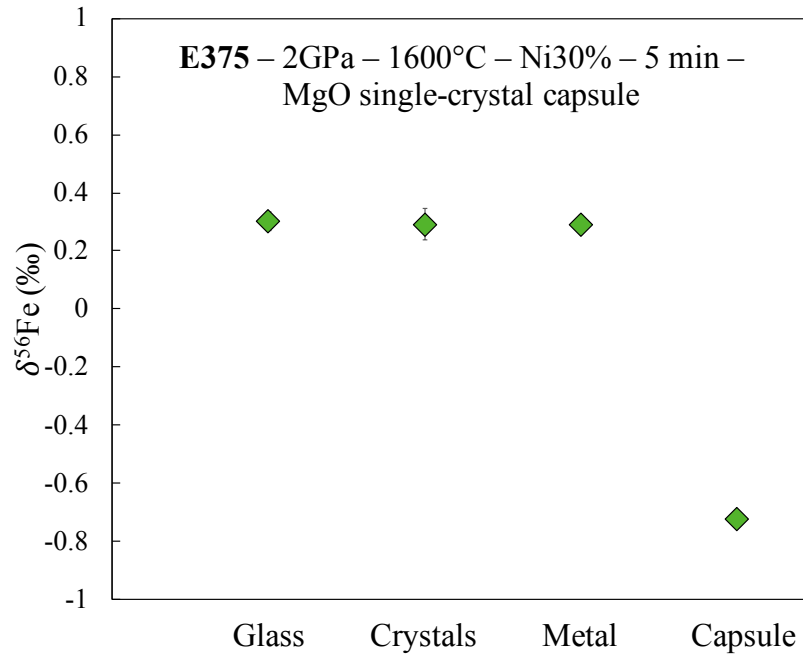


Figure 6.2 – Results of Fe isotopic compositions on a single experiment. E375 was performed at 2 GPa and 1873 K in a single-crystal MgO capsule with a time duration of 5 minutes. Its metal phase contains 30 *wt.*% of Ni. Iron isotopic measurements were performed on two silicate samples—a central glassy part and an outlying crystallised part—as well as the metal phase and the capsule. The two silicate parts and the metal present the same isotopic composition whereas the inner part of the capsule is enriched in light Fe isotopes.

Table 6.1 – Iron isotopic compositions of experimental run products and experimental parameters used for all experiments of this study. Replicated samples were split before column separation.

| Run | P | T | Ni | t | Capsule | $\delta^{57}\text{Fe}_{sil}$ | 2σ | $\delta^{57}\text{Fe}_{met}$ | 2σ | $\Delta^{57}\text{Fe}_{met-sil}$ | 2σ | $\delta^{56}\text{Fe}_{sil}$ | 2σ | $\delta^{56}\text{Fe}_{met}$ | 2σ | $\Delta^{56}\text{Fe}_{met-sil}$ | 2σ | |
|------|-----------|------|--------|-------|----------|------------------------------|-----------|------------------------------|-----------|----------------------------------|-----------|------------------------------|-----------|------------------------------|-----------|----------------------------------|-----------|------|
| | (GPa) | (K) | (wt.%) | (min) | | | | | | | | | | | | | | |
| E269 | 1 | 1873 | 20 | 15 | MgO | 0.61 | 0.01 | 0.73 | 0.02 | 0.12 | 0.03 | 0.40 | 0.01 | 0.48 | 0.01 | 0.08 | 0.02 | |
| E270 | 1 | 1873 | 10 | 15 | MgO | 0.75 | 0.01 | 0.78 | 0.01 | 0.02 | 0.01 | 0.50 | 0.01 | 0.51 | 0.01 | 0.01 | 0.01 | |
| E271 | 1 | 1873 | 20 | 60 | MgO | 0.60 | 0.01 | 0.77 | 0.01 | 0.17 | 0.02 | 0.39 | 0.01 | 0.51 | 0.01 | 0.12 | 0.02 | |
| E276 | 1 | 1873 | 30 | 15 | MgO | 0.46 | 0.01 | 0.73 | 0.02 | 0.27 | 0.04 | 0.30 | 0.01 | 0.49 | 0.02 | 0.19 | 0.03 | |
| E298 | 2 | 1873 | 30 | 15 | MgO | 0.78 | 0.01 | 0.75 | 0.01 | -0.02 | 0.02 | 0.49 | 0.01 | 0.49 | 0.01 | 0.00 | 0.01 | |
| E302 | 2 | 1873 | 0 | 15 | MgO | 0.72 | 0.01 | 0.75 | 0.01 | 0.04 | 0.02 | 0.47 | 0.02 | 0.49 | 0.02 | 0.02 | 0.03 | |
| E318 | 2 | 1873 | 30 | 15 | MgO SC | 0.65 | 0.03 | 0.68 | 0.04 | 0.03 | 0.07 | 0.47 | 0.03 | 0.48 | 0.03 | 0.00 | 0.05 | |
| E320 | 2 | 1873 | 0 | 3 | BN | 0.50 | 0.04 | 0.71 | 0.05 | 0.21 | 0.09 | 0.33 | 0.03 | 0.48 | 0.04 | 0.15 | 0.06 | |
| E321 | 2 | 1873 | 30 | 15 | BN | 0.57 | 0.05 | 0.64 | 0.06 | 0.07 | 0.11 | 0.36 | 0.02 | 0.42 | 0.02 | 0.05 | 0.04 | |
| E322 | 2 | 1873 | 30 | 15 | MgO | 0.52 | 0.02 | 0.70 | 0.02 | 0.17 | 0.04 | 0.36 | 0.02 | 0.49 | 0.02 | 0.13 | 0.04 | |
| E323 | 2 | 1873 | 0 | 3 | BN | 0.54 | 0.04 | 0.77 | 0.06 | 0.23 | 0.11 | 0.00 | 0.00 | 0.51 | 0.01 | 0.00 | 0.00 | |
| E324 | 2 | 1873 | 30 | 3 | MgO | 0.58 | 0.07 | 0.78 | 0.16 | 0.20 | 0.23 | 0.38 | 0.06 | 0.55 | 0.09 | 0.17 | 0.15 | |
| E325 | 2 | 1873 | 70 | 3 | MgO | 0.59 | 0.01 | 0.47 | 0.00 | -0.12 | 0.01 | 0.41 | 0.02 | 0.32 | 0.01 | -0.09 | 0.03 | |
| E373 | 2 | 1873 | 30 | 15 | MgO SC | 0.43 | 0.02 | 0.44 | 0.09 | 0.01 | 0.11 | 0.28 | 0.02 | 0.32 | 0.04 | 0.04 | 0.06 | |
| E375 | glass | 2 | 1873 | 30 | 5 | MgO SC | 0.40 | 0.05 | 0.41 | 0.04 | 0.01 | 0.09 | 0.30 | 0.03 | 0.29 | 0.03 | -0.01 | 0.06 |
| E375 | crystals | | | | | 0.46 | 0.05 | | | | | 0.29 | 0.05 | | | | | |
| E375 | capsule | | | | | -1.07 | 0.07 | | | | | -0.72 | 0.01 | | | | | |
| E376 | 2 | 1873 | 30 | 30 | MgO SC | 0.43 | 0.03 | 0.48 | 0.00 | 0.05 | 0.03 | 0.26 | 0.03 | 0.35 | 0.02 | 0.09 | 0.04 | |
| E377 | 2 | 1873 | 70 | 30 | MgO SC | 0.25 | 0.04 | 0.43 | 0.07 | 0.14 | 0.08 | 0.21 | 0.04 | 0.26 | 0.02 | 0.06 | 0.05 | |
| E377 | replicate | | | | | | | 0.43 | 0.07 | | | | | 0.27 | 0.02 | | | |
| E378 | 2 | 1873 | 0 | 30 | MgO SC | 0.40 | 0.07 | 0.50 | 0.01 | 0.15 | 0.05 | 0.28 | 0.05 | 0.37 | 0.02 | 0.10 | 0.04 | |
| E378 | replicate | | | | | 0.34 | 0.05 | | | | | 0.23 | 0.03 | | | | | |
| E379 | 2 | 1873 | 10 | 30 | MgO SC | 0.21 | 0.05 | 0.55 | 0.04 | 0.35 | 0.09 | 0.15 | 0.02 | 0.38 | 0.02 | 0.23 | 0.04 | |
| E380 | 2 | 1873 | 20 | 30 | MgO SC | 0.73 | 0.08 | 0.50 | 0.08 | -0.23 | 0.16 | 0.51 | 0.04 | 0.34 | 0.04 | -0.17 | 0.09 | |
| E381 | 2 | 1873 | 30 | 30 | graphite | 0.38 | 0.02 | 0.41 | 0.01 | 0.03 | 0.03 | 0.26 | 0.02 | 0.30 | 0.02 | 0.04 | 0.05 | |
| E382 | 2 | 1873 | 30 | 60 | MgO SC | 0.81 | 0.00 | 0.44 | 0.06 | -0.37 | 0.06 | 0.54 | 0.03 | 0.30 | 0.05 | -0.24 | 0.07 | |

Iron isotopic fractionation during core formation

Our experimental results include novel metal–silicate equilibrium iron isotope fractionation data with a wide range of Ni content. The large number of experiments of this study provides enhanced statistical accuracy, and shows that Ni proportion in the metal has limited effect on the Fe isotope fractionation between metal and silicate. While our conclusions may differ, the results presented here are consistent (figure 6.1a) with those reported in the study of Elardo and Shahar (2017)

where the observed trend can be attributed to a relatively smaller number of experiments. In fact, the data presented herein, combined with that of Elardo and Shahar (2017) yields an average fractionation factor of $\Delta^{56}\text{Fe}_{\text{metal-silicate}}=0.04\pm 0.10\%$, indicating no isotopic fractionation within uncertainty. Our results are also in agreement with previous experimental studies on Fe isotopic fractionation (Hin et al. 2012, Liu et al. 2017, Poitrasson et al. 2009) demonstrating the absence of iron isotope fractionation at metal-silicate equilibrium. Significant S content in the alloy may induce a positive metal-silicate isotope fractionation with light isotope enrichment in the mantle (Liu et al. 2017, Shahar et al. 2015). A similar fractionation has been observed for other components such as Si and C (Elardo et al. 2019, Shahar and Young 2020). Nevertheless, this vector of fractionation is opposite to that observed in Earth's mantle and in the mantles of other differentiated bodies relative to chondrites. As such, to a first-order there is no direct evidence for core-mantle segregation to cause significant isotopic fractionation of Fe in controlling the isotopic composition of planetary mantles. Indeed, equilibrium isotope fractionation evolves with a $1/T^2$ dependence so that enhanced fractionation is expected from low temperature core formation. However, chondritic values are observed in small bodies that underwent lower temperature core formation such as Mars and Vesta (~ 1900 K, Righter and Drake 1996) compared to the non-chondritic Earth whose core equilibrated with the mantle at 2500–3500 K (Wood et al. 2006). Therefore, core formation cannot explain alone the diversity of Fe isotope compositions in the inner solar system, although it has been previously proposed from diamond anvil coupled to inelastic nuclear resonance X-ray scattering experiments (Polyakov 2009).

Planetary iron isotopic variability

Core formation as the main process responsible for Fe isotopic variability among planetary mantles is not well supported by the experimental results of this study. Other processes including various accretion mechanisms need to be further investigated as potential causes for the Fe isotopes variability in inner solar system planetary bodies.

Investigating the differences in Fe isotope signatures between the Earth and

the Moon, an increasing amount of lunar rock measurements suggest that both planets share a common signature (Poitrasson et al. 2019, Sossi and Moynier 2017, Wang et al. 2015), promoting that element depletion of the Moon only affected more volatile elements. This result is in agreement with the widely-held view that volatilisation during Moon formation and evolution resulted in isotopic fractionation of multiple isotopic systems in the lunar mantle (e.g. Kato et al. 2015, Sossi et al. 2018) on a much larger scale than in Earth's mantle (e.g. Pringle and Moynier 2017, Sossi et al. 2017, Wang and Jacobsen 2016). The observation of the isotopically heavy Fe isotope signatures in ureilites and angrites suggests that collisions between accreting bodies in the inner solar system may be common and that the observed signatures in inner planetary bodies are the result of contrasted accretional histories possibly involving multiple complex volatile-depleting events (Sossi et al. 2016b). This also suggests that Mars and Vesta suffered very limited syn- and post-accretion Fe loss as inferred from their chondritic signatures. The crystallisation of perovskite in large planetary bodies such as the Earth may consist of another mechanism to enrich the mantle in heavy Fe isotopes (Williams et al. 2012) by disproportionation of Fe^{2+} into Fe^{3+} and metallic iron. In the case of the Earth, this process would solve the origin of the heavy Fe signature of the mantle without invoking volatilisation processes. However, this process would not explain the heavy isotope compositions of achondritic meteorites whose parent bodies were too small to have stabilised perovskite of Fe^{3+} -rich silicate melt in equilibrium with iron metal. Therefore, combined together, the mechanisms mentioned here provide means to explain the diverse Fe isotope signatures observed amongst inner solar system bodies.

A recent study by Lesher et al. (2020) argued that the core–mantle boundary could be enriched in heavier Fe isotopes and that pockets of this heavy core could be entrained in plumes towards the upper mantle and crust. High temperature diffusion experiments over a gradient of 250 degrees could provide a process of enrichment of the outer core in heavy isotopes. This process being slower than the mantle convection and recycling, according to the study, the proposed mechanism of transport of the heavier Fe core diapirs in magmatic plumes towards the upper mantle could be tested by thorough measurements on OIBs for a wide age range.

On ideality in Fe–Ni alloys

The amount of Ni in the core is estimated around 5 *wt.*% based on geochemical and cosmochemical models (McDonough 2003, McDonough and Sun 1995). Numerous studies have detected insignificant variations of physical properties such as density, compressibility, and wave velocities in (Fe,Ni) alloys as a function of their Ni content (e.g. Asker et al. 2009, Kantor et al. 2007, Lin et al. 2003, Martorell et al. 2013, Wakamatsu et al. 2018). Importantly, the constant density of such alloys does not uniquely constrain the amount of Ni in the core but implies that the entirety of the observed density deficit must be due to the presence of $\sim 10\%$ of light elements in the core (Birch 1952). Although physical properties of (Fe,Ni) alloys benefited from multiple experimental (Kantor et al. 2007, Lin et al. 2003) and ab initio calculations (Martorell et al. 2013) studies that demonstrated the negligible effect of Ni proportion, the same is not true for chemical properties.

To this day, less than 10 studies investigating experimentally the chemical behaviour of elements between metal and silicate have considered the effect of the amount of Ni. The effect of Ni has been widely assumed negligible in studies simulating or experimenting on core properties. Through the transpiration method and integration of the Gibbs-Duhem relation, early studies illustrated that the dissolution of Ni had little effect on the activity of Fe in binary alloys (Oriani 1953, Zellars et al. 1959). As such, it is frequently assumed that the alloying of Fe with small quantities of Ni has a negligible effect on the behaviour of the metal, as is relevant for studies simulating or experimenting on core properties. More recent Knudsen effusion mass spectrometric investigations of the activity-composition relations of liquid (Fe,Ni) alloys (Fraser and Rammensee 1982) show that the activity coefficient of Fe, γ_{Fe} , varies between 0.9 at $X_{\text{Ni}}=0.5$ to 1 at $X_{\text{Ni}}=0.05$ (X =mole fraction), illustrating that for all likely core compositions, Fe dissolution in (Fe,Ni) alloys is ideal at ambient pressures. At higher pressures (up to 94 GPa), Huang and Badro (2018) demonstrated that Ni (between 3.5 to 48.7 *wt.*% Ni) has no effect on the metal–silicate partitioning of Ni, Cr and V at high pressures. Our study suggests that Ni proportion has no effect on Fe isotopic behaviour in a metal–silicate equilibrium, also pointing towards chemical Fe–Ni ideality. Recent study by Xia et al. (2019) report opposite observations, with results presenting Zn and Cu isotope fractionation sensitivity to the Ni content

of the metal. Therefore, positive Ni-induced isotope fractionation were reported for Fe (Elardo and Shahar 2017), Zn and Cu (Xia et al. 2019), although unlike the work presented here, both studies dedicated less than 10 experiments to the determination of the effect of the Ni content on the isotopic fractionation of one of these 3 elements. The 22 experiments reported here not only propose enhanced statistical accuracy, but they were also designed to explore a much broader range of Ni concentrations in the metal, from 0 to 70 *wt.%* (~ 25 *wt.%* maximum in Xia et al. 2019 and Elardo and Shahar 2017). As no consensus exists regarding this question, more systemic studies investigating the Ni effect are needed. The assumption of chemical Fe–Ni ideality has extended implications regarding our understanding and knowledge of core formation related processes and needs to be further investigated.

Conclusion

We performed 22 metal–silicate equilibrium experiments with the prospect of establishing the effect of the Ni content of the metal on Fe isotope fractionation. All experiments were carried at 1–2 GPa and 1873 K and our study includes multiple capsule materials testing, time duration series as well as petrographic characterisation of the samples to establish chemical equilibrium. No significant effect of Ni concentration on Fe isotope fractionation was detected over a wide range of Ni contents (0–70 *wt.%* in the metal fraction), supporting the widely assumed physical and chemical ideality of (Fe,Ni) alloys. Therefore, our data does not support core formation as the main mechanism causing the diversity in iron isotope ratios observed amongst inner solar system planetary bodies. A combination of multiple accretion-related processes—including accretion from the solar nebula, volatile-depleting events such as giant impacts, and disproportionation of ferrous iron by perovskite crystallisation in larger bodies—could explain the presence of chondritic-mantle bodies such as Mars and Vesta as well as the presence of heavier signatures in the Earth and the Moon’s mantles.

Supplementary materials

Isotopic equilibrium

In each experiment, metal coalescence into a single metal sphere of roughly 1 mm diameter in the center of the capsule was observed as a result of achievement of superliquidus temperatures during sufficient time duration to allow elemental and isotopic equilibrium. Figure 6.3 represents backscatter electron images of typical run products. Silicate phases of the experiments of the time series (figure 6.3a-d) present skeletal olivine (dark gray dendrites) due to MgO enrichment, but their electron density is homogeneous. A thin dense ring of roughly 30 μm between the silicate and the capsule constitutes the transition zone and no Fe was detected with EDX in the capsule beyond this zone. The capsule of run E382 (figure 6.3d) appears to have broken during the run and some silicate material can be observed in the fracture. This may be the reason for the negative isotopic fractionation measured which could have been caused by a loss of light Fe out of the capsule resulting in a heavier Fe measured in the silicate. The metal phases (figure 6.3e-f) are also homogeneous in electron microscopy. Figures 6.4 and 6.5 present additional EDX measurement results for a silicate and a metal part. Major element compositions of the two phases are consistent across the samples, demonstrating chemical homogeneity. Figure 6.6 shows Fe isotopic fractionation results for experiments of the time series carried at 2 GPa, 1600°C and with 30 *wt.*% Ni in the metal phase. Up to 30 minutes, there is no resolvable evolution of the fractionation factor suggesting equilibrium achievement, which is combined with strong evidence of full equilibration from petrological and EDX measurements previously described. As mentioned above, the 60 min experiment may have interacted with the exterior of the capsule, causing a very negative fractionation. Our results support isotopic equilibrium achievement within a few minutes. Therefore, primary petrological observations and EDX measurements—from 5 to 60 minutes run durations—showed the metal and silicate phases of the experiments of this study to be fully molten with quench textures and, most importantly, chemically homogeneous which is crucial for achievement of an isotopic equilibrium.

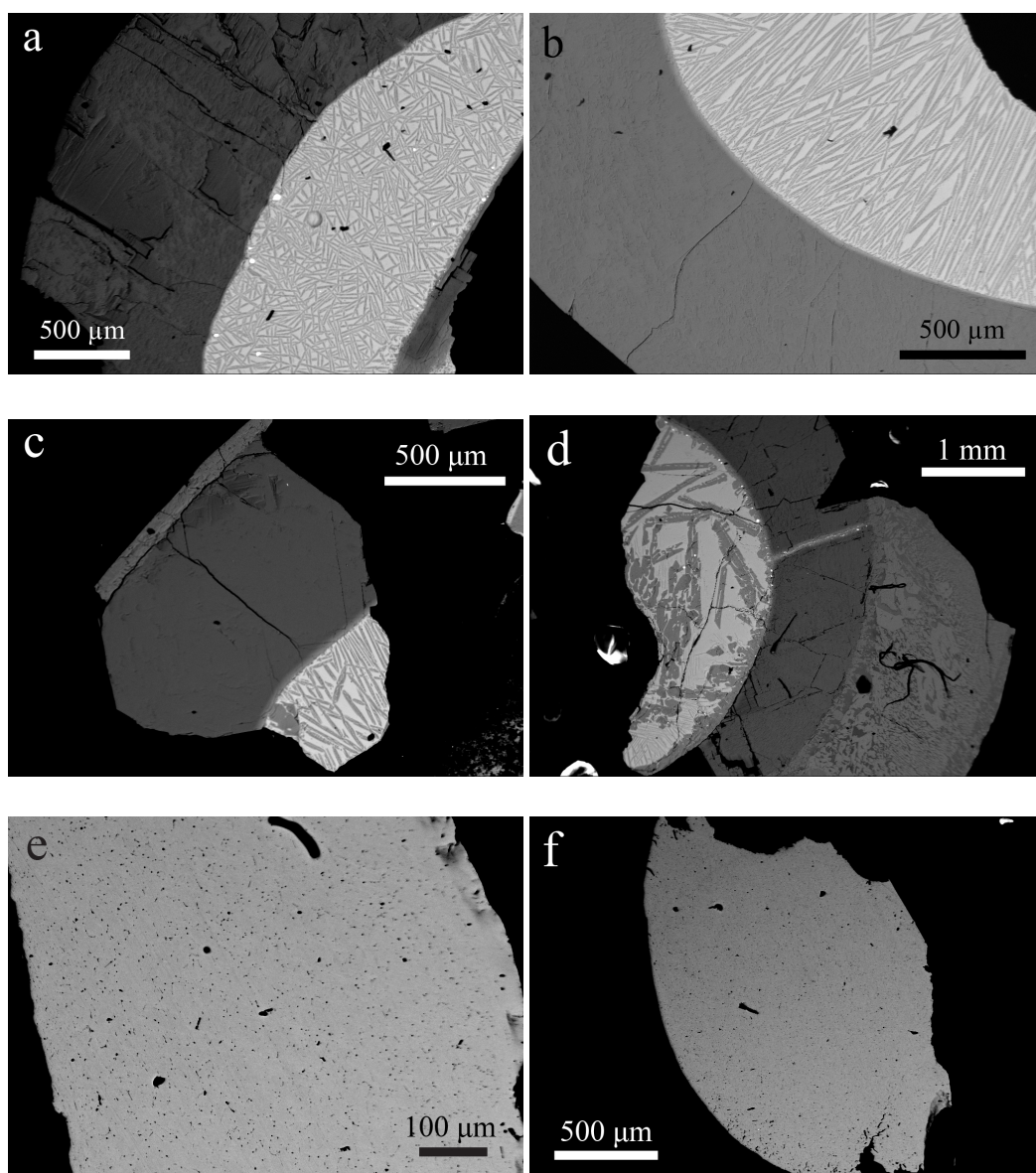


Figure 6.3 – Backscatterer electron images of typical run products. The first four images represent the silicate phase attached to its capsule—such that the silicate–capsule boundary is visible—for all experiments of the time series performed in single-crystal MgO capsules at 2 GPa and 1873 K and 30 *wt.*% Ni in the metal part. The last two images represent typical metal phases. **a.** BSE image of the silicate part of run E375 (5 minutes). **b.** Backscatterer electron (BSE) image of the silicate of run E373 (15 minutes). **c.** BSE image of the silicate phase of run E376 (30 minutes). **d.** BSE image of the silicate of run E382 (60 minutes). **e.** BSE image of the metal of run E376. **f.** BSE image of the metal phase of run 382.

CHAPTER 6. Iron isotope fractionation during core formation

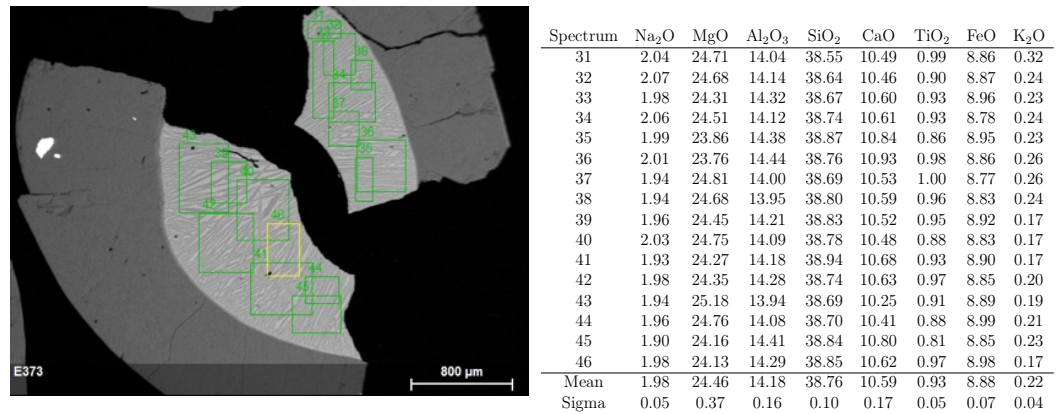


Figure 6.4 – Energy-dispersive X-ray spectroscopy (EDX) measurements on the silicate part of run E373 proving chemical homogeneity of the quenched melted silicate phase, after 15 minutes run duration.

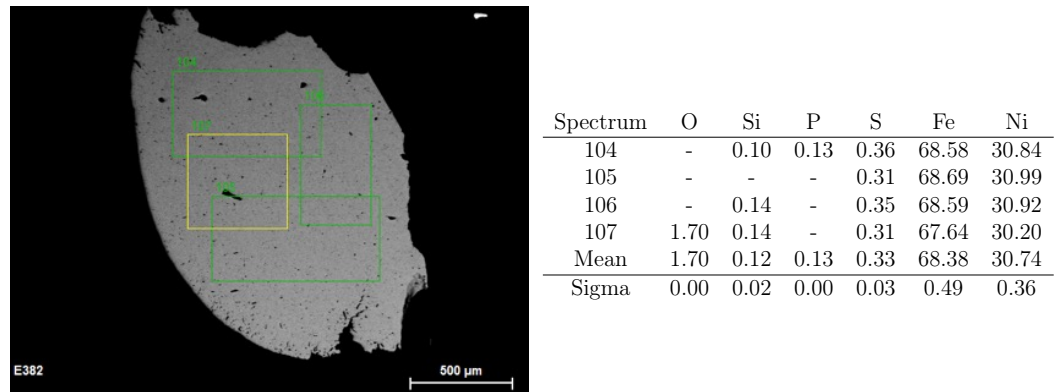


Figure 6.5 – Energy-dispersive X-ray spectroscopy (EDX) measurements on the metal part of run E382 presenting chemical homogeneity of the quenched melted metal.

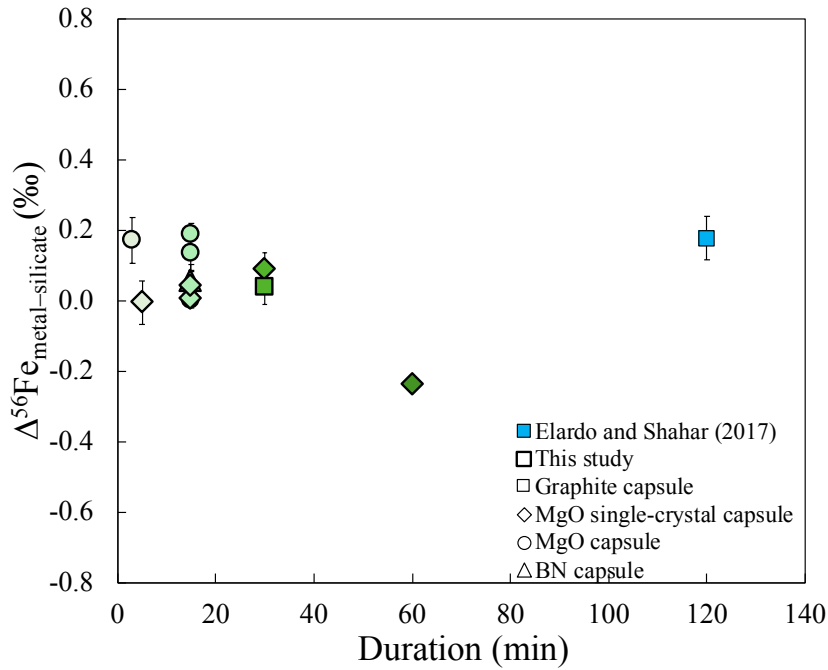


Figure 6.6 – $\Delta^{56}\text{Fe}_{\text{metal-silicate}}$ as a function of time duration for experiments containing 30 *wt.*% Ni in the metal fraction at 2 GPa and 1873 K. Experiments from this study are represented with a thick line symbol, experiment from Elardo and Shahar (2017) is represented with a blue thin line symbol. Graphite encapsulated experiments are coded by a square, experiments with single-crystal MgO capsules are coded by a diamond, circles represent crushable MgO experiments, and BN encapsulated experiments are represented by a triangle. Experiments are color coded according to their equilibrium temperature (same color code as figure 6.1b).

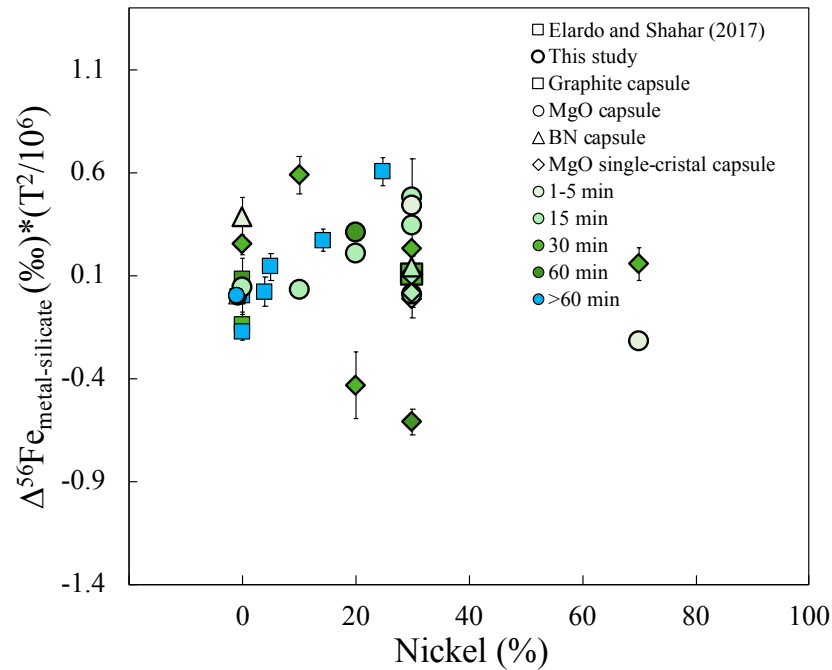


Figure 6.7 – $\Delta^{56}\text{Fe}_{\text{metal-silicate}}$ corrected for the temperature effect of all experiments from this study and from Elardo and Shahaar (2017) as a function of the Ni content of the metallic phase. As experiments were carried at different temperatures, their isotopic fractionation factors are presented here multiplied by T^2 in order to correct for the temperature effect.

On variability in isotopic fractionation data in metal–silicate experiments

To further investigate the quality of our data, it was compared to previous metal–silicate isotopic fractionation experimental works. As scatter can be expected from experimental data, such comparison allows to assess if the data from this study presents enhanced scatter or if it shares the same magnitude of scattering as other studies. When compared to the scatter/amu of previous studies using the same method (table 6.2), we find that the new data reported in this study is scattered to the same order of magnitude as other datasets, which is characteristic of such experimental method. In this compilation, the scatter was determined using experiments sharing the same P, T and composition, and experiments with distinct parameters were only included if such parameter was found to have no

effect.

Table 6.2 – Compilation of scatter/amu for other metal–silicate isotopic fractionation studies.

| | Element | Notation | Scatter ¹ | Scatter/amu ¹ | Scatter ² | Scatter/amu ² |
|--------------------------|----------|----------------------|----------------------|--------------------------|----------------------|--------------------------|
| | <i>M</i> | | (‰) | (‰) | (‰) | (‰) |
| This study | Fe | $\Delta^{56/54}Fe$ | 0.47 | 0.24 | 0.53 | 0.27 |
| Elardo and Shahar (2017) | Fe | $\Delta^{57/54}Fe$ | 0.32 | 0.11 | 0.43 | 0.14 |
| Hin et al. (2012) | Fe | $\Delta^{57/54}Fe$ | 0.33 | 0.11 | 0.84 | 0.28 |
| Poitrasson et al. (2009) | Fe | $\Delta^{57/54}Fe$ | 0.12 | 0.04 | 0.41 | 0.14 |
| Kubik et al. in review | Sn | $\Delta^{122/118}Sn$ | 0.63 | 0.16 | 0.88 | 0.22 |
| Mahan et al. (2017) | Zn | $\Delta^{66/64}Zn$ | 0.17 | 0.09 | 0.27 | 0.14 |
| Hin et al. (2014) | Si | $\Delta^{30/28}Si$ | 0.46 | 0.23 | 0.66 | 0.33 |

¹ Scatter corresponds to the maximum difference between data points of similar PT conditions excluding their error.

² Scatter corresponds to the maximum difference between data points of similar PT conditions including 2 S.D.

Synthesis

7.1 Conclusions

The origin of volatile elements and the timing of their delivery on Earth continue to be subject to intense debate. As part of this PhD thesis, 58 piston cylinder and 15 multianvil experiments were performed in order to determine the behaviour of moderately siderophile and volatile elements between metal and silicate with varying conditions of temperature, pressure, fO_2 and composition. Thermodynamics of metal–silicate equilibria was subsequently used in order to describe the behaviour of the elements of interest as empirical laws, as a function of physical and chemical conditions. Such laws, used as input in numerical core formation models, were used to predict the abundances of the elements of interest in the Earth’s mantle for a selection of plausible accretion and differentiation scenarios. These results were compared to natural abundances in the mantle, in an attempt to resolve one or a variety of scenarios capable of explaining the observed abundances, hence reconciling the experimental data with natural observables.

Following such methodology, the elemental distribution of Sn, Cd, Bi, Sb and Tl (chapters 4 and 5) between metal and silicate was thoroughly studied across a wide range of pressures (from 2 to 20 GPa) and temperatures (1700 to 2600 K), including precise determination of the effect of the S content of the metal, and considering the effect of the silicate melt and the use of various capsule materials. Proper parameterisation of the effect of each variable allowed us to model estimations of the final distribution of the elements of interest in a wide range of

accretion scenarios involving both homogeneous and heterogeneous accretion, full and partial equilibration processes as well as a possible late veneer. We find that a homogeneous accretion with full equilibration of the core with the mantle would induce a massive segregation of Sn, Bi, Sb and Tl into the core, preventing to reconcile the experimental data with observed present-day mantle abundances. Our data supports an accretion of the volatile elements in the late stages of Earth's formation, with material corresponding to 10 to 20% of the Earth's mass, in the form of a giant impactor that only partially equilibrated with the proto-Earth's core, as represented on figure 7.1. A significant amount of S in the Earth's core, ca. 3 *wt.%*, is also needed to account for the relatively high Sn abundance observed in the Earth's mantle. Bismuth is also found too abundant in the mantle which cannot be explained without the accretion of a 0.5% chondritic late veneer after core formation ceased.

Tin isotopic fractionation between metal and silicate was studied in chapter 4 and a significant fractionation factor was measured at the experimental conditions ($\Delta^{122/118}\text{Sn}_{\text{metal-silicate}}=0.3\%$ at 2 GPa, 1600–2300 K). This fractionation could result in the terrestrial mantle being isotopically lighter than the core by 150–200 ppm per amu. Ordinary and enstatite chondrites both present lighter signatures than the BSE (Badullovich et al. 2017, Creech and Moynier 2019, Wang et al. 2018) making them unlikely major contributors to the Sn budget of Earth's mantle. On the other hand, carbonaceous chondrites present identical Sn isotopic signature to the BSE, such that Earth's mantelic Sn budget could have been established by (1) accretion of carbonaceous chondrite-like material with subsequent core formation at high temperature (> 4000 K) preventing fractionation of the mantle with respect to its building blocks or (2) as our partitioning data suggests, accretion of carbonaceous chondrite-like material during the last stages of Earth's accretion with partial equilibration between the core and the mantle. Additionally, the isotopic fractionation predicted by our experimental data could explain the light Sn isotopic signature recorded in the lunar mantle, even though other processes involving mixing and liquid–vapour equilibration in the proto-lunar disk were also proposed to contribute to the light lunar signature (Wang et al. 2019).

As elemental and isotopic fractionations of siderophile elements between metal and silicate are sensitive to the composition of the metal, the effect of the Ni content of the metal on Fe isotopic fractionation was tested. The Ni effect has

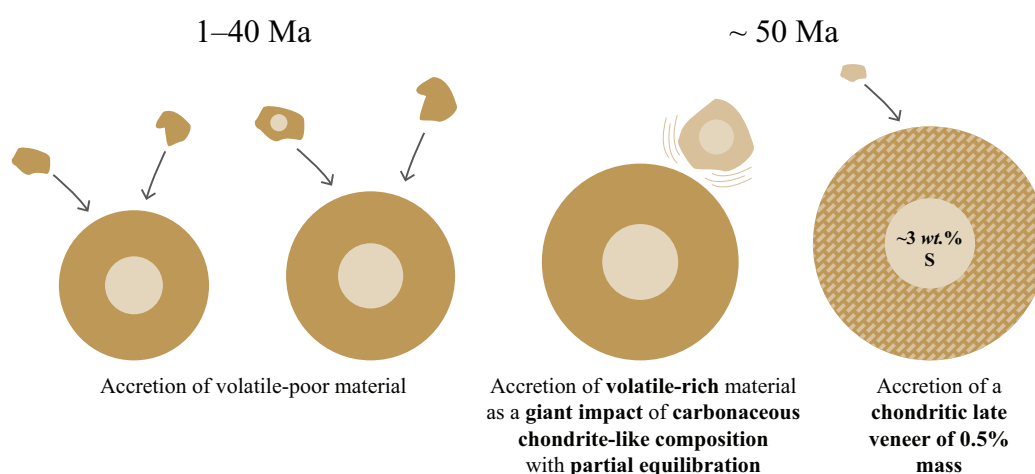


Figure 7.1 – Model for the delivery of volatile elements on Earth including the findings of this study (in bold). In this scenario, the volatile elements are accreted in the last 10 to 20% of Earth’s accretion as a giant impact of carbonaceous chondrite-like composition, with partial equilibration between core and mantle. A late veneer of chondritic composition representing 0.5% of Earth’s mass is subsequently accreted, after core formation ceased. The S budget of the core is estimated to ~ 3 wt.%. Figure by Alexia Schroeder.

been neglected in numerous metal–silicate studies based on assumed (Fe,Ni) alloy ideality, however, it was recently suggested by two studies that the Ni content of the metal may have an effect on isotopic fractionation factors of 3 siderophile elements (Fe, Cu, Zn; Elardo and Shahar 2017, Xia et al. 2019). Such topic therefore has extended implications regarding our understanding of core–mantle interactions. We report a large number of metal–silicate equilibrium experiments (22 piston cylinder experiments) over a wide range of Ni content (0 to 70 wt.% in the metal), with thorough consideration of capsule material and time duration (reported time series from 3 to 60 minutes) and find no effect of the Ni content of the metal on Fe isotopic fractionation between metal and silicate. Our results suggest that core formation alone cannot explain the variability of Fe isotope compositions observed in planetary mantles of the solar system. Our data also suggest chemical ideality of Fe and Ni in a (Fe,Ni) alloy, implying that neglecting the Ni effect in metal–silicate experiments is a correct assumption.

Therefore, the research work carried out during this PhD allowed us to bring new elements to light regarding the timing, process and origin of volatile elements

delivery to Earth, as well as insight on the effect of the core composition on the behaviour of siderophile elements during core formation.

7.2 Future work

7.2.1 Further investigation of MSVE partitioning— Diamond-anvil cell experiments

The experimental data on moderately siderophile and volatile elements (MSVE) presented in the chapters 4 and 5 of this thesis were collected at relatively low pressures with respect to the pressure of equilibration of the terrestrial mantle with the core (i.e. 40–60 GPa, Siebert et al. 2012, 2011, Wade and Wood 2005). Therefore, it can be used to directly interpret natural abundances in small planetary bodies, such as Mars, the Moon and Vesta, and can also be extrapolated to conditions more relevant to the differentiation of larger planetary bodies such as the Earth. In both studies, the behaviour of the elements of interest between metal and silicate was investigated across a relatively wide range of temperatures and pressures, from 1 to 20 GPa, allowing reasonably accurate extrapolation to higher temperature and pressure. However, experimental data at conditions that are directly relevant to the Earth's differentiation can be used to confirm the pressure and temperature effect previously extrapolated from lower pressure data. Therefore, three laser-heated diamond-anvil cell experiments were performed in order to be analysed to determine the partition coefficients of Sn, Cd, Bi, Sb and Tl at high pressure (table 7.1). In each experiment, two pyrolite disks were loaded in the experimental chamber with a small metal sample between them. They were heated with a laser (LHDAC) at IPGP (Université de Paris), resulting in melting of the center of the experimental chamber (figure 7.2).

These experiments will be used to more precisely determine the pressure and temperature effects on MSVEs partitioning over a much broader range of pressure. They will be complemented by piston cylinder experiments containing only one of the MSVEs studied in chapter 5 (i.e. Cd, Bi, Sb and Tl) as these elements were only studied in experiments containing all of them. The composition of the resulting metals therefore contains percent levels of each element, which could have

Table 7.1 – Experimental parameters for the three DAC experiments performed in this project.

| Experiment | Cell | Pressure (GPa) | Temperature(K) | Starting material |
|------------|------|----------------|----------------|----------------------------------|
| #1 | X9 | 45 | 4400 | Pyrolite+(Fe,Sn,Cd,Bi,Sb,Tl) |
| #2 | X17 | 51 | 4100 | Pyrolite+(Fe,Sn,Cd,Bi,Sb,Tl) |
| #3 | JS1 | 47.5 | 4200 | Pyrolite+(Fe,FeS,Sn,Cd,Bi,Sb,Tl) |

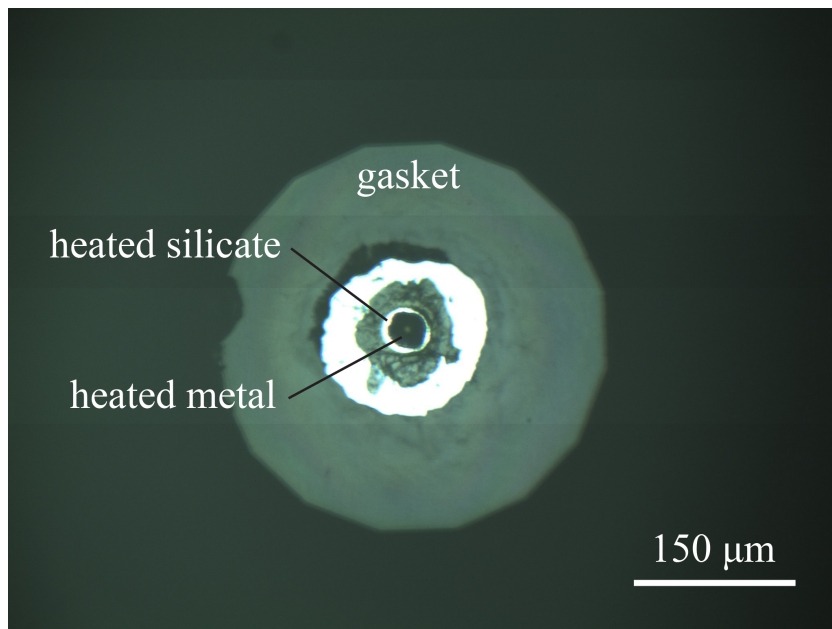


Figure 7.2 – Image of DAC run #2 showing the melted silicate and metal inside the experimental chamber located in a rhenium gasket.

an effect on their respective partition coefficient (that was therefore neglected in the study), interfering with the proper characterisation of their behaviour in an equilibrium between silicate and metal of relevant composition to the Earth's core. A few experiments containing only one element can therefore be used to assess the presence or absence of such an effect.

7.2.2 Further investigating the volatile delivery— Cadmium isotopic fractionation between core and mantle

The relative depletions of volatile elements in the Earth’s mantle with respect to CI chondrites could be the result of various processes that affected matter from the earliest stages of the solar system to the present day, such as volatilisation processes and core formation. The project presented here has two main objectives: first, constraining the accretion scenarios that could produce the observed abundances of volatile elements in the silicate Earth, and secondly, investigating the nature of the building blocks that brought volatile elements to Earth.

By studying the metal–silicate partitioning behavior of elements that are both volatile and siderophile, the effect of Earth’s differentiation can be isolated from the effect of volatile related processes, helping to discriminate between the three main volatile accretion scenarios. Cadmium is a moderately volatile and siderophile element ($T_c=652\text{--}502\text{ K}$; Lodders 2003, Wood et al. 2019) and, as such, is well suited to trace the accretion of volatile elements. Cadmium metal–silicate partitioning data has been reported in several studies (e.g. Wang et al. 2016, Wood et al. 2014) including the work presented here (figure 7.3), with very different conclusions, ranging from Cd mantle abundance being accounted for by core formation (Righter et al. 2017b, 2019; chapter 5 of this study), to not at all (Ballhaus et al. 2013). The contrasted results could be the consequence of the scarcity of high-pressure experimental data allowing to quantify the effect of pressure on Cd partitioning as well as a lack of study only dedicated to Cd. Furthermore, although Cd has been assumed to be present as a $2+$ cation in silicate melts (e.g. Wood et al. 2014), no proper characterisation of the Cd oxidation state has ever been carried in silicate melts under redox conditions relevant for core formation (roughly from 1 to 5 log units below the iron-wüstite buffer), which is critical for the parameterisation of its metal–silicate partitioning behaviour. A comprehensive experimental study focused on Cd elemental behaviour between metal and silicate including the effects of pressure, temperature, fO_2 and light element concentrations (e.g. S), and subsequent parameterisation, could help better understand the processes responsible for the observed Cd abundance in the Earth’s mantle.

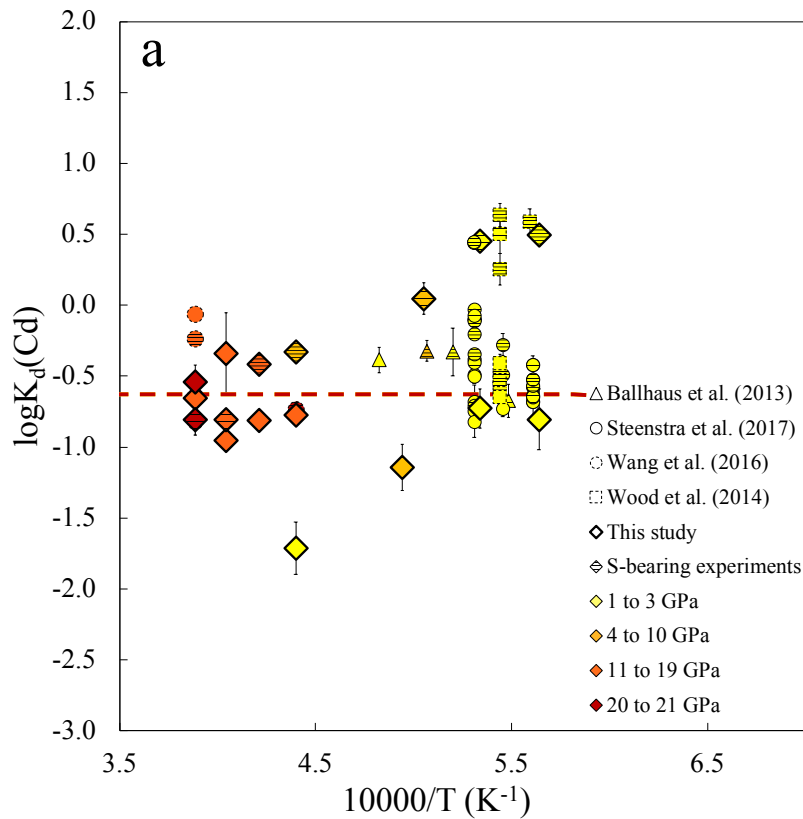


Figure 7.3 – Compilation of experimental Cd partitioning data between metal and silicate (Ballhaus et al. 2013, Steenstra et al. 2017, Wang et al. 2016, Wood et al. 2014; Kubik et al., *in review*, see chapter 5).

Measurements of metal–silicate isotopic fractionation provide a second and independent constraint on the timing and origin of the volatile accretion relative to Earth’s differentiation. Experimental metal–silicate fractionation of a given element can be compared to the isotopic composition of the bulk silicate Earth (BSE) and primitive meteorites to assess whether the element’s isotopic signature in the Earth’s mantle can be explained by the accretion and differentiation of primitive material from the solar system. A recent study by Toth et al. (2020) demonstrated nucleosynthetic homogeneity of Cd in chondrites, suggesting that the observed variations are mass-dependent (Wombacher et al. 2008, 2003), making Cd isotopes suitable for investigating planetary accretion related processes. However, Cd stable isotope data for planetary materials, meteorites and igneous terrestrial rocks is very scarce. Available published data shows that Cd exhibits enhanced variability

of the $\delta^{144/110}\text{Cd}$ amongst primitive meteorites, ranging from -8 to +16 ‰ (see figure 7.4; Wombacher et al. 2008). This variation in Cd isotopic composition may be attributed to secondary processes such as thermal metamorphism or alteration of sulphides (Toth et al. 2020, Wombacher et al. 2008) although it has also been suggested that it could reflect parent body processes (Wombacher et al. 2008, 2003). This opens the possibility to compare experimental isotopic fractionation results to distinctively resolvable signatures of various primitive meteorite groups. Measurements on samples from non-terrestrial inner planetary bodies are also very scarce and presently do not allow to detect variability amongst planetary bodies. The similar isotopic composition of the silicate Earth and CI chondrites (Wombacher et al. 2008) has been used as an argument for the absence of fractionation linked to core formation or volatilisation processes on Earth associated with a CI chondrite-like origin of the volatile elements. However, a potential core–mantle isotopic fractionation has never been investigated experimentally. A comprehensive experimental study of the isotopic behaviour of Cd between metal and silicate at equilibrium conditions would help to interpret planetary and meteorites data, and would have implications whether a fractionation is detected or not. (a) If no isotopic fractionation can be predicted at core formation conditions, the bulk silicate Earth (BSE) isotopic composition can be used as a proxy for the bulk Earth Cd isotopic composition, and confirm the chondritic origin of volatile elements on Earth. (b) If the comprehensive parameterisation of Cd isotopic fractionation between metal and silicate leads to a significant predicted fractionation factor at core formation conditions, core formation models can be used to test multiple accretion scenarios including a late delivery of the volatile elements and distinct source materials, in order to propose one or variety of scenarios capable of producing the observed Cd isotopic composition of the BSE. Such results could have implications regarding the origin and timing of the volatile delivery on Earth as well as the efficiency of the core–mantle equilibration.

Complementary to the experimental study, several meteorite samples (enstatite chondrites, achondrites, martian meteorites, silicate-bearing irons) and terrestrial (modern and archean) peridotite samples could be analysed as potential contributors and constraints on the bulk silicate Earth and Mars compositions.

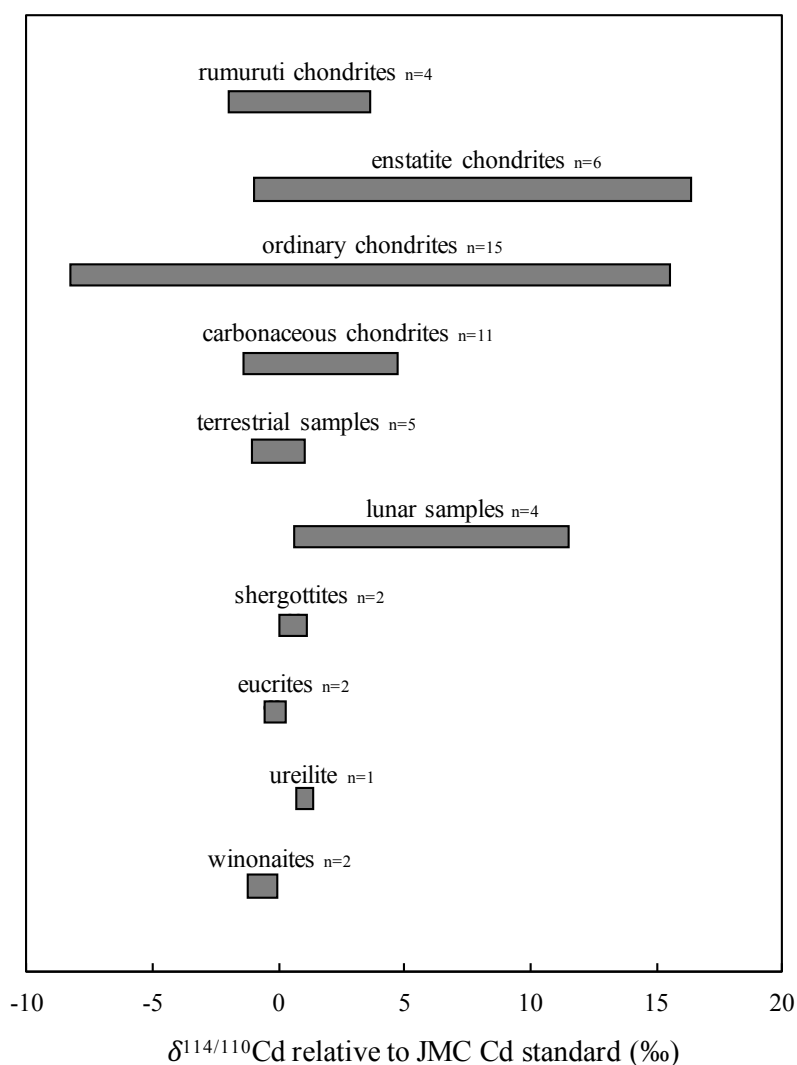


Figure 7.4 – $\delta^{114/110}\text{Cd}$ relative to JMC Cd standard (‰) for meteorites, lunar and terrestrial samples (Wombacher et al. 2008, 2003).

Wider implications

In terms of the timing, origin and mechanism of Earth's accretion, a lot is still unknown and/or subject to debate. In particular, the accretion of volatile elements, although intensely studied, has been explained with a very broad range of different scenarios. This research project would help to bring new elements to various crucial questions associated to this topic. These include but are not limited to:

- Characterisation of the elemental behaviour of Cd in a metal–silicate equilibrium and subsequent core formation modelling can help to resolve one or a variety of accretion scenarios that explain the observed Cd signature in the Earth’s mantle and thus help to constrain the **timing of volatile elements accretion on Earth**. This timing can also be independently characterised if a metal–silicate isotopic fractionation of Cd is measured and predicted at the conditions of Earth’s differentiation, pointing towards a late accretion of volatile elements with possible implications regarding the **efficiency of core segregation**.
- Experimental determination of the metal–silicate fractionation of Cd and its estimation at core formation conditions would allow to determine the isotopic composition of the bulk Earth and may have implications with respect to the **origin of volatile elements** on Earth.

7.2.3 Constraining the physical conditions of Earth’s differentiation—Molybdenum isotopic fractionation between core and mantle

Molybdenum is a refractory siderophile element, and as such, its isotopic signature in the Earth’s mantle is a record of the conditions of the core–mantle equilibration. A study by Hin et al. (2013) based on 3 metal–silicate experiments at 1 GPa reported a resolvable enrichment of heavy Mo in the silicate with respect to the metal. A systematic study of the isotopic fractionation of Mo at 2 GPa using piston cylinder apparatus as well as at higher pressures in multianvil experiments (up to 20 GPa) would allow to produce sufficient material for Mo isotope characterisation of both phases. Thorough parameterisation of the pressure and temperature effect on the isotopic fractionation confronted with the Mo isotopic compositions of different groups of chondrites can bring new evidence on the physical **conditions of the Earth’s differentiation** in relation with the chemical **nature of the building blocks** that accreted to form the Earth. Three preliminary metal–silicate experiments doped with 2% Mo with parameters detailed in table 7.2 were performed at IPGP (Université de Paris) and are currently processed for Mo isotopic analysis.

Elemental and stable isotopic fractionations of siderophile elements

Table 7.2 – Experimental parameters for the three DAC experiments performed in this project.

| Run | Starting material | Pressure (GPa) | Temperature (K) | Time duration (min) | Capsule |
|------|-------------------|----------------|-----------------|---------------------|---------|
| E359 | MORB, Fe, Mo | 2 | 1673 | 30 | MgO |
| E360 | MORB, Fe, Mo | 2 | 1773 | 30 | MgO |
| E362 | MORB, Fe, Mo | 2 | 1873 | 10 | MgO |

Bibliography

- F. Albarède, 2009. Volatile accretion history of the terrestrial planets and dynamic implications. *Nature*, 461(7268):1227–1233.
- F. Albarède, C. Ballhaus, J. Blichert-Toft, C. T. Lee, B. Marty, F. Moynier, and Q. Z. Yin, 2013. Asteroidal impacts and the origin of terrestrial and lunar volatiles. *Icarus*, 222(1):44–52.
- C. M. Alexander, R. Bowden, M. L. Fogel, K. T. Howard, C. D. Herd, and L. R. Nittler, 2012. The provenances of asteroids, and their contributions to the volatile inventories of the terrestrial planets. *Science*, 337(6095):721–723.
- D. Alfè, M. Gillan, and G. D. Price, 2002. Composition and temperature of the Earth’s core constrained by combining ab initio calculations and seismic data. *Earth Planet. Sci. Lett.*, 195(1-2):91–98.
- C. J. Allègre, J. P. Poirier, E. Humler, and A. W. Hofmann, 1995. The chemical composition of the Earth. *Earth Planet. Sci. Lett.*, 134(3-4):515–526.
- Y. Amelin, A. N. Krot, I. D. Hutcheon, and A. A. Ulyanov, 2002. Lead isotopic ages of chondrules and calcium-aluminum-rich inclusions. *Science*, 297(5587):1678–1683.
- A. Anbar, K. Knab, and J. Barling, 2001. Precise determination of mass-dependent variations in the isotopic composition of molybdenum using MC-ICPMS. *Anal. Chem.*, 73(7):1425–1431.
- E. Anders, 1964. Origin, age, and composition of meteorites. *Space Sci. Rev.*, 3(5-6):583–714.
- E. Anders and N. Grevesse, 1989. Abundances of the elements: Meteoritic and solar. *Geochim. Cosmochim. Acta*, 53(1):197–214.

BIBLIOGRAPHY

- O. Anderson and D. Isaak, 2002. Another look at the core density deficit of Earth's outer core. *Phys. Earth Planet. Inter.*, 131(1):19–27.
- D. Andraut, N. Bolfan-Casanova, G. L. Nigro, M. A. Bouhifd, G. Garbarino, and M. Mezouar, 2011. Solidus and liquidus profiles of chondritic mantle: Implication for melting of the Earth across its history. *Earth Planet. Sci. Lett.*, 304(1-2):251–259.
- R. J. Arculus and J. W. Delano, 1981. Siderophile element abundances in the upper mantle: evidence for a sulfide signature and equilibrium with the core. *Geochim. Cosmochim. Acta*, 45(8):1331–1343.
- R. Armytage, R. Georg, P. Savage, H. Williams, and A. Halliday, 2011. Silicon isotopes in meteorites and planetary core formation. *Geochim. Cosmochim. Acta*, 75(13):3662–3676.
- C. Asker, L. Vitos, and I. A. Abrikosov, 2009. Elastic constants and anisotropy in FeNi alloys at high pressures from first-principles calculations. *Phys. Rev. B - Condens. Matter Mater. Phys.*, 79(21):1–9.
- J. Badro, J. P. Brodholt, H. Piet, J. Siebert, and F. J. Ryerson, 2015. Core formation and core composition from coupled geochemical and geophysical constraints. *Proc. Natl. Acad. Sci.*, 112(40):12310–12314.
- J. Badro, A. S. Cote, and J. P. Brodholt, 2014. A seismologically consistent compositional model of Earth's core. *Proc. Natl. Acad. Sci.*, 111(21):7542–7545.
- N. Badullovich, F. Moynier, J. Creech, F. Teng, and P. Sossi, 2017. Tin isotopic fractionation during igneous differentiation and Earth's mantle composition. *Geochemical Perspect. Lett.*, 5:24–28.
- J. Baker, M. Bizzarro, N. Wittig, J. Connelly, and H. Haack, 2005. Early planetesimal melting from an age of 4.5662 gyr for differentiated meteorites. *Nature*, 436(7054):1127–1131.
- C. Ballhaus, R. O. Fonseca, C. Münker, A. Rohrbach, T. Nagel, I. M. Speelmanns, H. M. Helmy, A. Zirner, A. K. Vogel, and A. Heuser, 2017. The great sulfur depletion of Earth's mantle is not a signature of mantle–core equilibration. *Contrib. to Mineral. Petrol.*, 172(8).
- C. Ballhaus, V. Laurenz, C. Münker, R. O. Fonseca, F. Albarède, A. Rohrbach, M. Lagos, M. W. Schmidt, K.-P. Jochum, B. Stoll, U. Weis, and H. M. Helmy, 2013. The U/Pb ratio of the Earth's mantle—A signature of late volatile addition. *Earth Planet. Sci. Lett.*, 362:237–245.

- H. Bao, X. Cao, and J. A. Hayles, 2015. The confines of triple oxygen isotope exponents in elemental and complex mass-dependent processes. *Geochim. Cosmochim. Acta*, 170:39–50.
- N. R. Bennett, J. M. Brenan, and K. T. Koga, 2014. The solubility of platinum in silicate melt under reducing conditions: Results from experiments without metal inclusions. *Geochim. Cosmochim. Acta*, 133:422–442.
- W. Benz and A. G. W. Cameron, 1990. *Terrestrial effects of the Giant Impact*, volume Origin of the Earth. Oxford University Press, Newsom H.E. and Jones J.H. edition.
- A. J. Berry and H. S. C. O’Neill, 2004. A XANES determination of the oxidation state of chromium in silicate glasses. *Am. Mineral.*, 89(5-6):790–798.
- J. Bigeleisen and M. G. Mayer, 1947. Calculation of equilibrium constants for isotopic exchange reactions. *J. Chem. Phys.*, 15(5):261–267.
- F. Birch, 1952. Elasticity and constitution of the Earth’s interior. *J. Geophys. Res.*, 57(2):227–286.
- F. Birch, 1964. Density and composition of mantle and core. *J. Geophys. Res.*, 69(20):4377–4388.
- I. Blanchard, J. Badro, J. Siebert, and F. Ryerson, 2015. Composition of the core from gallium metal–silicate partitioning experiments. *Earth Planet. Sci. Lett.*, 427:191–201.
- H. Bloom, K. Lodders, H. Chen, C. Zhao, Z. Tian, P. Koefoed, M. K. Pető, Y. Jiang, and K. Wang, 2020. Potassium isotope compositions of carbonaceous and ordinary chondrites: Implications on the origin of volatile depletion in the early solar system. *Geochim. Cosmochim. Acta*, 277:111–131.
- S. R. Bohlen and A. Boettcher, 1982. The quartz–coesite transformation: a precise determination and the effects of other components. *J. Geophys. Res. Solid Earth*, 87(B8):7073–7078.
- J. Bollard, J. N. Connelly, M. J. Whitehouse, E. A. Pringle, L. Bonal, J. K. Jørgensen, Å. Nordlund, F. Moynier, and M. Bizzarro, 2017. Early formation of planetary building blocks inferred from Pb isotopic ages of chondrules. *Sci. Adv.*, 3(8):e1700407.
- P. Bonnard, H. Williams, I. Parkinson, B. Wood, and A. Halliday, 2016. Stable chromium isotopic composition of meteorites and metal–silicate experiments: Implications for fractionation during core formation. *Earth Planet. Sci. Lett.*, 435:14–21.

BIBLIOGRAPHY

- W. F. Bottke, R. J. Walker, J. M. Day, D. Nesvorny, and L. Elkins-Tanton, 2010. Stochastic late accretion to Earth, the Moon, and Mars. *Science*, 330(6010):1527–1530.
- M. A. Bouhifd and A. P. Jephcoat, 2003. The effect of pressure on partitioning of Ni and Co between silicate and iron-rich metal liquids: a diamond-anvil cell study. *Earth Planet. Sci. Lett.*, 209(1-2):245–255.
- A. Boujibar, D. Andrault, M. A. Bouhifd, N. Bolfan-Casanova, J. L. Devidal, and N. Trcera, 2014. Metal-silicate partitioning of sulphur, new experimental and thermodynamic constraints on planetary accretion. *Earth Planet. Sci. Lett.*, 391:42–54.
- B. Bourdon, M. Roskosz, and R. C. Hin, 2018. Isotope tracers of core formation. *Earth-Science Rev.*, 181(April):61–81.
- A. Bouvier, J. Blichert-Toft, F. Moynier, J. D. Vervoort, and F. Albarède, 2007. Pb–Pb dating constraints on the accretion and cooling history of chondrites. *Geochim. Cosmochim. Acta*, 71(6):1583–1604.
- A. Bouvier and M. Wadhwa, 2010. The age of the Solar System redefined by the oldest Pb–Pb age of a meteoritic inclusion. *Nat. Geosci.*, 3(9):637–641.
- J. W. Boyce, A. H. Treiman, Y. Guan, C. Ma, J. M. Eiler, J. Gross, J. P. Greenwood, and E. M. Stolper, 2015. The chlorine isotope fingerprint of the lunar magma ocean. *Sci. Adv.*, 1(8):2–10.
- A. D. Brandon and R. J. Walker, 2005. The debate over core–mantle interaction. *Earth Planet. Sci. Lett.*, 232(3-4):211–225.
- N. Braukmüller, F. Wombacher, C. Funk, and C. Münker, 2019. Earth’s volatile element depletion pattern inherited from a carbonaceous chondrite-like source. *Nat. Geosci.*, 12(7):564–568.
- L. J. Bridgestock, H. Williams, M. Rehkämper, F. Larnier, M. D. Giscard, S. Hammond, B. Coles, R. Andreasen, B. J. Wood, K. J. Theis, C. L. Smith, G. K. Benedix, and M. Schönbächler, 2014. Unlocking the zinc isotope systematics of iron meteorites. *Earth Planet. Sci. Lett.*, 400:153–164.
- J. M. Brown and R. G. McQueen, 1986. Phase transitions, Grüneisen parameter, and elasticity for shocked iron between 77 GPa and 400 GPa. *J. Geophys. Res. Solid Earth*, 91(B7):7485–7494.
- G. Budde, C. Burkhardt, and T. Kleine, 2019. Molybdenum isotopic evidence for the late accretion of outer Solar System material to Earth. *Nat. Astron.*, 3(August):1–6.

- C. Burkhardt, R. C. Hin, T. Kleine, and B. Bourdon, 2014. Evidence for Mo isotope fractionation in the solar nebula and during planetary differentiation. *Earth Planet. Sci. Lett.*, 391:201–211.
- C. Burkhardt, T. Kleine, F. Oberli, A. Pack, B. Bourdon, and R. Wieler, 2011. Molybdenum isotope anomalies in meteorites: constraints on solar nebula evolution and origin of the Earth. *Earth Planet. Sci. Lett.*, 312(3-4):390–400.
- A. Cameron, 2000. *Higher-resolution simulations of the giant impact*, volume Origin of the Earth and Moon. Canup R.M. and Righter K., The University of Arizona Press. edition.
- R. M. Canup, 2012. Forming a Moon with an Earth-like composition via a giant impact. *Science*, 338(6110):1052–1055.
- R. M. Canup and E. Asphaug, 2001. Origin of the Moon in a giant impact near the end of the Earth’s formation. *Nature*, 412(6848):708–712.
- X. Cao and H. Bao, 2017. Redefining the utility of the three-isotope method. *Geochim. Cosmochim. Acta*, 212:16–32.
- C. J. Capobianco, M. J. Drake, and J. De’Aro, 1999. Siderophile geochemistry of Ga, Ge, and Sn: Cationic oxidation states in silicate melts and the effect of composition in iron-nickel alloys. *Geochim. Cosmochim. Acta*, 63(17):2667–2677.
- R. W. Carlson, M. Boyet, J. O’Neil, H. Rizo, and R. J. Walker, 2015. Early differentiation and its long-term consequences for Earth evolution. *The Early Earth: Accretion and Differentiation*, pages 143–172.
- G. Caro, B. Bourdon, B. J. Wood, and A. Corgne, 2005. Trace-element fractionation in hadean mantle generated by melt segregation from a magma ocean. *Nature*, 436(7048):246–249.
- C. Cartier, T. Hammouda, M. Boyet, M. A. Bouhifd, and J.-L. Devidal, 2014. Redox control of the fractionation of niobium and tantalum during planetary accretion and core formation. *Nat. Geosci.*, 7(8):573–576.
- N. L. Chabot and C. B. Agee, 2003. Core formation in the Earth and Moon: new experimental constraints from V, Cr, and Mn. *Geochim. Cosmochim. Acta*, 67(11):2077–2091.
- J. E. Chambers, 2004. Planetary accretion in the inner solar system. *Earth Planet. Sci. Lett.*, 223(3-4):241–252.

BIBLIOGRAPHY

- J. E. Chambers and A. N. Halliday, 2007. The origin of the solar system. *Encyclopaedia of the solar system*, pages 29–52.
- S. Charnoz, F. C. Pignatale, R. Hyodo, B. Mahan, M. Chaussidon, J. Siebert, and F. Moynier, 2019. Planetesimal formation in an evolving protoplanetary disk with a dead zone. *Astron. Astrophys.*, 627:A50.
- C.-L. Chou, D. Shaw, and J. Crocket, 1983. Siderophile trace elements in the Earth's oceanic crust and upper mantle. *J. Geophys. Res. Solid Earth*, 88(S02):A507–A518.
- P. L. Clay, R. Burgess, H. Busemann, L. Ruzi -Hamilton, B. Joachim, J. M. Day, and C. J. Ballentine, 2017. Halogens in chondritic meteorites and terrestrial accretion. *Nature*, 551(7682):614–618.
- R. N. Clayton, T. K. Mayeda, and A. E. Rubin, 1984. Oxygen isotopic compositions of enstatite chondrites and aubrites. *J. Geophys. Res. Solid Earth*, 89(S01):C245–C249.
- V. Clesi, M. A. Bouhifd, N. Bolfan-Casanova, G. Manthilake, F. Schiavi, C. Raepsaet, H. Bureau, H. Khodja, and D. Andrault, 2018. Low hydrogen contents in the cores of terrestrial planets. *Sci. Adv.*, 4(3):e1701876.
- W. Compston and V. Oversby, 1969. Lead isotopic analysis using a double spike. *J. Geophys. Res.*, 74(17):4338–4348.
- J. N. Connelly, M. Bizzarro, A. N. Krot,  . Nordlund, D. Wielandt, and M. A. Ivanova, 2012. The absolute chronology and thermal processing of solids in the solar protoplanetary disk. *Science*, 338(6107):651–655.
- A. Corgne, S. Keshav, B. J. Wood, W. F. McDonough, and Y. Fei, 2008. Metal-silicate partitioning and constraints on core composition and oxygen fugacity during Earth accretion. *Geochim. Cosmochim. Acta*, 72(2):574–589.
- E. Cottrell, K. A. Kelley, A. Lanzirotti, and R. A. Fischer, 2009a. High-precision determination of iron oxidation state in silicate glasses using XANES. *Chem. Geol.*, 268(3-4):167–179.
- E. Cottrell and D. Walker, 2006. Constraints on core formation from Pt partitioning in mafic silicate liquids at high temperatures. *Geochim. Cosmochim. Acta*, 70(6):1565–1580.
- E. Cottrell, M. J. Walter, and D. Walker, 2009b. Metal-silicate partitioning of tungsten at high pressure and temperature: implications for equilibrium core formation in Earth. *Earth Planet. Sci. Lett.*, 281(3-4):275–287.

- P. R. Craddock and N. Dauphas, 2011. Iron Isotopic Compositions of Geological Reference Materials and Chondrites. *Geostand. Geoanalytical Res.*, 35(1):101–123.
- P. R. Craddock, J. M. Warren, and N. Dauphas, 2013. Abyssal peridotites reveal the near-chondritic Fe isotopic composition of the Earth. *Earth Planet. Sci. Lett.*, 365:63–76.
- J. B. Creech, J. Baker, M. Handler, J.-P. Lorand, M. Storey, A. Wainwright, A. Luguët, F. Moynier, and M. Bizzarro, 2017a. Late accretion history of the terrestrial planets inferred from platinum stable isotopes. *Geochemical Perspect. Lett.*, pages 94–104.
- J. B. Creech, J. A. Baker, M. R. Handler, and M. Bizzarro, 2014. Platinum stable isotope analysis of geological standard reference materials by double-spike MC-ICPMS. *Chem. Geol.*, 363:293–300.
- J. B. Creech and F. Moynier, 2019. Tin and zinc stable isotope characterisation of chondrites and implications for early Solar System evolution. *Chem. Geol.*, 511:81–90.
- J. B. Creech, F. Moynier, and N. Badullovich, 2017b. Tin stable isotope analysis of geological materials by double-spike MC-ICPMS. *Chem. Geol.*, 457:61–67.
- J. B. Creech, F. Moynier, and M. Bizzarro, 2017c. Tracing metal-silicate segregation and late veneer in the Earth and the ureilite parent body with palladium stable isotopes. *Geochim. Cosmochim. Acta*, 216:28–41.
- J. B. Creech and B. Paul, 2015. IsoSpike: Improved double-spike inversion software. *Geostand. Geoanalytical Res.*, 39(1):7–15.
- R. Criss, R. Gregory, and H. Taylor Jr, 1987. Kinetic theory of oxygen isotopic exchange between minerals and water. *Geochim. Cosmochim. Acta*, 51(5):1099–1108.
- M. Čuk and S. T. Stewart, 2012. Making the Moon from a fast-spinning Earth: a giant impact followed by resonant despinning. *Science*, 338(6110):1047–1052.
- T. W. Dahl and D. J. Stevenson, 2010. Turbulent mixing of metal and silicate during planet accretion—And interpretation of the Hf–W chronometer. *Earth Planet. Sci. Lett.*, 295(1-2):177–186.
- C. Dalou, E. Füri, C. Deligny, L. Piani, M. C. Caumon, M. Laumonier, J. Boulliang, and M. Edén, 2019. Redox control on nitrogen isotope fractionation during planetary core formation. *Proc. Natl. Acad. Sci. U. S. A.*, 116(29):14485–14494.
- R. T. Daly and P. H. Schultz, 2018. The delivery of water by impacts from planetary accretion to present. *Sci. Adv.*, 4(4):1–12.

BIBLIOGRAPHY

- L. Danielson, T. Sharp, and R. Hervig, 2005. Implications for core formation of the Earth from high pressure-temperature Au partitioning experiments. *Lunar and Planetary Science XXXVI, Part 4*.
- N. Dauphas, 2017. The isotopic nature of the Earth's accreting material through time. *Nature*, 541(7638):521–524.
- N. Dauphas and M. Chaussidon, 2011. A perspective from extinct radionuclides on a young stellar object: The sun and its accretion disk. *Annu. Rev. Earth Planet. Sci.*, 39:351–386.
- N. Dauphas, J. H. Chen, J. Zhang, D. A. Papanastassiou, A. M. Davis, and C. Travaglio, 2014. Calcium-48 isotopic anomalies in bulk chondrites and achondrites: Evidence for a uniform isotopic reservoir in the inner protoplanetary disk. *Earth Planet. Sci. Lett.*, 407:96–108.
- N. Dauphas and B. Marty, 2002. Inference on the nature and the mass of Earth's late veneer from noble metals and gases. *J. Geophys. Res. E Planets*, 107(12):1–7.
- J. M. Day, A. D. Brandon, and R. J. Walker, 2016. Highly siderophile elements in Earth, Mars, the Moon, and asteroids. *Rev. Mineral. Geochemistry*, 81(1):161–238.
- S. DeGroot and P. Mazur, 1962. Non-equilibrium thermodynamics. *Publ. Cy. Amsterdam*.
- R. Deguen, M. Landeau, and P. Olson, 2014. Turbulent metal-silicate mixing, fragmentation, and equilibration in magma oceans. *Earth Planet. Sci. Lett.*, 391:274–287.
- M. J. Drake and K. Righter, 2002. Determining the composition of the Earth. *Nature*, 416(6876):39–44.
- G. Dreibus and H. Palme, 1996. Cosmochemical constraints on the sulfur content in the Earth's core. *Geochim. Cosmochim. Acta*, 60(7):1125–1130.
- S. M. Elardo and A. Shahar, 2017. Non-chondritic iron isotope ratios in planetary mantles as a result of core formation. *Nat. Geosci.*, 10(4):317–321.
- S. M. Elardo, A. Shahar, T. D. Mock, and C. K. Sio, 2019. The effect of core composition on iron isotope fractionation between planetary cores and mantles. *Earth Planet. Sci. Lett.*, 513:124–134.
- W. Ertel, H. S. C. O'Neill, P. J. Sylvester, D. Dingwell, and B. Spettel, 2001. The solubility of rhenium in silicate melts: Implications for the geochemical properties of rhenium at high temperatures. *Geochim. Cosmochim. Acta*, 65(13):2161–2170.

- H. P. Eugster and D. R. Wones, 1962. Stability relations of the ferruginous biotite, annite. *J. Petrol.*, 3(1):82–125.
- T. Fang and Y. Liu, 2019. Equilibrium thallium isotope fractionation and its constraint on Earth's late veneer. *Acta Geochim.*, 38(4):459–471.
- G. Faure and T. Mensing, 2007. *Introduction to planetary science*, volume The geological perspective. Springer.
- B. Fegley, 2000. Kinetics of gas-grain reactions in the solar nebula. *Space Sci. Rev.*, 92(1-2):177–200.
- G. Fiquet, A. L. Auzende, J. Siebert, A. Corgne, H. Bureau, H. Ozawa, and G. Garbarino, 2010. Melting of Peridotite to 140 Gigapascals. *Science*, 329(5998):1516–1518.
- R. A. Fischer, Y. Nakajima, A. J. Campbell, D. J. Frost, D. Harries, F. Langenhorst, N. Miyajima, K. Pollok, and D. C. Rubie, 2015. High pressure metal-silicate partitioning of Ni, Co, V, Cr, Si, and O. *Geochim. Cosmochim. Acta*, 167:177–194.
- M. Fischer-Gödde, B. M. Elfers, C. Münker, K. Szilas, W. D. Maier, N. Messling, T. Morishita, M. Van Kranendonk, and H. Smithies, 2020. Ruthenium isotope vestige of Earth's pre-late-veener mantle preserved in Archaean rocks. *Nature*, 579(7798):240–244.
- C. Fitoussi and B. Bourdon, 2012. Silicon isotope evidence against an enstatite chondrite Earth. *Science*, 335(6075):1477–1480.
- R. A. Fogel, P. C. Hess, and M. J. Rutherford, 1989. Intensive parameters of enstatite chondrite metamorphism. *Geochim. Cosmochim. Acta*, 53(10):2735–2746.
- D. G. Fraser and W. Rammensee, 1982. Activity measurements by Knudsen cell mass spectrometry—the system Fe-Co-Ni and implications for condensation processes in the solar nebula. *Geochim. Cosmochim. Acta*, 46(4):549–556.
- B. R. Frost, 1991. Introduction to oxygen fugacity and its petrologic importance. *Rev. Mineral. Geochemistry*, 25:1–9.
- D. J. Frost, Y. Asahara, D. C. Rubie, N. Miyajima, L. S. Dubrovinsky, C. Holzappel, E. Ohtani, M. Miyahara, and T. Sakai, 2010. Partitioning of oxygen between the Earth's mantle and core. *J. Geophys. Res. Solid Earth*, 115(2):1–14.
- D. J. Frost, U. Mann, Y. Asahara, and D. C. Rubie, 2008. The redox state of the mantle during and just after core formation. *Philos. Trans. R. Soc. A Math. Phys. Eng. Sci.*, 366(1883):4315–4337.

BIBLIOGRAPHY

- D. J. Frost and C. A. McCammon, 2008. The redox state of earth's mantle. *Annu. Rev. Earth Planet. Sci.*, 36:389–420.
- D. J. Frost, B. T. Poe, R. G. Trønnes, C. Liebske, A. Duba, and D. C. Rubie, 2004. A new large-volume multianvil system. *Phys. Earth Planet. Inter.*, 143(1-2):507–514.
- Y. Fukai and S.-i. Akimoto, 1983. Hydrogen in the Earth's Core. *Proc. Jpn. Acad.*, 59(6):158–162.
- J. Geiss and A. P. Rossi, 2013. On the chronology of lunar origin and evolution. *Astron. Astrophys. Rev.*, 21(1):68.
- R. B. Georg, A. N. Halliday, E. A. Schauble, and B. C. Reynolds, 2007. Silicon in the Earth's core. *Nature*, 447(7148):1102–1106.
- C. Gessmann, B. Wood, D. Rubie, and M. Kilburn, 2001. Solubility of silicon in liquid metal at high pressure: implications for the composition of the Earth's core. *Earth Planet. Sci. Lett.*, 184(2):367–376.
- C. K. Gessmann and D. C. Rubie, 1998. The effect of temperature on the partitioning of nickel, cobalt, manganese, chromium, and vanadium at 9 GPa and constraints on formation of the Earth's core. *Geochim. Cosmochim. Acta*, 62(5):867–882.
- C. K. Gessmann and D. C. Rubie, 2000. The origin of the depletions of V, Cr and Mn in the mantles of the Earth and Moon. *Earth Planet. Sci. Lett.*, 184(1):95–107.
- V. M. Goldschmidt, 1937. The principles of distribution of chemical elements in minerals and rocks. the seventh hugo müller lecture, delivered before the chemical society on march 17th, 1937. *J. Chem. Soc.*, pages 655–673.
- R. Gomes, H. F. Levison, K. Tsiganis, and A. Morbidelli, 2005. Origin of the cataclysmic Late Heavy Bombardment period of the terrestrial planets. *Nature*, 435(7041):466–469.
- R. C. Greenwood, I. A. Franchi, A. Jambon, and P. C. Buchanan, 2005. Widespread magma oceans on asteroidal bodies in the early solar system. *Nature*, 435(7044):916–918.
- J. Guignard, G. Quitté, M. Méheut, M. J. Toplis, F. Poitrasson, D. Connetable, and M. Roskosz, 2020. Nickel isotope fractionation during metal-silicate differentiation of planetesimals: Experimental petrology and ab initio calculations. *Geochim. Cosmochim. Acta*, 269:238–256.
- A. N. Halliday, 2013. The origins of volatiles in the terrestrial planets. *Geochim. Cosmochim. Acta*, 105:146–171.

- A. N. Halliday and D. Porcelli, 2001. In search of lost planets—the paleocosmochemistry of the inner solar system. *Earth Planet. Sci. Lett.*, 192(4):545–559.
- U. Hans, T. Kleine, and B. Bourdon, 2013. Rb–Sr chronology of volatile depletion in differentiated protoplanets: BABI, ADOR and ALL revisited. *Earth Planet. Sci. Lett.*, 374:204–214.
- R. J. Hemley and H.-K. Mao, 2001. In situ studies of iron under pressure: New windows on the Earth’s core. *Int. Geol. Rev.*, 43(1):1–30.
- C. Herzberg and J. Zhang, 1996. Melting experiments on anhydrous peridotite KLB-1: Compositions of magmas in the upper mantle and transition zone. *J. Geophys. Res. B Solid Earth*, 101(4):8271–8295.
- R. C. Hin, C. Burkhardt, M. W. Schmidt, B. Bourdon, and T. Kleine, 2013. Experimental evidence for Mo isotope fractionation between metal and silicate liquids. *Earth Planet. Sci. Lett.*, 379:38–48.
- R. C. Hin, C. D. Coath, P. J. Carter, F. Nimmo, Y. J. Lai, P. A. Pogge von Strandmann, M. Willbold, Z. M. Leinhardt, M. J. Walter, and T. Elliott, 2017. Magnesium isotope evidence that accretional vapour loss shapes planetary compositions. *Nature*, 549(7673):511–527.
- R. C. Hin, C. Fitoussi, M. W. Schmidt, and B. Bourdon, 2014. Experimental determination of the Si isotope fractionation factor between liquid metal and liquid silicate. *Earth Planet. Sci. Lett.*, 387:55–66.
- R. C. Hin, M. W. Schmidt, and B. Bourdon, 2012. Experimental evidence for the absence of iron isotope fractionation between metal and silicate liquids at 1 GPa and 1250–1300 °C and its cosmochemical consequences. *Geochim. Cosmochim. Acta*, 93:164–181.
- G. Holland, M. Cassidy, and C. Ballentine, 2009. Meteorite Kr in Earth ’ s Mantle. *Science*, 326:1522–1526.
- A. Holzheid, P. Sylvester, H. S. C. O’Neill, D. C. Rubie, and H. Palme, 2000. Evidence for a late chondritic veneer in the Earth’s mantle from high-pressure partitioning of palladium and platinum. *Nature*, 406(6794):396–399.
- D. Huang and J. Badro, 2018. Fe-Ni ideality during core formation on Earth. *Am. Mineral.*, 103(10):1707–1710.
- M. Humayun and R. N. Clayton, 1995. Potassium isotope cosmochemistry: Genetic implications of volatile element depletion. *Geochim. Cosmochim. Acta*, 59(10):2131–2148.

BIBLIOGRAPHY

- S. A. Jacobson and A. Morbidelli, 2014. Lunar and terrestrial planet formation in the Grand Tack scenario. *Philos. Trans. R. Soc. A Math. Phys. Eng. Sci.*, 372(2024):20130174.
- D. Jana and D. Walker, 1997. The influence of silicate melt composition on distribution of siderophile elements among metal and silicate liquids. *Earth Planet. Sci. Lett.*, 150(3-4):463–472.
- M. Javoy, 1995. The integral enstatite chondrite model of the Earth. *Geophys. Res. Lett.*, 22(16):2219–2222.
- M. Javoy, E. Kaminski, F. Guyot, D. Andraut, C. Sanloup, M. Moreira, S. Labrosse, A. Jambon, P. Agrinier, A. Davaille, and C. Jaupart, 2010. The chemical composition of the Earth: Enstatite chondrite models. *Earth Planet. Sci. Lett.*, 293(3-4):259–268.
- R. Jeanloz, 1979. Properties of iron at high pressures and the state of the core. *J. Geophys. Res. Solid Earth*, 84(B11):6059–6069.
- A. Jephcoat and P. Olson, 1987. Is the inner core of the Earth pure iron? *Nature*, 325(6102):332–335.
- J. H. Jones and M. J. Drake, 1986. Geochemical constraints on core formation in the Earth. *Nature*, 322(6076):221–228.
- J.S.P.S., 1988. *Steelmaking data sourcebook*. Gordon and Breach Science Publishers, Montreux.
- E. Kaminski and M. Javoy, 2013. A two-stage scenario for the formation of the Earth's mantle and core. *Earth Planet. Sci. Lett.*, 365:97–107.
- A. P. Kantor, I. Y. Kantor, A. V. Kurnosov, A. Y. Kuznetsov, N. A. Dubrovinskaia, M. Krisch, A. A. Bossak, V. P. Dmitriev, V. S. Urusov, and L. S. Dubrovinsky, 2007. Sound wave velocities of fcc Fe-Ni alloy at high pressure and temperature by mean of inelastic X-ray scattering. *Phys. Earth Planet. Inter.*, 164(1-2):83–89.
- S.-I. Karato and V. R. Murthy, 1997. Core formation and chemical equilibrium in the Earth—I. Physical considerations. *Phys. Earth Planet. Inter.*, 100(1-4):61–79.
- C. Kato, F. Moynier, M. C. Valdes, J. K. Dhaliwal, and J. M. Day, 2015. Extensive volatile loss during formation and differentiation of the Moon. *Nat. Commun.*, 6:1–4.
- N. Kawai and S. Endo, 1970. The generation of ultrahigh hydrostatic pressures by a split sphere apparatus. *Rev. Sci. Instrum.*, 41(8):1178–1181.

- N. Kawai, M. Togaya, and A. Onodera, 1973. A new device for pressure vessels. *Proc. Jpn. Acad.*, 49(8):623–626.
- P. Kegler, A. Holzheid, D. J. Frost, D. C. Rubie, R. Dohmen, and H. Palme, 2008. New Ni and Co metal-silicate partitioning data and their relevance for an early terrestrial magma ocean. *Earth Planet. Sci. Lett.*, 268(1-2):28–40.
- K. Keil, D. Stoeffler, S. Love, and E. Scott, 1997. Constraints on the role of impact heating and melting in asteroids. *Meteorit. Planet. Sci.*, 32(3):349–363.
- J. Kempl, P. Z. Vroon, E. Zinngrebe, and W. van Westrenen, 2013. Si isotope fractionation between Si-poor metal and silicate melt at pressure-temperature conditions relevant to metal segregation in small planetary bodies. *Earth Planet. Sci. Lett.*, 368:61–68.
- J. D. Kendall and H. J. Melosh, 2016. Differentiated planetesimal impacts into a terrestrial magma ocean: Fate of the iron core. *Earth Planet. Sci. Lett.*, 448:24–33.
- K. Kimura, R. S. Lewis, and E. Anders, 1974. Distribution of gold and rhenium between nickel-iron and silicate melts: implications for the abundance of siderophile elements on the Earth and Moon. *Geochim. Cosmochim. Acta*, 38(5):683–701.
- S. van der Laan, Y. Zhang, A. K. Kennedy, and P. J. Wyllie, 1994. Comparison of element and isotope diffusion of K and Ca in multicomponent silicate melts. *Earth Planet. Sci. Lett.*, 123(1-3):155–166.
- J. Labidi, A. Shahar, C. Le Losq, V. J. Hillgren, B. O. Mysen, and J. Farquhar, 2016. Experimentally determined sulfur isotope fractionation between metal and silicate and implications for planetary differentiation. *Geochim. Cosmochim. Acta*, 175:181–194.
- C. Lazar, E. D. Young, and C. E. Manning, 2012. Experimental determination of equilibrium nickel isotope fractionation between metal and silicate from 500°C to 950°C. *Geochim. Cosmochim. Acta*, 86:276–295.
- C. E. Leshner, 1990. Decoupling of chemical and isotopic exchange during magma mixing. *Nature*, 344(6263):235–237.
- C. E. Leshner, J. Dannberg, G. H. Barfod, N. R. Bennett, J. J. Glessner, D. J. Lacks, and J. M. Brenan, 2020. Iron isotope fractionation at the core–mantle boundary by thermodiffusion. *Nat. Geosci.*, 13(5):382–386.
- V. Lherm and R. Deguen, 2018. Small-Scale Metal/Silicate Equilibration During Core Formation: The Influence of Stretching Enhanced Diffusion on Mixing. *J. Geophys. Res. Solid Earth*, 123(12):10,496–10,516.

BIBLIOGRAPHY

- J. Li and C. B. Agee, 2001. The effect of pressure, temperature, oxygen fugacity and composition on partitioning of nickel and cobalt between liquid Fe-Ni-S alloy and liquid silicate: Implications for the Earth's core formation. *Geochim. Cosmochim. Acta*, 65(11):1821–1832.
- Y. Li, R. Dasgupta, K. Tsuno, B. Monteleone, and N. Shimizu, 2016. Carbon and sulfur budget of the silicate Earth explained by accretion of differentiated planetary embryos. *Nat. Geosci.*, 9(10):781–785.
- J. F. Lin, V. V. Struzhkin, W. Sturhahn, E. Huang, J. Zhao, M. Y. Hu, E. E. Alp, H. Kwang Mao, N. Boctor, and R. J. Hemley, 2003. Sound velocities of iron-nickel and iron-silicon alloys at high pressures. *Geophys. Res. Lett.*, 30(21):1–4.
- J. Liu, N. Dauphas, M. Roskosz, M. Y. Hu, H. Yang, W. Bi, J. Zhao, E. E. Alp, J. Y. Hu, and J. F. Lin, 2017. Iron isotopic fractionation between silicate mantle and metallic core at high pressure. *Nat. Commun.*, 8:1–6.
- Y. Liu, M. J. Spicuzza, P. R. Craddock, J. M. Day, J. W. Valley, N. Dauphas, and L. A. Taylor, 2010. Oxygen and iron isotope constraints on near-surface fractionation effects and the composition of lunar mare basalt source regions. *Geochim. Cosmochim. Acta*, 74(21):6249–6262.
- E. C. Lloyd, 1971. *Accurate Characterization of the High-pressure Environment: Proceedings*, volume 13. US National Bureau of Standards.
- S. J. Lock and S. T. Stewart, 2017. The structure of terrestrial bodies: Impact heating, corotation limits, and synestias. *J. Geophys. Res. Planets*, 122(5):950–982.
- K. Lodders, 2003. Solar System Abundances and Condensation Temperatures of the Elements. *Astrophys. J.*, 591(2):1220–1247.
- J. M. Luck, D. B. Othman, and F. Albarède, 2005. Zn and Cu isotopic variations in chondrites and iron meteorites: Early solar nebula reservoirs and parent-body processes. *Geochim. Cosmochim. Acta*, 69(22):5351–5363.
- Z. Ma, 2001. Thermodynamic description for concentrated metallic solutions using interaction parameters. *Metall. Mater. Trans. B*, 32(1):87–103.
- B. Mahan, J. Siebert, I. Blanchard, J. Badro, E. Kubik, P. Sossi, and F. Moynier, 2018a. Investigating Earth's Formation History Through Copper and Sulfur Metal-Silicate Partitioning During Core-Mantle Differentiation. *J. Geophys. Res. Solid Earth*, 123(10):8349–8363.

- B. Mahan, J. Siebert, I. Blanchard, S. Borensztajn, J. Badro, and F. Moynier, 2018b. Constraining compositional proxies for Earth's accretion and core formation through high pressure and high temperature Zn and S metal-silicate partitioning. *Geochim. Cosmochim. Acta*, 235:21–40.
- B. Mahan, J. Siebert, E. A. Pringle, and F. Moynier, 2017. Elemental partitioning and isotopic fractionation of Zn between metal and silicate and geochemical estimation of the S content of the Earth's core. *Geochim. Cosmochim. Acta*, 196:252–270.
- W. D. Maier, S. J. Barnes, I. H. Campbell, M. L. Fiorentini, P. Peltonen, S.-J. Barnes, and R. H. Smithies, 2009. Progressive mixing of meteoritic veneer into the early Earth's deep mantle. *Nature*, 460(7255):620–623.
- U. Mann, D. J. Frost, and D. C. Rubie, 2009. Evidence for high-pressure core-mantle differentiation from the metal-silicate partitioning of lithophile and weakly-siderophile elements. *Geochim. Cosmochim. Acta*, 73(24):7360–7386.
- U. Mann, D. J. Frost, D. C. Rubie, H. Becker, and A. Audétat, 2012. Partitioning of Ru, Rh, Pd, Re, Ir and Pt between liquid metal and silicate at high pressures and high temperatures - Implications for the origin of highly siderophile element concentrations in the Earth's mantle. *Geochim. Cosmochim. Acta*, 84:593–613.
- S. Marchi, R. M. Canup, and R. J. Walker, 2018. Heterogeneous delivery of silicate and metal to the Earth by large planetesimals. *Nat. Geosci.*, 11(1):77–81.
- B. Martorell, J. Brodholt, I. G. Wood, and L. Vočadlo, 2013. The effect of nickel on the properties of iron at the conditions of Earth's inner core: Ab initio calculations of seismic wave velocities of Fe-Ni alloys. *Earth Planet. Sci. Lett.*, 365:143–151.
- B. Marty, 2012. The origins and concentrations of water, carbon, nitrogen and noble gases on Earth. *Earth Planet. Sci. Lett.*, 313-314(1):56–66.
- Y. Matsuhisa, J. R. Goldsmith, and R. N. Clayton, 1978. Mechanisms of hydrothermal crystallization of quartz at 250 C and 15 kbar. *Geochim. Cosmochim. Acta*, 42(2):173–182.
- P. McDade, B. Wood, W. Van Westrenen, R. Brooker, G. Gudmundsson, H. Soular, J. Najorka, and J. Blundy, 2002. Pressure corrections for a selection of piston-cylinder cell assemblies. *Mineral. Mag.*, 66(6):1021–1028.
- W. F. McDonough, 2003. Compositional Model for the Earth's Core. *Treatise On Geochemistry*, pages 547–568.

BIBLIOGRAPHY

- W. F. McDonough and S. S. Sun, 1995. The composition of the Earth. *Chem. Geol.*, 120(3-4):223–253.
- E. Médard, M. W. Schmidt, M. Wälle, N. S. Keller, and D. Günther, 2015. Platinum partitioning between metal and silicate melts: Core formation, late veneer and the nanonuggets issue. *Geochim. Cosmochim. Acta*, 162:183–201.
- H. J. Melosh, 1990. *Giant impacts and the thermal state of the early Earth*, volume Origin of the Earth. Oxford University Press, Newsom H.E. and Jones J.H. edition.
- G. Morard, J. Siebert, D. Andrault, N. Guignot, G. Garbarino, F. Guyot, and D. Antonangeli, 2013. The Earth’s core composition from high pressure density measurements of liquid iron alloys. *Earth Planet. Sci. Lett.*, 373:169–178.
- A. Morbidelli, J. Lunine, D. O’Brien, S. Raymond, and K. Walsh, 2012. Building Terrestrial Planets. *Annu. Rev. Earth Planet. Sci.*, 40(1):251–275.
- B. Mougél, F. Moynier, and C. Göpel, 2018. Chromium isotopic homogeneity between the Moon, the Earth, and enstatite chondrites. *Earth Planet. Sci. Lett.*, 481:1–8.
- F. Moynier, Z. Deng, A. Lanteri, R. Martins, M. Chaussidon, P. Savage, and J. Siebert, 2020. Metal-silicate silicon isotopic fractionation and the composition of the bulk Earth. *Earth Planet. Sci. Lett.*, 549:116468.
- F. Moynier, Q. Z. Yin, and E. Schauble, 2011. Isotopic evidence of Cr partitioning into Earth’s core. *Science*, 331(6023):1417–1420.
- V. R. Murthy, W. Van Westrenen, and Y. Fei, 2003. Experimental evidence that potassium is a substantial radioactive heat source in planetary cores. *Nature*, 423(6936):163–165.
- B. O. Mysen, D. Virgo, and F. A. Seifert, 1982. *The structure of silicate melts: Implications for chemical and physical properties of natural magma*, volume 20. Wiley Online Library.
- O. Nebel, K. Mezger, and W. van Westrenen, 2011. Rubidium isotopes in primitive chondrites: Constraints on Earth’s volatile element depletion and lead isotope evolution. *Earth Planet. Sci. Lett.*, 305(3-4):309–316.
- O. Nebel, P. A. Sossi, J. Foden, A. Bénard, P. A. Brandl, J. A. Stammeier, J. Lupton, M. Richter, and R. J. Arculus, 2018. Iron isotope variability in ocean floor lavas and mantle sources in the Lau back-arc basin. *Geochim. Cosmochim. Acta*, 241:150–163.
- F. Nimmo, D. O’Brien, and T. Kleine, 2010. Tungsten isotopic evolution during late-stage accretion: constraints on Earth–Moon equilibration. *Earth Planet. Sci. Lett.*, 292(3-4):363–370.

- C. A. Norris and B. J. Wood, 2017. Earth's volatile contents established by melting and vaporization. *Nature*, 549(7673):507–510.
- D. A. Northrop and R. N. Clayton, 1966. Oxygen-isotope fractionations in systems containing dolomite. *J. Geol.*, 74(2):174–196.
- D. P. O'Brien, A. Izidoro, S. A. Jacobson, S. N. Raymond, and D. C. Rubie, 2018. The Delivery of Water During Terrestrial Planet Formation. *Space Sci. Rev.*, 214(1).
- D. P. O'Brien, A. Morbidelli, and H. F. Levison, 2006. Terrestrial planet formation with strong dynamical friction. *Icarus*, 184(1):39–58.
- D. P. O'Brien, K. J. Walsh, A. Morbidelli, S. N. Raymond, and A. M. Mandell, 2014. Water delivery and giant impacts in the 'Grand Tack' scenario. *Icarus*, 239:74–84.
- P. Olson and Z. D. Sharp, 2018. Hydrogen and helium ingassing during terrestrial planet accretion. *Earth Planet. Sci. Lett.*, 498:418–426.
- H. S. C. O'Neill, 1991. The origin of the Moon and the early history of the Earth-A chemical model. Part 1: The Moon. *Geochim. Cosmochim. Acta*, 55(4):1135–1157.
- H. S. C. O'Neill, D. B. Dingwell, A. Borisov, B. Spettel, and H. Palme, 1995. Experimental petrochemistry of some highly siderophile elements at high temperatures, and some implications for core formation and the mantle's early history. *Chem. Geol.*, 120(3-4):255–273.
- H. S. C. O'Neill and S. M. Eggins, 2002. The effect of melt composition on trace element partitioning: an experimental investigation of the activity coefficients of FeO, NiO, CoO, MoO₂ and MoO₃ in silicate melts. *Chem. Geol.*, 186(1-2):151–181.
- H. S. C. O'Neill and H. Palme, 2008. Collisional erosion and the non-chondritic composition of the terrestrial planets. *Philos. Trans. R. Soc. A Math. Phys. Eng. Sci.*, 366(1883):4205–4238.
- R. A. Oriani, 1953. Thermodynamic activities in iron-nickel alloys. *Acta metall.*, 1(4):448–454.
- H. Palme and H. O'Neill, 2014. *Cosmochemical Estimates of Mantle Composition*, volume 3. Elsevier Ltd., second edition.
- H. Palme and H. S. C. O'Neill, 2003. *Cosmochemical Estimates of Mantle Composition*, volume 2. Elsevier Ltd., first edition.
- D. Perkins and R. Newton, 1981. Charnockite geobarometers based on coexisting garnet—pyroxene—plagioclase—quartz. *Nature*, 292(5819):144–146.

BIBLIOGRAPHY

- S. Péron and M. Moreira, 2018. Onset of volatile recycling into the mantle determined by xenon anomalies. *Geochemical Perspect. Lett.*, 9:21–25.
- A. H. Peslier, M. Schönbachler, H. Busemann, and S.-I. Karato, 2017. Water in the Earth's interior: Distribution and origin. *Space Sci. Rev.*, 212(1-2):743–810.
- L. Piani, Y. Marrocchi, T. Rigaudier, L. G. Vacher, D. Thomassin, and B. Marty, 2020. Earth's water may have been inherited from material similar to enstatite chondrite meteorites. *Science*, 369(6507):1110–1113.
- F. Poitrasson, 2007. Does planetary differentiation really fractionate iron isotopes? *Earth Planet. Sci. Lett.*, 256(3-4):484–492.
- F. Poitrasson, A. N. Halliday, D. C. Lee, S. Levasseur, and N. Teutsch, 2004. Iron isotope differences between Earth, Moon, Mars and Vesta as possible records of contrasted accretion mechanisms. *Earth Planet. Sci. Lett.*, 223(3-4):253–266.
- F. Poitrasson, M. Roskosz, and A. Corgne, 2009. No iron isotope fractionation between molten alloys and silicate melt to 2000 °C and 7.7 GPa: Experimental evidence and implications for planetary differentiation and accretion. *Earth Planet. Sci. Lett.*, 278(3-4):376–385.
- F. Poitrasson, T. Zambardi, T. Magna, and C. R. Neal, 2019. A reassessment of the iron isotope composition of the Moon and its implications for the accretion and differentiation of terrestrial planets. *Geochim. Cosmochim. Acta*, 267:257–274.
- V. B. Polyakov, 2009. Equilibrium iron isotope fractionation at core-mantle boundary conditions. *Science*, 323(5916):912–914.
- E. A. Pringle and F. Moynier, 2017. Rubidium isotopic composition of the Earth, meteorites, and the Moon: Evidence for the origin of volatile loss during planetary accretion. *Earth Planet. Sci. Lett.*, 473:62–70.
- E. A. Pringle, F. Moynier, P. Beck, R. Paniello, and D. C. Hezel, 2017. The origin of volatile element depletion in early solar system material: Clues from Zn isotopes in chondrules. *Earth Planet. Sci. Lett.*, 468:62–71.
- E. A. Pringle, F. Moynier, P. S. Savage, J. Badro, and J.-A. Barrat, 2014. Silicon isotopes in angrites and volatile loss in planetesimals. *Proc. Natl. Acad. Sci.*, 111(48):17029–17032.
- M. Pritchard and D. Stevenson, 2000. *Thermal aspects of a lunar origin by giant impact*, volume Origin of the Earth and Moon. University of Arizona Press Tucson, Canup R.M. and Righter K. edition.

- L. Qin, C. M. Alexander, R. W. Carlson, M. F. Horan, and T. Yokoyama, 2010. Contributors to chromium isotope variation of meteorites. *Geochim. Cosmochim. Acta*, 74(3):1122–1145.
- S. N. Raymond, T. Quinn, and J. I. Lunine, 2006. High-resolution simulations of the final assembly of Earth-like planets I. Terrestrial accretion and dynamics. *Icarus*, 183(2):265–282.
- M. Regelous, T. Elliott, and C. D. Coath, 2008. Nickel isotope heterogeneity in the early solar system. *Earth Planet. Sci. Lett.*, 272(1-2):330–338.
- A. Ricolleau, Y. Fei, A. Corgne, J. Siebert, and J. Badro, 2011. Oxygen and silicon contents of Earth’s core from high pressure metal-silicate partitioning experiments. *Earth Planet. Sci. Lett.*, 310(3-4):409–421.
- K. Righter, 2005. Highly siderophile elements: constraints on Earth accretion and early differentiation. *GMS*, 160:201–218.
- K. Righter and M. J. Drake, 1996. Core formation in Earth’s moon, Mars, and Vesta. *Icarus*, 124(2):513–529.
- K. Righter and M. J. Drake, 1997. Metal-silicate equilibrium in a homogeneously accreting earth: New results for Re. *Earth Planet. Sci. Lett.*, 146(3-4):541–553.
- K. Righter and M. J. Drake, 1999. Effect of water on metal-silicate partitioning of siderophile elements: a high pressure and temperature terrestrial magma ocean and core formation. *Earth Planet. Sci. Lett.*, 171(3):383–399.
- K. Righter and M. J. Drake, 2000. Metal/silicate equilibrium in the early earth—new constraints from the volatile moderately siderophile elements Ga, Cu, P, and Sn. *Geochim. Cosmochim. Acta*, 64(20):3581–3597.
- K. Righter and M. Ghiorso, 2012. Redox systematics of a magma ocean with variable pressure-temperature gradients and composition. *Proc. Natl. Acad. Sci.*, 109(30):11955–11960.
- K. Righter, M. Humayun, A. J. Campbell, L. Danielson, D. Hill, and M. J. Drake, 2009. Experimental studies of metal-silicate partitioning of Sb: Implications for the terrestrial and lunar mantles. *Geochim. Cosmochim. Acta*, 73(5):1487–1504.
- K. Righter, K. Nickodem, K. Pando, L. Danielson, A. Boujibar, M. Righter, and T. J. Lapen, 2017a. Distribution of Sb, As, Ge, and In between metal and silicate during accretion and core formation in the Earth. *Geochim. Cosmochim. Acta*, 198:1–16.

BIBLIOGRAPHY

- K. Righter, K. Pando, M. Humayun, N. Waesermann, S. Yang, A. Boujibar, and L. R. Danielson, 2018. Effect of silicon on activity coefficients of siderophile elements (Au, Pd, Pt, P, Ga, Cu, Zn, and Pb) in liquid Fe: Roles of core formation, late sulfide matte, and late veneer in shaping terrestrial mantle geochemistry. *Geochim. Cosmochim. Acta*, 232:101–123.
- K. Righter, K. Pando, N. Marin, D. K. Ross, M. Righter, L. Danielson, T. J. Lapen, and C. Lee, 2017b. Volatile element signatures in the mantles of Earth, Moon, and Mars: Core formation fingerprints from Bi, Cd, In, and Sn. *Meteorit. Planet. Sci.*, 22:1–22.
- K. Righter, K. Pando, D. K. Ross, M. Righter, and T. J. Lapen, 2019. Effect of silicon on activity coefficients of Bi, Cd, Sn, and Ag in liquid Fe-Si, and implications for differentiation and core formation. *Meteorit. Planet. Sci.*, 54(6):1379–1394.
- K. Righter, K. M. Pando, L. Danielson, and C. T. Lee, 2010. Partitioning of Mo, P and other siderophile elements (Cu, Ga, Sn, Ni, Co, Cr, Mn, V, and W) between metal and silicate melt as a function of temperature and silicate melt composition. *Earth Planet. Sci. Lett.*, 291(1-4):1–9.
- K. Righter, S. R. Sutton, L. Danielson, K. Pando, and M. Newville, 2016. Redox variations in the inner solar system with new constraints from vanadium XANES in spinels. *Am. Mineral.*, 101(9):1928–1942.
- A. E. Ringwood, 1977. Composition for of the core of the and implications for origin of the Earth. *Geochem. J.*, 11:111–135.
- L. Rose-Weston, J. M. Brenan, Y. Fei, R. A. Secco, and D. J. Frost, 2009. Effect of pressure, temperature, and oxygen fugacity on the metal-silicate partitioning of Te, Se, and S: Implications for earth differentiation. *Geochim. Cosmochim. Acta*, 73(15):4598–4615.
- M. Roskosz, Q. Amet, C. Fitoussi, N. Dauphas, B. Bourdon, L. Tissandier, M. Y. Hu, A. Said, A. Alatas, and E. E. Alp, 2020. Redox and structural controls on tin isotopic fractionations among magmas. *Geochim. Cosmochim. Acta*, 268:42–55.
- M. Roskosz, B. Luais, H. C. Watson, M. J. Toplis, C. M. Alexander, and B. O. Mysen, 2006. Experimental quantification of the fractionation of Fe isotopes during metal segregation from a silicate melt. *Earth Planet. Sci. Lett.*, 248(3-4):851–867.
- D. C. Rubie, 1999. Characterizing the sample environment in multianvil high-pressure experiments. *Phase Transit.*, 68(3):431–451.
- D. C. Rubie, D. J. Frost, U. Mann, Y. Asahara, F. Nimmo, K. Tsuno, P. Kegler, A. Holzheid, and H. Palme, 2011. Heterogeneous accretion, composition and core-mantle differentiation of the Earth. *Earth Planet. Sci. Lett.*, 301(1-2):31–42.

- D. C. Rubie, C. K. Gessmann, and D. J. Frost, 2004. Partitioning of oxygen during core formation on the earth and mars. *Nature*, 429(6987):58–61.
- D. C. Rubie, S. A. Jacobson, A. Morbidelli, D. P. O'Brien, E. D. Young, J. de Vries, F. Nimmo, H. Palme, and D. J. Frost, 2015. Accretion and differentiation of the terrestrial planets with implications for the compositions of early-formed Solar System bodies and accretion of water. *Icarus*, 248:89–108.
- D. C. Rubie, V. Laurenz, S. A. Jacobson, A. Morbidelli, H. Palme, A. K. Vogel, and D. J. Frost, 2016. Highly siderophile elements were stripped from Earth's mantle by iron sulfide segregation. *Science*.
- D. C. Rubie, H. J. Melosh, J. E. Reid, C. Liebske, and K. Righter, 2003. Mechanisms of metal-silicate equilibration in the terrestrial magma ocean. *Earth Planet. Sci. Lett.*, 205(3-4):239–255.
- D. C. Rubie, F. Nimmo, and H. Melosh, 2007. Formation of Earth's Core. *Treatise Geophys.*, 9:51–90.
- A. M. Rubin, 1995. Propagation of magma-filled cracks. *Annu. Rev. Earth Planet. Sci.*, 23(1):287–336.
- J. F. Rudge, T. Kleine, and B. Bourdon, 2010. Broad bounds on Earth's accretion and core formation constrained by geochemical models. *Nat. Geosci.*, 3(6):439–443.
- T. Rushmer, W. Minarik, and G. Taylor, 2000. *Physical processes of core formation*, volume Origin of the Earth and Moon. University of Arizona Press Tucson, canup r.m. and righter k. edition.
- A. E. Saal, E. H. Hauri, J. A. Van Orman, and M. J. Rutherford, 2013. Hydrogen isotopes in lunar volcanic glasses and melt inclusions reveal a carbonaceous chondrite heritage. *Science*, 340(6138):1317–1320.
- A. R. Sarafian, E. H. Hauri, F. M. McCubbin, T. J. Lapen, E. L. Berger, S. G. Nielsen, H. R. Marschall, G. A. Gaetani, K. Righter, and E. Sarafian, 2017. Early accretion of water and volatile elements to the inner Solar System: Evidence from angrites. *Philos. Trans. R. Soc. A Math. Phys. Eng. Sci.*, 375(2094).
- P. Savage, F. Moynier, H. Chen, G. Shofner, J. Siebert, J. Badro, and I. Puchtel, 2015. Copper isotope evidence for large-scale sulphide fractionation during Earth's differentiation. *Geochemical Perspect. Lett.*, pages 53–64.
- P. S. Savage and F. Moynier, 2013. Silicon isotopic variation in enstatite meteorites: Clues to their origin and Earth-forming material. *Earth Planet. Sci. Lett.*, 361:487–496.

BIBLIOGRAPHY

- M. Schiller, M. Bizzarro, and V. A. Fernandes, 2018. Isotopic evolution of the protoplanetary disk and the building blocks of Earth and the Moon. *Nature*, 555(7697):501–510.
- A.-D. Schmitt, S. J. Galer, and W. Abouchami, 2009. High-precision cadmium stable isotope measurements by double spike thermal ionisation mass spectrometry. *J. Anal. At. Spectrom.*, 24(8):1079–1088.
- R. Schoenberg and F. von Blanckenburg, 2006. Modes of planetary-scale Fe isotope fractionation. *Earth Planet. Sci. Lett.*, 252(3-4):342–359.
- R. Schoenberg, S. Zink, M. Staubwasser, and F. von Blanckenburg, 2008. The stable Cr isotope inventory of solid Earth reservoirs determined by double spike MC-ICP-MS. *Chem. Geol.*, 249(3-4):294–306.
- M. Schonbachler, R. W. Carlson, M. F. Horan, T. D. Mock, and E. H. Hauri, 2010. Heterogeneous Accretion and the Moderately Volatile Element Budget of Earth. *Science*, 328(5980):884–887.
- A. Seegers, K. van Zuilen, R. Stelwagen, P. Vroon, and W. van Westrenen, 2019. Quantifying the equilibration time of Fe, Cu and Zn concentrations and stable isotopes in metal-silicate partitioning experiments. *EPSC*, 2019:EPSC–DPS2019.
- A. Shahar, V. J. Hillgren, M. F. Horan, J. Mesa-Garcia, L. A. Kaufman, and T. D. Mock, 2015. Sulfur-controlled iron isotope fractionation experiments of core formation in planetary bodies. *Geochim. Cosmochim. Acta*, 150:253–264.
- A. Shahar, V. J. Hillgren, E. D. Young, Y. Fei, C. A. Macris, and L. Deng, 2011. High-temperature Si isotope fractionation between iron metal and silicate. *Geochim. Cosmochim. Acta*, 75(23):7688–7697.
- A. Shahar and E. D. Young, 2020. An assessment of iron isotope fractionation during core formation. *Chem. Geol.*, 554:119800.
- A. Shahar, E. D. Young, and C. E. Manning, 2008. Equilibrium high-temperature Fe isotope fractionation between fayalite and magnetite: An experimental calibration. *Earth Planet. Sci. Lett.*, 268(3-4):330–338.
- A. Shahar, K. Ziegler, E. D. Young, A. Ricolleau, E. A. Schauble, and Y. Fei, 2009. Experimentally determined Si isotope fractionation between silicate and Fe metal and implications for Earth’s core formation. *Earth Planet. Sci. Lett.*, 288(1-2):228–234.
- Z. D. Sharp, C. K. Shearer, K. D. McKeegan, J. D. Barnes, and Y. Q. Wang, 2010. The Chlorine Isotope Composition of the Moon and Implications for an Anhydrous Mantle. *Science*, 329(5995):1050–1053.

- J.-X. She, T. Wang, H. Liang, M. Muhtar, W. Li, and X. Liu, 2020. Sn isotope fractionation during volatilization of Sn(IV) chloride: Laboratory experiments and quantum mechanical calculations. *Geochim. et Cosmochim. Acta*, 269:184 – 202.
- J. Siebert, J. Badro, D. Antonangeli, and F. J. Ryerson, 2012. Metal-silicate partitioning of Ni and Co in a deep magma ocean. *Earth Planet. Sci. Lett.*, 321-322:189–197.
- J. Siebert, J. Badro, D. Antonangeli, and F. J. Ryerson, 2013. Terrestrial Accretion Under Oxidizing Conditions. *Science*, 339(6124):1194–1197.
- J. Siebert, A. Corgne, and F. J. Ryerson, 2011. Systematics of metal-silicate partitioning for many siderophile elements applied to Earth’s core formation. *Geochim. Cosmochim. Acta*, 75(6):1451–1489.
- J. Siebert, P. A. Sossi, I. Blanchard, B. Mahan, J. Badro, and F. Moynier, 2018. Chondritic Mn/Na ratio and limited post-nebular volatile loss of the Earth. *Earth Planet. Sci. Lett.*, 485:130–139.
- V. S. Solomatov and L.-N. Moresi, 2000. Scaling of time-dependent stagnant lid convection: Application to small-scale convection on Earth and other terrestrial planets. *J. Geophys. Res. Solid Earth*, 105(B9):21795–21817.
- P. A. Sossi, G. P. Halverson, O. Nebel, and S. M. Eggins, 2015. Combined separation of Cu, Fe and Zn from rock matrices and improved analytical protocols for stable isotope determination. *Geostand. Geoanalytical Res.*, 39(2):129–149.
- P. A. Sossi and F. Moynier, 2017. Chemical and isotopic kinship of iron in the Earth and Moon deduced from the lunar Mg-Suite. *Earth Planet. Sci. Lett.*, 471:125–135.
- P. A. Sossi, F. Moynier, and K. Van Zuilen, 2018. Volatile loss following cooling and accretion of the Moon revealed by chromium isotopes. *Proc. Natl. Acad. Sci. U. S. A.*, 115(43):10920–10925.
- P. A. Sossi, O. Nebel, M. Anand, and F. Poitrasson, 2016a. On the iron isotope composition of Mars and volatile depletion in the terrestrial planets. *Earth Planet. Sci. Lett.*, 449:360–371.
- P. A. Sossi, O. Nebel, and J. Foden, 2016b. Iron isotope systematics in planetary reservoirs. *Earth Planet. Sci. Lett.*, 452:295–308.
- P. A. Sossi, O. Nebel, H. S. C. O’Neill, and F. Moynier, 2017. Zinc isotope composition of the Earth and its behaviour during planetary accretion. *Chem. Geol.*, 477:73–84.

BIBLIOGRAPHY

- T. Spohn and G. Schubert, 1991. Thermal equilibration of the Earth following a giant impact. *Geophys. J. Int.*, 107(1):163–170.
- E. Steenstra, D. Dankers, J. Berndt, S. Klemme, S. Matveev, and W. van Westrenen, 2019. Significant depletion of volatile elements in the mantle of asteroid Vesta due to core formation. *Icarus*, 317:669 – 681.
- E. S. Steenstra, Y. Lin, D. Dankers, N. Rai, J. Berndt, S. Matveev, and W. Van Westrenen, 2017. The lunar core can be a major reservoir for volatile elements S, Se, Te and Sb. *Sci. Rep.*, 7(1):1–8.
- E. S. Steenstra, N. Rai, J. S. Knibbe, Y. H. Lin, and W. van Westrenen, 2016. New geochemical models of core formation in the Moon from metal-silicate partitioning of 15 siderophile elements. *Earth Planet. Sci. Lett.*, 441:1–9.
- L. Stixrude and J. M. Brown, 1998. The Earth’s core. *Rev. Mineral.*, 37:261–282.
- T. A. Suer, J. Siebert, L. Remusat, N. Menguy, and G. Fiquet, 2017. A sulfur-poor terrestrial core inferred from metal–silicate partitioning experiments. *Earth Planet. Sci. Lett.*, 469:84–97.
- S. Taylor and M. Norman, 1990. *Accretion of differentiated planetesimals to the Earth*, volume Origin of the Earth. Oxford Univ. Press, newsom h.e. and jones j.h. edition.
- S. R. Taylor, 2001. *Solar system evolution: A new perspective*. Cambridge University Press.
- F.-Z. Teng, N. Dauphas, S. Huang, and B. Marty, 2013. Iron isotopic systematics of oceanic basalts. *Geochim. Cosmochim. Acta*, 107:12–26.
- Y. Thibault and M. J. Walter, 1995. The influence of pressure and temperature on the metal-silicate partition coefficients of nickel and cobalt in a model C1 chondrite and implications for metal segregation in a deep magma ocean. *Geochim. Cosmochim. Acta*, 59(5):991–1002.
- M. M. Thiemens, P. Sprung, R. O. Fonseca, F. P. Leitzke, and C. Münker, 2019. Early Moon formation inferred from hafnium–tungsten systematics. *Nat. Geosci.*, 12(9):696–700.
- P. Thomas, J. W. Parker, L. McFadden, C. T. Russell, S. Stern, M. Sykes, and E. Young, 2005. Differentiation of the asteroid Ceres as revealed by its shape. *Nature*, 437(7056):224–226.

- E. Thompson, A. Davis, W. Bi, J. Zhao, E. Alp, D. Zhang, E. Greenberg, V. Prakapenka, and A. Campbell, 2018. High-pressure geophysical properties of Fcc phase FeHx. *Geochem. Geophys. Geosy.*, 19(1):305–314.
- W. B. Tonks and H. J. Melosh, 1993. Magma ocean formation due to giant impacts. *J. Geophys. Res.: Planets*, 98(E3):5319–5333.
- E. R. Toth, M. A. Fehr, M. Friebel, and M. Schönbacher, 2020. Cadmium isotopes in chondrites and acid leachates: Nucleosynthetic homogeneity and a monitor for thermal neutron capture effects. *Geochim. Cosmochim. Acta*, 274:286–301.
- A. Trinquier, J. L. Birck, C. J. Allègre, C. Göpel, and D. Ulfbeck, 2008. ^{53}Mn - ^{53}Cr systematics of the early Solar System revisited. *Geochim. Cosmochim. Acta*, 72(20):5146–5163.
- J. M. Tucker and S. Mukhopadhyay, 2014. Evidence for multiple magma ocean outgassing and atmospheric loss episodes from mantle noble gases. *Earth Planet. Sci. Lett.*, 393:254–265.
- J. Tuff, B. J. Wood, and J. Wade, 2011. The effect of Si on metal-silicate partitioning of siderophile elements and implications for the conditions of core formation. *Geochim. Cosmochim. Acta*, 75(2):673–690.
- B. Tuller-Ross, B. Marty, H. Chen, K. A. Kelley, H. Lee, and K. Wang, 2019. Potassium isotope systematics of oceanic basalts. *Geochim. Cosmochim. Acta*, 259:144–154.
- K. Umemoto and K. Hirose, 2015. Liquid iron-hydrogen alloys at outer core conditions by first-principles calculations. *Geophys. Res. Lett.*, 42(18):7513–7520.
- H. C. Urey, 1947. The thermodynamic properties of isotopic substances. *J. Chem. Soc.*, pages 562–581.
- M. I. Varas-Reus, S. König, A. Yierpan, J.-P. Lorand, and R. Schoenberg, 2019. Selenium isotopes as tracers of a late volatile contribution to Earth from the outer Solar System. *Nat. Geosci.*, 12(9):779–782.
- A. K. Vogel, E. S. Jennings, V. Laurenz, D. C. Rubie, and D. J. Frost, 2018. The dependence of metal-silicate partitioning of moderately volatile elements on oxygen fugacity and Si contents of Fe metal: Implications for their valence states in silicate liquids. *Geochim. Cosmochim. Acta*, 237:275–293.
- J. Wade and B. Wood, 2005. Core formation and the oxidation state of the Earth. *Earth Planet. Sci. Lett.*, 236(1-2):78–95.

BIBLIOGRAPHY

- J. Wade, B. J. Wood, and J. Tuff, 2012. Metal-silicate partitioning of Mo and W at high pressures and temperatures: Evidence for late accretion of sulphur to the Earth. *Geochim. Cosmochim. Acta*, 85:58–74.
- C. Wagner, 1952. Thermodynamics of alloys. Technical report, Addison-Wesley Press,.
- T. Wakamatsu, K. Ohta, T. Yagi, K. Hirose, and Y. Ohishi, 2018. Measurements of sound velocity in iron–nickel alloys by femtosecond laser pulses in a diamond anvil cell. *Phys. Chem. Miner.*, 45(6):589–595.
- D. Walker, 2000. Core participation in mantle geochemistry: geochemical society Ingerson lecture, GSA Denver, October 1999. *Geochim. Cosmochim. Acta*, 64(17):2897–2911.
- D. Walker and C. Agee, 1989. Partitioning “equilibrium”, temperature gradients, and constraints on Earth differentiation. *Earth Planet. Sci. Lett.*, 96(1-2):49–60.
- R. J. Walker, 2009. Highly siderophile elements in the Earth, Moon and Mars: Update and implications for planetary accretion and differentiation. *Chem. Erde*, 69(2):101–125.
- K. J. Walsh and A. Morbidelli, 2011. The effect of an early planetesimal-driven migration of the giant planets on terrestrial planet formation. *Astron. Astrophys.*, 526(16):1–8.
- K. J. Walsh, A. Morbidelli, S. N. Raymond, D. P. O’Brien, and A. M. Mandell, 2012. Populating the asteroid belt from two parent source regions due to the migration of giant planets-"The Grand Tack". *Meteorit. Planet. Sci.*, 47(12):1941–1947.
- M. J. Walter and Y. Thibault, 1995. Partitioning of tungsten and molybdenum between metallic liquid and silicate melt. *Science*, 270(5239):1186–1189.
- K. Wang and S. B. Jacobsen, 2016. Potassium isotopic evidence for a high-energy giant impact origin of the Moon. *Nature*, 538(7626):487–490.
- K. Wang, S. B. Jacobsen, F. Sedaghatpour, H. Chen, and R. L. Korotev, 2015. The earliest Lunar Magma Ocean differentiation recorded in Fe isotopes. *Earth Planet. Sci. Lett.*, 430:202–208.
- K. Wang, F. Moynier, N. Dauphas, J. A. Barrat, P. Craddock, and C. K. Sio, 2012. Iron isotope fractionation in planetary crusts. *Geochim. Cosmochim. Acta*, 89:31–45.
- X. Wang, Q. Amet, C. Fitoussi, and B. Bourdon, 2018. Tin isotope fractionation during magmatic processes and the isotope composition of the bulk silicate Earth. *Geochim. Cosmochim. Acta*, 228:320–335.

- X. Wang, C. Fitoussi, B. Bourdon, B. Fegley, and S. Charnoz, 2019. Tin isotopes indicative of liquid–vapour equilibration and separation in the Moon-forming disk. *Nat. Geosci.*, 12(9):707–711.
- Z. Wang and H. Becker, 2013. Ratios of S, Se and Te in the silicate Earth require a volatile-rich late veneer. *Nature*, 499(7458):328–331.
- Z. Wang, V. Laurenz, S. Petitgirard, and H. Becker, 2016. Earth’s moderately volatile element composition may not be chondritic: Evidence from In, Cd and Zn. *Earth Planet. Sci. Lett.*, 435:136–146.
- H. Wanke and T. Gold, 1981. Constitution of Terrestrial Planets. *Philos. Trans. R. Soc. London. Ser. A, Math. Phys. Sci.*, 303(1477):287–302.
- V. Wanless, A. Shaw, M. Behn, S. Soule, J. Escartín, and C. Hamelin, 2015. Magmatic plumbing at Lucky Strike volcano based on olivine-hosted melt inclusion compositions. *Geochem. Geophys. Geosy.*, pages 126–147.
- J. T. Wasson, G. W. Kallemeyn, S. K. Runcorn, G. Turner, and M. M. Woolfson, 1988. Compositions of chondrites. *Philos. Trans. R. Soc. London. Ser. A, Math. Phys. Sci.*, 325(1587):535–544.
- P. R. Weissman, 2014. The solar system and its place in the galaxy. In *Encyclopedia of the Solar System*, pages 3–28. Elsevier.
- G. Wetherill and G. R. Stewart, 1989. Accumulation of a swarm of small planetesimals. *Icarus*, 77(2):330–357.
- S. Weyer, A. D. Anbar, G. P. Brey, C. Münker, K. Mezger, and A. B. Woodland, 2005. Iron isotope fractionation during planetary differentiation. *Earth Planet. Sci. Lett.*, 240(2):251–264.
- U. Wiechert and A. N. Halliday, 2007. Non-chondritic magnesium and the origins of the inner terrestrial planets. *Earth Planet. Sci. Lett.*, 256(3-4):360–371.
- H. M. Williams, B. J. Wood, J. Wade, D. J. Frost, and J. Tuff, 2012. Isotopic evidence for internal oxidation of the Earth’s mantle during accretion. *Earth Planet. Sci. Lett.*, 321-322:54–63.
- F. Wombacher, M. Rehkämper, K. Mezger, A. Bischoff, and C. Münker, 2008. Cadmium stable isotope cosmochemistry. *Geochim. Cosmochim. Acta*, 72(2):646–667.
- F. Wombacher, M. Rehkämper, K. Mezger, and C. Münker, 2003. Stable isotope compositions of cadmium in geological materials and meteorites determined by multiple-collector ICPMS. *Geochim. Cosmochim. Acta*, 67(23):4639–4654.

BIBLIOGRAPHY

- B. Wood, 1991. Oxygen barometry of spinel peridotites. *Rev. Mineral. Geochemistry*, 25:417–432.
- B. J. Wood and A. N. Halliday, 2010. The lead isotopic age of the Earth can be explained by core formation alone. *Nature*, 465(7299):767–770.
- B. J. Wood, E. S. Kiseeva, and F. J. Mirolo, 2014. Accretion and core formation: The effects of sulfur on metal-silicate partition coefficients. *Geochim. Cosmochim. Acta*, 145:248–267.
- B. J. Wood, J. Li, and A. Shahar, 2013. Carbon in the core: its influence on the properties of core and mantle. *Rev. Mineral. Geochem.*, 75(1):231–250.
- B. J. Wood, S. G. Nielsen, M. Rehkämper, and A. N. Halliday, 2008. The effects of core formation on the Pb- and Tl- isotopic composition of the silicate Earth. *Earth Planet. Sci. Lett.*, 269(3-4):326–336.
- B. J. Wood, D. J. Smythe, and T. Harrison, 2019. The condensation temperatures of the elements: A reappraisal. *Am. Mineral.*, 104(6):844–856.
- B. J. Wood, M. J. Walter, and J. Wade, 2006. Accretion of the Earth and segregation of its core. *Nature*, 441(7095):825–833.
- A. B. Woodland and R. J. Angel, 1997. Reversal of the orthoferrosilite-high-P clinofersilite transition, a phase diagram for FeSiO_3 and implications for the mineralogy of the Earth's upper mantle. *Eur. J. Mineral.*, pages 245–254.
- A. B. Woodland and H. S. O'Neill, 1993. Synthesis and stability of $\text{Fe}_3^{2+}\text{Fe}_2^{3+}\text{-Si}_3\text{O}_{12}$ garnet and phase relations with $\text{Fe}_3\text{Al}_2\text{Si}_3\text{O}_{12}\text{-Fe}_3^{2+}\text{Fe}_2^{3+}\text{-Si}_3\text{O}_{12}$ solutions. *Am. Mineral.*, 78(9-10):1002–1015.
- Y. Xia, E. Kiseeva, J. Wade, and F. Huang, 2019. The effect of core segregation on the Cu and Zn isotope composition of the silicate Moon. *Geochemical Perspect. Lett.*, pages 12–17.
- T. Yagi, M. Akaogi, O. Shimomura, T. Suzuki, and S.-I. Akimoto, 1987. In situ observation of the olivine-spinel phase transformation in Fe_2SiO_4 using synchrotron radiation. *J. Geophys. Res. Solid Earth*, 92(B7):6207–6213.
- T. Yagi and S.-I. Akimoto, 1976. Direct determination of coesite-stishovite transition by in-situ X-ray measurements. *Tectonophysics*, 35(1-3):259–270.
- A. Yasuda, T. Fujii, and K. Kurita, 1994. Melting phase relations of an anhydrous mid-ocean ridge basalt from 3 to 20 GPa: implications for the behavior of subducted oceanic crust in the mantle. *J. Geophys. Res.*, 99(B5):9401–9414.

- W. Yi, A. N. Halliday, J. C. Alt, D.-c. Lee, and M. Rehk, 2000. Implications for chalcophile element fractionation in the Earth pressure. *J. Geophys. Res.*, 105:927–949.
- T. Yoshino, M. J. Walter, and T. Katsura, 2003. Core formation in planetesimals triggered by permeable flow. *Nature*, 422(6928):154–157.
- E. Young, A. Shahar, F. Nimmo, H. Schlichting, E. Schauble, H. Tang, and J. Labidi, 2019. Near-equilibrium isotope fractionation during planetesimal evaporation. *Icarus*, 323:1–15.
- G. Zellars, S. Payne, J. Morris, and R. Kipp, 1959. The activities of iron and nickel in liquid Fe-Ni alloys. *Trans. Metall. Soc.*, 215:181–185.
- K. Ziegler, E. D. Young, E. A. Schauble, and J. T. Wasson, 2010. Metal-silicate silicon isotope fractionation in enstatite meteorites and constraints on Earth’s core formation. *Earth Planet. Sci. Lett.*, 295(3-4):487–496.